STRUCTURAL, MAGNETIC AND MAGNETOCALORIC STUDIES IN SOME Gd-Si-Ge BASED INTERMETALLICS AND LANTHANUM TELLURIUM MANGANITES

THESIS SUBMITTED TO
THE UNIVERSITY OF KERALA
FOR THE AWARD OF THE DEGREE OF
DOCTOR OF PHILOSOPHY
IN PHYSICS
UNDER THE FACULTY OF SCIENCE

By

BHAGYA UTHAMAN

MATERIALS SCIENCE AND TECHNOLOGY DIVISION
CSIR - NATIONAL INSTITUTE FOR INTERDISCIPLINARY
SCIENCE & TECHNOLOGY (NIIST),
THIRUVANANTHAPURAM- 695 019
KERALA, INDIA

2017

Dedicated to……

My family

DECLARATION

I hereby declare that the Ph. D. thesis entitled **"STRUCTURAL, MAGNETIC AND MAGNETOCALORIC STUDIES IN SOME Gd-Si-Ge BASED INTERMETALLICS AND LANTHANUM TELLURIUM MANGANITES"** is an independent work carried out by me at the Materials Science and Technology Division of CSIR - National Institute for Interdisciplinary Science and Technology (NIIST), Thiruvananthapuram under the supervision of Dr. Manoj Raama Varma and it has not been submitted anywhere else for any other degree, diploma or title.

BHAGYA UTHAMAN

Place: Thiruvananthapuram
Date: 17-08-2017

राष्ट्रीय अंतर्विषयी विज्ञान तथा प्रौद्योगिकी संस्थान
NATIONAL INSTITUTE FOR INTERDISCIPLINARYSCIENCE AND TECHNOLOGY
वैज्ञानिक तथा औद्योगिक अनुसंधान परिषद् | Council of Scientific and Industrial Research
इंडस्ट्रियल इस्टेट पी.ओ, पाप्पनंकोड, तिरुवनंतपुरम, भारत - 695 019 | Industrial Estate P.O., Pappanamcode, Thiruvananthapuram, India - 695 019

CERTIFICATE

This is to certify that the work embodied in the thesis entitled **"STRUCTURAL, MAGNETIC AND MAGNETOCALORIC STUDIES IN SOME Gd-Si-Ge BASED INTERMETALLICS AND LANTHANUM TELLURIUM MANGANITES"** has been carried out by **Ms. Bhagya Uthaman** under my supervision and guidance at the Materials Science and Technology Division of CSIR - National Institute for Interdisciplinary Science and Technology (NIIST), Thiruvananthapuram.

Dr. Manoj Raama Varma
Senior Principal Scientist
CSIR-NIIST
Thiruvananthapuram

Acknowledgements

It is with great pleasure that I extend my deepest sense of gratitude to Dr. Manoj Raama Varma, my thesis supervisor, for suggesting me the research problem. His valuable support, encouragement and guidance throughout the research period has led to the successful completion of this work.

I am grateful to Dr. A. Ajayaghosh, (Director, NIIST) and Dr. Suresh Das and Dr. Gangan Prathap (Former Directors, NIIST) for providing the facilities for carrying out the research work. I am deeply indebted to Dr. P. Prabhakar Rao (Head, MSTD, NIIST), Dr. M. L. P. Reddy, Dr. U. Syamaprasad and Dr. M. T. Sebastian (Former Heads, MSTD, NIIST), Dr. Jose James (Head, Functional Materials) and Dr. Harikrishna Bhat (Head, Metals and Minerals).

I would like to express my sincere and heartfelt thanks to Dr. Senoy Thomas (DST Inspire Faculty and Assistant Professor, CUSAT) for his constant support, encouragement and creative discussions, which helped me to shape my research focus. I am extremely grateful to him for contributing his time and providing insightful suggestions and comments to improve the quality of this work. I would like to thank Dr. Vasundhara Mutta (Scientist, MSTD), Dr. Raj Shankar (Scientist Fellow) for the help rendered during the course of this work.

I would like to express my sincere thanks to Prof. K. G. Suresh, Indian Institute of Technology, Bombay for his constant encouragement and support during the research work. I would like to extend my sincere gratitude to Dr. P. N. Santhosh (Indian Institute of Technology, Madras) for scientific discussions and DSC measurements, which benefited me a lot. I would also like to thank Dr. Deepshikha Jaiswal Nagar (Assistant Professor, IISER, Trivandrum) for fruitful discussions and Low Temperature XRD measurements.

It is indeed my pleasure to thank Dr. G. Subodh, Head, Department of Physics, Kariavattom Campus, University of Kerala, and Dr. V. Biju, Assistant Professor, Department of Physics, Kariavattom Campus, University of Kerala, for their timely help and valuable suggestions. I am greatly indebted to my colleagues Dr. Vipin C. Bose, Ms. Maniammal, Ms. Aiswarya Raj, Ms. Asitha Subash, Ms. Venus at Department of Physics,

Kariavattom Campus, University of Kerala for their support. I am also grateful to Dr. G. Madhu, Assistant Professor, University College for his encouragement.

I am also grateful to the NIIST administration for extending all the timely help. I would like to acknowledge and express my deepest sense of gratitude to Kerala State Council for Science, Technology and Environment (KSCSTE) and Council for Scientific and Industrial Research (CSIR) for providing the research fellowships to carry out this work. Apart from that, I also wish to acknowledge the funding agencies such as DST and BRNS for financial support during the various stages of my research work.

I would also like to thank Dr. K. P. Surendran, Dr. S. Ananthakumar, Dr. E. Bhoje Gowd, Dr. U. T. S. Hareesh, Dr. T. P. D. Rajan, Dr. S. Savithri, Mr. C. K. Chandrakanth, Mr. Peer Muhammad, Mr. Antony for their support and encouragement. I would also grateful to the entire NIIST community for their support. I would like to thank Mr. P. Gurusamy, Mr. M. R. Chandran, Mrs. Lucy Paul, Mr. Prithviraj, Mrs. V. Soumya, Mr. Harish Raj V. for extending the XRD and SEM studies for the research work. The support of Mr. Robert Philip and Mr. Kiran Mohan for TEM measurements is greatly acknowledged. The support of all the other scientists of NIIST is greatly acknowledged.

I would like to thank our technical assistants Mr. S. Vishnu, Mr. M. Mahesh kumar Mr. Dinesh Jose and Mr. Firozkhan for helping me with the arc melting process. I am very much thankful to Mr. Ajeesh P. Paulose for his technical support in PPMS measurements. I am also highly thankful to Mr. Sisupalan and Mr. Brahmakumar for their timely technical support for vacuum sealing of the quartz tubes. I am also thankful to all the office and library staff at NIIST for their kind cooperation.

The valuable advice and help provided by the senior research scholars, Dr. C. P. Reshmi, Dr. P. Neenu Lekshmi, Ms. G.R. Raji, Dr. Neson Varghese, Dr. Pillai Aswathy Mohan and Dr. Anooja J. Babu are acknowledged with gratitude. Their constant support and advice has helped me greatly throughout this research. I am extremely grateful to Dr. P. Neenu Lekshmi and Ms. G.R. Raji for being with me throughout my research and extending their suggestions. I would also like to thank Mr. Rajesh Kumar R. for the valuable suggestions rendered during paper work.

The most important people who played the key role in shaping this thesis are my lab-mates. I would specially like to thank my colleagues Ms. K. Aswathi, Mr. Rojerce Brown Job, Ms. Revathy. R, Ms. Aswathy V. S., Mr. T. Thanveer and Mr. B. Arun. I would

also like to thank my lab mates Ms. P. P. Jasnamol, Ms. B. Sudakshina, Mr. S. Rahul, Ms. Annrose Sunny, Mr. M.V. Suneesh, for their help and support. Further, I thank all my seniors and friends at Fine Ceramics especially Dr. Dhanesh Thomas, Dr. K. M. Manu, Dr. Chameswary, Mr. P. Abhilash, Dr. L. K. Namitha, Ms. T. H. Gayathri, Mr. K. S. Dijith, Ms. R. Aiswarya, Mr. S. Arun , Ms. D. R. Leskhmi, Ms. Angel Mary Joseph, Ms. I.J. Induja, Ms. Kanakangi S Nair and Ms. Roshini S Babu for their love and support. I would also like to thank Ms. Parvathi S. Babu, Ms. Jerin, Ms. B. Lakshmi and Ms. Hridya Rajan for their timely help. I am also thankful to my former colleagues: Mr. Unnikrishnan and Ms. Chinthu Sukumar for their love and support. I would also like to thank all my friends at NIIST for their love and support. My heartfelt thanks are duly extended to my friends at IIT Bombay, IIT Madras and IISER, Trivandrum: Mr. Venketaswara Yenugonda, Ms. Sharannia Mappa, Ms. Karthika, Ms. Ranjana, Ms. P. Manju for their help in XRD, DSC and low temperature XRD measurements.

I am also thankful to all my teachers at Sharjah Indian School, Sharjah, UAE for their love and support. I would also like to thank my teachers at Government College for Women, Vazhuthacaud: Mr. S. Devarajan (Rtd.), Dr. Sudarsana kumar (Rtd.), Mr. Ajith kumar (Rtd.), Dr. Lathikadevi (Rtd.), Mrs. K.C.Geetha (Rtd.), Mr. Jayakumar (Rtd.), Dr. Gopakumar, Dr. Chandini Sam, Dr. Neena Sugathan, Mrs. Prabitha and our lab assistants Mr. Mahesh, Mr. Nataraj and Mr. Wilson for their support throughout my life.

I owe an unlimited debt of gratitude to my parents, especially my mother, Sushama Uthaman, my guide and my mentor, for her unconditional love. Without her support and encouragement, I would not have reached this stage of my life. I am also indebted to my father, Mr. M. Uthaman for his constant support and guidance at each and every stage of my life. I am also grateful to my husband, Mr. Akshay V.R. for his love, support, encouragement and understanding, without which I would not have achieved what I have. I am also indebted to all my family members for their encouragement, love, support and understandability throughout these years which has helped me in the successful and comfortable completion of this work.

Last but not the least, I thank GOD, the Almighty, for his blessings and being so kind to me throughout my life.

Bhagya Uthaman

Contents

List of tables

List of figures

Abbreviations

AC	Alternating current
AFM	Antiferromagnetic
Ar	Argon
B	Magnetic induction
BSE	Back-scattered electrons
C	Curie constant
CFCs	Chlorofluorocarbon
C_H	Specific heat
CW	Curie-Wiess
DC	Direct current
DE	Double exchange
DSC	Differential Scanning Calorimetry
EDS	Energy dispersive X-ray spectroscopy
ESR	Electron spin resonance
f	Frequency
FCC	Field cooled cool
FCW	Field cooled warm
FM	Ferromagnetic
FWHM	Full width half maximum
GKA	Goodenough-Kanamori-Anderson
GMCE	Giant magnetocaloric effect
GP	Griffiths like phases
GSAS	General structure analysis system

H	Magnetic Field
H_{ex}	Exchange Hamiltonian
H_C	Coercivity
HCFCs	Hydro chlorofluorocarbon
HFCs	Hydro fluorocarbon
HRTEM	High resolution transmission electron microscopy
ICDD	International Center for Diffraction Data
ICSD	Inorganic Crystal Structure Database
J	Total angular momentum quantum number
L	Orbital quantum number
M	Magnetization
MAP	Modified arrott plot
MCE	Magnetocaloric effect
MFT	Mean-field theory
M_r	Remanent magnetization
MR	Magnetic refrigeration
M_s	Saturation magnetization
N	Avogardo number
O	Oxygen
PM	Paramagnetic
PPMS	Physical property measurement system
RC	Refrigerant Capacity
RCP	Relative cooling power
RKKY	Ruderman-Kittel-Kasuya-Yosida

S	Spin quantum number
SAED	Selected area electron diffraction
SE	Super exchange
SEM	Scanning electron microscopy
SG	Spin glass
S_{el}	Electronic entropy
S_{Lat}	lattice entropy
S_M	Magnetic entropy
ΔS_M	Isothermal magnetic entropy change
T	Temperature
ΔT_{ad}	Adiabatic temperature change
T_C	Curie temperature
T_f	Freezing temperature
T_G	Griffiths temperature
TM	Transition metal
T_N	Néel temperature
T_{SG}	Spin glass freezing temperature
VSM	Vibrating sample magnetometer
XRD	X-ray diffraction
XPS	X-ray Photoelectron spectroscopy
ZFC	Zero field cooled

Preface

Magnetic refrigeration, a potential cooling technology based on magnetocaloric effect (MCE) has attracted worldwide attention owing to its higher efficiency and eco-friendly nature compared to the conventional vapour compression-expansion technique. MCE is the thermal response of the magnetic material to an applied magnetic field and is induced by the coupling of magnetic sub lattice with an external magnetic field. It is defined as the reversible change in the magnetic component of total entropy (and temperature) of a material upon the application or removal of magnetic field. Magnetic refrigerants, such as Gd-Si-Ge, La-Fe-Si and its hydrides, Mn-Fe-P-As, Ni-Mn-Z (Z= In, Sn, Sb, Ga) based Heusler alloys and manganites have come to research focus. Research on Gd-Si-Ge compounds are of special interest owing to the existence of a strong correlation between its crystal structure and magnetic properties. Giant MCE in Gd-Si-Ge system has been attributed to the coupled magneto-structural transition from the high temperature monoclinic paramagnetic phase to the low temperature orthorhombic ferromagnetic phase that occurs in the vicinity of the magnetic ordering temperature. In addition to intermetallics, electron-doped manganites have also been found to exhibit large magnetocaloric effect (MCE) under moderate applied fields. The present thesis work focuses on the magnetic and magnetocaloric properties of Gd-Si-Ge based intermetallics and lanthanum tellurium manganites.

The **first chapter** is an overview on the fundamentals of magnetism and its applications and the **second chapter** introduces the features of Gd-Si-Ge based intermetallics and lanthanum tellurium manganites in detail. The preparation and characterization techniques adopted throughout the research work are discussed in **third chapter**.

The **fourth chapter** discusses the structural, magnetic and magnetocaloric properties of Nd substituted $Gd_5Si_2Ge_2$ with x=0, 0.05, 0.1 and 0.2. The composition with x = 0.05 crystallizes in monoclinic $Gd_5Si_2Ge_2$ structure with $P112_1/a$ space group and undergoes a first order phase transition with a Curie temperature of 275 K. With increase in Nd content to x = 0.1, the compound is found to stabilize in orthorhombic Gd_5Si_4 phase with Pnma space group. The compounds with x = 0.1 and 0.2 undergoes a second order magnetic transition at 300 K and 293 K, respectively. A maximum entropy change for $Gd_{5-x}Nd_xSi_2Ge_2$ alloys with x = 0.05, 0.1, and 0.2 are 12.8, 7.6, and 7.2 J/kg K respectively, for a field change of 50 kOe. A large relative cooling power of 295, 205, and 188 J/kg are obtained for x = 0.05, 0.1, and 0.2,

respectively, fulfilling the required criteria for a potential magnetic refrigerant in the room temperature regime.

The **fifth chapter** examines the influence of cobalt on the structure, magnetic and magnetocaloric properties of $Gd_5Si_{2-x}Co_xGe_2$ (x=0, 0.1, 0.2 and 0.4). Structural studies show that the substituted compounds exhibit a multi-phase nature. An anomalous low field magnetic behavior indicating a Griffiths-like phase has been observed which is attributed to the local disorder within the crystallographic structure which is stabilized and enhanced by competing intra-layer and inter-layer magnetic interactions. The magnetostructural transition results in entropy changes ($-\Delta S_M$) of 9 J/kg K at 260 K for x=0.1, 8.5 J/kg K at 245 K for x=0.2 and 4.2 J/kg K at 210 K for x=0.4 for a field change of 50 kOe. Universal curve analysis has been carried out on substituted samples to study the order of magnetic transition.

Chapter 6 deals with the role of cobalt and iron in tuning the magnetocaloric properties of $Gd_5Si_{1.7}Ge_{2.3-x}TM_x$ (TM=Co and Fe) with x=0, 0.1, 0.2, 0.3 and 0.4. The Curie temperature could be tuned to near room temperature with the substitution of iron and cobalt. Cobalt substitution results in maximum entropy changes of 12.8 J/kg K at 243 K for x=0.1, 14.5 J/kg K at 262 K for x=0.2, 10.4 J/kg K at 270 K for x=0.3 and 5.8 J/kg K at 283 K for x=0.4 for a field change of 50 kOe. The maximum entropy change ($-\Delta S_M$) for iron substituted samples are 11.2J/kg K at 247 K for x=0.1, 12.7 J/kg K at 253 K for x=0.2, 8.3 J/kg K at 273 K for x=0.3 and 7 J/kg K at 287 K for x=0.4 for a field change of 50 kOe. Universal curve behavior of the substituted samples is also discussed in the chapter.

Chapter 7 highlights the effect of cobalt substitution on the structural, magnetic and magnetocaloric properties of electron-doped manganite $La_{0.7}Te_{0.3}Mn_{1-x}Co_xO_3$ (x =0, 0.1, 0.2, 0.25, 0.3 and 0.5). Cobalt substitution induces a structural transition from rhombohedral (R-3c space group) to orthorhombic (Pbnm space group). X-ray photoelectron spectroscopy (XPS) indicates that the structural transition is due to the disordered distribution of Mn^{2+}/Mn^{3+} and Co^{2+}/Co^{3+} ions. Re-entrant spin glass behavior is observed at low doping concentrations due to the presence of competing FM– AFM exchange interactions. Magnetocaloric property of the electron-doped manganite has been investigated. Relatively large values and broad temperature interval of MCE makes the present compounds promising candidates for sub-room magnetic refrigeration applications. The entire work has been summarized in the **Chapter 8** along with the prospects for some future work.

Chapter 1

Introduction

This chapter gives a brief introduction to magnetism and the different types of magnetic exchange interactions. A brief introduction to magnetocaloric effect is also presented.

1.1. Introduction to Magnetism

Magnetism is a fascinating and truly exciting phenomenon by which certain materials exert an attractive or repulsive force on one another. The history of magnetism dates back to centuries and begins with a mineral named magnetite (Fe_3O_4), the first magnetic material known to man. The fact that the magnets align in a unique manner together with the fact that the Earth itself is a magnet led to the discovery of the *compass*, an instrument used quite effectively for navigation purposes, and this has aided the faster development of civilization. Magnetic materials are indispensable in modern technology and constitute a wide variety of materials used in compass, toys, security, health care, communication, transportation, electronic devices, permanent magnets, magnetic recording media and numerous other aspects of daily life. The development of quantum mechanics gave more insights into the microscopic principles of magnetism, which has been able to explain the various magnetic properties quite successfully.

The breakthrough in understanding the principles of magnetism was made through the discovery of the relation between electricity and magnetism in the 19th century. The movement of charged particles in a wire or an atom produces an electric current, and each atom represents a tiny permanent magnet. The elementary quantity in solid-state magnetism is the magnetic moment ***m*** (Coey, 2009). The revolving electron produces an orbital magnetic moment associated with its orbital motion around the nucleus and a spin magnetic moment associated with the spin about its own axis. The nucleus itself possesses spin, but the corresponding nuclear moments are three orders of magnitude smaller than that associated with electrons, so we often neglect them. In most materials, these magnetic moments cancel each other out, and only a few transition metal atoms or ions retain a resultant moment on the atomic scale in solids. In certain materials, the magnetic moments of a large fraction of the electrons experience a force which tries to align it with an externally applied field, similar to a compass needle (Spladin, 2011).

When a magnetic field is applied to a material, the magnetic moments within the material tend to become aligned with the field, and produces a magnetic field, the magnetization (M), which is a measure of the magnetic moment per unit volume of the material. Magnetization (M) can also be expressed per unit mass and is called the specific magnetization (σ). The field applied to the material is known as the applied field (H) and represents the total field that would be present if it was applied to vacuum. Magnetic

induction (B) represents the total flux of magnetic field lines through a unit cross-sectional area of the material which, includes both lines of force from the applied field and from the magnetization of the material and is given by:

$$B = \mu_0(M+H) \qquad (1.1)$$

where μ_0 is the permeability of free space and is equal to $4\pi \times 10^{-7}$ H/m.

Magnetic susceptibility (χ), describes the magnetic response of a substance to an applied magnetic field and under low fields it the ratio of M and H.

$$\chi = \frac{M}{H} \qquad (1.2)$$

The permeability of a material is a measure of the degree to which the material can be magnetized, or it is the ease with which B can be induced in the presence of H. The permeability (μ) is given by

$$\mu = \frac{B}{H} \qquad (1.3)$$

The relative permeability (μ_r) is a dimensionless quantity and is defined as

$$\mu_r = \frac{\mu}{\mu_0} \qquad (1.4)$$

The magnetic susceptibility and the relative permeability are related as:

$$\chi = \mu_r - 1 \qquad (1.5)$$

1.2. Types of magnetic materials

All materials can be classified in terms of their magnetic behavior. The two most common type of magnetism are diamagnetism and paramagnetism, which accounts for the magnetic properties of most of the elements in the periodic table at room temperature. These elements are usually referred to as non-magnetic. Based on the ordering or exchange, magnetic materials can also be classified into ferromagnetic, antiferromagnetic and ferrimagnetic.

1.2.1. Diamagnetism

Diamagnetism is a very weak form of magnetism exhibited by atoms which have no net magnetic moment as a result of their shells being completely filled. It arises due to the change in the orbital motion of electrons caused by an external magnetic field. The induced magnetic moment is very small and acts in a direction opposite to that of the

applied field. When a diamagnetic material is placed between the poles of an electromagnet, it gets attracted towards regions where the magnetic field is weak. When the magnetic field is turned on, extra currents are generated in the atom by electromagnetic induction. According to Lenz's law, these currents are induced in the direction which opposes the applied field; therefore, the induced magnetic moments are directed opposite to the applied field. So, the stronger the field, the more "negative" the magnetization. Hence, even though the magnetic moments of the free atom cancel out, the changes in the magnetic moment always act to oppose the field. Hence, diamagnetic materials tend to expel magnetic flux from their interior, and therefore, they exhibit negative χ. All materials show diamagnetism, but since it is so weak, it can be observed only when other types of magnetism are completely absent. The susceptibility of a diamagnet is independent of temperature. Superconductors are perfect diamagnets, and when placed in an external magnetic field, they expel the field lines from their interior. Other examples include bismuth, water, noble gases, etc. The variation of magnetization with field and susceptibility with temperature for a diamagnetic material is shown in Figure. 1.1.

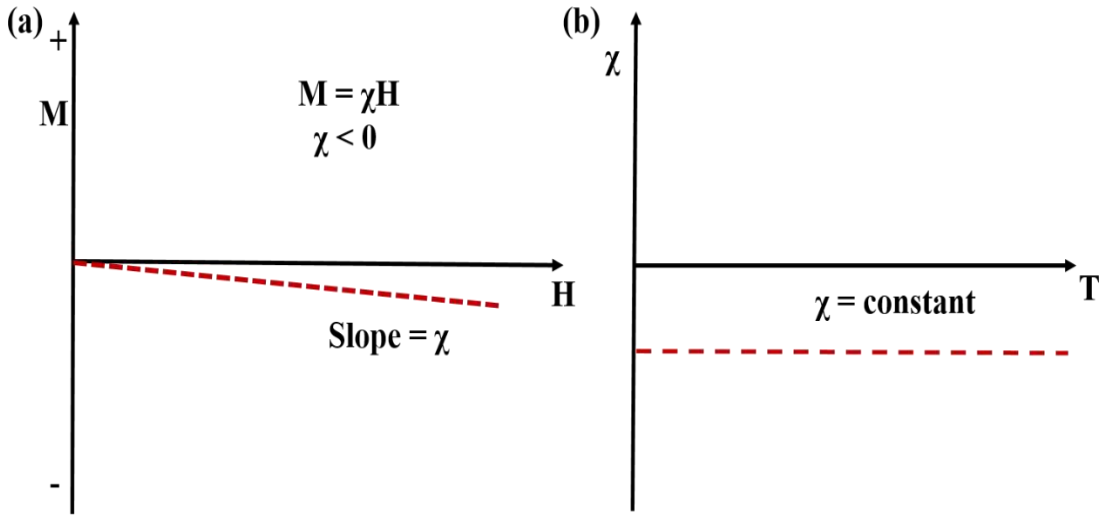

Figure 1.1. Variation of (a) Magnetization with field and (b) Susceptibility with temperature for a diamagnetic material.

1.2.2. Paramagnetism

In paramagnetic (PM) materials, the individual atoms or molecules have a net orbital or spin magnetic moment, which are randomly oriented. These moments are only weakly coupled to each other, and the thermal energy causes random alignment of the magnetic moments, and hence there is no net magnetization. When a magnetic field is applied, the moments start to align, but only a small fraction of them are aligned in the direction of field for all practical field strengths. Hence, they have a small and positive susceptibility between 10^{-3} and 10^{-5} and a relative permeability slightly greater than one. However, they do not retain magnetism once the field is removed. Paramagnetism occurs in atoms and molecules with unpaired electrons, for example, free atoms, free radicals, and in compounds of transition metals containing ions with unfilled electron shells. It also occurs in metals because of the magnetic moments associated with the spins of the conducting electrons. Several theories have been proposed to explain the paramagnetic behavior in materials. The Langevin model, applies to materials with non-interacting localized electrons. According to the Langevin model, each atom has a magnetic moment, which is randomly oriented as a result of thermal agitation. The application of magnetic field creates a slight alignment of these moments, and hence a low magnetization is induced in the same direction as the applied field. As the temperature increases, the thermal agitation increases, and it becomes difficult to align the atomic magnetic moments and hence the susceptibility decreases. This behavior is known as the Curie law and is given by,

$$\chi = \frac{N\mu_{eff}^2}{3k_B T} \qquad (1.6)$$

where N is the Avogadro number, k_B is the Boltzmann constant, T is the temperature and μ_{eff} is the effective magnetic moment given by

$$\mu_{eff} = g\,[J(J+1)]^{1/2} \qquad (1.7)$$

where *g* is the Lande g factor and $g = 1+\frac{J(J+1)+S(S+1)-L(L+1)}{2J(J+1)}$ (where L, S and J are the orbital, spin and total angular momentum quantum number). When the orbital contribution is neglected, this reduces to the spin-only value,

$$\mu_s = g\,[S(S+1)]^{1/2} \qquad (1.8)$$

Equation (1.6) can be written as

$$\chi = \frac{C}{T} \qquad (1.9)$$

where the Curie constant $C = \frac{N\mu_{eff}^{\ 2}}{3k_B}$.

In materials that obey this law, the magnetic moments are localized at the atomic or ionic sites, and there is no interaction between the neighbouring magnetic moments. In pure paramagnetism, the external magnetic field acts on each atomic dipole independently and there is no interaction between the individual atomic dipoles. This paramagnetic behavior can also be observed in ferromagnetic materials above their Curie temperature. In fact, many paramagnetic materials do not obey the Curie law, but follow a more general temperature dependence given by the Curie-Weiss (CW) law,

$$\chi = \frac{C}{T - \theta} \qquad (1.10)$$

where θ can either be positive, negative, or zero. Weiss explained the observed Curie–Weiss behavior by postulating the existence of an internal interaction between the localized moments, which he called the "molecular field". When θ = 0, the Curie-Weiss law reduces to the Curie law. A non-zero value of θ indicates that there is an interaction between the neighbouring magnetic moments, and the material becomes paramagnetic only above a certain transition temperature. When θ is positive, then the material is ferromagnetic below the transition temperature, and the value of θ corresponds to the Curie temperature, T_C. When θ is negative, then the material is antiferromagnetic below the transition temperature, known as the Neel temperature, T_N. This equation is only valid when the material is in the paramagnetic state. It is not valid for many metals, as the electrons contributing to the magnetic moment are not localized. However, the law applies to some metals, e.g. rare earths, where the 4f electrons, which create the magnetic moment, are closely bound. The variation of magnetization with field and susceptibility with temperature for a paramagnetic material is shown in Figure. 1.2.

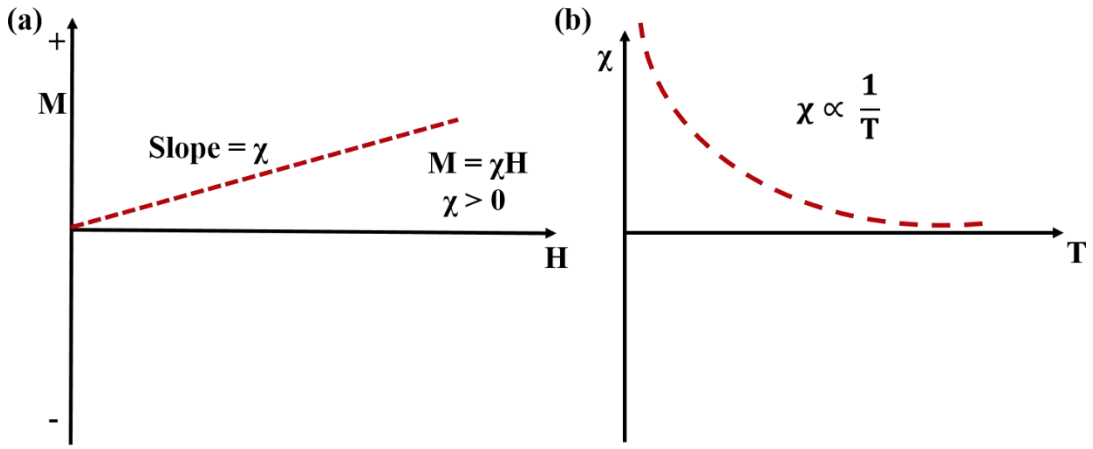

Figure 1.2. Variation of (a) Magnetization with field and (b) Susceptibility with temperature for a paramagnetic material.

1.2.3. Ferromagnetism

Ferromagnetic (FM) materials exhibit spontaneous magnetization and a clear magnetic ordering temperature. In ferromagnets, there is a strong internal interaction between the atomic magnetic moments which aligns them parallel to each other. In 1907, Weiss postulated that this effect is due to the presence of a molecular field within the ferromagnetic material which is sufficient to magnetize the material to saturation. Heisenberg model of ferromagnetism describes the parallel alignment of magnetic moments in terms of an exchange interaction between the neighbouring moments. Weiss postulated that magnetic domains are present within the material and the movement of these domains determines how the material responds to an applied magnetic field. At room temperature, only Fe, Co, and Ni are ferromagnetic. Their magnetic moments interact strongly with each other and hence, require a larger thermal energy to disrupt their magnetic ordering and make them paramagnetic, which results in a higher Curie temperature. When ferromagnetic materials are heated, the degree of alignment of the atomic magnetic moments decreases due to thermal agitation, and hence the saturation magnetization also decreases. Eventually, the thermal agitation becomes so great that the material becomes paramagnetic above the Curie temperature. The Curie temperature of Fe, Co and Ni are 1043 K, 1404 K and 631 K respectively. Above T_C, the susceptibility of ferromagnets varies according to the Curie-Weiss law. The variation of magnetization and the inverse susceptibility (χ^{-1}) as a function of temperature for a ferromagnetic material is shown in Figure. 1.3.

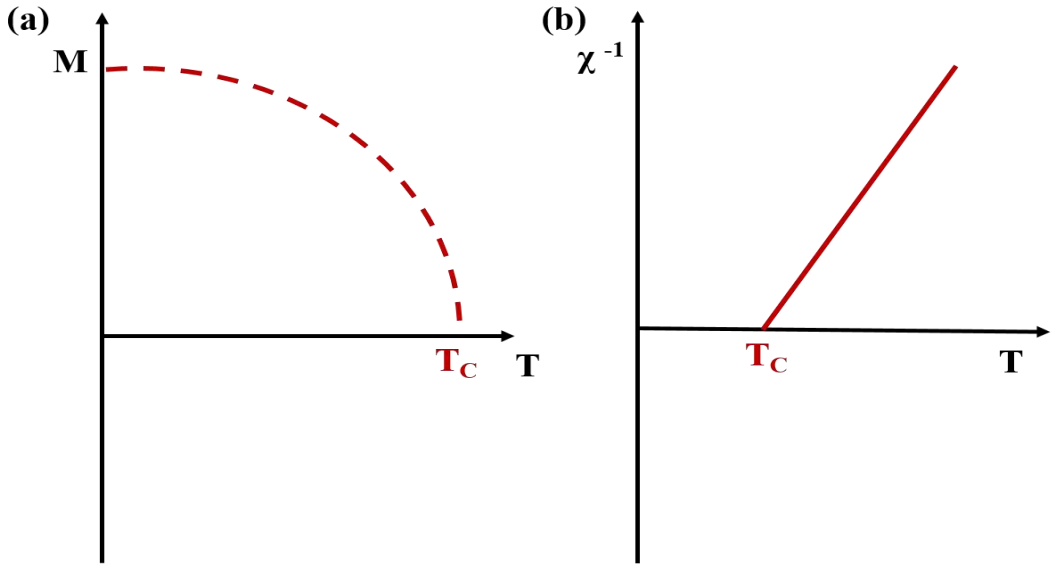

Figure 1.3. Variation of (a) Magnetization with temperature and (b) Inverse susceptibility with temperature for a ferromagnetic material.

A ferromagnet in the demagnetized state is composed of a number of small regions called domains. Each domain is spontaneously magnetized to its saturation value of magnetization. But the magnetization vectors in different domains have different orientations, and hence, the total magnetization averages to zero. The process of magnetization involves the conversion of the specimen from a multi-domain state into a single domain state. For a ferromagnetic material, the field dependence of magnetization is nonlinear, and at large values of H, the magnetization, M becomes constant at its saturation value M_s, as shown in Figure 1.4. But once saturated, a decrease in H to zero does not reduce M to zero. Hence, it possesses some magnetization called remanent magnetization (M_r). To demagnetize the material, a reverse field is required and the magnitude of this field is called coercivity (H_C). The M-H curve in the case of ferromagnets and ferrimagnets is called the magnetic hysteresis loop (Figure 1.4). It represents the energy loss during the process of magnetization and demagnetization and this amount of energy (the hysteresis loss) is proportional to the area inside the loop. In a typical M-H curve of a ferromagnet, at the low field region, magnetization increases due to domain wall motion. As a result, domains which are favourably oriented in the direction of the applied field grow at the expense of others, and beyond that, magnetization occurs only by domain wall rotation which occurs at higher field strengths as shown in Figure 1.4. But when the temperature increases the saturation magnetization

of a ferromagnetic substance decreases and at T_C, the domain structure is collapsed, and the material becomes paramagnetic above T_C.

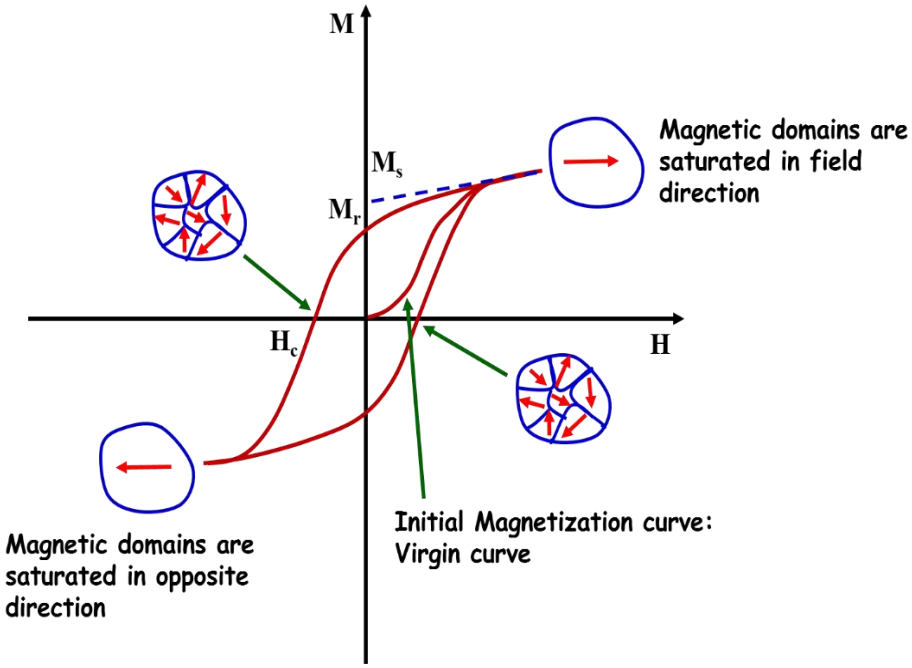

Figure 1.4. Hysteresis loop and magnetic domain morphology of ferromagnetic materials.

1.2.4. Antiferromagnetism

In antiferromagnetic (AFM) materials, the exchange interaction between the magnetic moments tends to align adjacent moments antiparallel to each other, and hence, there is no net zero field magnetization. We can consider antiferromagnets as consisting of two interpenetrating and identical sub lattices of magnetic ions, as illustrated in Figure 1.5. One set of magnetic ions is spontaneously magnetized in one direction below the critical temperature, called the Neel temperature, T_N, and the second set is spontaneously magnetized in the opposite direction by the same amount. As a result, antiferromagnets have no net spontaneous magnetization, and their response to external fields at a fixed temperature is similar to that of paramagnetic materials, i.e. the magnetization is linear in the applied field, and the susceptibility is small and positive. The temperature dependence of susceptibility above T_N is also similar to that of a paramagnet, but below T_N it decreases with decreasing temperature, as shown in Figure 1.6 (a). The susceptibility of AFM materials is also temperature dependent and is shown in Figure. 1.6 (b).

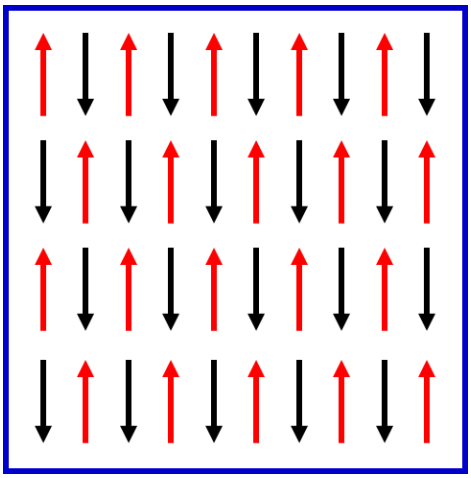

Figure 1.5. Ordering of magnetic ions in an antiferromagnetic lattice.

Above T_N, the moments are PM and below T_N the moments are arranged antiparallel. The paramagnetic susceptibility of an antiferromagnet is given by

$$\chi = \frac{C}{T + \theta} \qquad (1.11)$$

Examples of antiferromagnets include chromium and manganese. The variation of susceptibility and inverse susceptibility as a function of temperature for an AFM material is shown in Figure. 1.6.

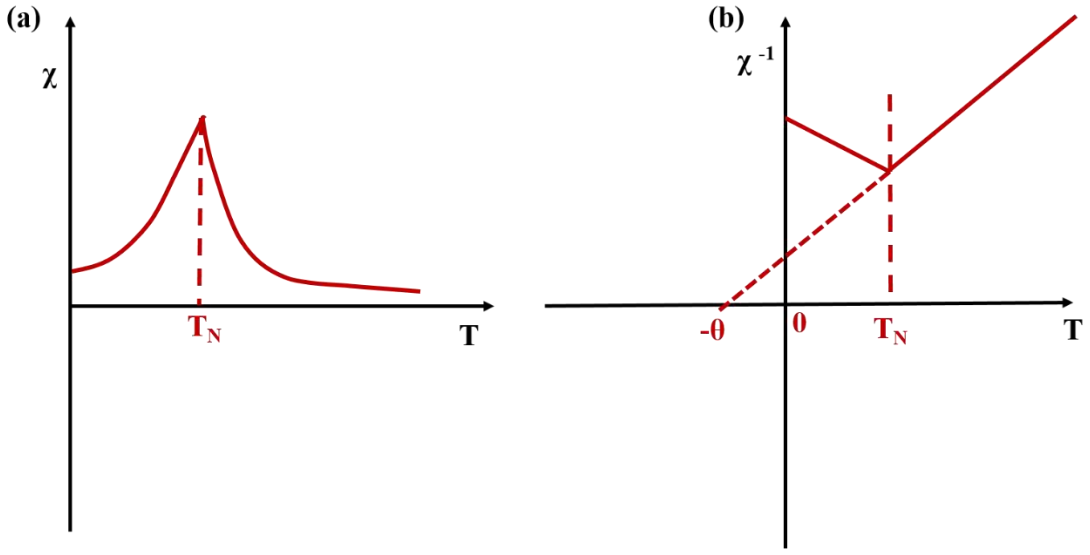

Figure 1.6. Variation of (a) Susceptibility with temperature and (b) Inverse susceptibility with temperature for an antiferromagnetic material.

1.2.5. Ferrimagnetism

Ferrimagnets exhibit a spontaneous magnetization below the critical temperature, T_C, similar to ferromagnets even in the absence of an applied field. However, the typical ferrimagnetic magnetization curve is distinctly different from that of the ferromagnetic curve. The exchange coupling between adjacent magnetic ions in a ferrimagnet leads to an antiparallel alignment of the localized moments similar to antiferromagnets. However, ferrimagnets possess a net magnetic moment, because the magnetization of one sub lattice is greater than that of the oppositely oriented sub lattice. A schematic representation of the ordering of magnetic moments in a ferrimagnet is shown in Figure 1.7. Figure 1.8 shows the typical magnetization and inverse susceptibility curves in ferromagnets and ferrimagnets (Spladin, 2011).

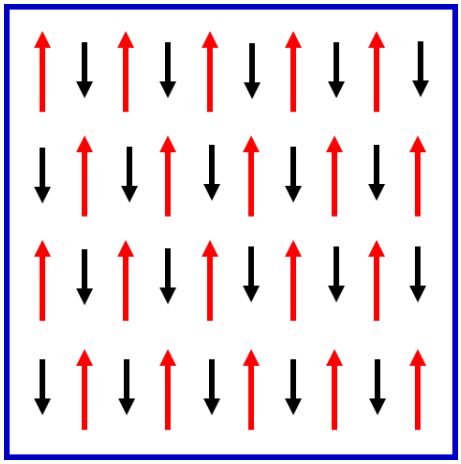

Figure 1.7. Ordering of magnetic ions in a ferrimagnetic lattice.

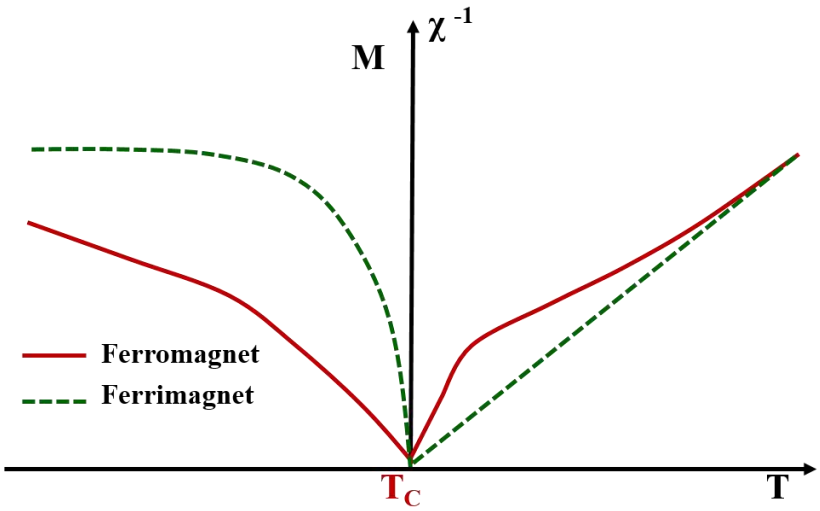

Figure 1.8. Comparison of magnetization and inverse susceptibility in ferromagnet and ferrimagnets.

1.2.6. Spin glass

Spin glasses (SG) are frustrated magnetic systems with mixed interactions characterized by a random, yet co-operative, freezing of spins at a well-defined temperature 'T_f' (the freezing temperature) below which a metastable frozen state appears without the usual magnetic long-range ordering (Blundell, 2001). This behavior is very similar to glasses. Glasses being amorphous have short range crystalline order and frustrated magnetic systems with inherent magnetic frustrations also make a short range magnetic order similar to the order parameter of glasses. Both randomness's in site occupancy and frustration of magnetic moments are necessary to produce an SG state. The divergence between the Field Cooled Cool (FCC) and Zero Field Cooled (ZFC) magnetic susceptibility below 'T_f', reflects the metastable nature of the magnetic transition. In a spin glass state, all the spins are independent and the orientation of the dipoles changes slowly. The glassy state in a magnetic system can be further proved by the temperature dependence of AC susceptibility in which susceptibility becomes frequency dependent below 'T_f'.

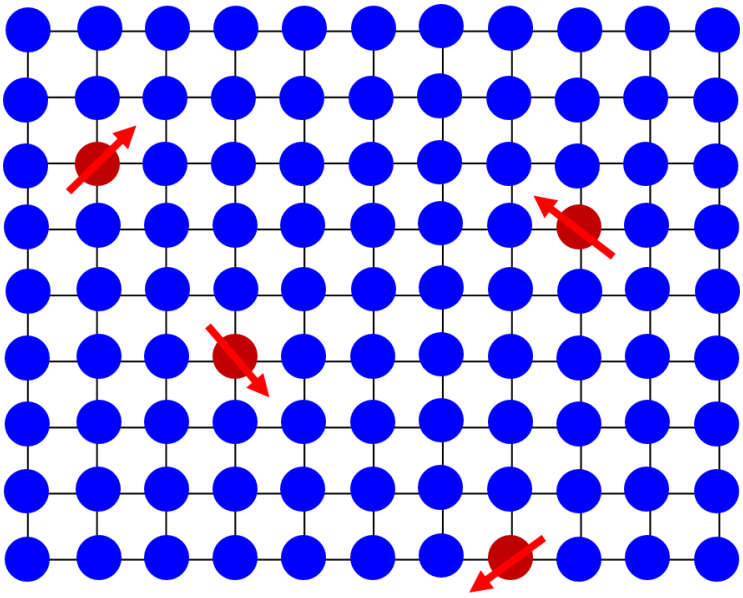

Figure 1.9. Orientation of magnetic moments in Spin Glass.

The glassy state in a magnetic system can be further proved by the temperature dependence of AC susceptibility in which susceptibility becomes frequency (f) dependent below 'T_f'. The empirical parameter δT_f is used to express the T_f vs. f dependence, as

following: $\delta T_f = \Delta T_f / (T_f \ \Delta \log \omega)$ where the angular frequency, $\omega = 2\pi f$. The value is typically 0.005-0.08 for SG whereas it lies in the range of ~0.1 for non-interacting super paramagnetic systems (Mydosh, 1993).

1.2.7. Griffith's like Phase

The Griffiths like phases (GP) was originally proposed for randomly diluted Ising ferromagnets, in which only a fraction of the lattice sites is occupied with spins and the rest are filled with non-magnetic atoms or remain vacant. According to Griffith's theory, there is always a finite probability of finding FM clusters with randomly distributed spins [i.e., in PM state] in the temperature range $T_C < T < T_G$, where T_C and T_G are CW temperature and Griffith's temperature, respectively. Thus, in the Griffith's regime, spontaneous magnetisation is absent due to the absence of any long range static FM order (Pramanik *et al.*, 2010). However, Bray extended this explanation to a bond distribution that reduces transition temperature and the GP is supposed to be present in the regime $T_C{}^R < T < T_G$, where $T_C{}^R$ is the critical temperature of the random FM where susceptibility diverges (Bray, 1987). Thus, GP is the region between the completely ordered states above $T_C{}^R$ and the disordered state below T_G. This is the region of PM phase, where FM clusters are formed. It is well established that quenched disorder and/or the competition between magnetic interactions are the fundamental ingredients for the onset of GP (Markovich, *et al.*, 2013). Usually, the susceptibility of a GP at low fields follows the power law

$$\chi^{-1}(T) \propto \left(\frac{T}{T_C^R} - 1 \right)^{1-\lambda} \qquad (1.12)$$

where λ is the magnetic susceptibility exponent ($0 \leq \lambda < 1$) and $T_C{}^R$ is the random critical temperature (Pereira *et al.*, 2010; Ouyang, 2010). $T_C{}^R$ is taken as the temperature for which the equation yields a λ (λ_{PM}) value close to zero above T_G. The value of λ lies in between 0 and 1 and decreases with increase in the field, a signature of GP.

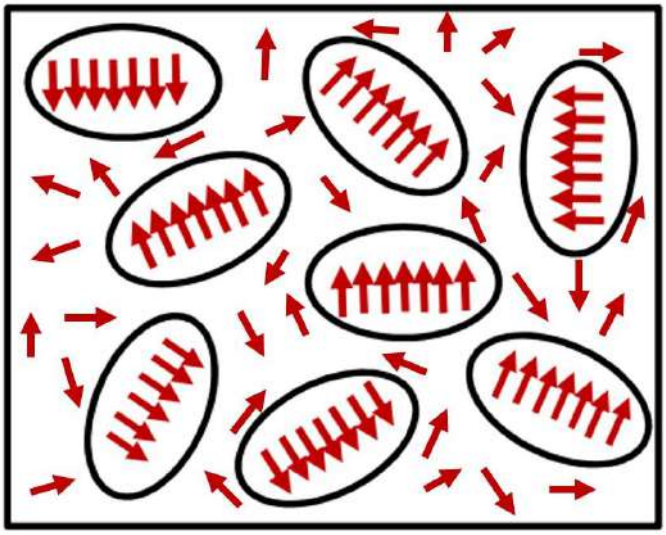

Figure 1.10. Magnetic moments in Griffiths like phases.

1.3. Magnetic exchange interactions

The most important characteristic of materials with long range magnetic order is the exchange interactions. The magnetic order in magnetic systems arises due to the co-operative effects between magnetic moments located at constituent ions. The interaction among the spins is mediated by spin dependent electrostatic interaction known as the exchange interaction. The lowering of the free energy of a magnetic material due to the exchange interaction leads to magnetic order, and it persists below a definite temperature, known as the magnetic ordering temperature or Curie temperature.

The first effort towards the understanding of magnetic order was given by Weiss by assuming the existence of an internal molecular magnetic field. The origin of this field was given by Heisenberg in terms of the exchange Hamiltonian (H_{ex}) (Blundell, 2001).

$$H_{ex} = -\frac{1}{2}\sum_{i,j} J_{ij} S_i . S_j \qquad (1.13)$$

The spin located at the lattice site 'i', S_i, interacts with the spin located at site 'j', S_j and the strength of interaction is determined by the exchange parameter J_{ij}. The summation in the above equation extends over all pairs of spins. The exchange parameter J_{ij} determines the ordering temperature and is of electrostatic origin. The interaction between the two spins arises from electrons present on the same atom or two different

atoms. When the two electrons are on the same atom, the exchange integral J_{ij} is positive. Magnetism due to co-operative effects of the moments is termed as "exchange interactions" and are broadly divided into direct exchange interactions and indirect exchange interactions.

1.3.1. Direct Exchange Interactions

Direct exchange interaction occurs between ions whose spins are close enough to have sufficient overlap of their wave functions. Electrons spend most of their time between neighboring atoms when the interatomic distance is small. This gives rise to antiparallel alignment and therefore negative exchange (antiferromagnetic) as shown in Figure 1.11 (a). If the atoms are far apart the electrons spend their time away from each other to minimize the electron-electron repulsion. This gives rise to parallel alignment or positive exchange (ferromagnetism) as shown in Figure 1.11 (b).

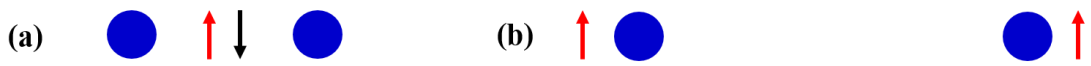

Figure 1.11. (a) Antiparallel alignment for small inter atomic distances favouring antiferromagnetism **(b)** Parallel alignment for large inter atomic distances favouring ferromagnetism.

Exchange in a roughly half-filled band is antiferromagnetic, because the energy gain associated with letting the wave functions expand onto neighbouring sites is only achieved when the neighbours are antiparallel, leaving empty orbitals on the neighbouring sites to transfer into. Nearly filled or nearly empty bands tend to be ferromagnetic (Figure 1.12) because electrons can then hop into empty states with the same spin.

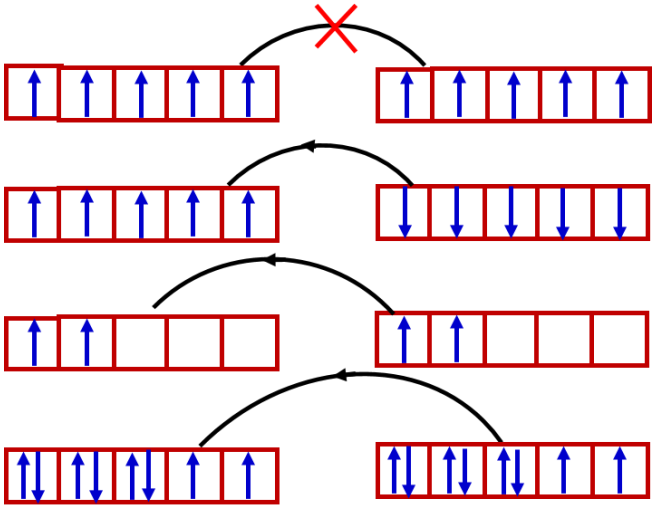

Figure 1.12. Illusration of ferromagnetism and antiferromagnetism in 3d elements.

In the case of 3d transitions series, the electrons responsible for the magnetism belong to 3d orbital and have large spatial spread with a strong overlap. Therefore, the exchange interaction is direct and is the strongest, leading to a ferromagnetic coupling between the 3d spins. The variation of the exchange strength across the 3d series is well illustrated by the Bethe-Slater curve shown in Figure 1.13. It is found that the ratio of r_{ab}/r_d can be correlated with the sign of the exchange interaction, where 'r_{ab}' denotes the interatomic distance and 'r_d' is the radii of the incompletely filled d subshell. For large values of r_{ab}/r_d (r_{ab}/r_d >3), but not very much larger, the exchange is positive while for small values, it is negative.

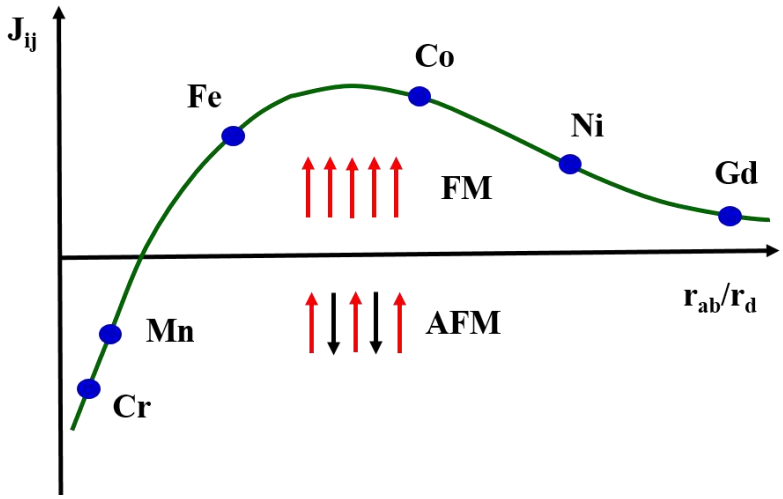

Figure 1.13. Bethe-Slater curve showing the variation of exchange strength across the 3d elements.

1.3.2. Indirect exchange interactions

1.3.2.1. Super exchange

Super exchange (SE) interaction occurs between two nearest-neighbour cations joined through a shared non-magnetic ion such as oxygen (O). Transition metal (TM) oxides are excellent models for super exchange interaction. Compared to all other interactions it is a long ranged; hence it is called as 'super' (Blundell, 2001). It is an oxygen-mediated exchange between TM ions based on the virtual hopping of the O_{2p_z} electrons. The O^{2-} ion with the electronic configuration $1s^2\ 2s^2\ 2p^6$ have fully occupied triply degenerate p orbitals ($2p_x$, $2p_y$, $2p_z$) with six electrons. In oxide systems, the five d orbitals of TM are not degenerate, but they split into triply degenerate t_{2g} orbitals ($3d_{xy}$, $3d_{yz}$, $3d_{xz}$), and doubly degenerate e_g orbitals ($3d_z^2$, $3d_{x^2-y^2}$). The e_g orbitals point along the crystal axes, and, therefore, overlap with the O_{2p_z} orbitals. SE interaction depends on the potential exchange as well as kinetic exchange. The potential exchange is due to the electron repulsion, which favours ferromagnetic ground states, but is small when the ions are well separated. The kinetic exchange depends on the degree of overlap of orbitals, which favours antiferromagnetic ordering. Therefore, super exchange strongly depends on the angle of the TM-O-TM bond. The super exchange interaction between Mn^{3+} ions is illustrated in Figure 1.14. Mn^{3+} with electronic configuration [Ar] $3d^4$ has four electrons in the five 3*d* orbitals, three of them occupying the t_{2g} orbitals and the fourth is located in one of the two e_g orbitals, which point along the crystal axes and therefore overlap with the O-2p orbitals. Virtual hopping of O-2p electrons to these overlapping Mn e_g orbitals leads to virtual excited states which can result in a reduction of the total energy of the system depending on the spin directions (Opel, 2012). The relation between the super exchange interaction and the symmetry of electron orbital is described by the Goodenough-Kanamori-Anderson (GKA) rules (Goodenough, 1955; Kanamori, 1959; Anderson, 1950; Goodenough, 1963) which are summarized below:

1. The 180^o exchange interaction between two half-filled or two empty TM orbitals will be strongly antiferromagnetic. For two TM cations along the z direction, with one electron each in their respective e_g orbitals, virtual hopping of the two O_{2p_z} electrons reduces the total energy of the system only if the TM core spins are aligned antiparallel.

2. The 180° exchange interaction between one half-filled and one empty TM orbitals is weakly ferromagnetic. For two TM cations along the z direction, where the first has one electron and the second with no electron in their respective e_g orbitals, virtual hopping of the two O_{2p_z} electrons will reduce the total energy of the system if the TM core spins are aligned parallel.
3. The 90° exchange interaction between two half-filled TM orbitals is weak and ferromagnetic. For two TM cations with one electron in their respective e_g orbitals sharing the same corner O^{2-} ion, virtual hopping of one electron in the O_{2p_z} orbital and one electron in the O_{2p_y} orbital will reduce the total energy of the system if the TM core spins are parallel.

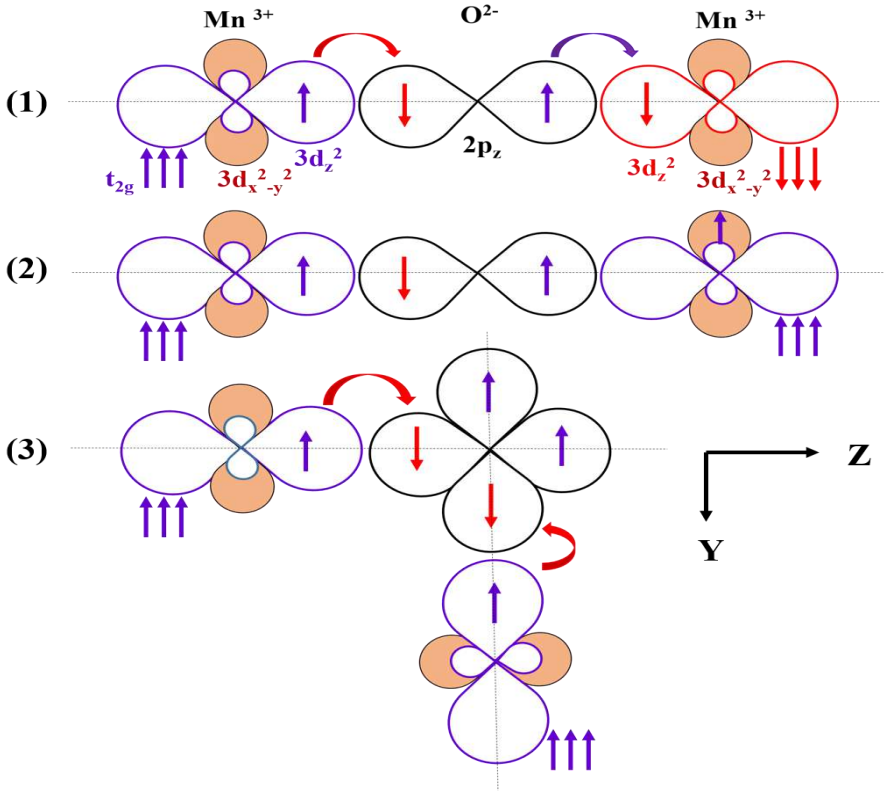

Figure 1.14. Super exchange interaction between Mn^{3+} ions in manganites.

1.3.2.2.Double exchange

Double Exchange (DE) was interaction proposed by Zener, in 1951 (Zener, 1951). It is usually observed in mixed valence manganites containing Mn^{3+} and Mn^{4+} ions or Mn^{3+} and Mn^{2+} ions and is based on the real hopping of electrons between the manganese ions. The innermost electron in the $3d_{z^2}$ orbital of Mn^{3+} ion can hop via the O_{2p_z} orbital

to the $3d_{z^2}$ orbital of Mn^{4+} ion and its spin gets coupled with those of both ion cores. The DE mechanism, observed in $La_{0.7}A_{0.3}MnO_3$ (A= tetravalent ions such as Te, Ce, etc), between Mn^{3+} and Mn^{2+} ion separated by an O^{2-}ion, is illustrated in Figure 1.15 and the ferromagnetic alignment due to the double exchange mechanism can be understood from the figure. The e_g electron on the Mn^{2+} ion hop to the e_g orbital of the Mn^{3+} ion favouring double exchange interaction. However, there is a strong single-centre exchange interaction between the e_g electron and the three electrons in the t_{2g} level which wants to keep them all aligned. Thus, it is not energetically favourable for an e_g electron to hop to a neighbouring ion in which the t_{2g} spins will be antiparallel to the e_g electron. Ferromagnetic alignment of neighbouring ions is therefore required to maintain the high-spin arrangement on both the ions. Since hopping reduces the kinetic energy saving, there is a gain in the overall energy due to hopping. Thus the system ferromagnetically aligns to save energy. Moreover, the ferromagnetic alignment allows the e_g electrons to hop through the crystal, and the material becomes metallic.

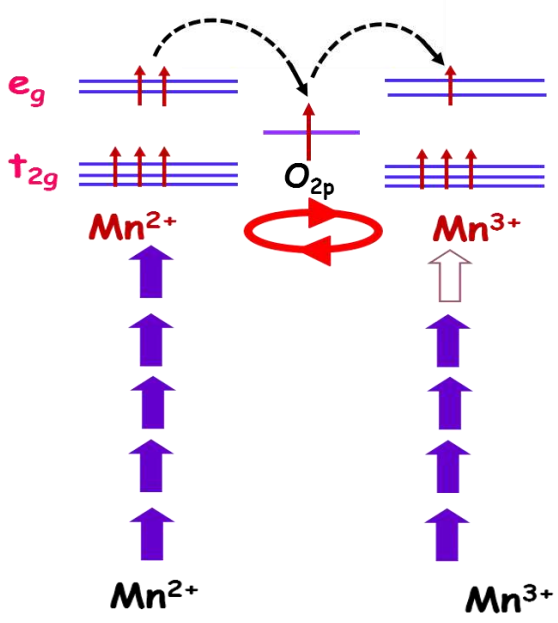

Figure 1.15. Double exchange interaction in manganites.

1.3.2.3. RKKY interaction

The exchange interaction between the magnetic ions in a metal mediated by the conduction electrons (itinerant electrons) is known as Ruderman-Kittel-Kasuya-Yosida (RKKY) exchange interaction. RKKY interaction describes the magnetic interaction

between the localized d or f electron spins (magnetic ion) and the delocalized conduction band electrons (sp-band). The localized moments in the 4f shell interact via electrons in the 5d/6s conduction band. The magnetic ordering seen in rare earth elements is due to this RKKY exchange interaction. In rare earth ions, the electrons in the (n-2) f shell are shielded by the ns and (n-1) p electrons. As a result, the direct exchange is rather weak and insignificant. Thus, the indirect exchange via the conduction electrons gives rise to magnetic order in these materials. A schematic representation of RKKY interaction is shown in Figure 1.16.

RKKY interaction is long range and has an oscillatory dependence on the distance between the magnetic moments. Hence, depending on the separation, it may be either FM or AFM. The coupling takes the form of an r-dependent exchange interaction $J_{RKKY}(r)$ given by

$$J_{RKKY}(r) \propto \frac{\cos(2k_F r)}{r^3} \qquad (1.14)$$

where, k_F is the radius of the Fermi surface.

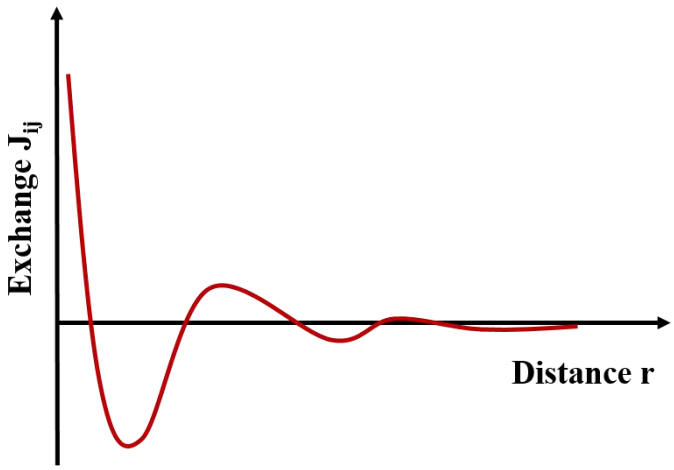

Figure 1.16. RKKY interaction in metals.

1.4. Introduction to Magnetocaloric Effect

Magnetocaloric effect (MCE) is the change in temperature of a material as a result of alignment of its magnetic spins that occurs on exposure to an external magnetic field. The isothermal magnetization of the material causes the entropy of the spin subsystem to decrease, leading to heating of the material due to the increase in its lattice entropy. When

this magnetic field is removed adiabatically, the material gets cooled as the magnetic entropy increases and the lattice entropy decreases. This heating and cooling of a magnetic material, in response to a changing magnetic field, is similar to the heating and cooling of a gaseous medium in response to an adiabatic compression and expansion. Therefore, by magnetizing and demagnetizing, a magnetic material can operate as a magnetic refrigerant. The temperature difference between the initial and final magnetic states of the material depends on various intrinsic and extrinsic factors. The intrinsic factors that determine the MCE of a material are chemical composition, crystal structure, and the magnetic phase of the compound while the extrinsic factors include temperature, surrounding pressure, and the change in magnetic field, *i.e.* whether the magnitude of magnetic field is increased or decreased. The development of magnetic refrigeration (MR) technology, is based on the principle of MCE (Tishin, 1999; [a]Pecharsky *et al.*, 1999), and is considered as a sound alternative to the conventional gas compression expansion technique ([a]Pecharsky *et al.*, 1999; Gschneidner *et al.*, 2000). The cooling efficiency of a magnetic refrigerator is high and can reach up to 60% of the Carnot cycle, whereas in case of compression expansion technique, the best achieved limit is only 40% (Franco *et al.*, 2012). Hence MR is more efficient than the gas compression expansion technique. The significant advantage of MR over the gas compression-expansion refrigeration is that it is an environmental friendly cooling technology as it does not use any ozone depleting or global warming greenhouse effect gases and hazardous chemicals (Gschneidner *et al.*, 2000). However, the realization of magnetic refrigeration at room temperature needs the availability of GMCE materials.

1.4.1. Historical Background

The connection between magnetism and heat goes back over 150 years when Faraday discovered that a time varying magnetic flux induces an electrical current (Smith, 2013). Later, in 1843, Joule observed that heat is evolved in samples of iron when it is subjected to a changing magnetic field (Joule, 1843). In 1860, William Thomson demonstrated on thermodynamic grounds that if the magnetization of a sample decreases (increases) as a function of temperature, the sample will heat (cool) reversibly when exposed to a magnetic field and will cool (heat) slightly when the field is withdrawn (Thomson, 1860; Thomson, 1878). In 1881, Warburg discovered the hysteresis of ferromagnets and put forth the Warburg's law which states that the heat dissipated during

a hysteresis loop is equal to the area enclosed by the loop in an M-H diagram (Warburg, 1881). J.A. Ewing discovered the same phenomenon independently, and gave the name, *hysteresis* (Ewing 1882). Warburg and Honig measured the hysteresis heat directly in 1882 (Warburg *et al.*, 1882). In 1917, Weiss and Piccard discovered MCE experimentally (Weiss *et al.*, 1917; Weiss *et al.*, 1918). They observed a sizable and reversible temperature change in Ni near its Curie temperature. In the late 1920s, the first practical use of MCE to reach temperatures lower than that of liquid helium, which has been the lowest achievable experimental temperature in those days, using the phenomenon called adiabatic demagnetization was independently proposed by Debye (Debye, 1926) and Giauque (Giauque, 1927). A few years later, in 1933, the process was demonstrated for the first time by Giauque and MacDougall (Giauque *et al*., 1933) using paramagnetic salts (e.g., Gd_2 $(SO_4)_3.8H_2O$). They achieved a temperature change of 0.25 K. In 1997, as a proof-of-principle, it was demonstrated that magnetic refrigeration is a feasible and eco-friendly cooling technology near room temperature with potential energy savings of up to 30% (Zimm *et al.*, 1998). Since then there has been an increase in the research activities in this area. During the last few years, MCE has been investigated intensively because of its potential application in magnetic refrigeration near room temperature.

1.4.2. Principle of MCE

The physical origin of MCE is due to the coupling of the magnetic sub lattice with the applied magnetic field H, which produces a change in the magnetic contribution to the entropy of the system. MCE is measured in terms of isothermal magnetic entropy change (ΔS_M) or adiabatic temperature change (ΔT_{ad}). The two stages involved in MCE are isothermal magnetization and adiabatic demagnetization. In the first stage, the application of magnetic field reduces the magnetic entropy of the solid which, in turn, is reflected as the increase in its lattice entropy. The heat emitted from the system is removed in the reversible process. In the second stage, upon the adiabatic removal of the magnetic field, the sample is cooled as the magnetic entropy increases and the lattice entropy decreases to maintain the entropy of a closed system at a constant value (Min *et al.*, 2009). Figure 1.17. shows the basic principle behind MCE. Initially the application of a magnetic field on the magnetocaloric material aligns the randomly oriented magnetic moments, resulting in heating of the material. The heat evolved is then extracted from the material by a heat-transfer medium to the ambient. On removing the magnetic field

adiabatically, the magnetic moments randomize. Consequently, the sample temperature decreases below the ambient temperature. Heat from the system to be cooled can then be extracted by using the heat-transfer medium.

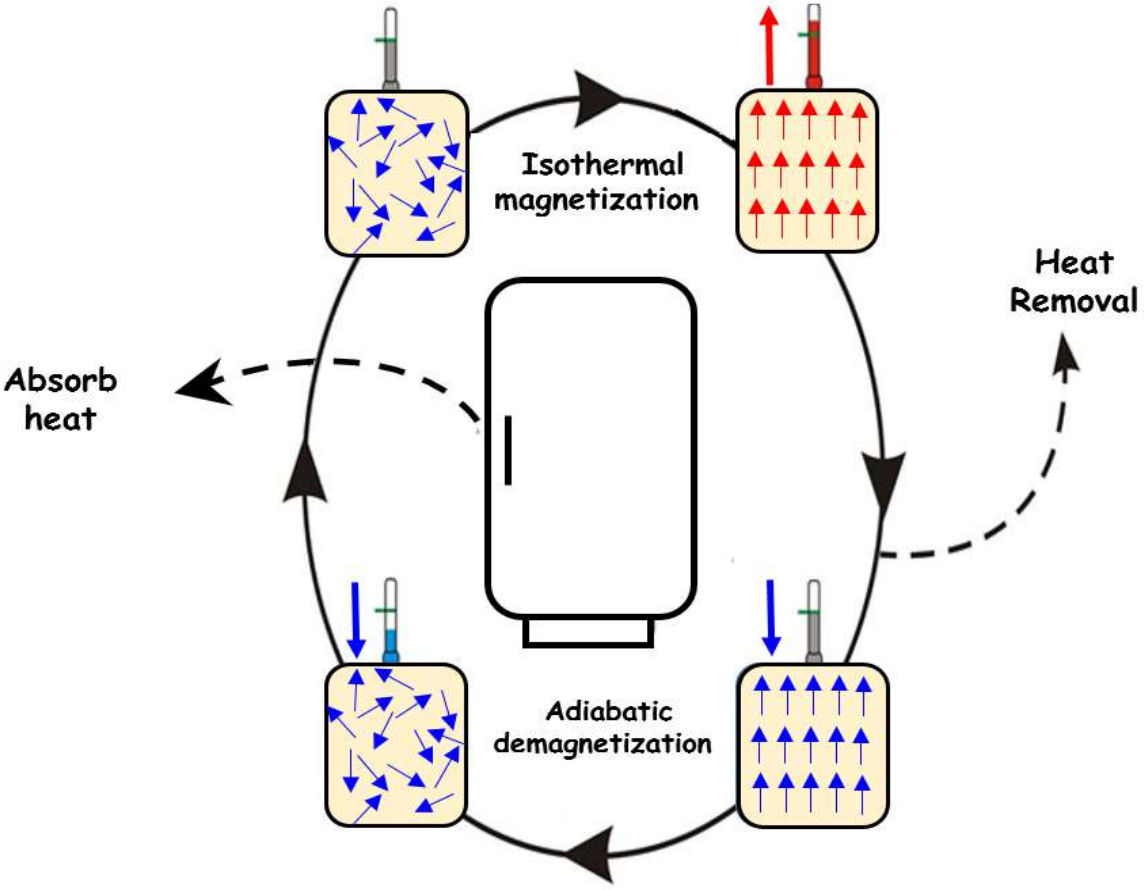

Figure 1.17. Schematic representation of the basic principle behind MCE when a magnetic field is applied and removed in an isolated magnetic system.

The total entropy (S) of a ferromagnet at constant pressure is a function of both the applied magnetic field (H), and temperature (T), and the contributions arise from the lattice entropy (S_{Lat}), electronic entropy (S_{el}), and the magnetic entropy (S_M),

$$S(T,H) = S_M(T,H) + S_{Lat}(T) + S_{el}(T) \qquad (1.15)$$

The schematic representation of the S vs. T plots of a ferromagnet near its Curie temperature T_C is depicted in Figure 1.18. The total entropy, along with the magnetic entropy, is displayed for zero field, H_0 and for an applied field, H_1. The relevant processes shown in the figure to understand the thermodynamics of MCE are:

a) When H is applied isothermally, the total entropy of the system decreases due to the increase in the magnetic order and the isothermal magnetic entropy change (ΔS_M) in the process is defined as

$$\Delta S_M = S(T_{0,}\ H_0) - S(T_{0,}\ H_1) \qquad (1.16)$$

b) When H is applied adiabatically in a reversible process, the magnetic entropy decreases as the total entropy remains a constant, i.e.

$$S(T_0, H_0) = S(T_1, H_1) \qquad (1.17)$$

This leads to an enhancement in the temperature of the material. The adiabatic temperature change (ΔT_{ad}), which is the difference between the initial temperature T_0 and the final temperature T_1 is the MCE in the material.

Here, S_0 and T_0 represents zero field entropy and temperature whereas S_1 and T_1 are entropy and temperature at a higher field H_1. Therefore, the two quantities ΔT_{ad} and ΔS_M are used to characterize the MCE. Hence, if raising the field increases the magnetic order, i.e., decreases the magnetic entropy, then ΔT_{ad} is positive and magnetic solid heats up, while ΔS_M is negative. But if the field is reduced, magnetic order decreases and ΔT_{ad} is negative, while ΔS_M is positive, giving rise to a cooling of the magnetic solid.

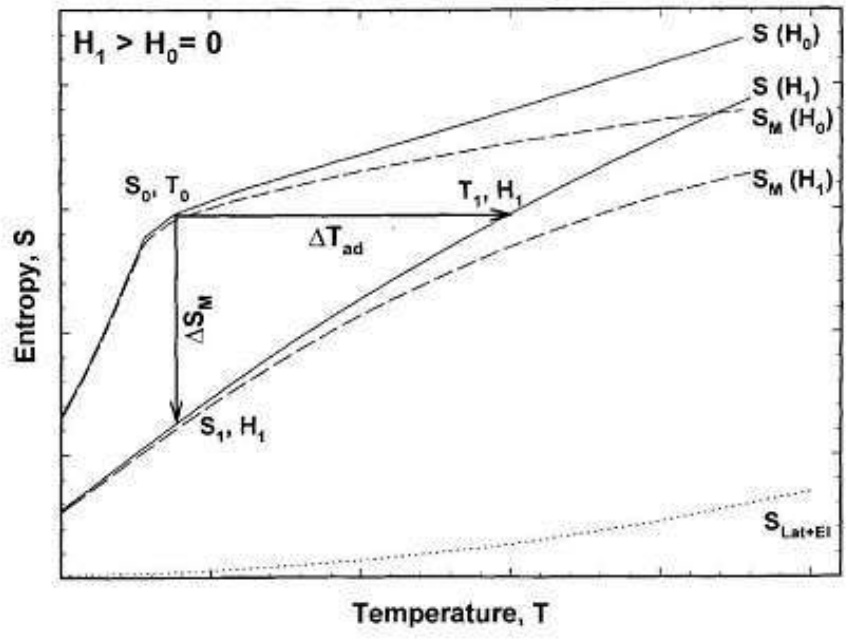

Figure 1.18. S-T plots showing the MCE. (*Adapted from reference Yu et al., 2003*).

In Figure 1.18, solid lines represent the total entropy in two different magnetic fields, H_0 =0 and H_1>0. The dotted line shows the combined lattice and electronic

(nonmagnetic) contributions to entropy, and the dashed lines show the magnetic entropy (ΔS_M) in the two fields. The horizontal arrow shows the adiabatic temperature change (ΔT_{ad}) and the vertical arrow shows the isothermal magnetic entropy change (ΔS_M), when the magnetic field is changed from H_0 to H_1.

Using Maxwell's relation, the MCE parameter ΔS_M is correlated with the magnetization (M), the magnetic field strength (H), and the absolute temperature (T) as:

$$\left[\frac{\partial S(T,H)}{\partial H}\right]_T = \left[\frac{\partial M(T,H)}{\partial T}\right]_H \qquad (1.18)$$

The integration of the above equation for an isothermal and isobaric process gives

$$\Delta S_M(T, \Delta H) = \int_{H_0}^{H_1}\left[\frac{\partial M(T, H)}{\partial T}\right]_H dH \qquad (1.19)$$

From the above equation, it is clear that the magnetic entropy change is proportional to the temperature derivative of magnetization at a constant field. For magnetization measurements made at discrete field and temperature intervals, ΔS_M (T, H) can be approximately calculated by the following relation,

$$\Delta S_M(T, \Delta H) = \sum_i \frac{M_{i+1}(T_{i+1}, H) - M_i(T_i, H)}{T_{i+1} - T_i} \Delta H \qquad (1.20)$$

Combining the above equation with the relation

$$C_H = T\left[\frac{\partial S}{\partial T}\right]_H \qquad (1.21)$$

where C_H is the specific heat of the material, the infinitesimal adiabatic temperature rise for the reversible adiabatic-isobaric process is given by

$$dT = -\left[\frac{T}{C(T, H)}\right]_H \left[\frac{\partial M(T, H)}{\partial T}\right]_H dH \qquad (1.22)$$

Integration of Eqn. (1.22) gives the value of MCE as (Tishin *et al*., 2003),

$$\Delta T_{ad}(T, \Delta H) = -\int_{H_0}^{H_1}\left[\frac{T}{C(T, H)}\right]_H \left[\frac{\partial M(T, H)}{\partial T}\right]_H dH \qquad (1.23)$$

A careful examination of the above equations provides the following information,

a) In the case of a ferromagnet $\left|\left(\frac{\partial M}{\partial T}\right)\right|_H$ is maximum at the Curie temperature (T_C) and therefore, $|\Delta S_M(T)_{\Delta H}|$ should peak at T_C.

b) For the same value of $|\Delta S_M(T)_{\Delta H}|$, the ΔT_{ad} will be larger at higher absolute temperature, and lower heat capacity.

From Eqs. (1.19) and (1.23), it can be seen that both ΔS_M and ΔT_{ad} are proportional to $(\partial M/\partial T)_H$ and ΔT_{ad} is proportional to the absolute temperature (T) and inversely proportional to the heat capacity C_H at constant magnetic field. Since $(\partial M/\partial T)_H$ peaks at the magnetic ordering temperature, a large MCE is often expected when its magnetization changes rapidly with temperature, i.e. in the vicinity of a spontaneous magnetic-ordering temperature. MCE gradually decreases both below (magnetization is nearly saturated and is weakly dependent on the temperature in an ordered state) and above (magnetization shows only a paramagnetic response) the magnetic-ordering temperature. The change in magnetization with temperature is more near the magnetic transition temperature. Hence, ΔS_M and ΔT_{ad} attain their maximum values near the magnetic transition temperature, and decreases below and above the transition temperature. Materials with large magnetic moments are expected to show a large MCE

1.4.3. Measurement of MCE

Direct and indirect methods are available for the measurement of MCE. In the direct method, the initial temperature (T_0) and final temperature (T_F) of the sample is measured when the external magnetic field is changed from H_0 to H_F. Then, ΔT_{ad} is given by the relation,

$$\Delta T_{ad}\ (H_F - H_0) = T_F - T_0 \qquad (1.24)$$

MCE can be measured directly using contact and non-contact techniques. In contact technique, the temperature sensor is in direct thermal contact with the sample and in non-contact technique, the sample temperature is measured without the sensor being directly connected to the sample. During the direct measurement of MCE, a rapid change of magnetic field is required, and hence the measurements are carried out on immobilized samples when the magnetic field change is provided either by charging/discharging the magnet, or by moving the sample in and out of a uniform magnetic field volume. The required field is usually provided by a superconducting solenoid or electromagnets, which

produce fields of 100 kOe and 20 kOe, respectively, whereas the time scale required for achieving these values varies in seconds in an electromagnet to minutes in a superconducting solenoid (Tishin *et al*., 2003).

Unlike the direct measurement, which only yields ΔT_{ad}, indirect experiments allow the calculation of both ΔT_{ad} and ΔS_M. Heat capacity measurements yield both ΔT_{ad} and ΔS_M, while the magnetization measurement gives only ΔS_M. The accuracy of ΔS_M calculated from magnetization data depends on the accuracy of the measurements of M, T and H. It is also affected by the fact that the exact differentials in Eqn. (1.19) are replaced by the measured variations (dM, dH and dT). Considering all these facts, it is found that the error in the value of ΔS_M lies within the range of 3-10% (Foldeaki *et al*., 1995; [a]Pecharsky *et al*., 1999). Based on the studies of MCE properties on some compounds, Pecharsky and Gschneidner have shown that the determination of MCE using the indirect method is reliable (Pecharsky *et al*., 1996). In the present thesis work, indirect technique using Eqn. (1.19) has been used to derive the value of ΔS_M from magnetization measurement and the most commonly used unit of ΔS_M is J /kg K.

Refrigerant capacity (RC) is a very relevant parameter which determines the cooling capacity of a magnetocaloric material. It indicates how much heat can be transferred from the cold end (T_1) to the hot end (T_2) of the refrigerator in one ideal thermodynamic cycle for a magnetic field change of ΔH and is defined as

$$RC = -\int_{T_1}^{T_2} \Delta S_M(T)_{\Delta H}\, dT \qquad (1.25)$$

where $\Delta S_M(T)$ is the isothermal entropy change. Another important parameter which determines the cooling efficiency of a magnetic refrigerant material for its use in magnetic refrigeration is the relative cooling power (RCP). It is the measure of the amount of heat that can be transferred between the cold and hot reservoirs in an ideal refrigeration cycle and is expressed as:

$$RCP = -\Delta S_M(T)_{\Delta H} \,.\, \delta T_{FWHM} \qquad (1.26)$$

where δT_{FWHM} is the full width at half maximum of the ΔS_M-T curve.

RCP can be considered as a figure-of-merit and may be used for comparison of different magnetocaloric materials. At a given value of magnetic field, the material with a larger

value of RCP is considered as a better magnetocaloric material, since it supports a greater amount of heat transfer in a real cycle, provided all other parameters of the magnetic refrigerator remain the same.

Chapter 2

Introduction to Gd-Si-Ge series and Lanthanum Tellurium Manganites

This chapter introduces the different magnetocaloric materials. The features of Gd-Si-Ge series and Lanthanum Tellurium manganites is also discussed along with an overview of the studies conducted so far in these materials.

2.1. Introduction

Refrigeration systems have become an indispensable part of modern society. About a century ago, fluids such as, air, CO_2, NH_3 were used in refrigeration systems, which were more or less eco-friendly. However, their refrigeration efficiency was low and the problems associated with the design of compressors, led to the development of chlorofluorocarbons (CFCs) and hydro chlorofluorocarbons (HCFCs) which gave a big boost to the mechanical refrigeration industry in terms of reduced cost, higher reliability, increased efficiency, etc. However, the use of compressor, evaporator, condenser, throttling valve, etc. reduced the overall efficiency of the system. Later, it was observed that CFCs contain reactive gaseous atoms of chlorine or bromine, which reduces the stratospheric ozone to ordinary oxygen thus depleting the ozone layer, which pose serious threats to the environment. The ozone layer plays the pivotal role in absorbing the harmful ultraviolet rays (UV-B) coming towards the Earth. The Montreal Protocol, signed in 1987 was the first step to protect the stratospheric ozone by phasing out the production and consumption of ozone depleting substances such as CFCs. HCFCs was considered the interim solution to the use of CFCs because of their lower ozone depleting potential than CFCs. However, HCFCs possessed high global warming potential which makes them harmful to the environment and hence, in 2007, an amendment was made to the Montreal Protocol to phase-out HCFCs. Later, hydro fluorocarbons (HFCs) were used as alternatives to HCFCs. HFCs do not deplete the stratospheric ozone, but they are greenhouse gases having a very high global warming potential. The 28th Meeting of the Parties to the Montreal Protocol on Substances that Deplete the Ozone Layer held on 15 October 2016 in Kigali, Rwanda reached an agreement to eliminate hydro fluorocarbons (HFCs) by 2050. In this scenario, it is crucial to find alternatives sources of refrigeration that do not harm the environment. In this regard, some alternatives like magnetic refrigeration, which uses MCE, thermoelectric refrigeration that uses Peltier effect have been researched.

Magnetic refrigeration (MR), a potential cooling technology based on MCE has attracted worldwide attention owing to its higher efficiency and eco-friendly nature compared to the conventional vapour compression-expansion technique that is employed today (Franco *et al.*, 2012). Magnetic refrigerators use solid refrigerants (usually in the form of spheres or thin sheets), and common heat transfer fluids like water, water-alcohol

solution, inert gases like helium depending on the operating temperature, and hence do not produce any ozone-depleting or global-warming effects. An ideal magnetocaloric material operating at room temperature can effectively contribute to lowering the energy consumption by 20%–30%. Magnetic refrigeration in the low-temperature regime have been exploited in space science applications, liquefaction of hydrogen in the fuel industry, etc. On the other hand, materials exhibiting MCE near room temperature can be used for domestic and industrial refrigeration (Gschneidner *et al.*, 2005; Provenzano *et al.*, 2003). The search for new materials, which show GMCE near room temperature for small changes in magnetic field led to the development of a series of MCE materials such as Laves phases (Wohlfarth *et al.*, 1962; Khmelevskyi *et al.*, 2000; Singh *et al.*, 2007; Paul-Boncour *et al.*, 2009; Zhang *et al.*, 2009), La $(Fe_{1-x}Si_x)_{13}$ and its hydrides (Hu *et al.*, 2001; Fujita *et al.*, 2003), $Gd_5(Si_xGe_{1-x})_4$ series ([a]Pecharsky *et al.*, 1997; Pecharsky *et al.*, 2009;), $MnAs_{1-x}Sb_x$ (Wada *et al.*, 2001), $MnFe(P_{1-x}Si_x)$, ([a]Tegus *et al.*, 2002), NiMn-X (X= Ga,In,Sn) based Heusler alloys (Pakhomov *et al.*, 2001; Krenke *et al.*,2005) and Lanthanum manganites (Morelli *et al.*, 1996; Zhang *et al.*, 1996; Phan *et al.*, 2007). Experimental studies of pure lanthanide metals revealed that Gd is the best magnetic refrigerant and can be used to provide cooling between ~270 K and ~310 K (Brown, 1976; Zimm *et al.*, 1998). Other two lanthanides, Tb and Dy show lower MCE, and can be used to provide magnetic cooling between ~210 K and ~250 K, and ~160 Kand ~200 K, respectively ([a]Gschneidner *et al.*, 2000). Among the pure metals, Gadolinium (Gd) is one of the most widely studied magnetic refrigerant material (Tishin *et al.*, 1999), as Gd is known to have the largest magnetocaloric effect at 293 K and is, therefore, considered to be one of the best magnetic refrigerant material for air conditioning and refrigeration applications. Rare-earth metals (4f metals) and their alloys have been studied more extensively than 3d transition metals and their alloys, because the available magnetic entropy in the magnetic ordering of rare earths is considerably larger than in 3d transition metals. Alloying with different rare-earth elements provides an opportunity to tune the magnetic transition temperatures as well as the nature of magnetic phase transitions. Figure 2.1 shows the maximum magnetic entropy change versus temperature of different families of MCE materials for $\Delta H = 50$ kOe.

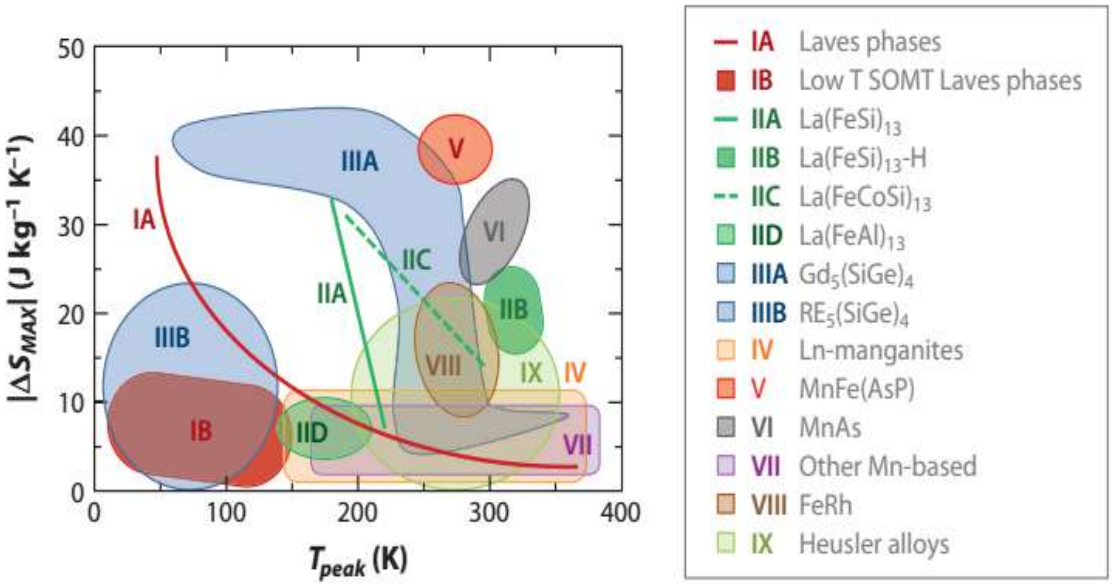

Figure 2.1. Maximum magnetic entropy change versus temperature of different families of MCE materials for ΔH = 50 kOe (*Adapted from Franco et al., 2012*).

2.2. Introduction to the Gd-Si-Ge family

The R_5T_4 family of intermetallic compounds (R= rare-earth metal, T=Si/Ge) was first studied by Smith *et al.* (Smith *et al.*, 1966) nearly half a century ago. Initially, both the silicides R_5Si_4 and germanides R_5Ge_4 were assigned to the layered Sm_5Ge_4 crystal structure ([a]Smith *et al.*, 1967, [b]Smith *et al.*, 1967). Later, Holtzberg *et al.* (Holtzberg *et al.*, 1967) found that the silicides and germanides of R_5T_4 compounds are not isostructural, even though they adopt the same space group symmetry, Pnma and have similar lattice parameters, which was later confirmed by Iglesias *et al.* (Iglesias *et al.*, 1972). Holtzberg *et al.* found that Gd_5Si_4 has an orthorhombic structure which orders ferromagnetically at a Curie temperature, T_C=336 K which is 43 K higher than that of pure Gd (Holtzberg *et al.*, 1967). The substitution of 50% of Ge for Si in the silicide structure, produced relatively little change in the structure and the magnetic properties. Magnetic measurements revealed that the silicides are ferromagnetic with relatively high ordering temperatures. The germanides are antiferromagnetic, but replacement of a small amount of Ge by Si in Gd_5Ge_4 produces solid solutions, which are ferromagnetic at low temperatures and have intermediate transitions to antiferromagnetism before becoming paramagnetic (Holtzberg *et al.*, 1967).

In 1997, Pecharsky and Gschneidner discovered the giant magnetocaloric effect in $Gd_5Si_2Ge_2$ alloys ([a]Pecharsky *et al.*, 1997). The magnetization measurements yielded

a value of -18.5 J/kg K at 276 K, which is two times larger than that of Gd, which shows a ΔS_M of -9 J/kg K at 293 K. Heat capacity measurements also confirmed the giant value of ΔS_M and the adiabatic temperature change, ΔT_{ad}, was also evaluated. The MCE parameters obtained for $Gd_5Si_2Ge_2$ is ΔS_M = -18.5 J/kg K and ΔT_{ad} = 15 K at 276 K for a field change of H = 50 kOe. Since this discovery, researchers have focussed on the tuning of transition temperature of $Gd_5(Si_xGe_{1-x})_4$ alloys for room temperature magnetic refrigeration applications.

2.2.1. Structure and Phase diagram of Gd-Si-Ge series

$Gd_5(Si_xGe_{1-x})_4$ system contains 36 atoms per unit cell; 20 atoms of Gd and 16 atoms of Si(Ge) distributed among six to nine independent crystallographic sites. The phase diagram of $Gd_5(Si_xGe_{1-x})_4$ system consists of three phase regions with different crystallographic structures built from essentially equivalent sub-nanometer thick slabs of the composition R_5T_4 (here, T= Si(Ge) mixture) composed of distorted cubes and trigonal prisms, varying in the inter-slab Si(Ge) bonding ([a]Pecharsky *et al.*, 2002). Gd atoms form a two-dimensional (3^2434) net (represented as blue spheres in the Figure 2.2) occupying the corners of the cube and trigonal prisms as well as inside the cubes. The T atoms (represented as green spheres in the Figure 2.2) occupy the trigonal prisms, sharing a common rectangular face to produce a T-T dimer (intra-slab bond) with, distances in the range 2.55–2.64 Å. These distances are within the range of single-bonded T–T contacts. The Gd atom at the center of each cube is octahedrally coordinated by T atoms. Each slab can be considered as a 1:1 condensation of two distinct units: (1) a R atom surrounded by a cube of eight R atoms and an octahedron of six T atoms, i.e., $[(R)_8\,R\,(T)_6]$; and (2) a T-T dimer with each T atom coordinated by a trigonal prism of R atoms and the open rectangular faces capped by R atoms, i.e., $[(R)_8\,T_2\,(R)_4]$. The T atoms inside the slab (represented as green spheres in the Figure 2.2) form partial covalent bonds, while those on the slab surface (represented as red spheres in the Figure 2.2) play a crucial role in the inter-slab bonding giving rise to different crystal structures and properties of the alloys (Choe *et al.*, 2000).

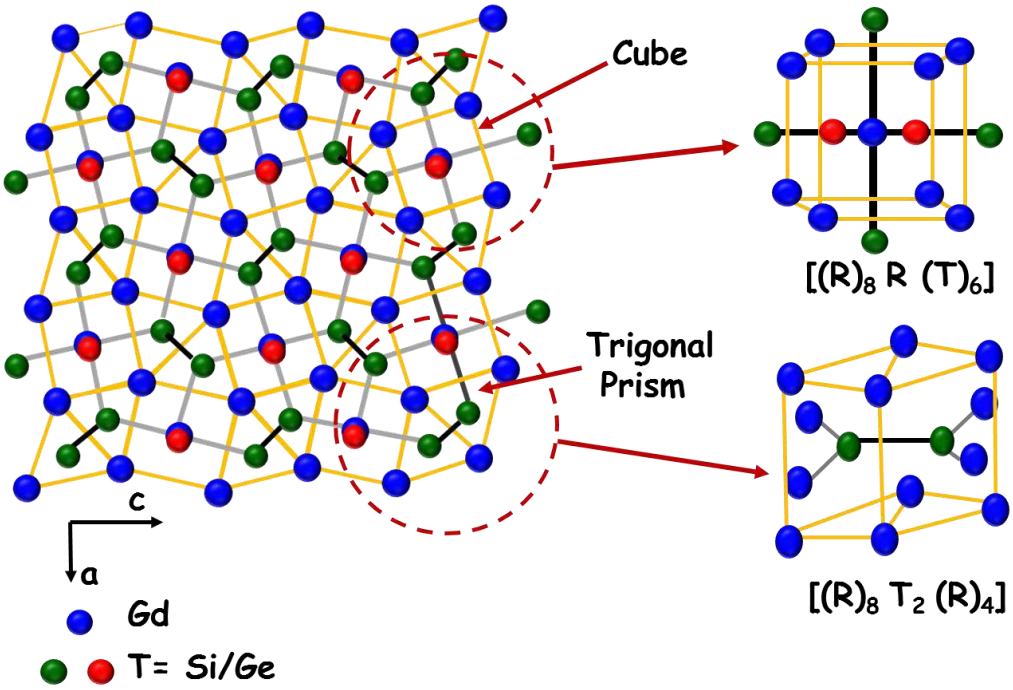

Figure 2.2. Structure of $Gd_5(Si_xGe_{1-x})_4$ series.

The phase diagram of the $Gd_5(Si_xGe_{1-x})_4$ series is shown in Figure 2.3. For compositions between $0.5 < x < 1$, the alloys have an orthorhombic O (I) Gd_5Si_4 type structure with Pnma space group, where all the slabs are interconnected via the partially covalent Si(Ge)-Si(Ge) bonds. For these x values, the alloys order ferromagnetically on cooling via a second order phase transition (SOPT) without any change in its crystal structure. In the intermediate region with $0.24 < x < 0.5$, one-half of the inter-slab Si(Ge)-Si(Ge) bonds are broken, and the room temperature crystal structure of these alloys is monoclinically distorted and is composed of alternating strongly and weakly interacting slabs. At low temperatures, these alloys transform to orthorhombic structure and become FM. When $0 < x < 0.2$, the compound stabilizes in the Gd_5Ge_4 type structure, in which all the inter-slab Si(Ge)-Si(Ge) bonds remain broken, giving rise to a different orthorhombic O(II) Sm_5Ge_4 structure (space group-Pnma) and the system becomes AFM near 125 K. On further cooling, the compound undergoes a FOPT from the AFM to FM state, which is attributed to the crystallographic transition forming the Gd_5Si_4-type structure, where all the slabs are connected to one another ([c]Pecharsky *et al.*, 1997). Ge enrichment shifts the transition temperatures to lower values but enhances the MCE signal. In the shaded region, two phases coexist. Ouyang reported the presence of short range FM correlations both the AFM and PM states of $Gd_5(Si_xGe_{1-x})_4$ with $x < 0.5$ by the

low magnetic field dc and ac magnetic susceptibility measurements. The presence of FM correlations in the PM state was ascribed to the GP like state that develops below T_G, above T_N or T_C. The evolution of the GP-like state is due to the orthorhombic-M structural distortion, which leads to disorder and enhances the competing inter-slab and intra-slab magnetic interactions. The appearance of GP has also been included in the phase diagram in Figure 2.3. The crystallographic structures of the Gd_5Ge_4, $Gd_5Si_2Ge_2$ and Gd_5Si_4 are shown in Figure 2.4.

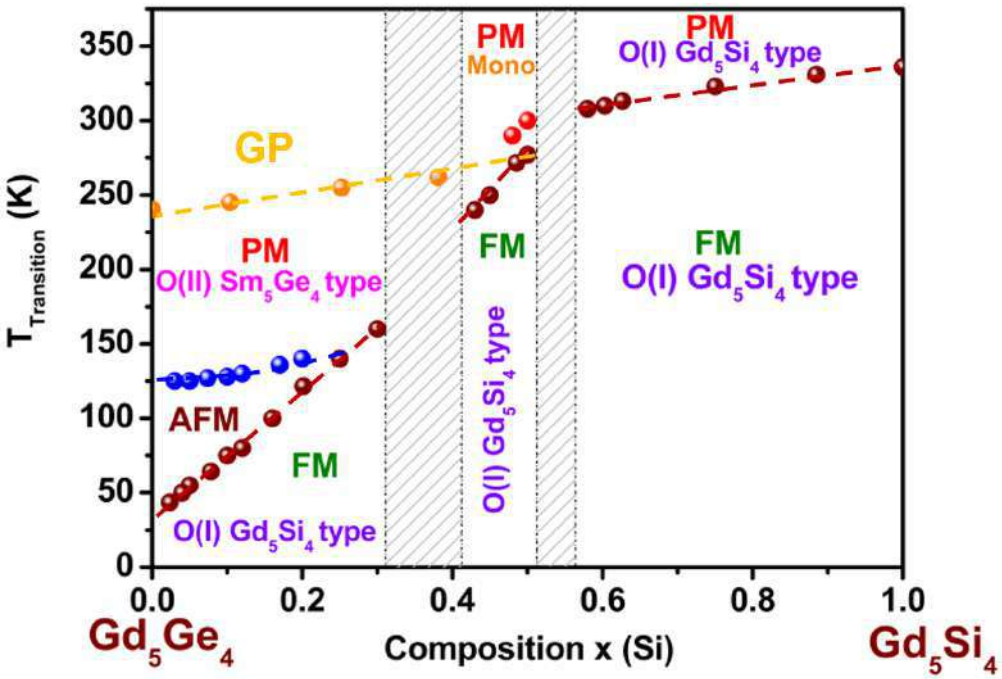

Figure 2.3. Phase diagram of $Gd_5(Si_xGe_{1-x})_4$ series.

Choe *et al.* elucidated the distribution of Si and Ge atoms among the three crystallographic sites from single crystal diffraction experiments. The inter-slab T atoms are labeled as T_1 (T^I) and the intra-slab T atoms are labelled as T_2 (T), T_3 (T) (Choe *et al.*, 2000). The orthorhombic crystal structure has six non-equivalent atomic positions in the asymmetric unit: (1) three distinct sites for Gd atoms : with Gd_1 and Gd_2 occupying the 3^2434 nets and Gd_3 within the cube, and (2) three distinct sites for Si or Ge atoms: with T_1 between the slabs forming inter-slab T_1-T_1 contacts; T_2 and T_3, within the slabs forming T_2-T_3 dimers (Iglesias *et al.*, 1972; Choe *et al.*, 2000). The Wycoff sites for Gd_1, Gd_2, Gd_3, T_1, T_2 and T_3 are 4c, 8d, 8d, 4c, 4c and 8d respectively. For the monoclinic structure, each of the eightfold sites of the orthorhombic structure splits into pairs of non-

equivalent fourfold sites. Hence, there are nine atoms in the asymmetric unit with the Gd_1 and Gd_2 sites each splitting into two pairs, Gd_{1A}, Gd_{1B} and Gd_{2A}, Gd_{2B} respectively. The T_1 site responsible for inter-slab bonding also splits into a pair of distinct sites, T_{1A} and T_{1B} ([c]Pecharsky *et al.*,1997; Choe *et al.*, 2000). These different crystallographic sites allow numerous chemical substitutions and exploration of relationships between chemical composition, structure, and properties.

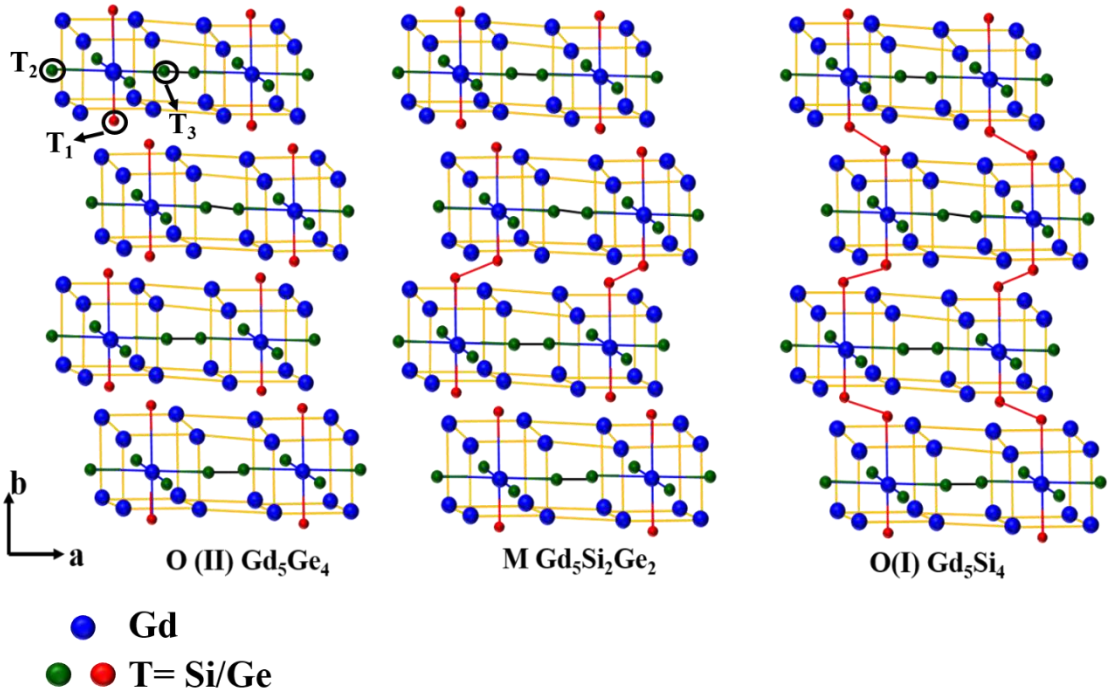

Figure 2.4. Three different crystallographic structures.

A non-statistical mixture of Si and Ge atoms (60% Si and 40% Ge) occupies the intra-slab T sites. The T atoms occupy the trigonal prisms in these slabs, which share a common rectangular face to create T_2 dimers (T-T distance is 2.56 Å). The Gd atom in the center of each cube (blue) is surrounded by an octahedral arrangement of four T atoms (green spheres in Figure 2.2) and two T^I atoms (red spheres in Figure 2.2). The inter-slab T^I sites represent a mixture of 40% Si and 60% Ge atoms. Each 3^2434 slab is connected to two adjacent slabs by T^I - T^I bonds (ca. 2.62 Å), when viewed along the **c** direction in Figure 2.4. In Gd_5Si_4, all the Si and Ge atoms are involved in dimers. In $Gd_5Si_2Ge_2$ structure, the inter-slab Si (Ge) atomic sites split into T_{1A} and T_{1B}. One-half of the T_{1B}-T_{1B} bonds connecting these slabs are broken, their T_{1B}-T_{1B} distance expands by 32.7% from 2.629(3) Å in monoclinic phase at 243 K to 3.488(3) Å in orthorhombic phase at

292 K. The inter-slab bonds in the Ge-rich dimers break while the short T_{1A}-T_{1A} distance remains at 2.614(3) Å (Choe *et al.*, 2003b; Misra *et al.*, 2006). The eightfold T^{I} site is richer in Ge compared to the fourfold T_2 and T_3 sites. This indicates that the slab structure itself prefers the smaller Si atoms inside and larger Ge atoms on the slab surface. Since Ge and Si are isoelectronic, the atomic positions of the outer layer of the slab are located in the atomic environment that can accommodate larger atoms more freely. This supports the notion that the intra-slab environment is more rigid and resists expansion (Mudrayk *et al.*, 2014).

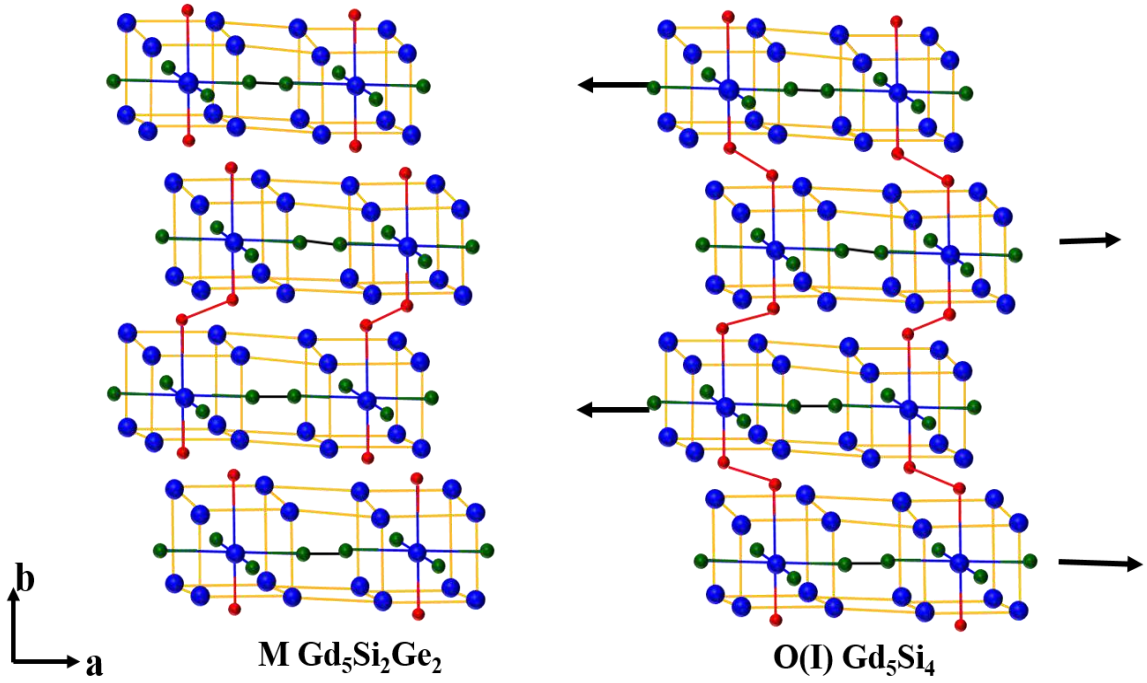

Figure 2.5. Transformation from monoclinic structure to orthorhombic structure via shear movement of the slabs.

The martensitic-like collective shear movement of these slabs via changing specific Si(Ge)-Si(Ge) bonds gives rise to different crystal structures in this family of materials. When the monoclinic structure transforms into the O(I) Gd_5Si_4 through massive shear movements of the slabs along the a-direction, the intra-slab T_{1B}–T_{1B} atoms reconnect, and the non-equivalent fourfold T_{1A} and T_{1B} positions of the M structure become the same eightfold T_1 position of the O(I) structure. The transformation from monoclinic structure to orthorhombic structure via shear movement of the slabs is shown in the Figure 2.5. Hence, in $Gd_5(Si_xGe_{1-x})_4$ system, each intermetallic phase is formed by

a periodic arrangement of well-defined building blocks of sub-nanometer thickness, consisting of layers with strongly interacting Gd, Si, and Ge elements. Any change in the chemical composition affects the interactions between these slabs considerably, thereby giving rise to a wide range of magnetic and physical properties ([b]Pecharsky *et al.*, 2002) Hence, there is a clear correlation between the crystal structure type and magnetic properties in R_5T_4 compounds (Morellon *et al.*, 1998; [c]Pecharsky *et al.*, 1997, Pecharsky *et al.*, 2001; Rao, 2000).

Application of the Zintl–Klemn formalism to these crystal structures reveals that the electron concentration change depending on the presence of the T-T bonds (Choe *et al.*, 2000, [a]Choe *et al.*, 2003). The formal charges on Gd atoms are assumed to be 3^+, and for isolated T atoms and T_2 dimers, the charges are assumed to be 4^- and 6^-, to satisfy closed shell configurations for Si or Ge, assuming a single bond in each T-T dimer. Then, the charge-balanced formula of the Gd_5Si_4 compound can be written as $(Gd^{3+})_5(T_2^{6-})_2(3e^-)$. The three electrons are assigned to the conduction band, because all Si (T) atoms in this structure form covalently bonded T_2 dimers each using one electron for such chemical bonding. When half of these bonds are broken, as in $Gd_5Si_2Ge_2$, the dimers change into a pair of T^{4-} monomers. Hence, $Gd_5Si_2Ge_2$ has 1.5 T_2 dimers and 1 T monomer/formula unit. Therefore, the charge-balanced formula for $Gd_5Si_2Ge_2$ is $(Gd^{3+})_5(T_2^{6-})_{1.5}(T^{4-})(2e^-)$. Gd_5Ge_4 contains 1 T_2 dimer and 2 T monomers/formula unit, giving $(Gd^{3+})_5(T_2^{6-})(T^{4-})_2(1e^-)$. The decrease in the number of electrons associated with the conduction band available for metallic bonding brings about changes in electronic structure and magnetic properties of these alloys (Choe *et al.*, 2000, [a]Choe *et al.*, 2003). The physical properties of the $Gd_5(Si_xGe_{1-x})_4$ systems are strongly determined by their uniquely layered crystallographic structure, and the strong interplay between the structural and magnetic degrees of freedom.

An intrinsic structural feature of the monoclinic phase, not observed in either of the orthorhombic structures, is the intrinsic presence of the nonmerohedral twinning. The single crystal X-ray diffraction of $Gd_5Si_2Ge_2$ (Choe *et al.*, 2000) showed a considerable number of Bragg reflections with non-integer indices, all multiples of 1/9, along the b-axis. The nonmerohedral twinning in a crystal produces a diffraction pattern in which only a small fraction of reflections from two macroscopic components are superimposed, while majority of the reflections remain separate. This is found to be very common in

compounds with the monoclinic crystal structure ([a]Choe *et al.*, 2003). The microstructural investigation of $Gd_5Si_2Ge_2$ by Meyers *et al.* ([a]Meyers *et al.*, 2002) revealed a twin law, which transforms one twin component into the other. When the monoclinic phase transforms to the O(I) phase, for example, via cooling below the transition temperature, the twinning disappears, but after the system returns to the stable monoclinic phase, the twinning reappears (Mudrayk *et al.*, 2014).

2.2.2. Magnetism in Gd-Si-Ge series

The crystallographic phase and the nature of the magnetic interactions in Gd-Si-Ge series are controlled by the number of inter-slab covalent-like T-T bonds connecting the slabs (Choe *et al.*, 2000; Rao, 2000). The intra-slab interaction is ruled by the conventional 4f - 4f RKKY indirect exchange, and the inter-slab interactions, are strongly influenced by an additional R-T-T-R super exchange interaction via the existing T-T bonds, formed by mainly non-magnetic elements like Si and Ge (Pecharsky *et al.*, 2001). In $Gd_5(Si_xGe_{1-x})_4$, the ferromagnetic state is always associated with the O(I)-Gd_5Si_4 crystal structure, and, therefore, with shorter T-T bonds (Pecharsky *et al.*, 2007; [b]Pecharsky *et al.*, 2003). The physical phenomena occurring at the magneto-structural transition region is due to the breaking and formation of bonds in a single pair of the non-magnetic tetralide atoms. Haskel *et al.* established the role of the Ge atoms in bridging ferromagnetic interactions in $Gd_5Si_2Ge_2$ and $Gd_5Si_{0.5}Ge_{3.5}$ using X-ray magnetic circular dichroism (XMCD) spectroscopy (Haskel *et al.*, 2007). The induced magnetic polarization of Ge electrons, caused by the hybridization of Gd 5d and Ge 4p conduction bands plays the key role in supporting three dimensional ferromagnetism in $Gd_5(Si_xGe_{1-x})_4$ alloys enabling long-range exchange interactions between Gd 4f moments in adjacent slabs. Breaking of the Ge (Si)-Ge (Si) inter-slab bonds weakens such interactions and effectively destroys the long-range ferromagnetic order.

2.2.3. Magnetocaloric effect in Gd-Si-Ge series

The occurrence of GMCE in $Gd_5(Si_xGe_{1-x})_4$ is attributed to the coupled magneto-structural first order phase transition from the high temperature monoclinic PM phase to the low temperature orthorhombic FM phase that occurs in the vicinity of the magnetic ordering temperature (Provenzano *et al.*, 2004) This phase transition can be induced reversibly by changes in temperature ([a]Pecharsky *et al.*, 1997; [b]Pecharsky *et al.*, 1997), hydrostatic pressure (Carvalho *et al.*, 2005; Magen *et al.*, 2005; Zou, 2012) and magnetic

field (Morellon *et al.*, 1998) as well as by tuning the Si:Ge ratio ([c]Pecharsky *et al.*, 1997). The order of a transition is evident from the presence of thermal hysteresis in the temperature dependent magnetization and heat capacity measurements of the given material. $Gd_5Si_2Ge_2$ shows a sharp first-order peak in its heat capacity data at T_C ([a]Pecharsky *et al.*, 1997) and in the Si-rich region, the heat capacity at the transition region shows a λ-shaped anomaly that reflects the second order nature of the transition (Gschneidner *et al.*, 1999). Inspite of the fact that, Si-rich alloys do not show GMCE, they still remain interesting candidates due to their high T_C and large magnetization, which could be easily tuned between 40˚C and 45˚C for designing materials potentially suitable for magnetic hyperthermia, a treatment for tumors (Ahmad *et al.*, 2005, Ahmad *et al.*, 2009).

2.2.3.1. Effect of impurities on the MCE of Gd-Si-Ge series

The presence of impurities in $Gd_5Si_2Ge_2$ has an adverse effect on its MCE (Gschneidner *et al.*, 1999; Gschneidner *et al.*, 2000; Mozharivskyj *et al.*, 2005). Commercial grade Gd is 95–98 at. % pure, and it contains considerable amounts of interstitial impurities such as, N (0.43 at. %), C, (0.43 at. %) and O (1.83 at %). The presence of C destroys the giant MCE in these alloys and raises the T_C thereby making the transition second order ([d]Pecharsky *et al.*, 1997). Gschneidner *et al.* developed a preparation route to reduce carbon content in the alloys made from commercial Gd. It involves the prolonged melting of Gd in Tantalum (Ta) crucible in vacuum, allowing the release of C and O in the form of gases like CO and CO_2 ([a]Gschneidner *et al.*, 2000). However, various contaminants and secondary phases like $Gd(Si_xGe_{1-x})$, $Gd_5(Si_xGe1\text{-}x)_3$, and Ta_2Si were observed as a result of the reaction with Ta crucible, during the synthesis of large batches of $Gd_5Si_{1.95}Ge_{2.05}$ from "commercial grade" Gd ([b]Meyers *et al.*, 2002). Thuy *et al.* and Wu *et al.* independently observed a GMCE (ΔS_M = -20 J/kg K) in as-cast $Gd_5Si_2Ge_2$ prepared using commercial grade Gd metal (Thuy *et al.*, 2002). Alves *et al.* obtained a GMCE of 19 J/kg K for a field change of 70 kOe at T_C=274 K in $Gd_5Si_2Ge_2$ alloy prepared from low-purity Gd by using the high-temperature heat treatment of the cast alloy at 1650˚C for 48 hours ([a]Alves *et al.* 2004). Hence, high-purity Gd metal is an essential criterion for obtaining the highest possible MCE. Gama *et al.* observed only a second-order transition at 299 K in the as-cast sample of $Gd_5Si_2Ge_2$ obtained from the commercial grade Gd. However, after annealing the sample at 1873˚C for 48 hours, two

transitions were observed, a second-order transition at 299 K, and a first order transition at 274 K. A GMCE of 18 J/kg K for a field change of 70 kOe in the heat-treated sample was observed, which meant that a substantial amount of the monoclinic phase has formed during the heat treatment (Gama *et al.*, 2004). Wu *et al.* studied the effect of oxygen on the MCE of a series of $Gd_5Si_{1.95}Ge_{2.05}O_x$ alloys (x=0.05, 0.10, 0.15, 0.40, and 0.50), in which oxygen was added as Gd_2O_3. Even the lowest amount of added oxygen (x=0.05) destroys the GMCE, by stabilizing the orthorhombic phase, and decreasing the amount of the monoclinic phase that undergoes a FOPT transition. Higher concentrations of oxygen led to the decomposition of the 5:4 phase into 1:1 (GdSi) and 5:3 (Gd_5Si_3) phases ([a]Wu *et al.*, 2005). Carvalho *et al.* studied the effect of hydrogen on the structural and magnetic properties of $Gd_5Si_{1.9}Ge_{2.1}H_x$ alloy ($0 < x < 2.5$) and found that even the smallest amount of hydrogen (x=0.09) stabilizes the O(I) Gd_5Si_4-type crystal structure, thereby changing the PM to FM transition from first order to second order (Carvalho *et al.*, 2007), thereby destroying the MCE. The The influence of hydrogen absorption on the Curie temperature and saturation magnetization of the $Gd_5Ge_2Si_2H_x$ alloys, with $0.1 \leq x \leq 2.5$ was studied by Alves *et al.* The saturation magnetization was found to increase with increase in Hydrogen content, which reveled that large amounts of hydrogen absorbed in to the unit cell can bring about remarkable changes in the microstructure and magnetic properties ([b]Alves *et al.*, 2004).

2.2.3.2. Effect of heat treatment on the MCE of Gd-Si-Ge series

In the as-cast alloy, the Si and Ge atoms are distributed randomly among the different crystallographic sites. Heat treatment leads to the reordering of the Si and Ge atoms in their corresponding sites within the monoclinic structure and helps in the removal of the retained polymorphic orthorhombic phase. This leads to the enrichment of Ge sites responsible for the inter-slab bonding. These changes produce a considerable enhancement of both the ΔS_M and ΔT_{ad}. The heat treatment at 1570 K for 1 hour results in the phase purification and homogenization of arc-melted $Gd_5Si_2Ge_2$ prepared from high-purity components and gives the optimal annealing condition for the formation of the single-phase monoclinic structure with highest MCE. However, the magnetic ordering temperature is slightly reduced from 277 K in the as-cast material to 272 K in the uniformly homogenized and annealed $Gd_5Si_2Ge_2$ ([a]Pecharsky *et al.*, 2003). Hence,

appropriate heat treatment of the $Gd_5Si_2Ge_2$ alloy prepared from high-purity Gd results in the significant enhancement of $-\Delta S_M$ by 80%, from ~20 to 36 J/kg K and ΔT_{ad} by 55%, from ~11 to 17 K for a magnetic field change of 50 kOe when compared to the as-cast material ([b]Pecharsky *et al.*, 2003). Several studies showed that longer annealing times even at optimal temperatures are detrimental to the phase purity and magnetocaloric properties of the $Gd_5Si_2Ge_2$ (Belo *et al.*, 2012; [a]Pecharsky *et al.*, 2003). Yan *et al.* reported the effects of composition and cooling rate on the structure and magnetic entropy change in $Gd_5Si_xGe_{4-x}$ alloys with x=1.7 and 2. Higher Ge content and higher cooling rate are favorable for the formation of the monoclinic $Gd_5Si_2Ge_2$-type phase, and thus a higher ΔS_M can be obtained due to a magnetic field-induced FOPT. This transition is significantly weakened in higher Si content alloys and slowly cooled samples, leading to the formation of O(I) phase with Gd_5Si_4 structure and thus a lower ΔS_M is obtained for Si-rich alloys (Yan *et al.*, 2004).

2.2.3.3. Effect of varying Si:Ge ratio on the MCE of Gd-Si-Ge series

A valuable feature of $Gd_5(Si_xGe_{1-x})_4$ alloys is that its T_C can be linearly increased by Si-doping, as shown in Figure 2.3 (phase diagram). The ordering temperature is tunable from 20 to 290 K ($0 < x \leq 0.5$) by adjusting the Si/Ge ratio without losing the GMCE ([a]Pecharsky *et al.*, 1997, [b]Pecharsky *et al.*, 1998). However, this striking feature disappears when the Si-content is larger than $x = 0.5$, where a purely, second order FM(O(I))→PM(O(I)) transition takes place on warming ($0.5 < x \leq 1.0$) without a concomitant structural change ([c]Pecharsky *et al.*, 1997, [b]Pecharsky *et al.*, 2003). Si has smaller atomic size than Ge and its role in occupying the three inequivalent crystallographic sites (Figure 2.4) is to exert chemical pressure upon the lattice causing a reduction in unit cell volume. This volume reduction directly enhances both the intra-slab and inter-slab magnetic interactions, resulting in an increase in the FM ordering temperature.

2.2.3.4. Effect of rare-earth substitution on the MCE of Gd-Si-Ge series

Alloying $Gd_5Si_2Ge_2$ with different elements at the Si (Ge) site, or Gd site can tune the transition temperature T_C, but this has an adverse effect on the magnitude of MCE due to a significant change in the nature of magnetic transition from first-order to second-order. Several studies have been performed on different $R_5(Si_xGe_{1-x})_4$ series (R= Pr, Nd,

Dy, Tb and Ho) to understand the correlation between the magnetic and crystallographic phases (Wang *et al.*, 2007, Magen *et al.*, 2004, [a]Nirmala *et al.*, 2007, [b]Tegus *et al.*, 2002, Thuy *et al.*, 2002, Pereira *et al.*, 2008). The MCE of $Nd_5Si_2Ge_2$ with monoclinic structure was investigated by Gschneidner *et al.* and was found to be 5.6 J/ kgK for 50 kOe at 65K ([a]Gschneidner *et al.*, 2000). Deng *et al.* reported an MCE of 13.79 J/kg K at 232 K and 18.89 J/kg K at 195 K for a field change of 20 kOe in $(Gd_{0.74}Tb_{0.26})_5Si_2Ge_2$ and $(Gd_{0.74}Tb_{0.26})_5(Si_{0.43}Ge_{0.57})_4$ respectively ([a]Deng *et al.*, 2007) and 25.13 J/kg K at 230 K in $(Gd_{0.94}Tb_{0.06})_5Si_{1.72}Ge_{2.28}$ ([b]Deng *et al.*, 2007). Nirmala *et al.* reported that substituting heavy rare earth Dy leads to the lowering of the ferromagnetic ordering temperature in $Gd_5Si_2Ge_2$ with a loss of FOPT ([b]Nirmala *et al.*, 2007). Chen *et al.* investigated the effects of Er substitution on the magnetocaloric property of $Gd_5Si_2Ge_2$ and reported a value of 16.1 J/kg K at 222 K for a field change of 20 kOe in $(Gd_{0.9}Er_{0.1})_5Si_2Ge_2$ (Chen *et al.*, 2011).

2.2.3.5. Effect of transition metal substitution on the MCE of Gd-Si-Ge series

It has been reported that the addition of small amounts of 3d elements (Fe, Co, Ni, or Cu) and p elements (Al, C) (0.33 % at. wt.) for Si and Ge in the $Gd_5Si_2Ge_2$ alloy increase the Curie temperature (T_C) but destroys the first order magnetic phase transition and the GMCE ([d]Pecharsky *et al.*, 1997). According to Pecharsky *et al.*, the addition of small amounts of Ga (0.33 % at. wt.) to $Gd_5Si_2Ge_2$ alloy i.e. $Gd_5Si_{1.985}Ge_{1.985}Ga_{0.03}$, not only preserves the GMCE of 17.6 J/kg K, but also raises the temperature of the FOPT by 10 K, from 276 K to 286 K ([d]Pecharsky *et al.*, 1997). However, upon increasing the Ga content to 0.67 at%, the ΔS_{max} shifts to even higher temperatures, but unfortunately it changes the magnetic behavior of the parent $Gd_5Si_2Ge_2$ from first order to second order with the loss of the GMCE. However, Aksoy *et al.* observed a reduction in the MCE of $Gd_5Si_{2-x}Ge_{2-x}Ga_{2x}$ alloys with Ga substitution for 2x=0.03 and higher, and found that the stability of the O(I) phase increases with x (Aksoy *et al.*, 2008). A similar result was also observed by Raj Kumar *et al.* with Ga doping in $Gd_5Si_2(Ge_{1-x}Ga_x)_2$ alloys with x=0, 0.01, 0.02 and 0.03 (Raj Kumar *et al.*, 2008). The Curie temperatures of these Ga-substituted alloys correspond to the second-order transition of the O(I) phase (299 K). The composition with x=0 contained a significant amount of the O(I) phase, and its $-\Delta S_M$ was only 7 J/kg K. SEM measurements revealed the presence of both 5:3 Gd_5Si_4 and 1:1 GdSi minor phases in these Ga-doped alloys. Palacios *et al.* studied the magnetocaloric

properties of $Gd_5Si_2Ge_{1.9}Ga_{0.1}$ sample by means of heat capacity and direct magnetocaloric measurements and obtained a $-\Delta S_M$ of 6.93 J/kg K and ΔT_{ad} of 8 K (Palacios *et al.*, 2010).

Zhang *et al.* reported a considerable reduction in thermal hysteresis with the addition of transition elements such as Fe, Co, Mn, and Ni due to the formation of the Gd_5Si_4 structure (Zhang *et al.*, 2007). The reduction in hysteresis losses with the substitution of Fe was reported by Provenzano *et al.* (Provenzano *et al.*, 2004). Lewis *et al.* compared the magnetic entropy change of $Gd_5Si_{1.5}Ge_{2.5}$ and of the same specimen coated with 100 nm layer of Fe and Al and found an enhancement in MCE, as a result of Fe coating (Lewis *et al.*, 2004). Shull *et al.* found that the addition of Cu, Co, Ga, Mn, and Al (0.1% at. wt.) at the Ge site completely eliminated the hysteresis loss, broadened the magnetic entropy change and shifted its peak position from 275 K to 305 K. However, doping the same amount of either Sn or Bi had a negligible effect on the magnetocaloric properties (Shull *et al.*, 2006). Podmiljšak *et al.* observed that the substitution of Fe at the Si site does not suppress the structural transition in $Gd_5Si_{2-x}Fe_xGe_2$ alloys, but promotes the formation of the 5:3 phase ([a]Podmiljšak *et al.*, 2009; [b]Podmiljšak *et al.*, 2009; [c]Podmiljšak *et al.*, 2009). Iron was mainly found to segregate into the grain-boundary phases, and the main effect of its substitution was to the change the Si/Ge ratio in the 5:4 matrix. This holds true for other transition metal substitutions, i.e. when the $Gd_5Si_2Ge_2$-based matrix becomes Si-rich, then the orthorhombic O(I) structure forms, in agreement with the $Gd_5(Si_xGe_{1-x})_4$ phase diagram described in Figure 2.3, However, the matrix becomes enriched in Ge, the monoclinic structure remains stable. In another work, they found that the substitution of Fe at the Si site result in the decrease of T_C and MCE while Fe substitution at the Ge site would result in an increase of T_C but with a reduced MCE ([b]Podmiljšak *et al.*, 2009). The reduction in magnetic entropy change with Fe substitution in $Gd_5Si_2Ge_2$ and $Gd_5Si_xGe_{3.9-x}Fe_{0.1}$ alloys was reported by Raj Kumar *et al.* (Raj Kumar *et al.*, 2009, Raj Kumar *et al.*, 2010) which was attributed to the stabilization of the O(I) Gd_5Si_4 structure. Yucel *et al.* studied the effect of Mn doping on the phase composition and magnetic properties of $Gd_5Si_{2-x}Ge_{2-x}Mn_{2x}$ alloys with x=0.01, 0.025, 0.04, 0.05, 0.07, and 0.10, where a second-order PM to FM transition was observed in the as-cast alloys with no GMCE (Yucel *et al.*, 2006). The partial substitution of Nb in $Gd_5Si_{2-x}Ge_{2-x}Nb_{2x}$ alloys (2x= 0, 0.05, 0.1, 0.15, 0.2) annealed at 1200˚C for 1 hour was investigated by

Prabahar *et al*. Nb substitution increased the Curie temperature and MCE signal as x increased to 0.05 (T_C~ 295 K and ΔS_M = -9.6 J/ kg K for a field change of 20 kOe, ~50% enhancement over the Nb-free alloy). However, Nb addition results in the formation of $Nb_5(Si,Ge)_3$ and α-Nb phases (Prabahar *et al.*, 2010). Li *et al.* reported the enhancement of MCE in $Gd_5Si_{1.95}Ge_{2.05}$ by Sn doping. Among the five $Gd_5Si_{1.95-x}Ge_{2.05-x}Sn_{2x}$ samples (2x =0, 0.01, 0.03, 0.05, 0.10), the sample with 2x=0.03 showed the largest MCE, ΔS_M =-28.9 J/kg K for a field change of 20 kOe (Li *et al.*, 2006). Zhang *et al.* investigated the effect of Sn doping on the phase formation of $Gd_5Si_{2-x}Ge_{2-x}Sn_{2x}$ alloys (x=0.25), and found that Sn addition enhances the stability of the monoclinic phase in alloys made from the commercial grade Gd (Zhang *et al.*, 2008). Aghababyan *et al.*prepared a series of $Gd_5Si_{2-x}Ge_{2-x}Sn_2x$ samples (2x=0, 0.01, 0.03, 0.05, 0.10) and measured the temperature dependence of their dynamic magnetic susceptibility. They observed that the magnetic ordering temperatures of Sn-doped alloys vary from 275 to 278 K, which is 15 K higher than the T_C of their un-doped $Gd_5Si_2Ge_2$ (262 K) (Aghababyan *et al.*, 2009) The MCE in a series of $Gd_5Si_{2-x}Ge_{2-x}Pb_{2x}$ alloys with 2x=0, 0.01, 0.03, 0.05 and 0.10 was investigated by Zhuang *et al.* and a large MCE of -27.5 J/kg K for ΔH=20 kOe was observed at 274 K for $Gd_5Si_{1.975}Ge_{1.975}Pb_{0.05}$ (Zhuang *et al.*, 2006). Franco *et al.* performed the scaling analysis of the magnetocaloric effect in $Gd_5Si_2Ge_{1.9}X_{0.1}$ alloys (X=Al, Cu, Ga, Mn, Fe, Co)(Franco *et al.*, 2010). In Al, Cu, Ga, and Mn doped alloys, the FOPT is fully suppressed, and the universal curve can be constructed using a single reference temperature. Moreover, the magnetic energy curves for all compositions undergoing second-order transition fit onto the same universal curve constructed using the phenomenological scaling model (Franco *et al.*, 2006). In the Fe-doped sample, the first-order character almost disappeared, but the presence of a weak hysteresis made the scaling procedure more complicated, as two reference temperatures are needed. In the Co-doped alloy, there is a significant thermal hysteresis, which makes the scaling results inconclusive.

Prabahar *et al.* investigated the effect of doping Zr on a series of $Gd_{5-x}Zr_xSi_2Ge_2$ alloys with x=0, 0.05, 0.1, 0.15, and 0.2. The Zr substitution results in the formation of the orthorhombic O(I) phase in all the Zr-containing samples and hence, ΔS_M decreased from -7.8 to -5.5 J/kg K for ΔH = 20 kOe, when x increased from 0 to 0.05, and the Curie temperature increased to 295 K for x=0.05 alloy compared to the pure $Gd_5Si_2Ge_2$ (278

K)(Prabahar *et al.*, 2011). Zhong *et al.* reported the magnetocaloric properties of $Gd_5Si_{2.05-x}Ge_{1.95-x}Ni_{2x}$ (2x = 0.08, 0.1) and found that the compounds crystallized in a combination of monoclinic $Gd_5Si_2Ge_2$-type phase, O(I) Gd_5Si_4-type phase, and a small amount of hexagonal Gd_5Si_3-type phase. $Gd_5Si_{2.01}Ge_{1.91}Ni_{0.08}$ alloy undergoes a SOPT around 300 K, whereas $Gd_5Si_2Ge_{1.9}Ni_{0.1}$ exhibits two transitions including a FOPT at 295 K and SOPT at 301 K. The maximum ΔS_M of $Gd_5Si_{2.05-x}Ge_{1.95-x}Ni_{2x}$ alloys with 2x=0.08 and 0.1 are -4.4 and -5.0 J/kg K, respectively, for a field change of 20 kOe, and 8.0 and 9.1 J/kg K, respectively, for a field change of 50 kOe (Zhong *et al.*, 2013). A large ΔS_M of 20 J/kg K were obtained in as-cast samples of $Gd_5Ge_2Si_{2-x}Sn_x$ (x = 0, 0.10, 0.20, 0.40, 1.00, 1.50) for a magnetic field variation of 20 kOe. First-order-magneto-structural phase transition is induced by the substitution of Si by Sn, and the Curie temperature shifted to lower temperatures with increase in Sn content (Carvalho *et al.*, 2013).

2.3. Introduction to Manganites

Perovskites are a large family of crystalline ceramics, which derive their name from a specific mineral $CaTiO_3$, discovered by German chemist and mineralogist Gustav Rose in 1839, and named it in honor of the Russian dignitary Lev Alexeievich Perovsky (Navrotsky *et al.*, 1989). In their ideal form, perovskites are described by the generalized formula ABX_3. A,and B are metallic cations, and X represents non-metallic anions. The perovskite family of oxides (ABO_3) is probably the best-studied family of oxides. Interest over compounds belonging to this family of crystal structure is rooted in the fact that they show a wide variety of properties and their flexibility to accommodate almost all the elements in the periodic table. Manganites with general formula $Ln_{1-x}A_xMnO_3$ (Ln = Rare earth element and A = divalent alkaline-earth ions such as Ca, Sr, Ba, etc. or tetravalent ions such as Te, Ce, Hf, Sn, etc.), have attracted considerable attention owing to their peculiar magnetic properties and their promise for future technological applications such as colossal magnetoresistance (CMR), devices for information storage and magnetic sensors, magnetic refrigeration (MR), spintronics, etc. (Yang *et al.*, 2007). These compounds are used as sensors and catalyst electrodes in certain types of fuel cells and are suitable candidates for memory devices and spintronic applications. (Tokura *et al.*, 1999; Tokura, 2000; [a]Phan *et al.*, 2007; [b]Phan *et al.*, 2007). The parent compound $LaMnO_3$ is a charge-transfer insulator with trivalent manganese arranged in different layers coupled among themselves antiferromagnetically through super exchange

mechanism. But within a layer, these Mn^{3+} ions are coupled ferromagnetically (Zanen *et al.*, 1985; Mandal *et al.*, 1997). Manganites crystallize in an ABO_3 type structure as shown in Figure 2.6. The A atoms occupy the corners of the cube, and the B atoms which occupy the center of the cube are octahedrally coordinated to six oxygen (O) ions. The A site is usually occupied by rare-earth or alkaline-earth divalent ions while B site is usually occupied by manganese (Mn). The electronic configuration of manganese is $Ar\ 3d^5 4s^2$. In an octahedral environment, the electrostatic interaction between Mn and O leads to the splitting of the five degenerate d orbitals of Mn into two sets, a lower energy t_{2g} state and a higher energy e_g state. The crystal field splitting between the t_{2g} and e_g states is about 1 eV (Tokura, 2000). The doping of $LaMnO_3$ with divalent or tetravalent ions drives the manganese ions into a mixed valence state. The introduction of divalent ions like Sr^{2+}, Ca^{2+} into the manganite system drives the manganese ions into a mixed valence state of Mn^{3+} ($t_{2g}^3\ e_g^1$) and Mn^{4+} (t_{2g}^3) (Goodenough, 2003; Coey *et al.*, 2009). But if the rare-earth ion is partially replaced by some tetravalent ions like Te^{4+}, Ce^{4+}, etc., the manganese ion exists in Mn^{2+} ($t_{2g}^3\ e_g^2$) and Mn^{3+} states. The introduction of the tetravalent ion drives Mn^{3+} ions of $LaMnO_3$ into Mn^{2+} ions, which is equivalent to introducing an electron into the e_g band. CMR behavior occurs in these compounds due to the mixed-valence state of Mn^{2+} /Mn^{3+}. In hole-doped manganites, Mn exists as Mn^{3+}/Mn^{4+} ions depending up on the amount of divalent ions. The spin only moments of Mn^{3+} and Mn^{4+} are 4.9 μ_B and 3.88 μ_B respectively.

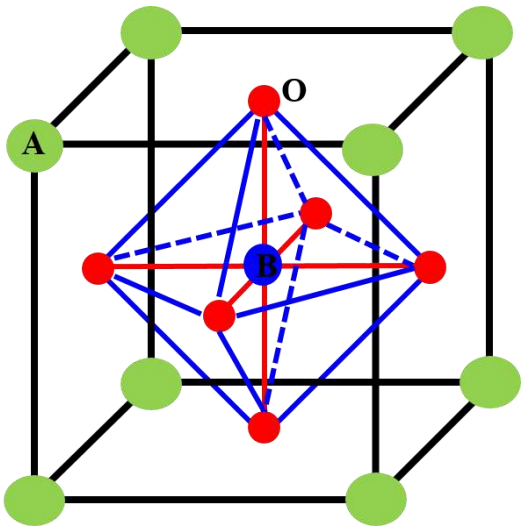

Figure 2.6. Structure of manganite.

It is well established that the manganites are flexible with distortion of MnO_6 octahedra. The factors which leads to the distortion of the prototypical cubic structure to a lower symmetry structure include Jahn−Teller effects, average radius of A site cation ($<r_A>$), size variance ($\sigma^2(r_A)$), thermal fluctuations, external strain etc. Goldschmidt has shown that the perovskite structure is stable within the tolerable limits of cations sizes (Goldschmidt, 1926) and he defined tolerance factor t as,

$$t = \frac{r_A + r_o}{\sqrt{2}(r_B + r_o)} \qquad (2.1)$$

where, r_A , r_B and r_O are the radii of A, B and O ions which are summarized in the literature (Shannon, 1976). Tolerance factor, t=1 corresponds to an ideal cubic structure, while the value away from 1 suggests a high degree of internal strain due to size mismatch, which leads to a distorted perovskite structure. As 'r_A' decreases, the lattice structure transforms to rhombohedral ($0.96 < t < 1$) and then to the orthorhombic structure ($t < 0.96$), in which Mn−O−Mn bond angle is bent and deviates from 180^o. The MnO_6 tilting angle $\omega = 180^o - \langle \text{Mn-O-Mn} \rangle$ decreases with decrease in 't'. The bond length mismatch created by $t < 1$ is accommodated by co-operative rotation of MnO_6 octahedra, which is accompanied by a corresponding shift of the A cations.

The presence of two or more A-site cations of different radius also leads to disorder and can modify the properties of the perovskites. The A− site disorder can be defined by a term called size variance. The size variance is defined as,

$$\sigma^2(r_A) = \sum x_i r_i^2 - \langle r_A \rangle^2 \qquad (2.2)$$

where 'x_i' and 'r_i' are the atomic fraction and ionic radii of i-type ions at A-site respectively. 'r_A' is the ionic radii of A cation. $\sigma^2(r_A)$ is a measure of the consequent perturbation of the periodic potential of the MO_3 array (Goodenough, 1955; Goodenough, 2003).

2.3.1. Hole doping and electron doping in manganites

The substitution of divalent ions at the A site has been the subject of intensive research over the years. The research on electon doped manganites started with the work of Mandal and Das (Mandal *et al.*, 1997). Since then, considerable research has emphasised on electron-doped compounds such as $La_{1-x}B_xMnO_3$ where B= Te, Ce, Hf, Sb, Zr, etc. Both electron-doping and hole-doping in ferromagnetic (FM) manganites

opens up interesting applications in the emerging field of spintronics. The introduction of divalent ions like Sr^{2+}, Ca^{2+} into the A site drives the manganese ions into a mixed valence state of Mn^{3+} (t_{2g}^3 e_g^1) and Mn^{4+} (t_{2g}^3) (Goodenough, 2003; Coey *et al*., 2009). This is equivalent to introducing a hole in the system and hence, the name hole doped manganites. But if the rare-earth ion is partially replaced by some tetravalent ions like Te^{4+}, Ce^{4+}, etc., the manganese ion exists in Mn^{2+} (t_{2g}^3 e_g^2) and Mn^{3+} states. The introduction of the tetravalent ion drives Mn^{3+} ions into Mn^{2+} ions, which is equivalent to introducing an electron into the e_g band, hence the name electron doped manganites. CMR behavior occurs in these compounds due to the mixed-valence state of Mn^{2+} /Mn^{3+}.

2.3.2. Magnetocaloric effect in $La_{1-x}Te_xMnO_3$

The compound $La_{1-x}Te_xMnO_3$ (x = 0.04, 0.1), in which the La ions are replaced by the non-metal element Te in the chalcogenide series, has a rhombohedral lattice with the space group of *R*-3*c*, and Te ions are in the tetravalent state. Tan *et al.* investigated the electrical and magnetic properties of $La_{1-x}Te_xMnO_3$ with x=0.1 and 0.15. The compounds showed a Curie temperature (T_C) of 240 K and 255 K for x=0.1 and 0.15, respectively. The maximum magnetoresistance was about 51% in $La_{0.9}Te_{0.1}MnO_3$ and 47 % in $La_{0.85}Te_{0.15}MnO_3$ at 200 K in an applied magnetic field of 40 kOe ([a]Tan *et al.*, 2003). They also reported the magnetic and electrical properties $La_{1-x}Te_xMnO_3$ in the composition range x=0.04, 0.1, 0.15, and 0.2. A magnetoresistance of about 63% was observed for x=0.04 in an applied magnetic field of 40 kOe. ESR studies indicated that the compound was in the paramagnetic phase above 230 K, and in single ferromagnetic state below 170 K. In the temperature range, 230 K to 170 K, the compound showed phase separation ([b]Tan *et al.*, 2003). Guo *et al.* explained the spin glass behavior in electron-doped $La_{1-x}Te_xMnO_3$ thin films epitaxially grown on MgO substrates and attributed this behavior to magnetic interactions arising due to spin phonon coupling (Guo *et al.*, 2004). Yang *et al*. studied the effect of grain size on the structural, magnetic and transport properties of electron-doped $La_{0.9}Te_{0.1}MnO_3$ manganite. They found that both magnetization and T_C decreased with increasing grain size, which was ascribed to the increase in the Mn–O bond length. They found that both the intrinsic CMR and the extrinsic interfacial magnetoresistance can be effectively tuned in $La_{0.9}Te_{0.1}MnO_3$ by varying the grain size ([a]Yang *et al.*, 2004). The effect of Pr-doping on the structural,

magnetic and transport properties of $La_{0.9-x}Pr_xTe_{0.1}MnO_3$ ($0 \leq x \leq 0.9$) was investigated by Yang *et al*. With Pr doping, Curie temperature of the samples decreased ([b]Yang *et al*., 2004). A magnetic phase diagram of $La_{1-x}Te_xMnO_3$ ($0.1 \leq x \leq 0.6$) compounds as a function of temperature and the doping level x was also established by Yang *et al*. (Yang *et al*., 2005). Gebhardt *et al.* investigated the magnetic and transport properties of Ce doping in $R_{1-x}A_xMnO_3$ (R=La, Ce, and A=Sr, Ce). They found that the increase in Ce concentration resulted in the increase of T_C from 225 K to 236 K, and an increase in the electrical resistivity. A maximum magnetoresistance ratio of 40% was observed in $Ce_{1-x}Sr_xMnO_3$, which becomes insulating below its Curie temperature of 43 K and 53% was observed for $La_{1-x}Ce_xMnO_3$ (Gebhardt *et al.,* 1999). Raychaudri *et al.* reported the electronic, transport, and magnetic properties of $La_{1-x}Ce_xMnO_3$ and suggested that this material could find profound application in spintronics (Raychaudri *et al.*, 2003). The magnetotransport characteristics of a trilayer ferromagnetic tunnel junction built of an electron doped manganite - $La_{0.7}Ce_{0.3}MnO_3$ and a hole doped manganite -$La_{0.7}Ca_{0.3}MnO_3$ suggested that $La_{0.7}Ce_{0.3}MnO_3$ is a minority spin carrier ferromagnet with a high degree of spin polarization, i.e., a transport half-metal (Mitra *et al.*, 2003). The effect of Cu-doping at Mn-site in $La_{0.85}Te_{0.15}Mn_{1-x}Cu_xO_3$ ($0 \leqslant x \leqslant 0.20$) was investigated by Yang *et al.* Cu doping decreases the Curie temperature and the transition becomes broader with increasing Cu-doping. The insulator-metal (I-M) transition shifts to lower temperatures with increasing Cu-doping content and disappears as x increase to 0.1 ([c]Yang *et al.*, 2004). Tan *et al.* observed spin glass behaviour in $La_{1-x}Te_xMnO_3$ with x = 0.04 and 0.1, at the low magnetic fields, at the freezing temperature of 200 K under the applied field of 0.01 T ([c]Tan *et al.* , 2003). The effects of Cr doping in $La_{0.9}Te_{0.1}MnO_3$ has been investigated by Zheng *et al*. They observed that Cr doping decreases the Curie temperature and the magnetization due to the destruction of DE interaction (Zheng *et al.*, 2007). Mahato *et al.* prepared nanocrystalline $La_{0.7}Te_{0.3}MnO_3$ and observed the co-existence of giant magnetoresistance and large MCE near room temperature. A large magnetic entropy change of -12.5 J/kg K was observed at 280 K for a field change of 50 kOe. A giant magnetoresistance of 52% was also observed in 50 kOe (Mahato *et al.*, 2010). The effect of grain size on the MCE of nanocrystalline $La_{0.8}Te_{0.2}MnO_3$ was examined by Mahato *et al.* and found that MCE decreases with decrease in grain size. The maximum entropy change of 3.2 J/kg K, 3 J/kg K and 2 J/kg K was observed for samples with particle size

55 nm, 40 nm and 25 nm for a field change of 20 kOe at 278 K, 270 K and 260 K respectively (Mahato *et al.*, 2011). Meenakshi *et al.* reported the effect of Fe substitution in nanocrystalline $La_{0.7}Te_{0.3}Mn_{1-x}Fe_xO_3$ for x=0.1 and 0.3 and found a $-\Delta S_M$ of 1.17 J/kg K for x=0.1 and 0.44 J/ kg K for x=0.3 for a field change of 20 kOe at 171 k and 78 K respectively (Meenakshi *et al.*, 2017).

2.4. Motivation for the present study

During the literature survey on various magnetic materials, it has been realized that Gd-Si-Ge series of alloys undergoing first order transition give many interesting functional as well as fundamental properties. The GMCE in $Gd_5(Si_xGe_{1-x})_4$ series is attributed to the coupled magneto-structural transition from the high temperature monoclinic PM phase to the low temperature orthorhombic FM phase that occurs in the vicinity of the magnetic ordering temperature. Due to the magneto-structural transition, these alloys show various multifunctional properties like GMCE and giant magnetoresistance. The search for materials with GMCE near room temperature has motivated us to carry on further research on these alloys to identify optimum compositions, which can act as potential magnetic refrigerants that could replace the currently persisting HFC's used in refrigerator and air conditioners. In addition, we wanted to acquire the capability of tuning the Curie temperature and entropy change in these materials by adjusting the composition. In this regard, we chose Gd-Si-Ge series and an electron doped managanite for our present study. In Gd-Si-Ge series, two compositions were chosen, namely $Gd_5Si_2Ge_2$ and $Gd_5Si_{1.7}Ge_{2.3}$. The stabilization of the monoclinic phase is the essential criterion for inducing a FOPT in Gd-Si-Ge alloys, which gives rise to GMCE. In $Gd_5Si_2Ge_2$ alloy, the monoclinic phase is metastable while in $Gd_5Si_{1.7}Ge_{2.3}$, the monoclinic phase remains a stable phase. Hence, we prepared $Gd_5Si_2Ge_2$ alloys with Nd, Co and Fe substitution. The effect of Co and Fe substitution on the MCE properties of $Gd_5Si_{1.7}Ge_{2.3}$ alloys has been investigated. The observation of a large $-\Delta S_M$ of 12.5 J/kg K at 280 K in nanocrystalline $La_{0.7}Te_{0.3}MnO_3$ by Mahato *et al.* motivated us to study the effect of transition elements on the MCE of $La_{0.7}Te_{0.3}MnO_3$. In this attempt, we studied the effects of Co doping in electron doped $La_{0.7}Te_{0.3}MnO_3$ manganite is also investigated.

The main objectives of the present study include:

- Synthesis of the Gd-Si-Ge alloy series; (i) $Gd_{5-x}Nd_xSi_2Ge_2$ (x=0, 0.05, 0.1 and 0.2), (ii) $Gd_5Si_{2-x}Co_xGe_2$ (x=0, 0.1, 0.2 and 0.4), (iii) $Gd_5Si_{1.7}Ge_{2.3-x}Co_x$ (x=0, 0.1, 0.2, 0.3 and 0.4) and (iv) $Gd_5Si_{1.7}Ge_{2.3-x}Fe_x$ (x=0, 0.1, 0.2, 0.3 and 0.4) compositions.
- Synthesis of the $La_{0.7}Te_{0.3}Mn_{1-x}Co_xO_3$ with x=0, 0.1, 0.12, 0.2, 0.3 and 0.5.
- Crystal structure characterization using X-ray diffraction (XRD) and Reitveld refinement and further confirmation of the structure using HRTEM studies.
- Microstructure and composition analysis using SEM and EDS.
- Investigation of thermomagnetic behavior, magnetocaloric effect, relative cooling power and Universal analysis.
- Make magnetic refrigerant compositions with T_C near 300 K and maximum ΔS_M for a known field change.

Chapter 3

Synthesis and Characterization Techniques

This chapter describes the synthesis techniques adopted for the preparation of Gd-Si-Ge alloys and Lanthanum Tellurium Manganites. The different characterization techniques used in the present study are also explained in detail.

3.1. Introduction

This chapter summarizes the preparation routes adopted for the synthesis of two classes of magnetocaloric materials namely the $Gd_5(Si_xGe_{1-x})_4$ series and the Lanthanum Tellurium manganites. The various experimental techniques used for their structural and magnetic characterization are also discussed.

3.1.1. Preparation of $Gd_5(Si_xGe_{1-x})_4$ series

The $Gd_5(Si_xGe_{1-x})_4$ compounds used in the present study were prepared by arc melting under an inert argon gas atmosphere. In the arc-melting setup, an electric arc is used to melt the constituent elements for making the alloy. The arc-melting unit consists of a copper hearth with cups of one electrical polarity and electrodes of opposite polarity. The elements to be melted are placed in a cup of the hearth, and electrodes are used to strike the arc for melting the material. Temperatures above 3500°C can be achieved in the furnace, which is sufficient to melt the pure metals constituting the alloy. This hearth consists of an upper and lower water-cooled sections separated by a pyrex observation tube. There are three copper stinger rods penetrating the top section, which carry tungsten electrodes. Each copper rod is mounted on a swivel ball to allow angular as well as vertical movement of the electrode. The bottom section has a tapered opening, which accepts a variety of copper hearths. A mechanical pump is also attached to the melting chamber for evacuation before inert gas backfilling.

In the present work, we have used Centorr Vacuum 5TA tri-arc furnace to prepare $Gd_5(Si_xGe_{1-x})_4$ alloys. In this method, high purity metals were stoichiometrically weighed, and kept in one cup of the copper hearth along with a small piece of titanium in the other cup. The hearth is inserted into the tapered hole at the bottom of the furnace and clamped into position. The furnace chamber is maintained at a high vacuum of 10^{-3} torr and then flushed with argon gas. This procedure is repeated several times to ensure that there are no trapped air molecules inside the chamber. When the thoriated tungsten cathode is brought close to the copper hearth anode, the ionized argon gas in the chamber leads to an arc, which produces temperatures high enough to melt the elements under an argon atmosphere. The temperature of the arc can be controlled by varying the current between the two electrodes. The melting is carried out under a continuous supply of argon, and chilled water is circulated in the upper and lower sections to carry away the heat generated during melting. For the present work, the current was varied up to 50 A. Initially, a piece

of titanium is melted by striking the arc to remove any possible oxygen impurity in the melting chamber. Then, the arc is struck on the material to be melted under the continuous flow of argon. The stingers are moved around and over the material to obtain a uniform and homogeneous melt. The samples are turned over and remelted several times to achieve chemical homogeneity. Then the arc is turned off by gradually decreasing the current to zero. After melting, it is ensured that the weight loss of the samples is less than 0.01%. The ingots are then vacuum-sealed in quartz tubes and annealed at 1300 ºC for 1 hour. Figure 3.1 gives the schematic representation of the synthesis route adopted for the Gd-Si-Ge samples.

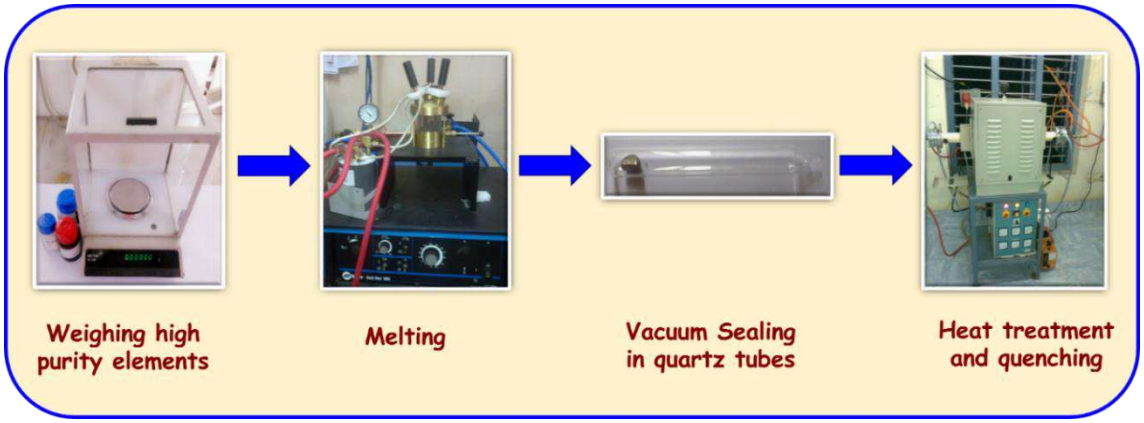

Figure 3.1. Schematic representation of the preparation methods used for Gd-Si-Ge samples.

3.1.2. Preparation of Lanthanum Tellurium Manganites

Numerous synthesis techniques have been adopted for the preparation of manganites like solid-state reaction route, sol-gel synthesis, hydrothermal, citrate decomposition route, etc. (Arai, 1996). The synthesis condition can tailor the material properties through gently or completely changing its microscopic structures. A careful selection of the preparation technique is required to prepare powders consisting of particles with specific properties to yield the bulk component. The most common method of preparing bulk powders is the solid-state reaction route, as it is the simplest, easiest and cost effective method to synthesize complex oxide materials (Nanni *et al.*, 1999).

In the present study, we have employed the conventional solid-state synthesis route for the preparation of Lanthanum Tellurium manganites (LTMO). Solid state reaction route involves four steps (a) intimate mixing of the stoichiometric oxides (b) high temperature firing/calcination (c) intermediate grinding and (d) sintering. The initial step

is to weigh the different oxides or carbonates according to the required stoichiometry. The raw materials are then mixed thoroughly using an agate mortar and pestle for 2 hours using a suitable medium such as deionised water, ethanol or acetone. In the present work, deionised water was used as the solvent. Mixing increases the point of contacts between the reactant particles. This, in turn act as product layer formation centres (Onoda *et al.*, 1978). During the mixing process, agglomerates are broken and defects are introduced into the grains that enhance the diffusion mechanism. After thoroughly mixing, the sample is then dried to get the precursor powder. Calcination is an intermediate heat treatment process at a lower temperature prior to sintering, involving the chemical decomposition reactions. During the calcining process, the unwanted volatiles such as H_2O, CO_2, etc. are removed. The calcination conditions such as temperature, duration of heating and atmospheric conditions are important factors that control the phase formation. Intermediate grinding helps to homogenise the compositional variations that may arise during calcination. Finally, the calcined powder is compacted to the desired shape and sintered at elevated temperatures. Sintering is the thermal treatment process involving the heating of "green" compact pellets to a high temperature below the melting point of the main constituent for increasing its grain size and strength by bonding together the particles. The driving force behind the sintering process is the reduction in the surface energy of the powder compacts by decreasing their vapour-solid interfaces. During the sintering process, the pores present in the "green compact," diminish or even close up due to grain boundary diffusion and grain growth resulting in densification and improvement in the overall physical and mechanical properties (Kang, 2004).

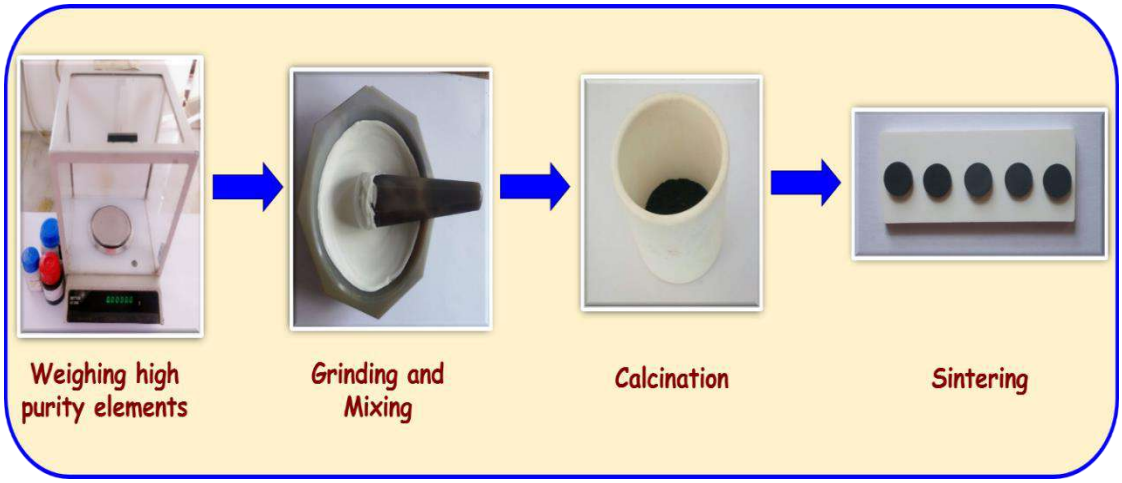

Figure 3.2. Schematic representation of the preparation methods used for LTMO.

In the present study, polycrystalline samples of $La_{0.7}Te_{0.3}Mn_{1-x}Co_xO_3$ (x=0, 0.1, 0.2, 0.25, 0.3 and 0.5) were synthesized by solid state reaction route in air. Stoichiometric amounts of La_2O_3 (Sigma-Aldrich, 99.99%), TeO_2 (Sigma-Aldrich, 99.99+%), MnO_2 (Sigma-Aldrich, 99.99+%), and Co_3O_4 (Sigma-Aldrich, 99.99+%) were mixed well and calcined at 700°C for 24 hours followed by 1050°C for 12 hours with intermediate grindings. Prior to mixing, La_2O_3 powder was preheated at 1000°C for 10 hours to remove residual carbonates. The powders thus obtained were ground, pelletized, and sintered at 1050°C for 12 hours with two intermediate grindings for homogenization to get the phase pure material. The density of the LTMO pellets were determined using an Archimedes setup and found to be above 92% for all the samples. Figure 3.2 gives a schematic representation of the preparation route adopted for the synthesis of LTMO.

3.2 Characterization techniques used in the present study

Experimental techniques form an integral part of any research. A good understanding of the techniques employed is highly essential for the right interpretation of results. Both preparative, as well as analytical techniques, are equally important. Hence, this chapter discusses the various characterization techniques that have been used for the present investigation. Structural characterization of the samples for identification of different phases, determination of the crystal structure, calculation of the crystal lattice parameters, etc. was carried out using the Powder X-Ray Diffraction (XRD) technique. Microstructural characterization techniques used in the present study include Scanning Electron Microscopy (SEM) to examine the homogeneity, Energy Dispersive Spectroscopy (EDS) for compositional analysis and Transmission Electron Microscopy (TEM) for high-resolution lattice images. Differential Scanning Calorimetry (DSC) was employed in $Gd_5(Si_xGe_{1-x})_4$ series to understand the nature of transition. The samples were subjected to magnetic characterization using physical property measurement system (PPMS).

3.2.1. Powder X-Ray Diffraction

X-Ray Diffraction (XRD) is a versatile and non-destructive technique extensively used for the structural determination, phase identification and estimation of unit cell dimensions of a crystalline material. In 1912, Max von Laue discovered that crystals act as 3D diffraction gratings for X-ray wavelengths because their wavelength λ is typically

of the same order of magnitude (1-100 Å) as the interplanar spacing **d** between the planes in the crystal (Bish, 1989; Cullity, 2001). In 1919, Hull pointed out in his paper entitled "A New Method of Chemical Analysis" that, "every crystalline substance gives a pattern; the same substance always gives the same pattern, and in a mixture of substances each produces its pattern independently of the others" (Hull, 1919). Thus, powder diffraction method is preferably suited for characterization and identification of polycrystalline phases. Each crystalline material has its own unique X-ray diffraction pattern, which is a "fingerprint" of its identification. By analyzing the XRD data, we can identify the different phases present in the sample and estimate the phase assemblage quantitatively. A crystal can be considered as a regular three-dimensional periodical arrangement of atoms in space. For any crystal, planes exist in a number of different orientations each with its own **d** spacing. When a beam of electromagnetic radiation is incident on a crystal, then the atoms in the path of the beam scatter the X -rays simultaneously. In certain specific directions, the scattered X-rays are in-phase and they interfere constructively. The intensities of the diffracted waves depend on the kind and arrangement of atoms in the crystal structure. W.L. Bragg developed an equation for diffraction by treating this diffraction mathematically as reflection from the diffracting planes and any crystal can be considered as a set of equidistant parallel planes that pass through all the atoms in the crystal, called "Bragg" planes. For obtaining a sharp peak in the intensity of scattered radiation, the X-rays should be specularly reflected, i.e. the angle of incidence should be equal to the angle of reflection and the reflected rays from successive planes should interfere constructively. Figure 3.3 gives a schematic representation of X-ray diffracting from crystal planes. The path difference between the rays is $2d\sin\theta$. For constructive interference, this path difference must be equal to an integral number of wavelengths, giving the Bragg criterion.

$$2d \sin \theta = n \lambda \qquad (3.1)$$

where n is an integer. This equation is called Bragg's equation. In polycrystalline powder, small crystallites of all possible orientations are assumed to be present. The schematic representation of Bragg's Law is depicted in Figure 3.3.

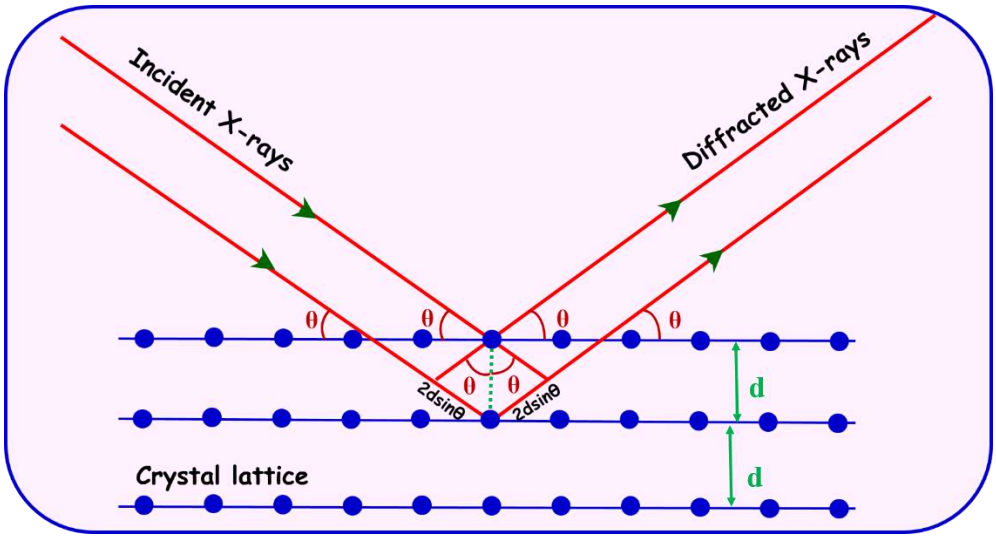

Figure 3.3. Bragg's representation of X-ray radiation diffracting from crystal planes.

Even though the Bragg's law is satisfied, sometimes the diffracted lines from some planes may not appear in XRD patterns. This is because the intensities of such lines become zero due the destructive interference of X-rays scattered by different atoms present in the unit cell. Hence, the unit cell determines the XRD line position and the atom position, and scattering factor determines the line intensities. Intensities of diffracted lines (ignoring temperature and absorption factors) are obtained using the equation,

$$I = |F|^2 \, p\left(\frac{1+\cos^2 2\theta}{\sin^2\theta \, \cos\theta}\right) \qquad (3.2)$$

where 'I' is the relative integrated intensity, 'F' is the structure factor, 'p' is the multiplicity factor and 'θ' is the Bragg angle. The structure factor is the ratio between the amplitude of the waves scattered by all atoms in the unit cell to the amplitude of the wave scattered by one electron. For a diffracted line to occur, it is necessary to have the angular position of the line satisfying the Bragg equation and must have a non-zero structure factor. The structure factor can be calculated using the equation,

$$F_{hkl} = \sum_{1}^{N} f_n e^{2\pi i(hu_n + kv_n + lw_n)} \qquad (3.3)$$

where 'f_n' is the atomic scattering factor of the n^{th} atom and h, k and l are the Miller indices of (hkl) planes and u, v and w are the coordinates of the atoms. The

multiplicity factor accounts for the diffracted intensities of lines from lattice planes having different Miller indices but same interplanar spacing.

X-ray diffractometer consists of an X-ray source, a sample holder, and a detector. The source is a cathode ray tube (X-ray tube) which is capable of producing a beam of monochromatic X-rays. A current is applied to the heating filament within the tube thereby emitting electrons and a high voltage, typically 15-60 kilovolts. This high voltage accelerates the electrons, which then hit the target and produces X-rays. The wavelength of these X-rays produced is characteristic of the target used. These X-rays are collimated and directed onto the sample placed inside the sample holder. The detector detects the diffracted X-ray signal. The signal is then processed either electronically or by a microprocessor, converting the signal to a count rate. A schematic representation of the basic components of a typical X-ray diffractometer is shown in Figure 3.4.

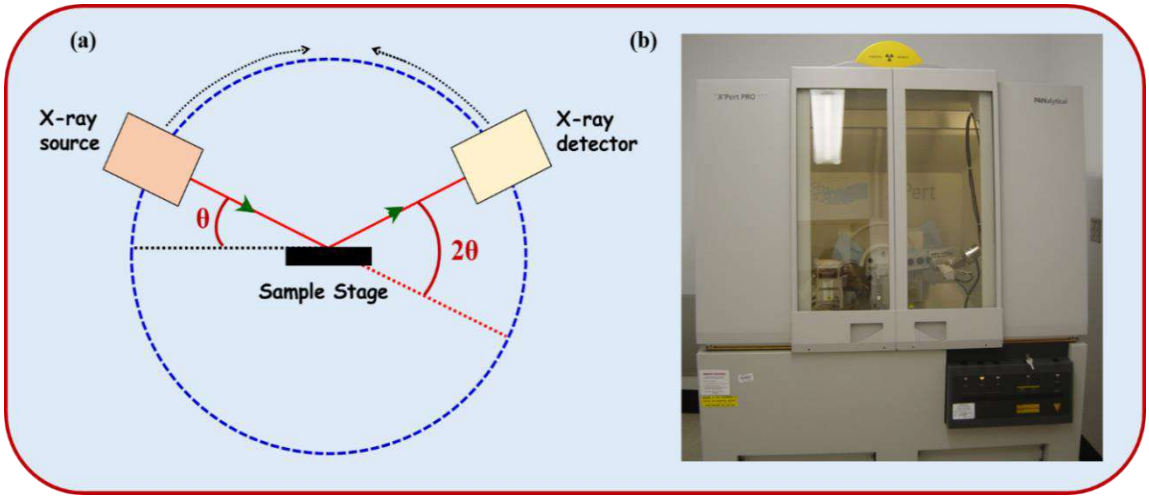

Figure 3.4. Schematic representation of X-ray diffractometer

In the present study, powder XRD analysis of the samples was conducted by an automated X-ray diffractometer (PANalytical X'pert Pro Diffractometer). It consists of an X-ray source (Cu Kα radiation, λ = 1.54060 Å) on the incident beam side and a monochromator and a proprietary detector, X'celerator at the diffracted beam side. This instrument has θ-θ Bragg-Brentano geometry (both the source and detector make an angle θ with the sample surface) with the fully automated operation and data acquisition. The scans were performed under a tube voltage of 40 kV and current of 30 mA, and the scanning angle (2θ) ranged from 20° to 80° with a step size of 0.0167°. To obtain accurate

results, the samples were thoroughly grounded into fine powders, filled inside a standard sample holder, and the XRD data was recorded at ambient conditions. In the case of less amount of powder, a zero background holder was used. To avoid excessive exposure of X-ray beam to the sample area, programmable slits were used in the incident beam side. From the XRD data obtained, the Rietveld refinement was performed using GSAS-EXPGUI software. Low temperature powder X-ray diffraction measurements were done on an Oxford Cryosystems closed cycle helium cryostat (Model: PheniX) mounted on a vertical goniometer in a PANalytical Empyrean powder X-ray diffractometer with $CuK_{\alpha 1}$ *and* CuK_{α_2} radiations for 1 hour in the 2θ range 5° to 80° with a step size of 0.017°.

3.2.2. Rietveld refinement for structural analysis

Rietveld refinement is a unique technique designed by Hugo Rietveld for exploiting the detailed crystal structure from XRD and neutron diffraction data (Rietveld, 1969). The XRD and neutron diffraction data of powder samples result in a pattern characterized by reflections (intensity peaks) at certain positions. The height, width, and position of these reflections can be used to determine many aspects of the crystal structure. The Rietveld method refines user-selected parameters to minimize the difference between the experimental or observed diffraction pattern and the calculated pattern based on the hypothesized crystal structure and instrumental parameters.

The method plays a vital role in extracting the detailed structural information of the materials from XRD data (Rietveld, 1969; Young, 1993).This method uses an iterative procedure by least squares method, with some initial parameters such as space group, lattice constants, atom types, atomic positions, etc., for each structural model. Using these initial parameters, a calculated X-ray pattern is first generated and is compared with the experimentally observed XRD pattern. Refinement is done on each factor until the difference between the observed pattern, and the calculated pattern reaches a minimum. The minimization function in the refinement (S_y) is the weighted difference between the observed, and calculated diffraction patterns. i.e.

$$S_y = \sum_i w_i (Y_{io} - Y_{ic})^2 \qquad (3.4)$$

where 'w_i'is the corresponding weight, 'Y_{io}' is the observed intensity at angular step *i* and 'Y_{ic}' is the corresponding calculated intensity. In a particular measurement, each intensity

value is calculated by summing the contributions of all Bragg reflections and background as,

$$Y_{ic} = I_0 \ \Sigma k_h F_h^2 m_h L_h P(\Delta_h) + I_b \qquad (3.5)$$

where 'I_0' is the incident intensity, 'k_h' is the scale factor for the particular phase, 'F_h' is the structure factor for the particular reflection, 'm_h' is the reflection multiplicity, 'L_h' is the correction factors for the intensity-texture, etc. '$P(\Delta_h)$' is the peak shape function and 'I_b' is the background contribution. The instrument related factors are the instrumental profile function, zero position, background, and wavelength. The parameters reflecting contribution from the sample are lattice parameters, atomic coordinates, occupancies, temperature factors, scale factors, absorption coefficients, etc. The peak shape is usually fitted with a Pseudo-Voigt function, which allows flexible variation of the Gaussian and Lorentzian character of the peak shape.

The quality of the refinement is controlled by several agreement factors such as the profile factor, the weighted profile factor, the expectation factor and the Bragg factor. (Young, 1993). The profile factor is defined as,

$$R_p = \left(\frac{\sum_i |Y_{io} - Y_{ic}|}{\sum_i Y_{io}} \right) \qquad (3.6)$$

The weighted profile factor, R_{wp} is more valuable, and its absolute value does not depend on the absolute value of the intensities, but it depends on the background. R_{wp} is weighted to emphasize intense peaks over the background.

$$R_{wp} = \left(\frac{\sum_i w_i (Y_{io} - Y_{ic})^2}{\sum_i w_i Y_{io}^2} \right)^{\frac{1}{2}} \qquad (3.7)$$

The expectation factor is given as,

$$R_{exp} = \left(\frac{N-P+C}{\sum_i w_i Y_{io}^2} \right)^{\frac{1}{2}} \qquad (3.8)$$

where (N-P+C) is the number of degrees of freedom. N is the number of points in the pattern, P is the number of refined parameters and C is the number of constraints applied.

The Bragg factor is,

$$R_{Bragg} = \left(\frac{\sum_j \left| I_{jo} - I_{jc} \right|}{\sum_j I_{jo}} \right) \qquad (3.9)$$

where, I_{jo} and I_{jc} are the observed and calculated integrated intensities for the different Bragg peak, *j*. The measure of the goodness of fit, χ^2, can be obtained from the residuals 'R_{wp}' and 'R_{exp}' and are given by,

$$\chi^2 = \left(\frac{R_{wp}}{R_{exp}} \right)^2 \qquad (3.10)$$

In the present study, Rietveld refinement of the XRD patterns of all the samples was carried out using the GSAS-EXPGUI software (Toby, 2001). The background was refined using the shifted Chebyshev polynomial with ten variables, and a Pseudo-Voigt function was selected to refine the shape of the peak. The order of refining the parameters was the scale factor, zero correction for 2θ, background parameters, the cell parameters, the peak shape parameters, the fractional coordinates, the isotropic displacement parameters and the thermal factors. To estimate the quality of the refined results, we must consider a global view of the difference between the calculated profiles and the measured data combined with the agreement factors. From the mathematical point of view, R_{wp} is the most meaningful of these R's because the numerator is the residual being minimized in the refinement. The integrated intensity factor, R_{Bragg} is based on a comparison of observed and calculated integrated intensities. In the present work, Rietveld refinement has been carried out on the alloy samples and LTMO manganites to analyse the crystal structure. The refined data was used to generate the crystal structure using CrystalMaker® Software.

3.2.3. Scanning electron microscopy

Scanning electron microscopy is a non-destructive technique used to examine a large area of the sample and obtain information on its microstructure and morphology at the sub-micron level. The scanning electron microscope (SEM) uses a focused beam of high-energy electrons to generate a range of signals at the surface of solid specimens. These signals derived from electron-sample interactions reveal information about the

sample including external morphology (texture), crystalline nature, chemical composition, and orientation of materials making up the sample. In most applications, data are collected over a selected area at the surface of the sample, and a two-dimensional image is generated that displays spatial variations in these properties. The working principle of SEM is shown in Figure 3.5. The primary electrons produced from the electron gun are focused into a small-diameter electron probe and is scanned across the specimen. It uses the fact that electrostatic or magnetic fields, applied at right angles to the beam, can be used to change its direction of travel. By scanning synchronously in two perpendicular directions, a square or rectangular area of the specimen (known as raster) can be covered, and an image is formed by collecting the signals from this area. These signals include Secondary electrons (SE), Backscattered electrons (BSE), Characteristic X-rays, Auger electrons, etc. SE and BSE are commonly used for imaging samples. The electron beam interaction volume is depicted in Figure 3.6. SE is the most valuable for showing morphology and topography of samples while BSE is used for explaining contrasts in the composition in multiphase samples (i.e. for rapid phase discrimination).

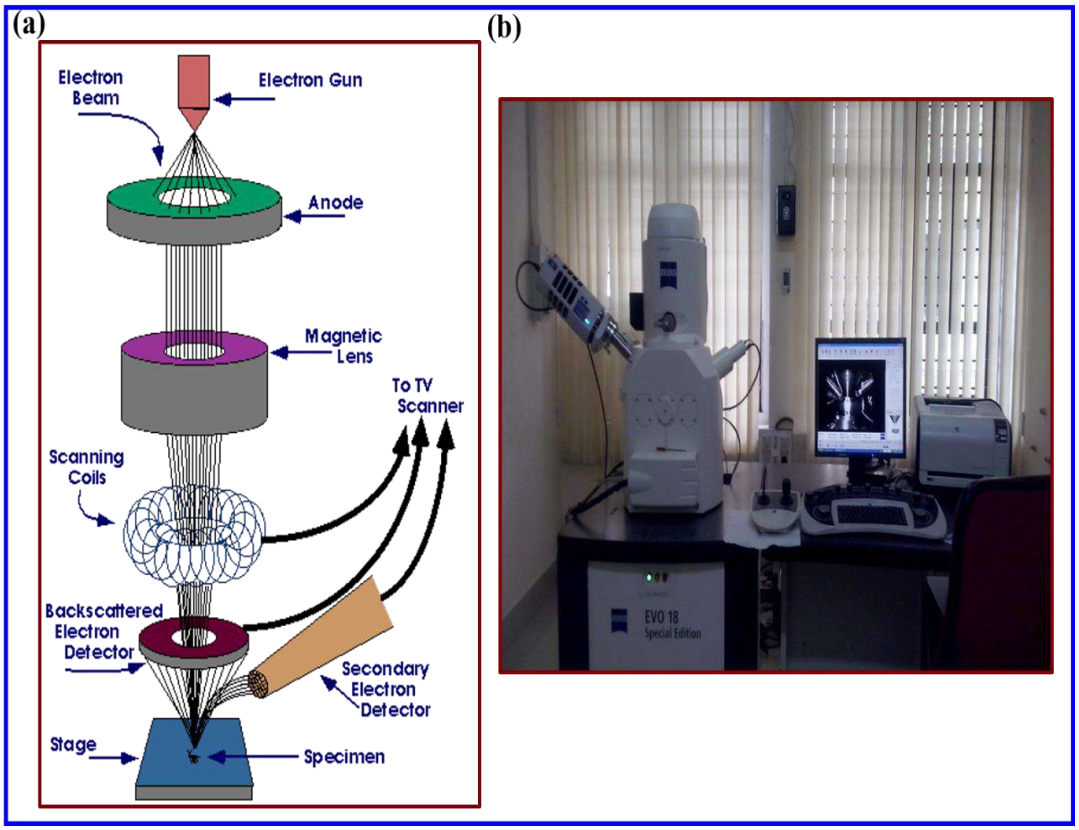

Figure 3.5. (a) Schematic representation of SEM (b**)** Carl Zeiss Evo 18 SEM equipped with an energy dispersive x-ray spectrometer.

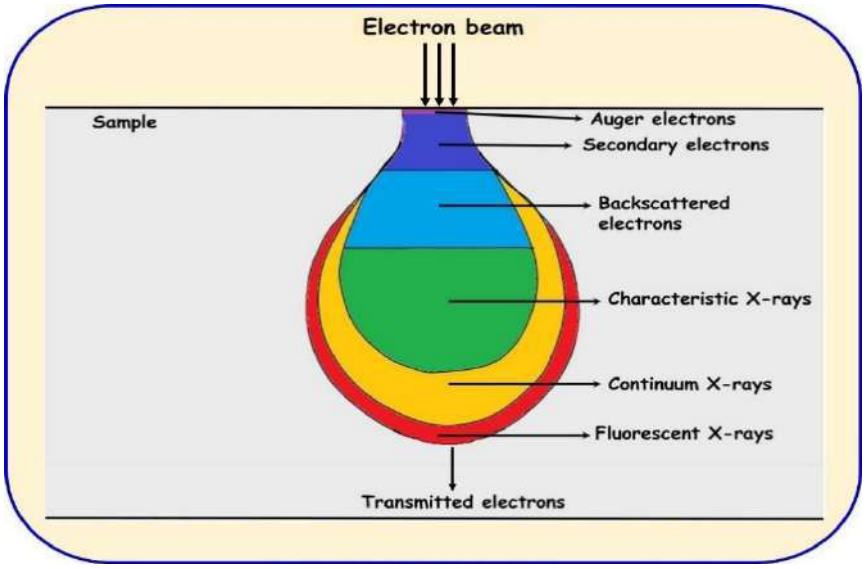

Figure 3.6. Electron beam interaction volume in SEM

SE is produced when the energy from the primary beam causes the atoms of the specimen to ionize. As a result of ionization, secondary electrons are ejected from the k orbitals of the sample. BSE consist of high-energy electrons that are reflected or backscattered from the sample by elastic scattering. They emanate from deeper locations within the specimen, and the intensity of the BSE signal is strongly related to the atomic number (Z) of the specimen. BSE images can provide information about the distribution of different elements in the sample. Elements with higher atomic number scatter more electrons than those with low atomic number and hence appears to be brighter in the image. The intensity of one of the detected signals (at a time) is amplified and gives rise to the intensity of a pixel on the image on the computer screen. The electron beam then moves to next position on the sample, and the detected intensity gives the intensity in the second pixel and so on. The essential requirement for good imaging is that the samples must be electrically conductive, at least on the surface, and electrically grounded to prevent the accumulation of electrostatic charge at the surface. Nonconductive samples must be coated with an ultrathin coating of electrically conducting material like gold.

In the present study, the microstructure of the Gd-Si-Ge samples was done using a Carl Zeiss Evo 18 SEM equipped with an energy dispersive X-ray spectrometer used in BSE imaging mode. The $Gd_5(Si_xGe_{1-x})_4$ ingots were cut and polished well to see the microstructural features of the samples. These samples were then mounted on brass studs using adhesive carbon tapes. No gold coating was used since the samples were electrically

conducting. Then, the brass studs with the mounted samples were loaded on the sample holder of the SEM. The typical magnifications value chosen for the images in the present study were 5000X and 3000X.

3.2.4. Energy dispersive spectroscopy (EDS)

Energy dispersive X-ray spectroscopy (EDS) is an analytical technique, which can provide information regarding the elemental distribution in the samples. EDS is based on the detection of Characteristic X-rays, which are produced when an outer shell electron fills a vacancy in the inner shell, created by a high energy electron beam, resulting in the emission of X-rays characteristic to each element. When a high beam of electrons fall on the surface of the sample, an electron from an inner K shell of an atom is ejected due to the collision with a primary electron, and it creates a hole (vacancy). Another electron from higher energy level (L-shell) within the atom fills this vacancy, and this transition results in the release of energy, which is equal to the difference in energy between the two shells. The schematic representation of this process is shown in Figure 3.7. This excess energy, which is unique for every atomic transition, will be emitted by the atom either as an X-ray photon or will be self-absorbed and emitted as an Auger electron. The energy of each X-ray photon is characteristic of the atom from which it escapes. The EDS system collects the X-rays, sorts them by energy and displays the intensity versus binding energy values. The position of the peak with appropriate energies gives information about the qualitative composition of the sample. This qualitative EDS spectrum can be further analyzed to produce a linear elemental analysis (displayed as a line scan) or an area elemental analysis (displayed as a dot map), giving the overall distribution of all the elements in the sample. EDS allows one to identify the particular elements present and their relative proportions in atomic %. X-ray mapping of elements helps in identifying the positions of specific elements emitting characteristic X-rays within an inspection field, which can be indicated by a unique color. Hence, elemental mapping can be used to great advantage to show positions of inclusions, phases with varying composition, etc. The limitation of EDS is that it cannot detect elements having atomic weight lesser than carbon. In the present study, EDS analysis was done using automated EDS system integrated to SEM. EDS analysis was performed on multiple areas, and the average is presented throughout the study.

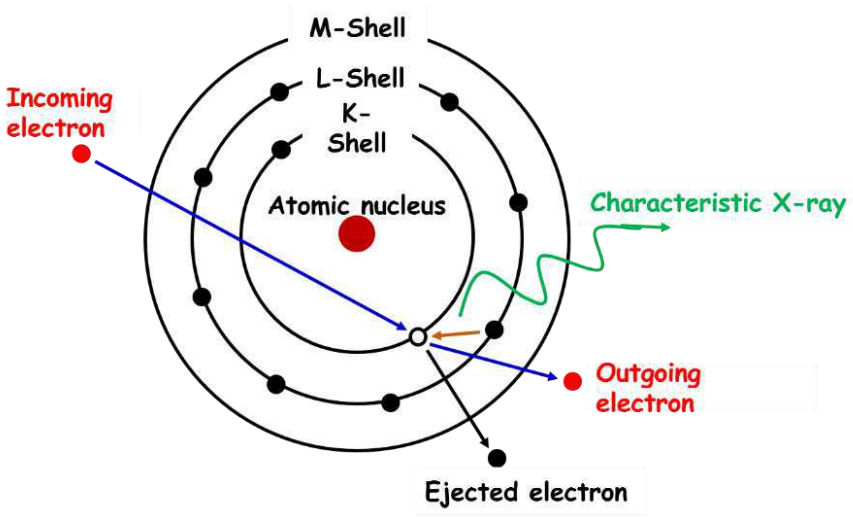

Figure 3.7. Schematic representation of X-ray emission from an atom when an electron from higher energy level fills the vacancy created due to excitation of an inner level electron by a high energy electron beam.

3.2.5. Transmission electron microscopy

Transmission electron microscopy (TEM) is a technique used for analyzing the morphology, crystallographic structure, particle size, defects, and composition of a specimen. In this technique, a beam of electrons is transmitted through an ultra-thin specimen of the sample to produce a magnified image of the object. An image is formed from the interaction of the electrons transmitted through the specimen, which is magnified and focused onto an imaging device, such as a layer of photographic film, a fluorescent screen or is detected by a sensor such as a CCD camera.

Initially, an electron source is heated up in an electron gun, which acts as cathode, and generates a beam of electrons. The first crossover is made by the Welnet cylinder which is given a high negative voltage. The second condenser lens defocuses and concentrates the electrons to a small virtual source having very high spatial and temporal coherence. This beam is directed by condenser lens onto a certain part of the specimen. The first intermediate image is generated by the objective lens, the quality of which determines the resolution of the final image. The intermediate lens and apertures helps to choose between the imaging mode and diffraction mode. The image is further magnified by the projector lens, which is focused onto a fluorescent screen and the image is viewed on a TV screen. TEM offers two methods of specimen observation : (1) in Image mode and (2) in Diffraction mode. In image mode, a magnified image of the specimen is formed

on the fluorescent screen. In diffraction mode, a diffracted electron image focused at the back focal plane of the objective lens is projected onto the screen to produce a diffraction pattern or selected area diffraction pattern (SAED), which is the image of the reciprocal lattice. The imaging mode and diffraction mode used in TEM is depicted in Figure 3.8. A single crystal will produce a spot pattern on the screen while a polycrystalline sample will produce a ring pattern. The microstructure, grain size, and lattice defects can be studied in the image mode, while the crystalline structure can be studied using the diffraction mode. The two primary image modes in TEM differ by the way in which the objective aperture is used as a filter in electric optics system. In bright field imaging, only the transmitted beam is allowed to pass through the objective aperture and the scattered beam is excluded. In the corresponding dark field-imaging mode, the primary beam is excluded and the scattered beam is used for imaging. The technique known as bright field is particularly sensitive to extended crystal lattice defects, such as dislocations. The electron rays corresponding to bright field and dark field imaging are shown in Figure. 3.9 respectively and the experimental set up for TEM is shown in Figure. 3.10.

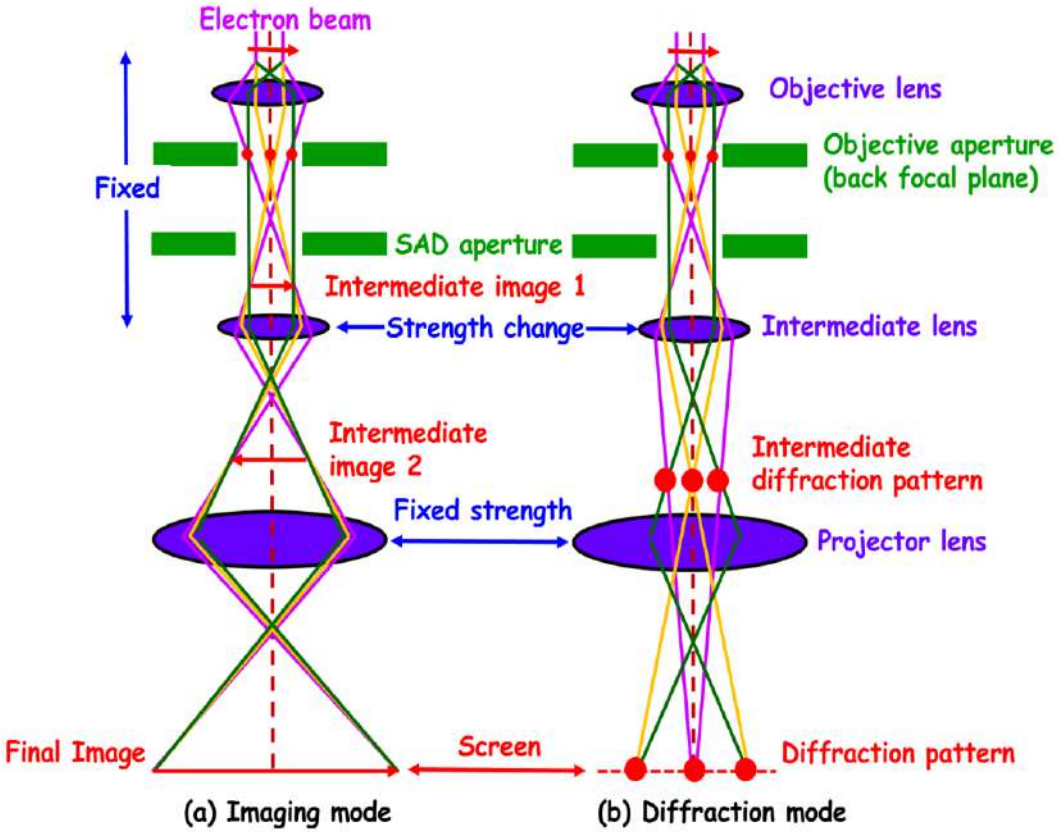

Figure 3.8. (a) Imaging mode and (b) Diffraction mode in TEM.

Also, TEM builds an image by way of differential phase contrast. Those electrons that pass through the sample go on to form the image while those that are stopped or diffracted by dense atoms in the specimen are subtracted from the image. In this way, a black and white image, called the bright field image, is formed. If the scattered beam is used to produce the image, it is called the dark field image. Sometimes the image of the scattered beams is used for further projection giving the selected area diffraction pattern which provides useful information about the inter-atomic spacing and crystal structure. Finally, one uses the projector lens to project the final magnified image onto the phosphor screen. It is in the projector lens that the majority of the magnification occurs. Thus, total magnification is a product of the objective and projector magnifications. For higher magnifications, an intermediate lens is often added between the objective and projector lenses. This lens serves to further magnify the image. The information obtained through SAED pattern has been correlated with the X-ray diffraction patterns.

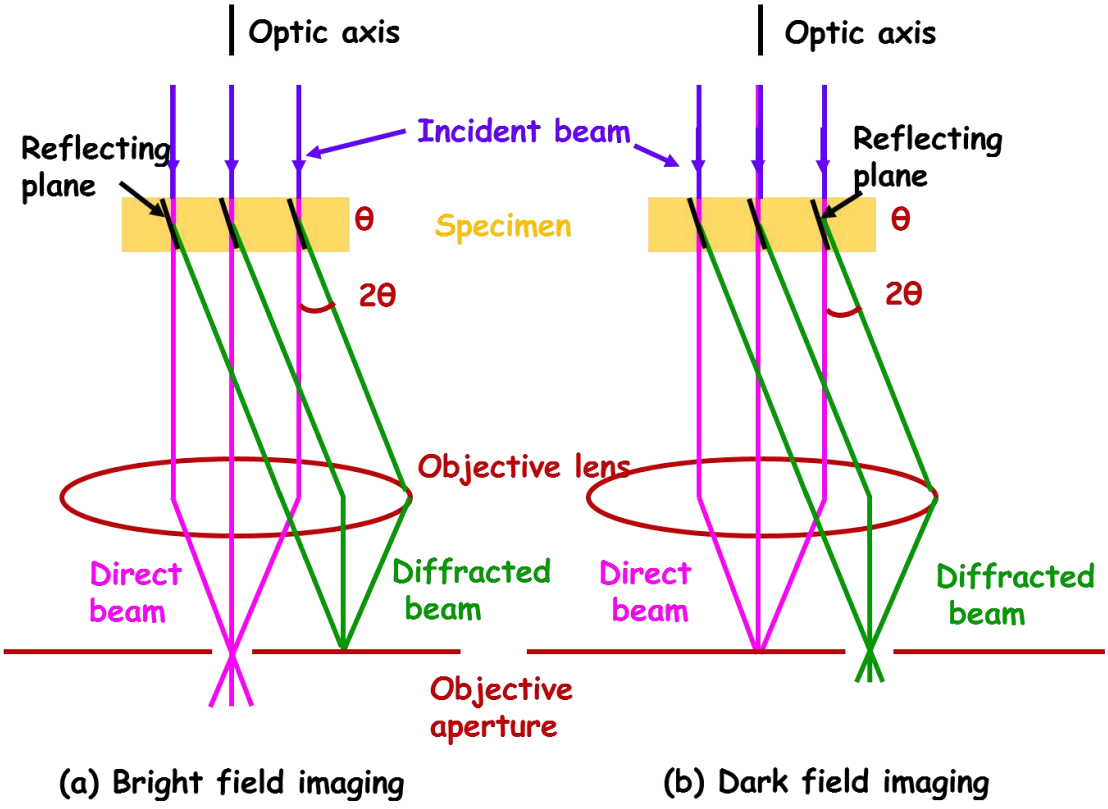

Figure 3.9. (a) Bright field and (b) Dark field imaging in TEM.

Figure 3.10. FEI Tecnai G230S Twin 300 kV TEM facility at NIIST, Trivandrum.

3.2.6. Magnetization measurements

The Physical Property Measurement System (PPMS) is a versatile and indispensable instrument with a provision to measure many physical properties such as AC & DC magnetizations, resistivity, specific heat, thermal conductivity, Seebeck coefficient, Hall effect, etc. as a function of temperature, magnetic field and time. The magnetization (M) measurements up to a maximum field (H) of 50 kOe were carried out using vibrating sample magnetometer (VSM) attached to a PPMS (Quantum Design, Dynacool). During the course of this work, we have used PPMS for measuring the magnetization as the function of temperature and magnetic field.

For DC magnetization, a small external field is applied, and magnetization (M) is measured as a function of temperature at a constant applied field. The temperature-dependent magnetization measurements have been performed in the temperature (T) range of 5–350 K in different modes. In the Zero Field Cooled (ZFC) mode, the sample was initially cooled to 5 K in the absence of an applied field, and the measurement was carried out while heating the sample to room temperature in an applied field. In the Field-Cooled-Cool (FCC) mode, the data was collected while cooling the sample to 5 K under an applied field and in the Field-Cooled-Warming (FCW) mode, the data was collected

during the subsequent warming, after field cooling to 5 K. MCE properties were performed for all the samples from the isothermal magnetization curves near the structural as well as the magnetic phase transition region by sweeping the magnetic field from 0 to 50 kOe, and back to 0 at different temperatures. A brief description of the working principle of Vibrating Sample Magnetometer (VSM) and a brief introduction to the principle of AC magnetic measurements is also given below.

3.2.6.1. Vibrating sample magnetometer

DC magnetic measurements were carried out using VSM attached to PPMS. A maximum field of 90 kOe and temperature ranging from 1.8 K-400 K can be achieved in the present model and it is used for measuring the magnetic behavior of materials. The technique was first highlighted by Foner (Foner, 1959) and has been universally accepted for various magnetic and superconducting materials.

The working principle of VSM is based on the Faraday's law of electromagnetic induction (Foner, 1959; Cullity, 1972). When a magnetic material is subjected to a DC magnetic field, a moment is induced in it. If the material is subjected to a sinusoidal motion, the oscillating flux will induce an electromotive force (e.m.f.) in the pick-up coils placed in the vicinity of the material. This induced e.m.f is directly proportional to the magnetic moment of the material under investigation. The magnitude of the AC signal produced is proportional not only to the magnetic moment induced in the sample, but also to the amplitude and frequency of vibration. To separate out the contribution to the pick-up voltage from the magnetic moment, the pick-up voltage is fed to one of the inputs of a differential amplifier. The greater the magnetization, greater will be the induced current. By measuring the induced current, we can understand how much the sample is magnetized and how its magnetization depends on the strength of the constant magnetic field.

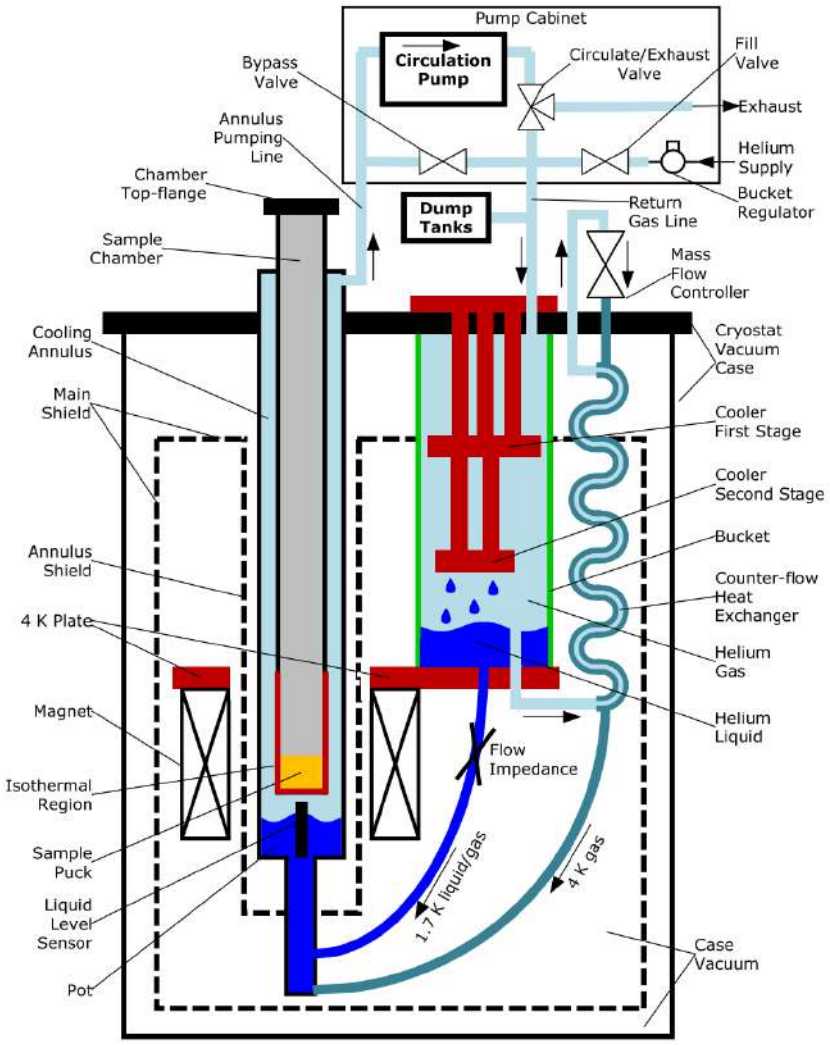

Figure 3.11. The configuration of the PPMS DynaCool System

Figure 3.12. PPMS DynaCool System at NIIST, Trivandrum

Figure 3.11 shows the configuration of the PPMS DynaCool System. In this instrument, the magnetic field is generated using superconducting coil NbTi alloy. A single two stage pulse tube cooler is used in the system to cool both the superconducting magnet and the temperature control system, which provides a vibration free environment for different measurements. The sample chamber and the superconducting magnet is cooled by a minimum amount of condensed liquid helium-4 in PPMS Dynacool. Therefore, only a minimum volume of bottled helium gas is required for smooth and continuous working. The cooling power and temperature stability is improved by utilising a novel gas flow regulation system. Along with sophisticated control software, this system provides stable and efficient operation in the temperature range 1.8 K -400 K, with cooling provided by evaporating liquid helium. An integrated cryopump is used to pump out the sample space to a vacuum of less than 10^{-4} Torr. Multiple thermometers and heaters manage temperature gradients and ensure smooth temperature control throughout the accessible temperature range. A magnetic measurement is accomplished by oscillating the sample near a pickup coil and synchronously detecting the voltage induced. The system can resolve magnetization changes of less than 10^{-6} emu at a data rate of 1 Hz by using a compact gradiometer pickup coil configuration, relatively large oscillation amplitude (1-3mm peak) and a frequency of 40 Hz. The VSM option of PPMS consists primarily of a VSM linear motor transport for vibrating the sample, a coil set puck for detection, electronics for driving the linear motor transport and detecting the response from the pickup coils, and the MultiVu software for automation and control. The sample is attached to the end of a sample rod that is driven sinusoidally. The center of oscillation is positioned at the vertical center of a gradiometer pickup coil. The precise position and amplitude of oscillation is controlled from the VSM motor module using an optical linear encoder signal readback from the VSM linear motor transport. The voltage induced in the pickup coil is amplified and lock in detected in the VSM detection module. This encoder signal is obtained from the VSM motor module, which interprets the raw encoder signals from the VSM linear motor transport. The VSM detection module detects the in phase and quadrature phase signals from the encoder and from the amplified voltage from the pickup coil. These signals are averaged and sent over the CAN bus to the VSM application running on the PC. Magnetic measurements has been carried out in PPMS facility at NIIST, Trivandrum.

3.2.6.2. AC susceptibility versus temperature measurements

The *ac* Susceptibility technique is valuable tool extensively used to study superconducting transitions, vortex dynamics and critical current density, grain connectivity, relaxation process and to map magnetic phase diagram. In *ac* magnetic measurements, an *ac* field is applied to the sample and the resulting induced sample moment is time-dependent. Hence, ac measurements yield information about the magnetization dynamics that are not obtained in DC measurements, where the sample moment is constant during the measurement time. The *ac* Susceptibility technique works on the principle of mutual induction. A primary coil which generates an *ac* magnetic field and two oppositely wound secondary coils form the basic unit of the measuring circuitry. In the absence of the sample, the voltage measured across these two detection coils is ideally zero. Inserting a sample centered in one of the secondary coils will result in a non-zero signal in the secondary coil due to the electromotive force induced by the primary coil and this is directly proportional to the amplitude of *ac* susceptibility of the sample being measured. The schematic representation of working principle of an *ac* susceptometer is given in Figure 3.13. The magnetic susceptibility, χ is a measure of how "magnetic" a material is and describes the response of the material to an applied field H, i.e., $\chi = M/H$, where M is the sample's magnetization. Since the actual response of the sample to an applied *ac* field is measured, the magneto dynamics of the system can be studied through the complex susceptibility ($\chi' + i\chi''$). The real component χ' represents the magnitude of the susceptibility that is in phase with the applied ac field, while χ'' represents the component that is out of phase. The imaginary component χ'' represents the energy losses, i.e., the energy absorbed by the sample from the *ac* field. The two representations are related by

$$\chi' = \chi \cos\phi \qquad \chi'' = \chi \sin\phi \tag{3.11}$$

$$\chi = \sqrt{\chi'^2 + \chi''^2} \qquad \phi = \arctan\left(\frac{\chi''}{\chi'}\right) \tag{3.12}$$

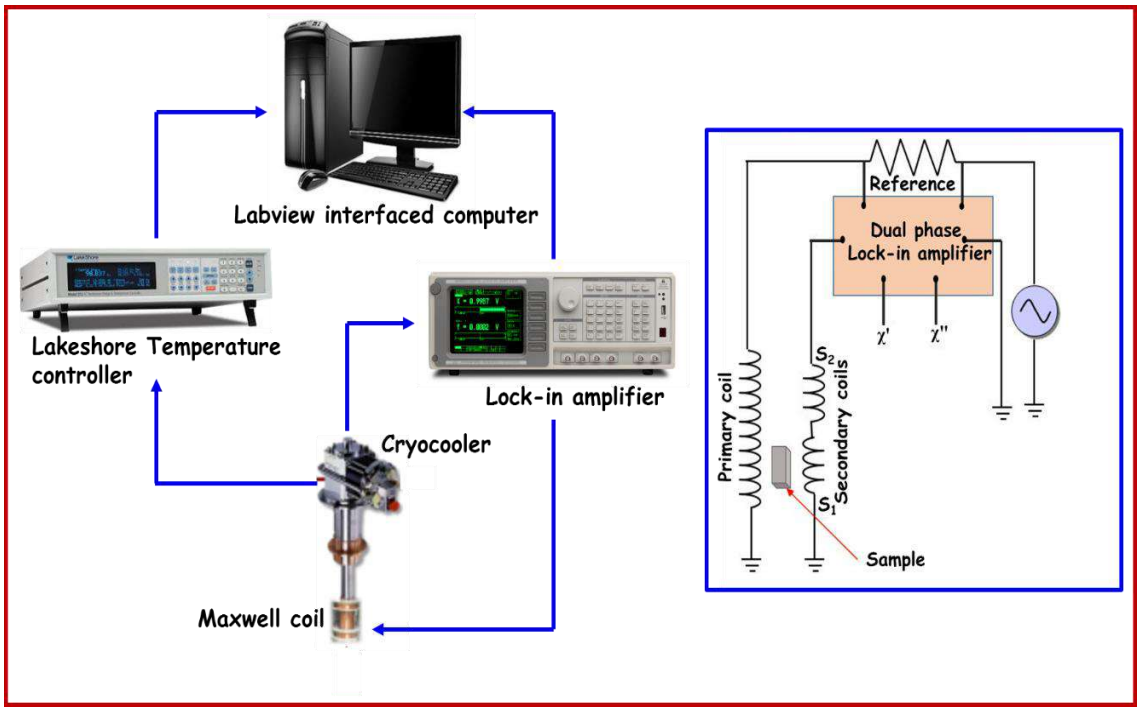

Figure 3.13. Schematic representation of working principle of an *ac* susceptometer

In the low frequency limit, *ac* measurements are similar to dc measurements, the real component is slope of the M(H) curve. Both χ' and χ" are sensitive to thermodynamic phase changes, and hence can be used to measure transition temperatures. In the lower frequency limit, AC measurement is analogous to DC analysis. For conductive samples, the dissipation arises due to eddy currents. In spin glasses, relaxation and irreversibility give rise to a non-zero χ". In ferromagnets, a non-zero imaginary susceptibility can indicate irreversible domain wall movement or absorption due to permanent moments. In the present work, the *ac* susceptibility measurements of the $Gd_5(Si_xGe_{1-x})_4$ series has been performed using *ac* susceptibility setup attached to PPMS (Quantum Design, Dynacool). The *ac* susceptibility measurements of Lanthanum Tellurium Manganites (LTMO) were measured using a closed-cycle *ac* susceptometer (Advanced Research Systems, ARS-CS202S-DMX-19 SCC, Macungie, PA) to understand the spin glass behaviour in LTMO. The block diagram of the *ac* magnetic susceptibility measurement unit (Advanced Research Systems, Model: CS202*F-DMX-19 SCC) used in the present study is given in Figure 3.13. The bulk samples of LTMO are fixed in the sample holder tube and then inserted into a system containing both primary and secondary coils (ARS). An excitation field is applied to the primary coil and the secondary coils pick up the change of induction voltage across the coils using a lock-in-amplifier (Stanford Research Systems (SRS 850),

USA). The temperature of the sample was precisely monitored using Lakeshore-340 temperature controller. The measurements were programmed with a computer using GPIB interfaced Labview software. In the present study, χ-T of specific samples were measured at different frequencies of f = 111, 333, 533, 733, and 999 Hz for H_{ac} = 0.49 mT.

Spin glass behavior is usually characterized by *ac* susceptibility. In a spin glass, the magnetic spins have random interactions with other magnetic spins which result in a highly irreversible and metastable state characterized by the frustration of spins. The spin glass state is realized below the freezing temperature, and it is determined by measuring χ' vs.T, a curve which reveals a cusp-like anomaly at the freezing temperature. Moreover, the location of the cusp is dependent on the frequency of the *ac* susceptibility measurement. This feature is not present in other magnetic systems and therefore confirms the spin glass phase. The irreversibility in spin glasses leads to a nonzero out-of-phase component (χ''), below the spin glass freezing temperature. Since spin glasses have unique magnetization dynamics, many interesting effects are observed in the susceptibility behavior.

3.2.7. X-ray Photoelectron Spectroscopy

X-Ray Photoelectron Spectroscopy (XPS) also called Electron Spectroscopy for Chemical Analysis (ESCA) is a widely used technique for characterizing the chemical composition at the surface of a solid. ESCA can also provide insights into the chemical bonding at the surface. It utilizes the photo-ionization and analysis of the kinetic energy distribution of the emitted photoelectrons to study the composition and electronic state at the surface region of the sample. When a solid substance is irradiated with X-rays of known energy, photoelectrons from the core and valence energy levels, secondary electrons, and Auger electrons are emitted. The missing inner core electron (photoelectrons) represents an unstable hole in the electronic shell. An electron from the valence shell thus fills the freshly created hole, causing an Auger electron to be emitted from the valence shell to conserve energy, causing Auger relaxation. Not only electrons from primary ionization (photoelectrons) are detected, but also electrons from the Auger relaxation process (Auger electrons) can be detected. The photoelectron transition is the basis of XPS.

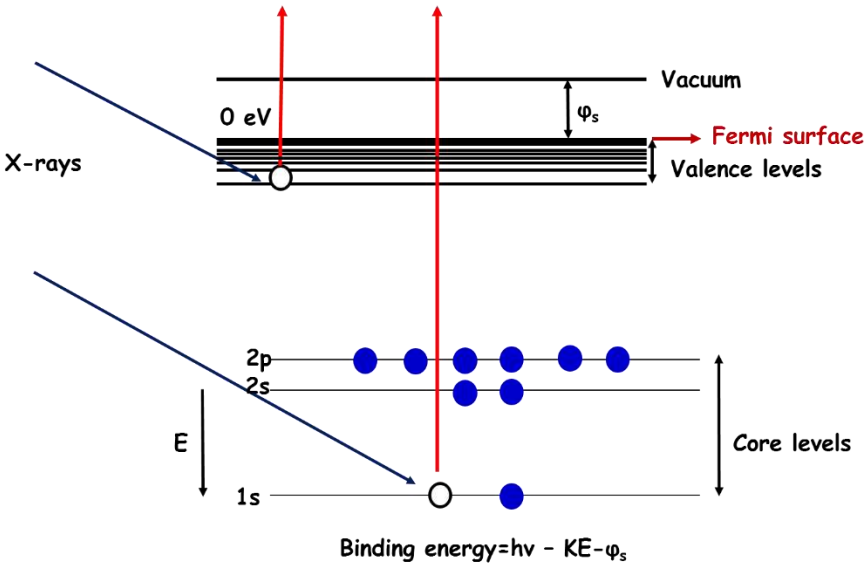

Figure 3.14. Principle of XPS

Figure 3.14 shows the excitation of carbon (C) core electrons from the 1s level with X-ray photons. The binding energy is characteristic of an atom and its bonding state. The C 1s electrons that are excited by the X-ray beam overcome the binding energy of the C 1s orbital, since the energy of the X-ray photon is transferred. Hence the electron that leaves the 1s orbital reach the material-vacuum interface, and travel through vacuum to reach the analyser, and then to a detector. XPS is based upon two simple processes which result from interactions between X-rays and electrons. The first and most important is the Compton scattering in which an incident X-ray photon collides with a core electron, and the collision causes the electron to be ejected from the electronic shell. The energy of the X-ray photons must be equal to the binding energy, work function and kinetic energy of the photoelectrons. The photoelectron released will have a particular kinetic energy that is directly related to the binding energy of the electron in the atom. The binding energy of the emitted electrons can be calculated as:

$$BE = h\upsilon - KE - \varphi_s \qquad (3.13)$$

where KE is the kinetic energy of the emitted electron (eV), h υ is the excitation energy, BE is the binding energy (eV) and φ is the work function.

In the present study, XPS measurements of selected LTMO samples were carried out using an Omicron Nanotechnology Multiprobe Instrument. The spectra was obtained using a high- resolution hemisphere analyzer EA 125 HR equipped with a detection system consisting of seven channeltrons. A monochromated Al Kα source of hν = 1486.6

eV was used to probe $La_{0.7}Te_{0.3}Mn_{1-x}Co_xO_3$ pellets with x=0.1 and x=0.3 attached by double-sided tape to the molybdenum sample holder. The pressure in the XPS chamber was maintained at 5×10^{-10} mbar during the measurements. The binding energies were corrected by C 1s as reference energy (C 1s = 284.8 eV) (Moulder *et al.*, 1992). A wide scan was collected to ensure that no foreign materials were present on the sample surface. Narrow scans of Mn 2p and Co 2p regions were collected at an analyzer pass energy of 20 eV. Curve fitting to the XPS spectrum was done using CasaXPS software. Background subtraction was done using the Shirley method.

3.2.8. Differential scanning calorimetry

Differential scanning calorimetry (DSC) is a thermal analysis technique where the differences in the heat flow into a sample, and a reference is measured as a function of temperature, while both are subjected to a controlled temperature program. DSC can be used to determine phase transformation, melting temperatures, crystallization temperatures, glass transition temperatures, etc. Moreover, the chemical reaction such as thermal curing, heating history, specific heat capacity, and purity analysis can also be determined. When a sample undergoes a physical transformation such as a phase transition, either heat is absorbed or liberated out of the sample with respect to that of the reference to maintain both at the same temperature. The process may be exothermic or endothermic depending on whether heat flows out of the sample or into the sample. In the present study, power compensation DSC is used where the heat flow between the sample side and reference side is measured directly using two separate, low mass furnaces. Both the sample and reference pans are heated by different furnaces. When a phase change occurs in the sample, the sensitive Platinum Resistance Thermometer (PRT) detects the change, and power (energy) is applied or removed from the sample furnace to compensate for the change in heat flow to or from the sample. Hence, the temperature difference is maintained at zero all times. The amount of power required to maintain the system in equilibrium is directly proportional to the energy changes occurring in the sample. No complex heat flux equations are required with a power compensation DSC because the system directly measures the energy flow to and from the sample. In the present work, DSC measurements were carried out on the Gd-Si-Ge samples using the Mettler Toledo DSC 822 which a power compensation DSC. An empty aluminum pan is used as the reference, and the sample is placed in another aluminum pan in the DSC cell. The

measurements were carried out in the heating as well as cooling cycles with a scanning rate of 5 K/min. The schematic diagram of power compensation DSC is shown in Figure 3.15.

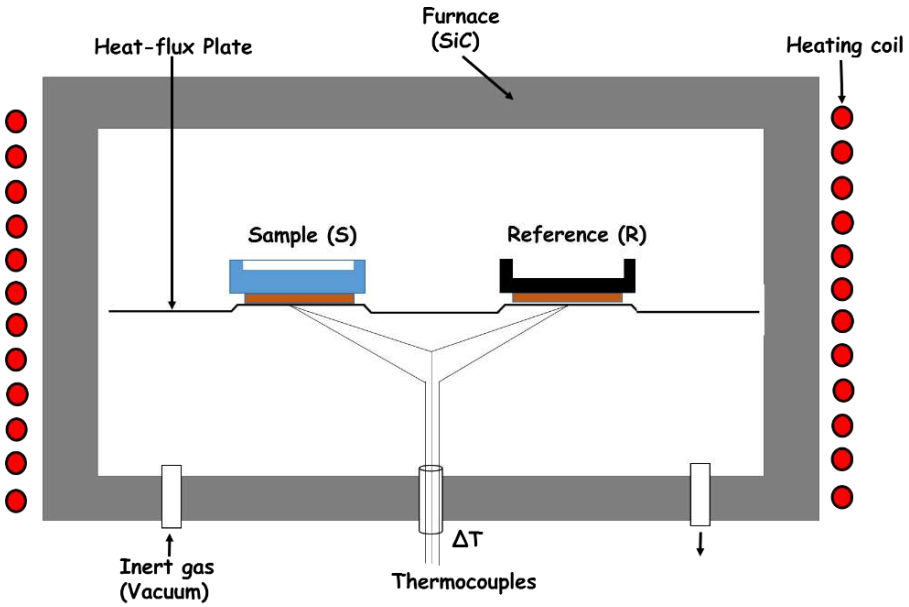

Figure 3.15. Schematic representation of a Power compensation DSC.

3.2.9. Electron Spin Resonance

Electron Spin Resonance (ESR) spectroscopy, also known as Electron Paramagnetic Resonance (EPR) spectroscopy, is a versatile, and nondestructive analytical technique based on the absorption of microwave radiation by molecules or compounds with unpaired electrons when placed in a strong magnetic field. When any compound containing unpaired electron is subjected to a static magnetic field, the interaction between the spin magnetic moment of the electron and the applied magnetic field splits the spin energy levels, which is known as Zeeman effect. The alignment along the direction of the magnetic field corresponds to the lower energy state m_s = - ½ and the alignment opposite (antiparallel) to the direction of the applied magnetic field corresponds to m_s = + ½. The two alignments have different energies, and this difference in energy lifts the degeneracy of the electron spin states. The difference between the two spin states, m_s = +1/2 and m_s = -1/2 corresponds to frequencies in the microwave region. The difference in energies is given by:

$$\Delta E = h\upsilon = g\mu_B B \qquad (3.14)$$

where h is the Planck's constant, υ is the frequency, g is the Lande g factor, μ_B is the Bohr magneton and B is the applied magnetic field. Transitions between these spin states is induced by applying suitable microwave radiation perpendicular to the magnetic field. The resulting absorption of the microwave radiation is modulated to record the first derivative of the absorption to improve the resolution. Thus, for a particular applied field strength, an absorption of microwave radiation of a particular frequency results in the resonance. The block diagram of an ESR spectrometer is shown in the Figure 3.16. This is a continuous wave (CW) ESR spectrometer that employs field modulation and phase sensitive detection. The Microwave Bridge consists of the Gundiode which acts as the source of radiation and the Detector. The sample whose ESR spectra is to be measured is placed in a resonant cavity which admits microwaves through an iris. The cavity is placed in the middle of an electromagnet which helps to amplify the weak signals from the sample. Other components such as attenuator, field modulator, and amplifier also enhance the performance of the instrument. However, in a typical EPR spectrometer, the experiments are carried out at a fixed frequency of microwave radiation and varying the applied field. Two common frequencies are in the X-band frequency range (8.75- 9.65 GHz), and the Q-band frequency (35.5 GHz). In the present study, ESR spectra of selected Gd-Si-Ge samples were obtained using JES-FA200 ESR (ESR-JEOL, Japan) at selected temperatures between 200 K and 320 K in the X-band region.

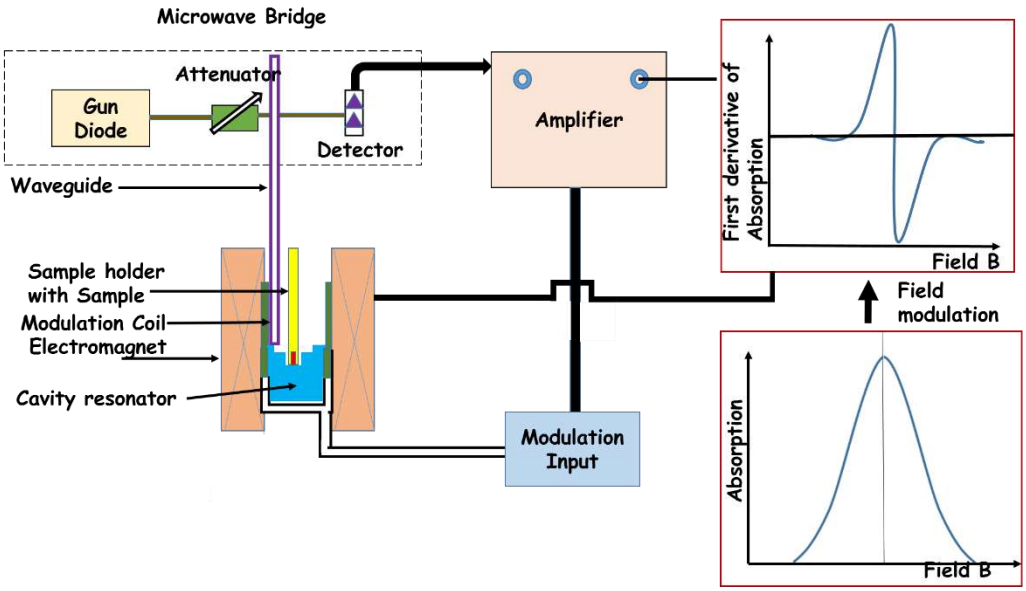

Figure 3.16. The block diagram of ESR spectrometer

Chapter 4

Tuning the structural and magnetocaloric properties of $Gd_5Si_2Ge_2$ with Nd substitution

This chapter discusses the effect of Nd substitution on the structural, magnetic and magnetocaloric behavior of $Gd_{5-x}Nd_xSi_2Ge_2$ with $x = 0$, 0.05, 0.1, and 0.2. Universal Curve Analysis has been carried out to understand the nature of the transition.

4.1. Introduction

Compounds with first order phase transitions (FOPT) leads to a GMCE. Since the discovery of GMCE in $Gd_5Si_2Ge_2$ ([a]Pecharsky *et al.*, 1997), extensive research on Gd_5 $(Si_xGe_{1-x})_4$ compounds has been carried out to increase the isothermal entropy change (and adiabatic temperature change) around room temperature. Research on $Gd_5(Si_xGe_{1-x})_4$ compounds are of special interest owing to the existence of a strong correlation between its crystal structure and magnetic properties (Pereira *et al.*, 2010; Morellon *et al.*,1998) and GMCE in $Gd_5Si_2Ge_2$ makes it a promising candidate for room temperature magnetic refrigeration applications. Giant MCE in $Gd_5(Si_xGe_{1-x})_4$ system has been attributed to the coupled magneto-structural transition from the high-temperature monoclinic PM phase to the low-temperature orthorhombic FM phase that occurs in the vicinity of the magnetic ordering temperature (Provenzano *et al.*, 2004). This phase transition can be induced by changes in temperature ([a]Pecharsky *et al.*, 1997; [b]Pecharsky *et al.*, 1997), hydrostatic pressure (Carvalho *et al.*, 2005) and magnetic field (Morellon *et al.*, 1998) as well as by tuning the Si: Ge ratio ([c]Pecharsky *et al.*, 1997).

Several studies have been performed on different $R_5(Si_xGe_{1-x})_4$ series (R= Pr, Nd, Dy, Tb and Ho) to understand the correlation between the magnetic and crystallographic phases (Wang *et al.*, 2007; Magen *et al.*, 2004; [a]Nirmala *et al.*, 2007; [b]Tegus *et al.*, 2002; Thuy *et al.*, 2002; Pereira *et al.*, 2008). Alloying $Gd_5Si_2Ge_2$ with different rare earths at the Gd site such as Tb, Dy, Er, etc which occupy to the right of $Gd_5Si_2Ge_2$ in the periodic table leads to a decrease in the Curie temperature. However, the magnetocaloric property gets enhance with Tb and Er substitution and are discussed in Chapter 2 ([a]Deng *et al.*, 2007; [b]Deng *et al.*, 2007, Nirmala *et al.*, 2007, Chen *et al.*, 2011). The magnetocaloric property of $Nd_5Si_2Ge_2$ with monoclinic structure was investigated by Gschneidner *et al.* and was found to be 5.6 J/ kg K for 50 kOe at 65K (Gschneidner *et al.*, 2000). Hence, in the present study, we report the evolution of magnetic as well as magnetocaloric properties of $Gd_5Si_2Ge_2$ with Nd substitution at the Gd site. With Nd substitution, the T_C could be tuned to room temperature although with a decrease in ΔS_M. However, the compounds show a significant relative cooling power (RCP) showing the potential of these materials for room temperature magnetic refrigeration applications.

4.2. Experimental details

Alloys with the nominal composition $Gd_{5-x}Nd_xSi_2Ge_2$ (x=0, 0.05, 0.1 and 0.2) were prepared by arc melting the constituent elements in a water cooled copper hearth under high pure argon conditions. The purity of the starting elements was 99.9 wt. % for Gd (Alfa Aesar) and Nd (Alfa Aesar) and 99.9999 wt. % for Ge (Alfa Aesar) and Si (Alfa Aesar). The ingots were re-melted several times to ensure compositional homogeneity during melting. Weight loss of the samples after the arc-melting process was found to be less than 0.01%. As-cast ingots were sealed in evacuated quartz tubes and annealed at 1573 K for 1 hour and subsequently quenched in ice water. The crystal structure of the samples were analyzed by X-ray powder diffraction using Cu-Kα radiation (PANalytical X'pert Pro diffractometer) operated at 40 kV and 30 mA. The diffraction measurements were performed in the 2θ range 10° to 90° with a step size of 0.017°. Rietveld refinement of the diffraction pattern was carried out using GSAS (General Structure Analysis System) software. Differential scanning calorimetry was performed (PerkinElmer – Pyris 6) with a scanning rate of 5°C/min under nitrogen atmosphere. Magnetization measurements were made as a function of both temperature and field using a PPMS [Quantum Design, Dynacool] up to a maximum field (H) of 50 kOe in a temperature range 100-320 K. MCE was estimated, in terms of isothermal magnetic entropy change (ΔS_M), from Maxwell relations (Gschneidner *et al.*, 2005) using equation (1.19) described in Chapter 1.

4.3. Results and discussion

4.3.1. Structural Analysis

Powder X-ray diffraction patterns of $Gd_{5-x}Nd_xSi_2Ge_2$ (x=0, 0.05, 0.1and 0.2) alloys are shown in Figure 4.1. According to the X-ray diffraction patterns, the parent compound $Gd_5Si_2Ge_2$ crystallizes in a mixed state of monoclinic $Gd_5Si_2Ge_2$-type and O(I) Gd_5Si_4 phase at room temperature. $Gd_{5-x}Nd_xSi_2Ge_2$ alloys with x=0.05 stabilizes in the monoclinic $Gd_5Si_2Ge_2$-type structure at room temperature and has been indexed with ICSD pattern No. 84084 (space group $P112_1/a$). The refinement result of $Gd_{5-x}Nd_xSi_2Ge_2$ for x=0, 0.05, 0.1 and 0.2 are shown in Figure 4.2-4.5 respectively. Rietveld refinement confirms the monoclinic phase of $Gd_{5-x}Nd_xSi_2Ge_2$ with x=0.05. However, the increase in Nd content favours the formation of the O(I) Gd_5Si_4 structure and the compositions with

x=0.1 and x=0.2 has been indexed with ICSD pattern no. 84083 (Space group Pnma). The formation of the Gd_5Si_4 structure is attributed to the changes in the inter-slab bonding with increase in Nd substitution. A small fraction of hexagonal Gd_5Si_3 phase is found in the parent compound. However, the presence of Gd_5Si_3 phase is almost negligible in the Nd substituted compounds. Details of the lattice parameters extracted along with refinement parameters are summarized in Table 4.1.

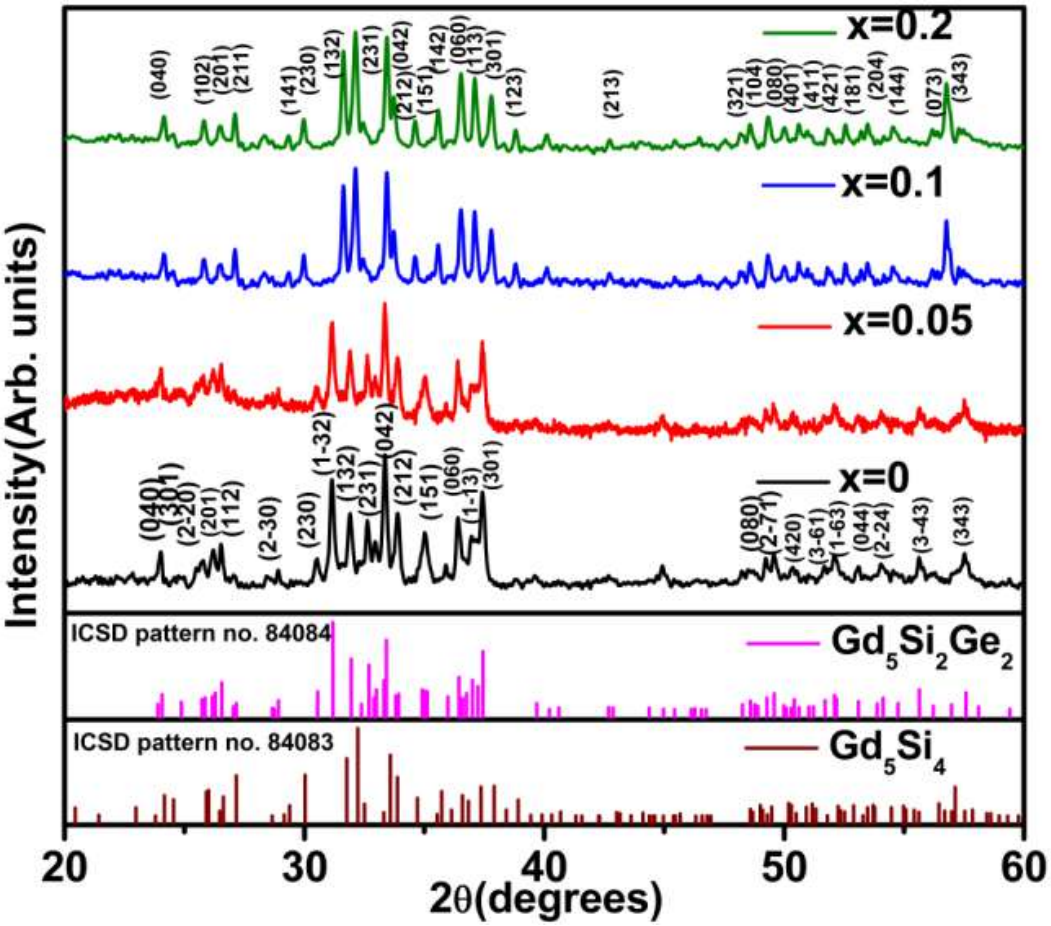

Figure 4.1. XRD patterns of $Gd_{5-x}Nd_xSi_2Ge_2$ (x = 0, 0.05, 0.1 and 0.2) at room temperature.

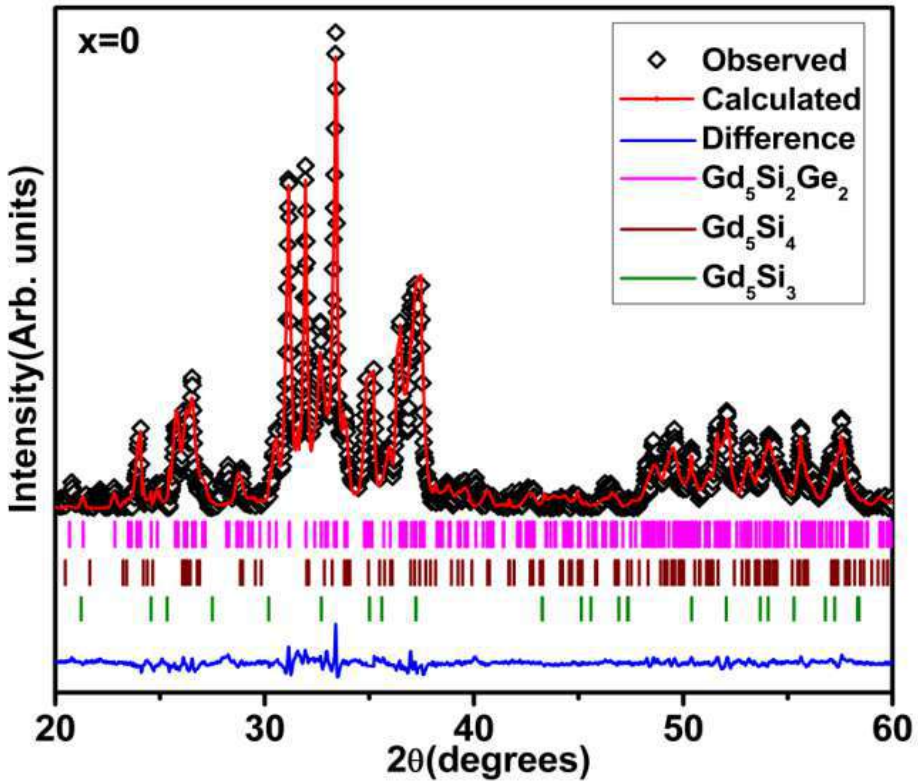

Figure 4.2. Rietveld refined XRD pattern of $Gd_5Si_2Ge_2$.

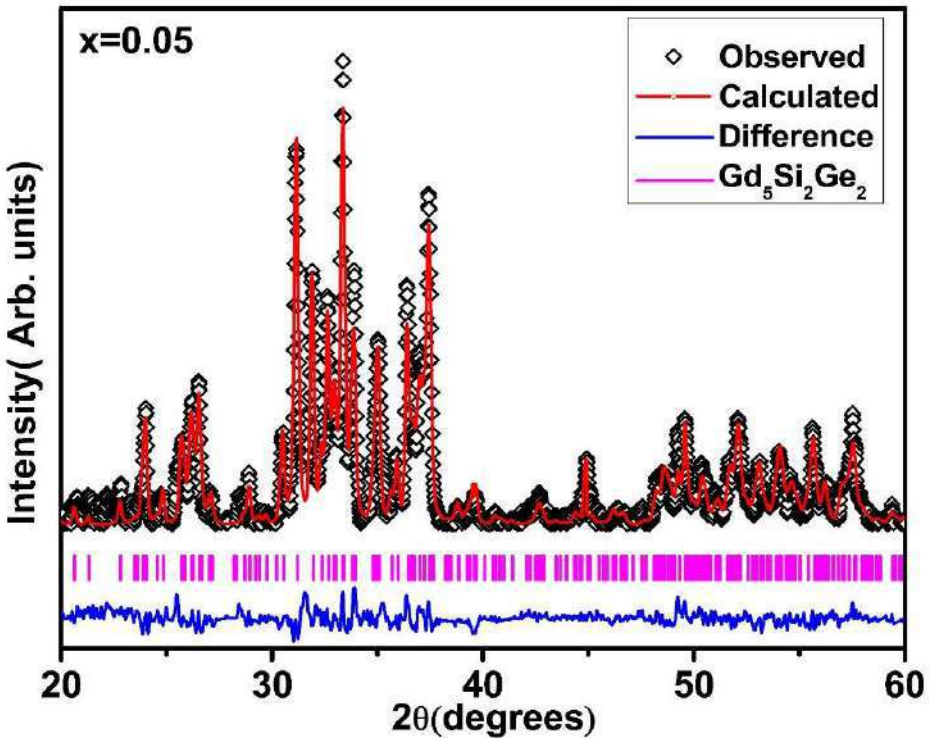

Figure 4.3. Rietveld refined XRD pattern of $Gd_{4.95}Nd_{0.05}Si_2Ge_2$.

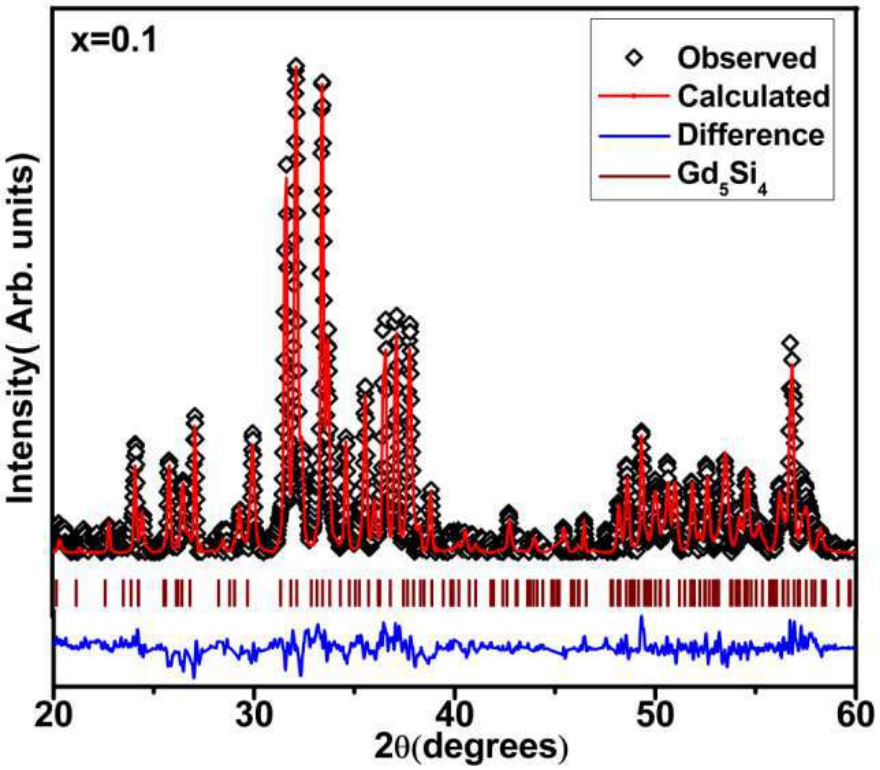

Figure 4.4. Rietveld refined XRD pattern of $Gd_{4.9}Nd_{0.1}Si_2Ge_2$.

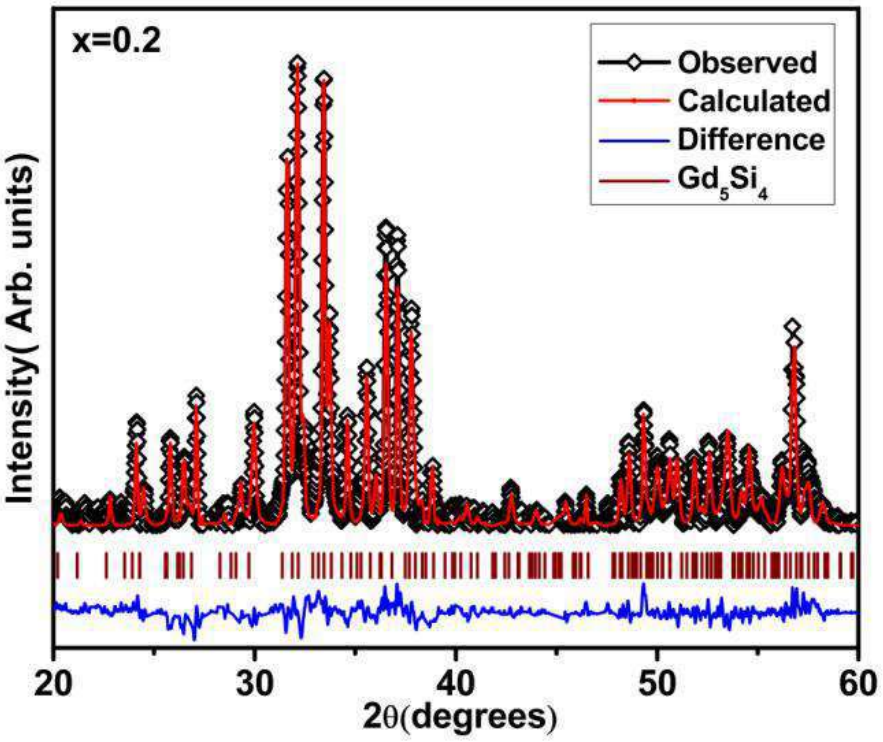

Figure 4.5. Rietveld refined XRD pattern of $Gd_{4.8}Nd_{0.2}Si_2Ge_2$.

Table 4.1. Lattice parameters, unit cell volume, and reliability factors from the Rietveld refinement of $Gd_{5-x}Nd_xSi_2Ge_2$ (x =0, 0.05, 0.1 and 0.2).

$Gd_{5-x}Nd_xSi_2Ge_2$	Crystal Structure	Space group	Lattice parameters					Residual Parameters	
			a (Å)	b (Å)	c (Å)	γ (deg)	Volume $(Å)^3$	R_{wp} %	R_p %
x = 0	M	$P112_1/a$	7.55(1)	14.75(1)	7.75 (1)	93.12(5)	862.28(6)	1.56	1.17
	O(I)	Pnma	7.66(2)	14.62(1)	7.53(1)	90	844.38(1)		
	H	$P6_3/mcm$	8.35(1)	8.35(1)	6.48(1)	120	391.22(7)		
x =0.05	M	$P112_1/a$	7.56(3)	14.77(6)	7.77(4)	93.09(4)	866.25(5)	2.00	1.57
x = 0.1	O (I)	Pnma	7.51 (3)	14.79(6)	7.81(2)	90	867.65(5)	2.40	1.82
x = 0.2	O (I)	Pnma	7.52 (3)	14.81(6)	7.82(3)	90	871.77(5)	1.40	1.79

4.3.2. SEM and TEM Analysis

The backscattered scanning electron (BSE) micrographs of Nd substituted $Gd_5Si_2Ge_2$ alloys are shown in Figures 4.6-4.8. The microstructures of the parent composition display a multi-phase nature showing the presence of a brighter $Gd_5(Si,Ge)_4$ matrix phase (5:4-type) along with darker $Gd_5(Si,Ge)_3$ (5:3-type) secondary phase. The Nd substituted show the presence of $Gd_5(Si,Ge)_4$ matrix phase along with traces of $Gd_5(Si,Ge)_3$ (5:3-type) phase. Elemental mapping analysis has been performed on all the samples and the results are included in Figures 4.6-4.8. Elemental mapping reveals that Nd has been uniformly distributed throughout the matrix phase. The EDS results are summarized in Table 4.2. This is concordant with our Rietveld refinement results shown in Table 4.1. The increase in lattice parameters with Nd substitution is attributed to lattice expansion caused by the large size of Nd (2.64 Å) compared to Gd (2.54 Å).

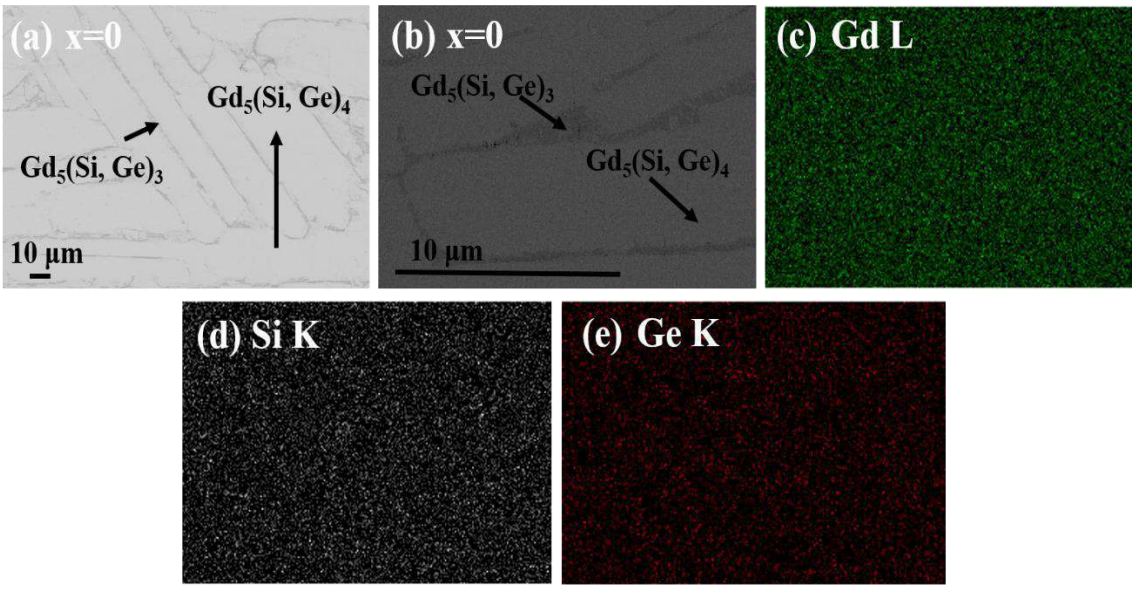

Figure 4.6. Backscattered SEM images of $Gd_{5-x}Nd_xSi_2Ge_2$ alloys for (a) x=0 at low magnification (b) x=0 at high magnification (c) Gd mapping (d) Si mapping and (e) Ge mapping [Matrix phase is 5:4-type, Dark phase is 5:3-type].

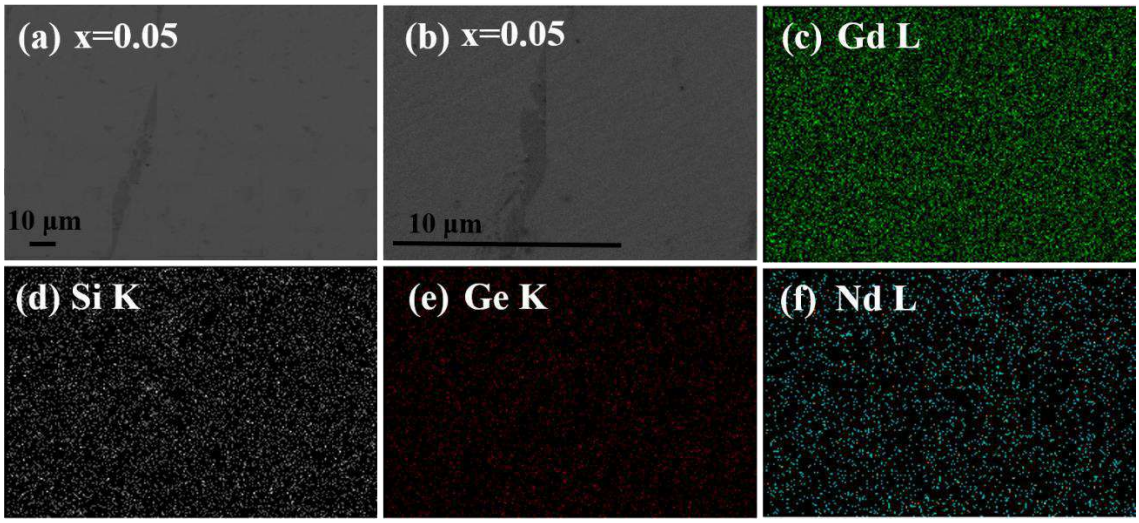

Figure 4.7. Backscattered SEM images of $Gd_{5-x}Nd_xSi_2Ge_2$ alloys for (a) x=0.05 at low magnification (b) x=0.05 at high magnification (c) Gd mapping (d) Si mapping and (e) Ge mapping and (f) Nd mapping. [Matrix phase is 5:4-type, Dark phase is 5:3-type].

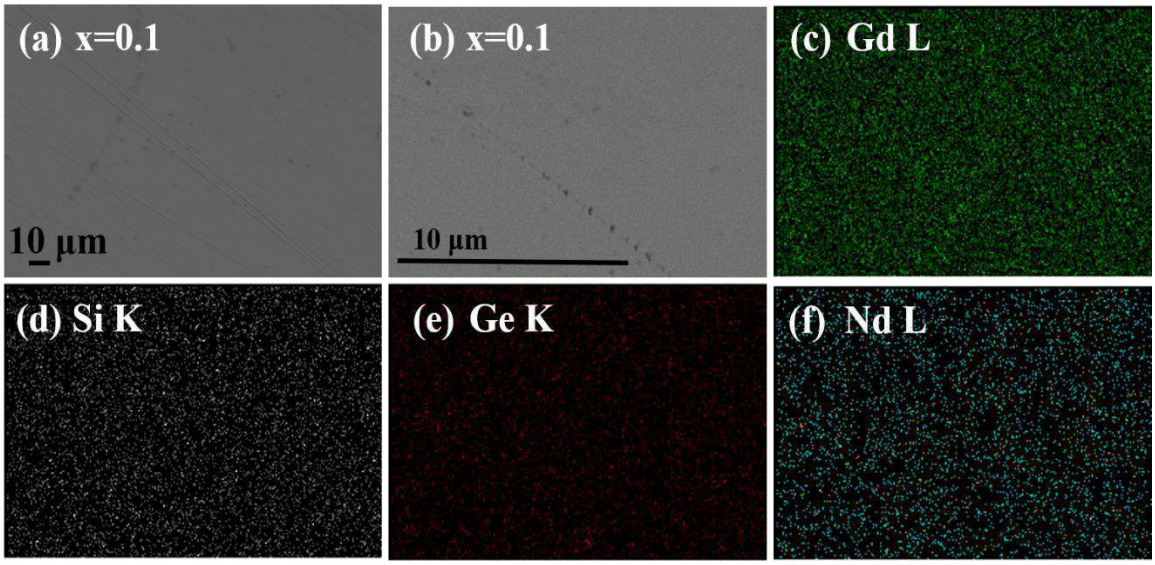

Figure 4.8. Backscattered SEM images of $Gd_{5-x}Nd_xSi_2Ge_2$ alloys for (a) x=0.1 at low magnification (b) x=0.1 at high magnification (c) Gd mapping (d) Si mapping and (e) Ge mapping and (f) Nd mapping [Matrix phase is 5:4-type].

Table 4.2. Compositions of $Gd_{5-x}Nd_xSi_2Ge_2$ with x= 0, 0.05, 0.1 and 0.2 determined by EDS analysis. The estimated error in determining the concentration of each element is 0.1 at%.

x	Phase	Composition (at %)				Phase type
		Gd	Si	Ge	Nd	
0	Matrix	55.08	22.13	22.79	-	5:4
	Grain Boundry phase	62.03	22.28	15.9	-	5:3
0.05	Matrix	54.73	22.25	21.87	0.95	5:4
0.1	Matrix	53.27	22.97	22.73	1.03	5:4
0.2	Matrix	55.93	22.79	22.57	2.11	5:4

From the SEM images, it is quite difficult to distinguish the presence of monoclinic and O(I) phases in the parent compound. Hence, to have a better understanding of the different matrix phases, we have carried out the High-Resolution Transmission electron microscopy (HRTEM) analysis on the substituted samples $Gd_{5-x}Nd_xSi_2Ge_2$ with x=0, 0.05, 0.1 and 0.2 and the results are depicted in Figure 4.9.

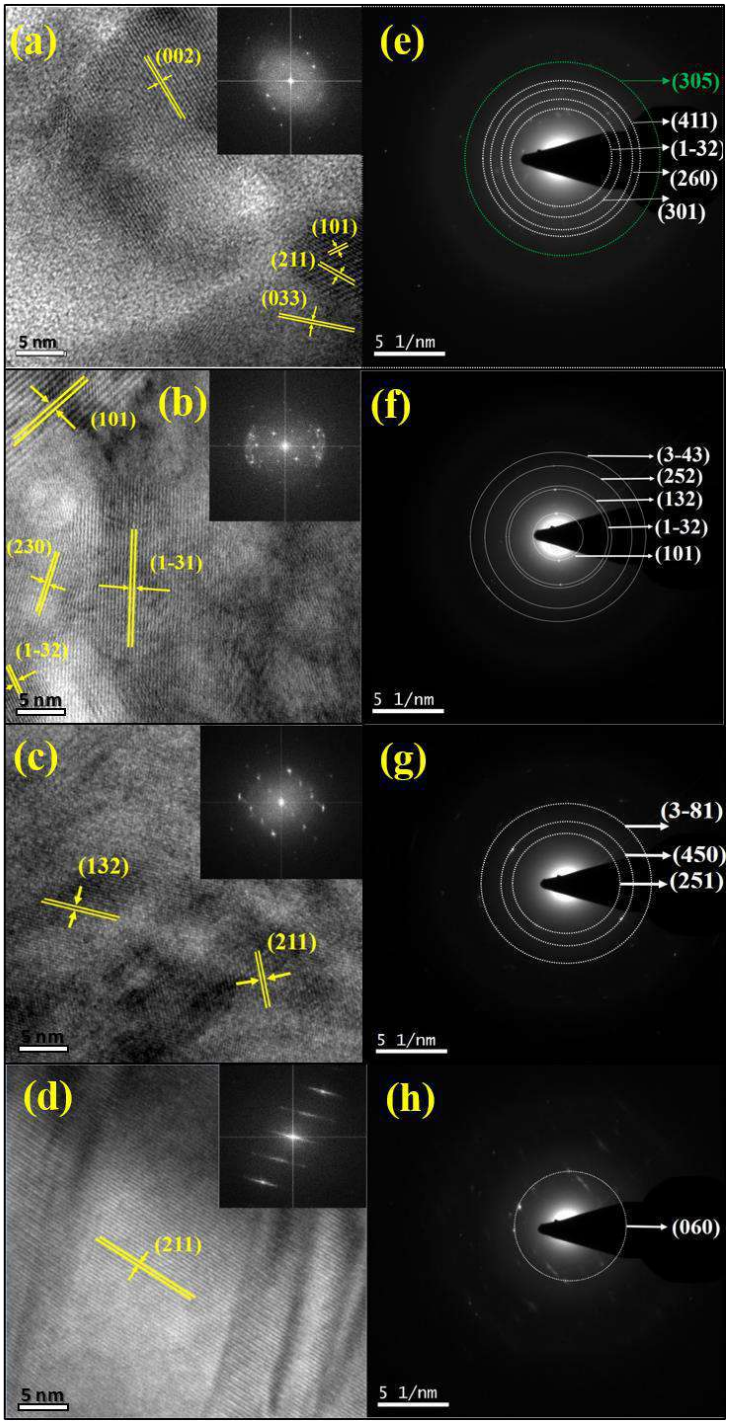

Figure 4.9. HRTEM images of the samples $Gd_{5-x}Nd_xSi_2Ge_2$ with (a) x= 0, (b) x=0.05 (c) x=0.1 and (d) x=0.2. Inset shows the corresponding FFTs. SAED patterns obtained for (e) x= 0, (f) x=0.05, (g) x=0.1 and (f) x=0.2 (circles are a guide to the eye).

The dominant planes seen in the high-resolution bright field images of x=0 matches with the planes of the monoclinic and O(I) phase. Interplanar spacing *(d)* of these planes measured from the TEM images match with the calculated values of the corresponding planes. The selected area electron diffraction (SAED) patterns recorded shows a spotty nature. The *d* values corresponding to these spots and the corresponding SAED patterns are indexed as shown in Figure 4.9.

4.3.3. DSC Measurements

Figure 4.10. shows the DSC curves of $Gd_{5-x}Nd_xSi_2Ge_2$ during heating and cooling cycles for x=0.05 and x=0.2. During heating, for alloys with x=0.05, there is an endothermic peak at around 270 K. The peak at 270 K during heating is attributed to a FOPT from an orthorhombic Gd_5Si_4 phase to a monoclinic $Gd_5Si_2Ge_2$ phase (Huo *et al.*, 2011). Moreover, it can be noted that the phase transformation corresponding to the endothermic peak is reversible causing a dip in the DSC curve at around 264K during the cooling cycle. On the other hand, as the Nd content increases to x=0.2, no other signatures corresponding to the FOPT is seen in the DSC curves for x=0.2. XRD together with DSC results indicates that $Gd_{4.95}Nd_{0.05}Si_2Ge_2$ shows a first order structural phase transition at around 270 K and as the Nd content increases to x=0.2, the orthorhombic crystal structure remains stable in the temperature range 250-370 K.

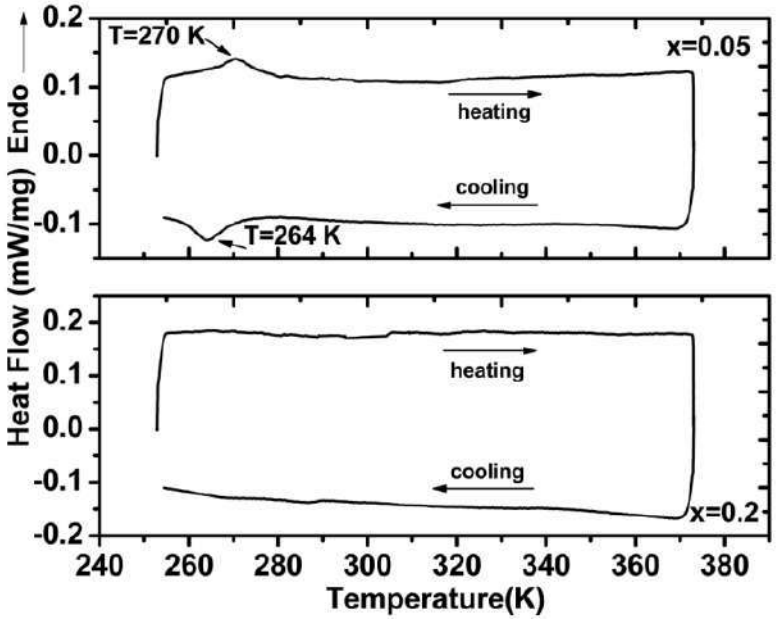

Figure 4.10. DSC scans of $Gd_{5-x}Nd_xSi_2Ge_2$ for (a) x=0.05 and (b) x=0.2.

4.3.4. Magnetic characterization

Figure 4.11 shows the temperature dependence (100 K−320 K) of magnetization M(T) under field cooled cool (FCC) and field cooled warm (FCW) conditions measured in a field of 100 Oe and 500 Oe for $Gd_5Si_2Ge_2$. The FCC and FCW curves of $Gd_{5-x}Nd_xSi_2Ge_2$ with x=0.05, 0.1 and 0.2 are shown in Figure 4.12. The FCC and FCW magnetization curves almost follow the same path below the magnetic ordering temperature for all the compositions. However, there is a significant hysteresis in the FCC and FCW curves, for x=0 and 0.05, near the magnetic ordering temperature. The thermal hysteresis between FCC and FCW curves is ~15 K for x=0.05 and is attributed to a FOPT. This is in line with the conclusion drawn from the DSC curve depicted in Figure 4.10 (a). The Curie temperature (T_C) of $Gd_{5-x}Nd_xSi_2Ge_2$ was determined from dM/dT curves, and it was found to be around 275 K, 300 K and 293 K for x = 0.05, 0.1 and 0.2 respectively. Nd substitution in $Gd_5Si_2Ge_2$ leads to a lowering of the ferromagnetic ordering temperature for x=0.05 from 277 K in $Gd_5Si_2Ge_2$ alloy to 275 K without the loss of FOPT. Due to the larger size of Nd compared with Gd, the lattice parameters gradually increase with increase in Nd substitution. This leads to the weakening of the exchange coupling between the rare earth atoms leading to a decrease in the Curie temperature for monoclinic $Gd_{4.95}Nd_{0.05}Si_2Ge_2$. However, with increase in Nd substitution to 0.1, the structure changes from monoclinic to orthorhombic O (I), where all the slabs are interacting strongly. As a result, the exchange coupling between the slabs increases. Also, there is direct Gd(Nd)-Si (Ge)-Gd(Nd) super exchange interaction, in addition to the indirect Ruderman-Kittel-Kasuya-Yosida (RKKY) 4f-4f exchange in the O(I) Gd_5Si_4-type phase resulting in a higher Curie temperature (Levin *et al.*, 2000; Belo *et al.*, 2013). For the composition with x=0.2, the Curie temperature again decreases. This is due to the weakening of the exchange coupling with increase in lattice parameters as the Nd concentration is increased.

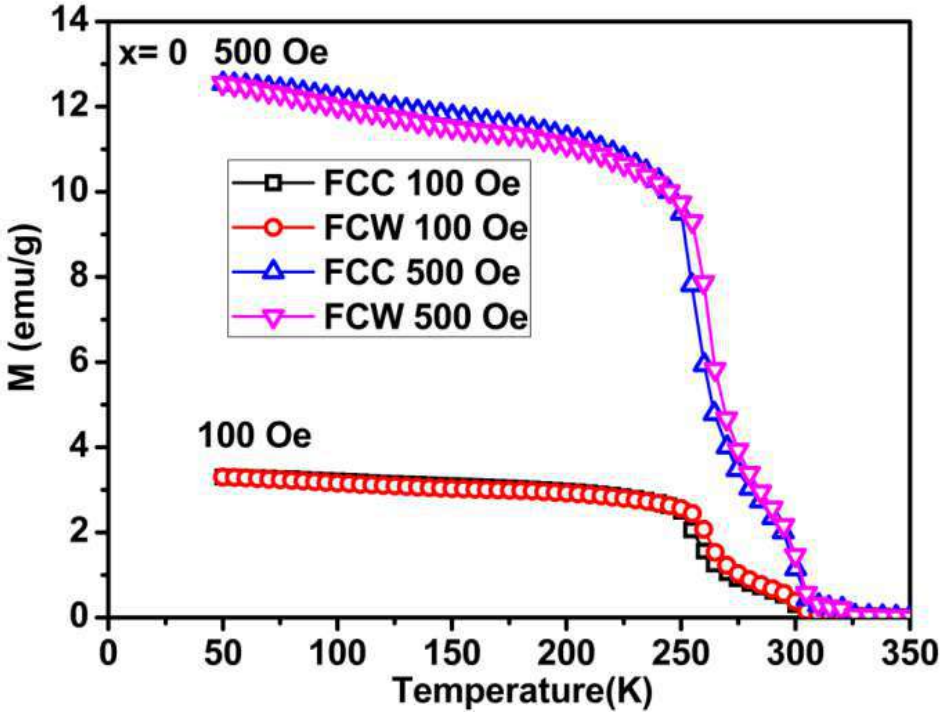

Figure 4.11. M-T curves of $Gd_5Si_2Ge_2$ (x=0) alloys measured in a magnetic field of 100 Oe and 500 Oe during FCC and FCW processes.

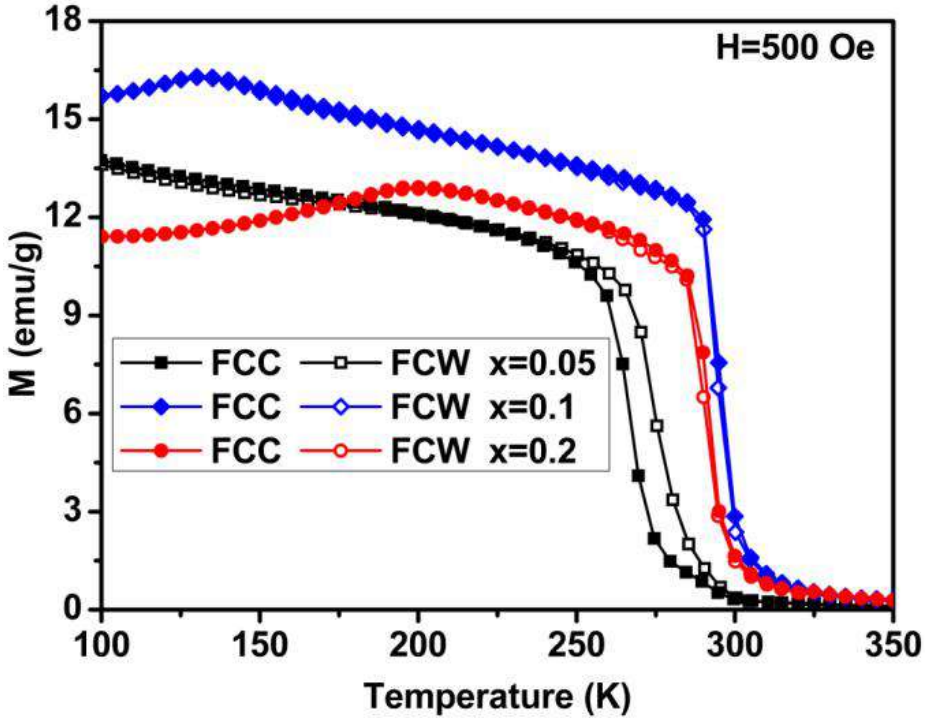

Figure 4.12. M-T curves of $Gd_{5-x}Nd_xSi_2Ge_2$ (x=0.05, 0.1 and 0.2) alloys measured in a magnetic field of 500 Oe during field cooling and field warming processes.

Isothermal magnetization curves were measured in the temperature range of 210−320 K with a temperature interval of 5 K. For the magnetization measurement at a particular temperature, the field was swept from 0-50 kOe and back to 0 Oe and the results are depicted in Figures 4.13(a) – 4.13(d). It is clear from the M (H) curves that the magnetization decreases with increase in temperature and becomes linear in H as the temperature exceeds the magnetic ordering temperature. It can be seen from Figure 4.13 (a) - 4.13(b) that for x = 0 and 0.05, there is a considerable field hysteresis around the ordering temperature, signifying a FOPT. This hysteresis is due to a field induced first order crystallographic phase change from monoclinic PM phase to orthorhombic FM phase. It can be clearly seen that this field-induced phase transition reverses upon decreasing the field, but with some hysteresis around the transition region (Provenzano *et al.*, 2004). This feature, further suggests the reversible character of the structural transition, at which the structure of the alloy returns to the initial state once the magnetic field is completely removed. It can be seen that the hysteresis is maximum in the vicinity of $T_{C,}$ where the structural transition occurs. For compounds with x=0.1 and x=0.2, the magnetic hysteresis is reduced considerably. This is due to the suppression of FOPT with increase in Nd substitution.

In order to understand the exact nature of magnetic phase transitions, Arrott plots (M^2 versus H/M) have been constructed. According to the Banerjee criterion, (Banerjee, 1964) a negative slope in the Arrott plot signifies a first order magnetic transition while a positive slope indicates a second order transition. The Arrott plots indicate a negative slope for x=0 and 0.05, thus confirming the first order nature of phase transition while for x=0.1 and x=0.2, the positive slope in the Arrott plot indicate a second order phase transition. The Arrott plots for all the compositions are shown in Figures 4.13(e) - 4.13(h) respectively.

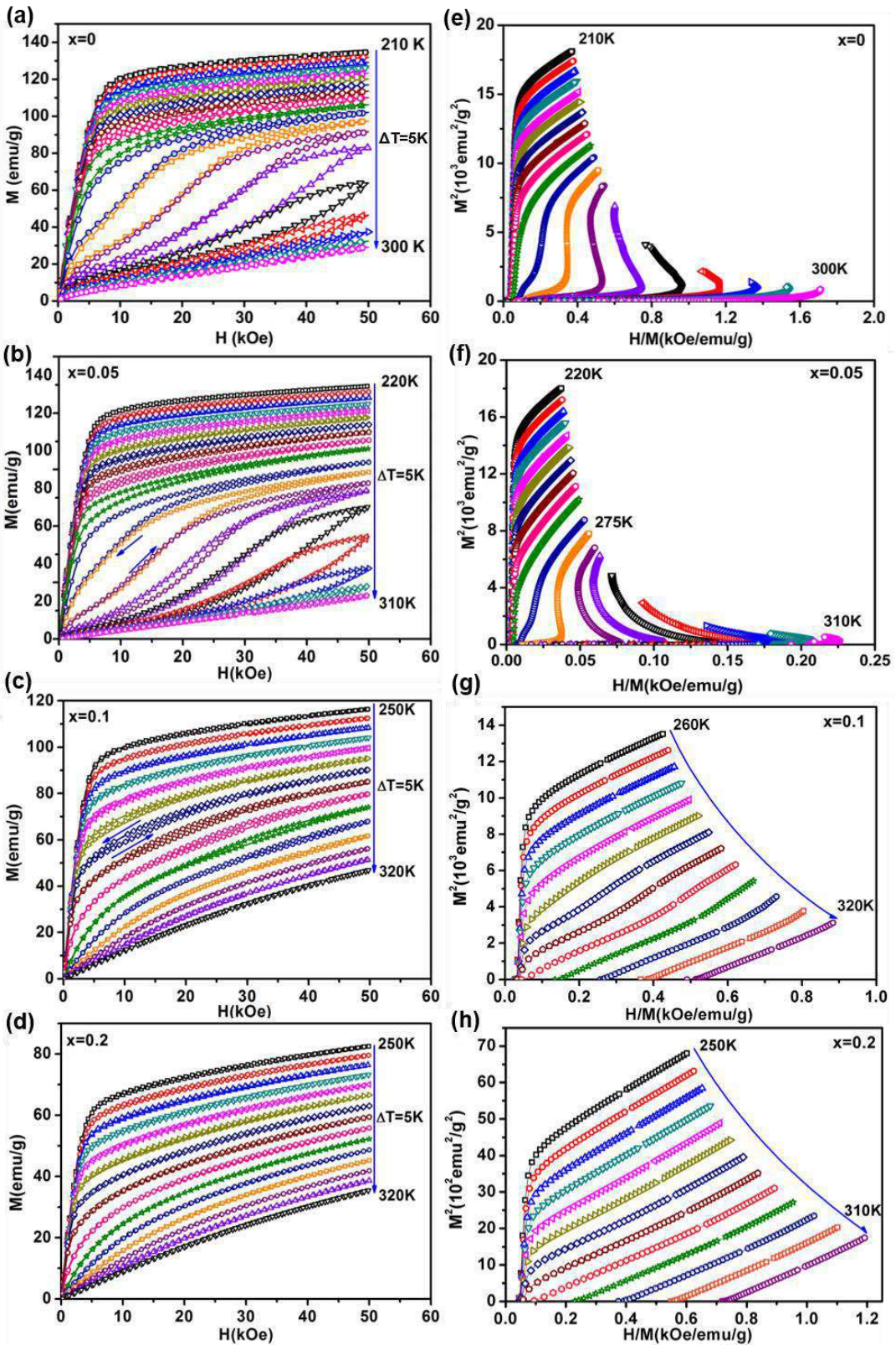

Figure. 4.13. Field dependence of magnetization at different temperatures for $Gd_{5-x}Nd_xSi_2Ge_2$ (a) x=0, (b) x=0.05, (c) x= 0.1 and (d) x= 0.2, corresponding Arrott plots of $Gd_{5-x}Nd_xSi_2Ge_2$ for (e) x=0, (f) x=0.05, (g) x= 0.1 and (h) x= 0.2.

4.3.5. Magnetocaloric effect

The magnetocaloric effect (ΔS_M) in these compounds has been evaluated from isothermal magnetization data using the thermodynamic Maxwell relations (Gschneidner *et al.*, 2005). Figures 4.14(a) – 4.14(d) represent the change of magnetic entropy (ΔS_M) as a function of temperature under different magnetic fields for x=0, 0.05, 0.1 and 0.2 respectively. It can be seen that the temperature dependence of ΔS_M shows a positive peak at temperature corresponding to the Curie temperature. The maximum magnetic entropy change (ΔS_M) for $Gd_{5-x}Nd_xSi_2Ge_2$ with x= 0, 0.05, 0.1 and 0.2 are 8.5, 7.9, 3.7 and 3.2 J/kg K, respectively, for a field change of 20 kOe, and 13.6, 12.8, 7.6 and 7.2 J/kg K, respectively, for a field change of 50 kOe. The ΔS_M value obtained for the parent compound is less than that the ΔS_M of -18 J/kg K obtained by Pecharsky *et al.* ([a]Pecharsky *et al.*, 1997). This reduction in MCE is due to the presence of two phases coexisting in the system at room temperature. MCE is positive over the entire temperature range as is the case for ferromagnetic materials because of magnetic ordering phenomenon with the application of the field (Samanta *et al.*, 2007). It can be seen that with increase in Nd substitution, ΔS_M versus T curve significantly broadens, reducing the maximum magnetic entropy change. For the composition with x=0.05, the compound undergoes a FOPT. As a result, the change of magnetic moment with temperature due to the coupled magneto-structural transition is quite high around the transition temperature resulting in an increased MCE. But for the composition with x=0.1 and x=0.2, the compounds undergo a SOPT and the change of magnetic moment with temperature is gradual. This results in a reduced MCE in the case of x =0.1 and x=0.2. The RC values obtained for x=0, 0.05, 0.1 and 0.2 for a field change of 50 kOe are 288, 251, 157 and 142 J/kg. The RCP values obtained for x=0, 0.05, 0.1 and 0.2 for a field change of 50 kOe are 305, 295, 205 and 188 J/kg respectively. It is to be noted that the hysteresis losses defined as the area enclosed by the ascending and descending magnetization curves has been estimated while calculating the RCP. The maximum hysteresis losses around T_C for $Gd_{5-x}Nd_xSi_2Ge_2$ alloys with x= 0, 0.05, 0.1 and 0.2 are 55, 53, 7 and 2 J/kg respectively, when measured under a field of 50 kOe. The effective RC and RCP has been calculated by subtracting the hysteresis losses from the calculated RCP. The variation of effective RC and RCP as a function of field is shown in Figure 4.15. The thermal hysteresis, magnetic hysteresis, entropy changes and the effective RC and RCP values are tabulated in Table 4.3. The

RCP value of 295 J/kg obtained for x=0.05, after accounting for the hysteresis losses is comparable to that obtained for $Gd_5Si_2Ge_2$ (305 J/kg) (Provenzano *et al.*, 2004) for a field change of 50 kOe, making it a promising candidate for near room temperature magnetic refrigeration. The compounds with x=0.1 and x=0.2 have comparatively less RCP values, but the operating temperature could be tuned to room temperature suggesting that these compounds could be used for room temperature magnetic refrigeration applications.

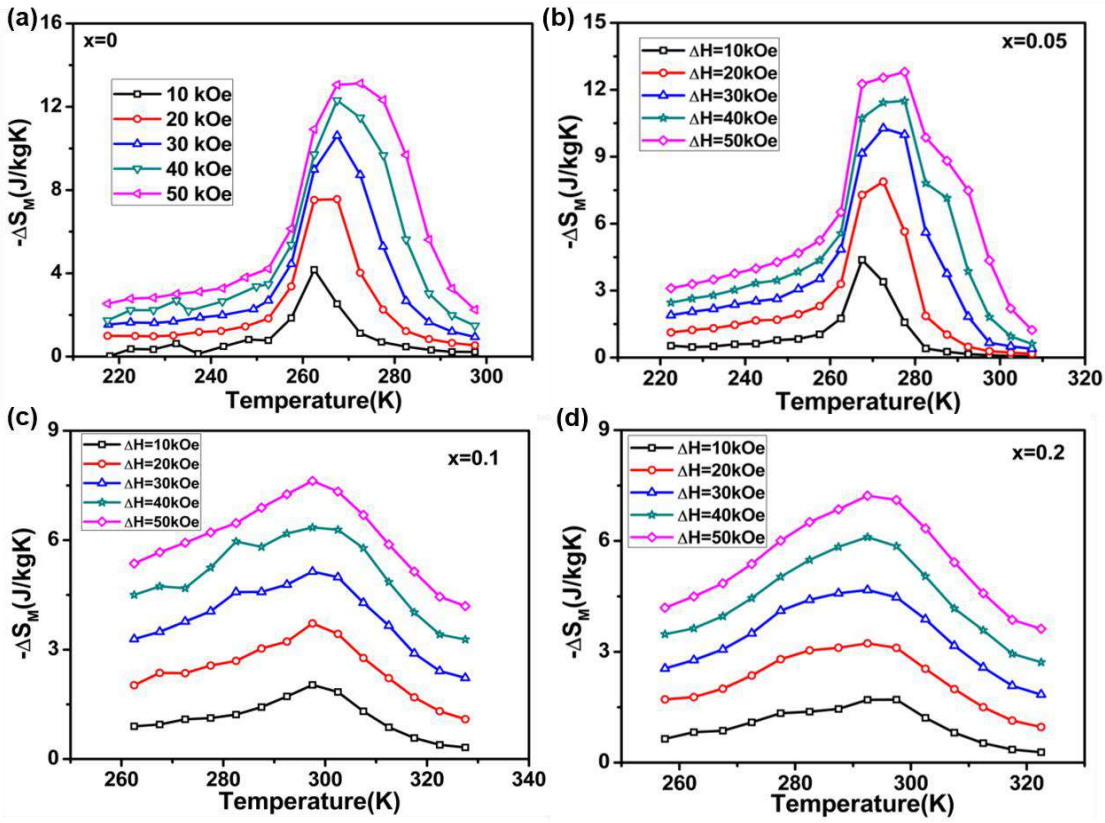

Figure. 4.14. Isothermal magnetic entropy change (ΔS_M) of $Gd_{5-x}Nd_xSi_2Ge_2$ (a) x=0, (b) x=0.05, (c) x= 0.1 and (d) x= 0.2 as a function of temperature for different field changes.

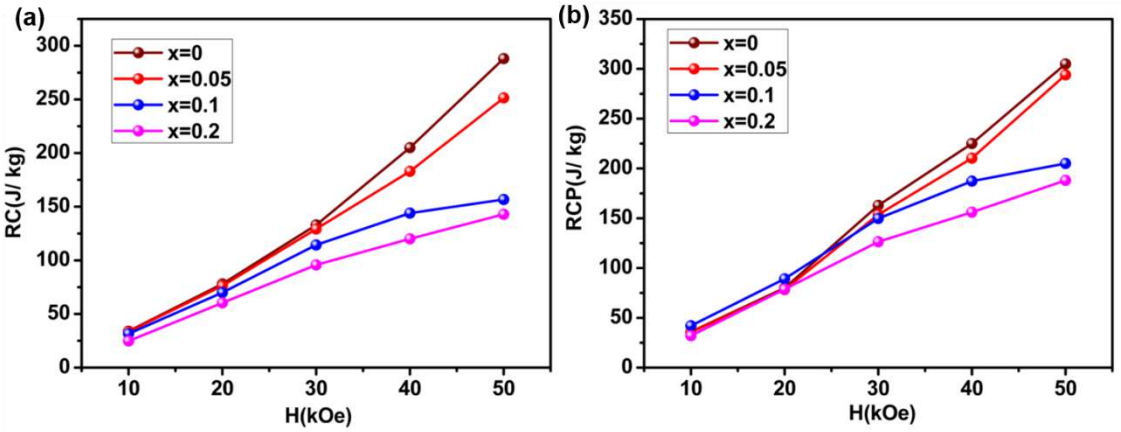

Figure 4.15. Variation of effective RC and RCP with field for $Gd_{5-x}Nd_xSi_2Ge_2$ (x=0, 0.05, 0.1 and 0.2).

Table 4.3. Transition temperatures, entropy changes, effective refrigerant capacity and relative cooling power calculated for $Gd_{5-x}Nd_xSi_2Ge_2$

x	Transition temperature	Thermal Hysteresis (K)	Magnetic hysteresis at 50 kOe (J/kg)	$-\Delta S_M$ (J/kgK) ΔH=50 kOe	Effective RC (J/kg) H=50 kOe	Effective RCP (J/kg) H=50 kOe
0	**272**	**10**	**60**	**13.1**	**288**	**305**
0.05	**275**	**15**	**53**	**12.8**	**251**	**295**
0.1	**300**	**-**	**2**	**7.63**	**157**	**205**
0.2	**294**	**-**	**-**	**7.23**	**143**	**188**

4.3.6. Universal Curve Analysis

A new criterion based on the universal curve has been proposed for determining the order of phase transition based on the re-scaling of magnetic entropy change curves (Franco *et al*., 2006; Dong *et al*., 2006; Bonilla *et al*., 2010). The phenomenological universal curve can be calculated from purely magnetic measurements and results in the collapse of entropy change curves after a scaling process, regardless of the applied magnetic field. Hence, the major assumption is based on the fact that if a universal curve exists, then the equivalent points of the ΔS_M curves measured at different applied fields should collapse onto the same universal curve. For materials undergoing a second order phase transition, the rescaled magnetic entropy change for different applied fields

collapse onto a single curve (Bonilla *et al*., 2010; Franco *et al*., 2007;). However, the scaling assumptions that underlie this behaviour break down when applied to materials with first order phase transitions such as $DyCo_2$, $HoCo_2$, and $La_{2/3}Ca_{1/3}MnO_3$, and the scaled ΔS_M curves do not follow the universal behaviour (Bonilla *et al*., 2010). As a result, the universal curve can be used as a method for distinguishing first and second order phase transitions. Figure 4.16 shows the universal curve constructions for each sample by plotting the rescaled entropy change, $\Delta S_M / \Delta S_M^{peak}$ against the temperature variable, θ where θ is defined by

$$\theta = \begin{cases} -(T - T_C)/(T_{r_1} - T_C) & T \le T_C \\ (T - T_C)/(T_{r_2} - T_C) & T \ge T_C \end{cases} \qquad (4.1)$$

Here, the reference temperatures T_{r_1} and T_{r_2} are chosen such that

$$\Delta S_M(T_{r_1}) = \Delta S_M(T_{r_2}) = \Delta S_M^{max}/2 \qquad (4.2)$$

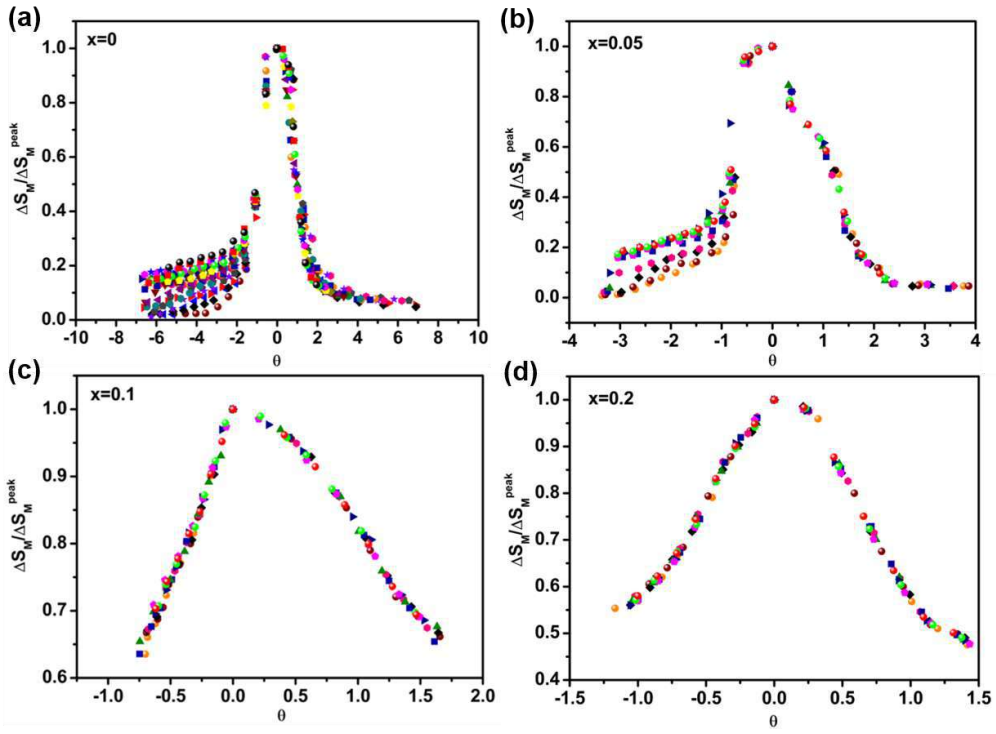

Figure 4.16. Normalized entropy change as a function of the rescaled temperature θ for (a) x=0, (b) x=0.05, (b) x=0.1 and (c) x=0.2.

From Figure 4.16, it is evident that the curves do not collapse for x=0 and x=0.05, for temperatures below T_C, indicating the first order nature of phase transition. As the Nd concentration increases to x=0.1, the curves collapse on to a single curve which is a signature of SOPT. In the range, $-1 < \theta < 0$, the collapse is real for second order transitions and is only apparent for first order transitions. For temperatures above T_C, $\theta > 0$, the collapse of the curves is due to the paramagnetic behaviour. This is concordant with the trends observed in the Arrott plots shown in Figure 4.13(e)-4.13 (h). Hence, in the Nd substituted compounds, a transition from FOPT to SOPT is observed, with increase in Nd content. This is attributed to the stabilisation of the orthorhombic O(I) phase with increase in Nd substitution.

4.4. Conclusions

In conclusion, Nd substituted $Gd_{5-x}Nd_xSi_2Ge_2$ alloys with x = 0, 0.05, 0.1 and 0.2 have been synthesized by arc melting. The composition with x = 0.05 shows a FOPT from monoclinic PM phase to O(I) FM phase while the compositions with x = 0.1 and x = 0.2 undergoes a second order magnetic phase transition. The order of magnetic phase transition is confirmed from the Arrott plots. MCE was calculated from Maxwell's relation and were estimated to be 8.5, 7.9, 3.7 and 3.2 J/kg K, respectively, for a field change of 20 kOe, and 13.6, 12.8, 7.6 and 7.2 J/kg K, respectively, for a field change of 50 kOe. The effective RCP values obtained for x=0, 0.05, 0.1 and 0.2 are 295, 205 and 188 J/kg for a field change of 50kOe. Universal analysis indicate a transformation from first order to second order with increase in Nd substitution. Significant MCE and large RCP around room temperature make Nd substituted $Gd_{5-x}Nd_xSi_2Ge_2$ potential candidates for room temperature magnetic refrigeration.

Chapter 5

Observation of short range ferromagnetic interactions and magnetocaloric effect in cobalt substituted $Gd_5Si_2Ge_2$

This chapter discusses the effect of cobalt substitution on the structural, magnetic and magnetocaloric properties of $Gd_5Si_{2-x}Co_xGe_2$ with x = 0, 0.1, 0.2 and 0.4. Structural studies show that the substituted compounds crystallize in a combination of $Gd_5Si_2Ge_2$ and Gd_5Si_4 phases. DC magnetization measurements reveal an anomalous low field magnetic behaviour indicating a Griffiths-like phase. This unusual behaviour is attributed to the local disorder within the crystallographic structure indicating the presence of short-range magnetic correlations and ferromagnetic clustering, which is stabilized and enhanced by competing intra-layer and inter-layer magnetic interactions. The magnetostructural transition results in entropy changes ($-\Delta S_M$) of 9 J/kg K at 260 K for x = 0.1, 8.5 J/kg K at 245 K for x = 0.2 and 4.2 J/kg K at 210 K for x = 0.4 for a field change of 50 kOe. Universal curve analysis has been carried out on the substituted samples to study the order of the magnetic transition.

5.1. Introduction

The $Gd_5(Si_xGe_{1-x})_4$ intermetallic compounds constitute an interesting class of compounds exhibiting multifunctional properties such as GMCE ([a]Pecharsky *et al*., 1997; [b]Pecharsky *et al*., 1997), colossal magnetostriction (Morellon *et al*., 1998), , and spontaneous generation of voltage (Levin *et al*., 2001). The unusually strong magneto-responsive properties in this system is attributed to the first-order magnetostructural transition from a high-temperature monoclinic (M) PM phase to the low-temperature O(I) FM phase in the vicinity of the magnetic ordering temperature (Morellon *et al*., 1998).

The remarkable properties of $Gd_5(Si_xGe_{1-x})_4$ family is associated with its unique, intrinsically layered crystal structure built by the stacking of stable two-dimensional subnanometer-thick slabs of Gd and Si/Ge atoms. The crystallographic phase and the nature of the magnetic interactions are controlled by a number of interlayer covalent like Si(Ge)-Si(Ge) bonds connecting the slabs (Choe *et al*., 1998; Pecharsky *et al*., 2001; Pecharsky *et al*., 2002). In this chapter, we report the observation of short-range ferromagnetic correlations within the PM matrix, in cobalt substituted $Gd_5Si_2Ge_2$. The substitution of Co at the Si site has a strong influence on the structure and magnetic properties of $Gd_5Si_2Ge_2$ which is attributed to the stabilization of the O(I) component. The effect of Co substitution on the magnetocaloric behaviour of $Gd_5Si_2Ge_2$ is investigated and the universal scaling analysis based on magnetic entropy change is also applied to understand the nature of magnetic transition.

5.2. Experimental details

Polycrystalline ingots of $Gd_5Si_{2-x}Co_xGe_2$ with x= 0, 0.1, 0.2 and 0.4 were prepared by arc melting the constituent elements in a water cooled copper hearth in high purity argon atmosphere. The purity of the starting elements was 99.9 wt. % for Gd (Alfa Aesar) and 99.9999 wt. % for Ge (Alfa Aesar), Si (Alfa Aesar) and Co (Alfa Aesar). The ingots were turned over after each melting and remelted four times to ensure compositional homogeneity during melting. Weight loss of the samples after the arc-melting process was estimated to be less than 0.01%. As-cast ingots were sealed in evacuated quartz tubes and annealed at 1573 K for 1 hour and subsequently quenched in ice water. The crystal structure of all the samples were analyzed by powder XRD using PANalytical X'pert Pro diffractometer with Cu-Kα radiation operated at 40 kV and 30 mA at room temperature. The diffraction measurements were performed in the 2θ range 20° to 60° with a step size

of 0.017°. Rietveld refinement of the diffraction pattern was carried out using GSAS (General Structure Analysis System)-EXPGUI software (Toby *et al*., 2001). The low temperature powder X-ray diffraction measurements were done on an Oxford Cryosystems closed cycle helium cryostat (Model: PheniX) mounted on a vertical goniometer in a PANalytical Empyrean powder X-ray diffractometer with $CuK_{\alpha 1}$ *and* CuK_{α_2} radiations for 1 hour in the 2θ range 5° to 80° with a step size of 0.017°. The microstructural features were seen under Backscattered secondary electron (BSE) imaging mode by using scanning electron microscope (SEM) of Carl Zeiss Evo 18 equipped with an energy dispersive X-ray spectroscopy (EDS) system (Oxford EDAX X-Max^N). Qualitative analysis was carried out by EDS to know the chemical composition of these alloys. Differential scanning calorimetry was performed (PerkinElmer – Pyris 6) with a scanning rate of 5°C/min under nitrogen atmosphere. Electron spin resonance (ESR) measurements were obtained using JES – FA200 ESR Spectrometer (ESR-JEOL, Japan) at selected temperatures between 200 K and 320 K. Magnetization measurements were made as a function of both temperature and field using a PPMS up to a maximum field of 50 kOe in a temperature range 100-320 K. MCE was estimated, in terms of isothermal magnetic entropy change (ΔS_M), from Maxwell relations described in Chapter1 (Gschneidner *et al*., 2000; Gschneidner *et al*., 2005).

5.3. Results and Discussion

5.3.1. Structural Analysis

Figure 5.1 shows the X-ray diffraction patterns of $Gd_5Si_{2-x}Co_xGe_2$ with x= 0, 0.1, 0.2 and 0.4 at room temperature. All the compositions crystallize in a mixed state of monoclinic (M) $Gd_5Si_2Ge_2$ phase and O(I) Gd_5Si_4 phase at room temperature. The monoclinic $Gd_5Si_2Ge_2$ phase has been indexed with ICSD pattern No. 84084 (space group $P112_1/a$) while the O(I) Gd_5Si_4 structure has been indexed with ICSD pattern no. 84083 (space group Pnma). A small fraction of hexagonal (Hex) Gd_5Si_3 secondary phase is also present in our samples and has been indexed with ICSD pattern No. 99641 (space group $P6_3/mcm$). Rietveld refinement results shown in Figures 5.2-5.5 confirms the presence of monoclinic, O(I) and hexagonal phases in $Gd_5Si_{2-x}Co_xGe_2$ with x= 0, 0.1, 0.2 and 0.4. The lattice parameters extracted along with refinement parameters are summarized in Table 5.1. The presence of the secondary Gd_5Si_3 phase has been confirmed from SEM and EDS analysis of the samples and more details are discussed in the next section.

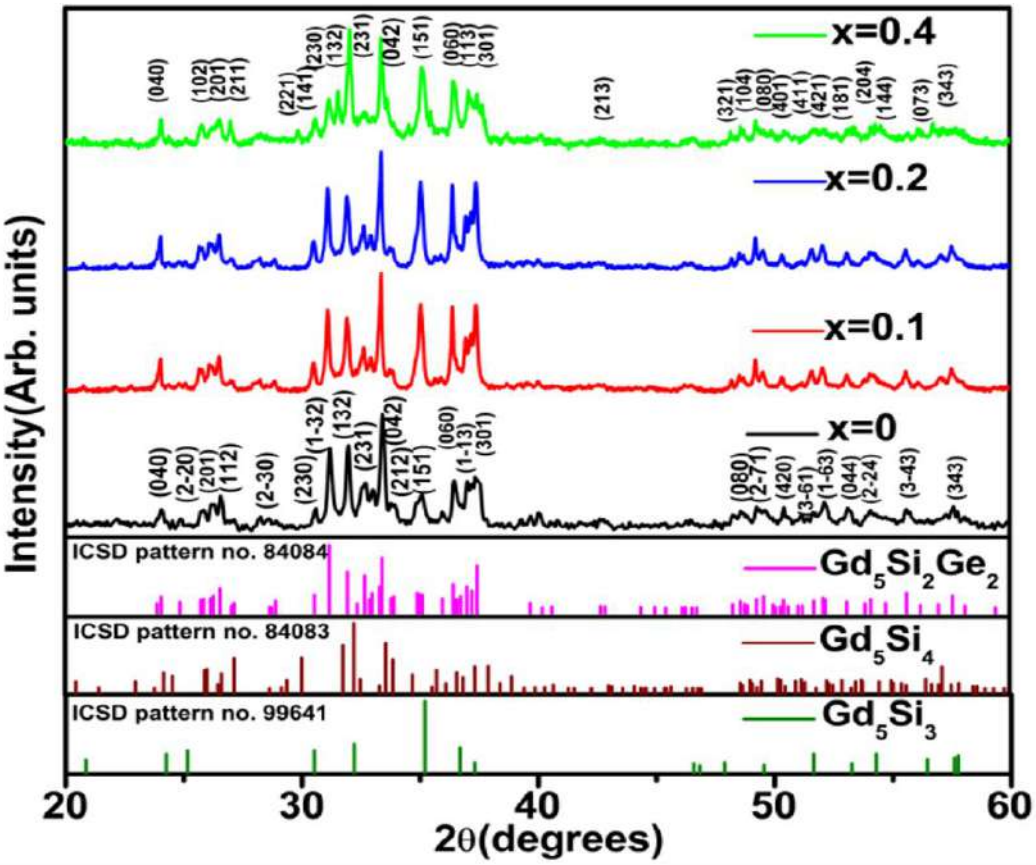

Figure 5.1. XRD patterns of $Gd_5Si_{2-x}Co_xGe_2$ with x= 0, 0.1, 0.2 and 0.4 at room temperature.

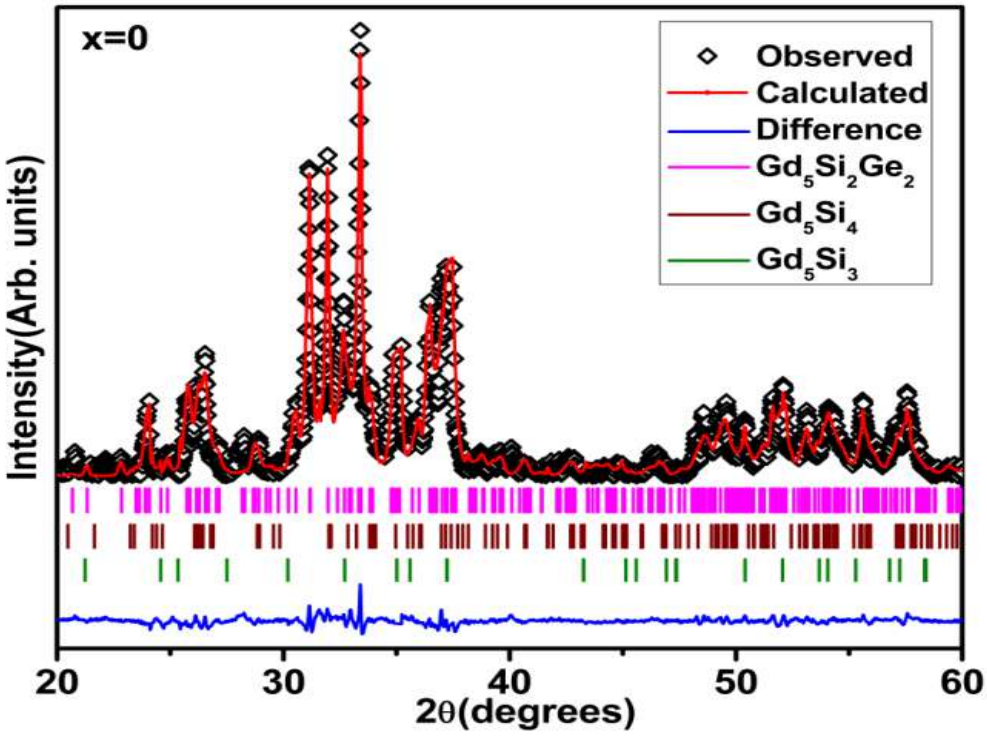

Figure 5.2. Rietveld refined XRD pattern of $Gd_5Si_2Ge_2$.

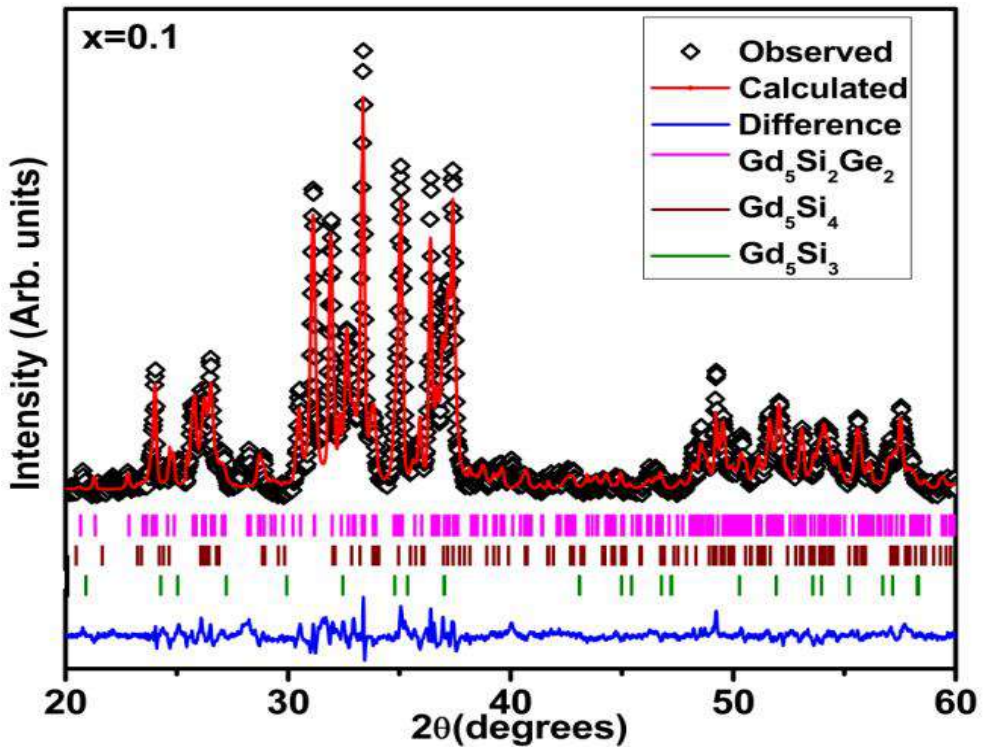

Figure 5.3. Rietveld refined XRD pattern of $Gd_5Si_{1.9}Co_{0.1}Ge_2$.

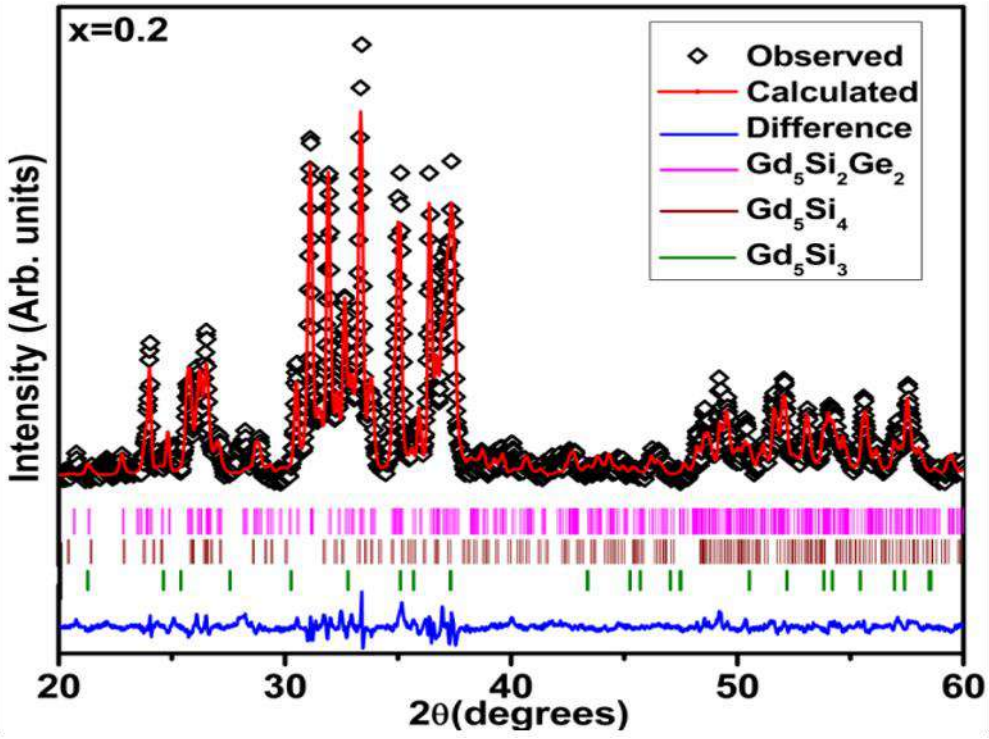

Figure 5.4. Rietveld refined XRD pattern of $Gd_5Si_{1.8}Co_{0.2}Ge_2$.

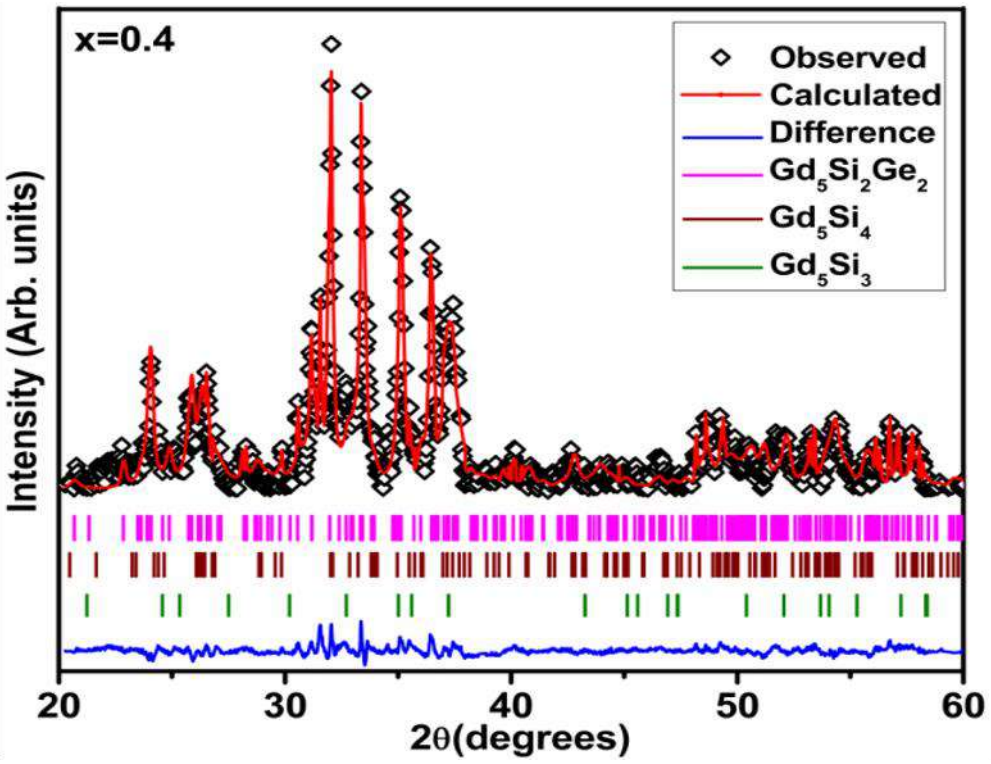

Figure 5.5. Rietveld refined XRD pattern of $Gd_5Si_{1.6}Co_{0.4}Ge_2$.

Table 5.1. Lattice parameters, unit cell volume, and reliability factors from the Rietveld refinement of $Gd_5Si_{2-x}Co_xGe_2$ with x= 0, 0.1, 0.2 and 0.4.

$Gd_5Si_{2-x}Co_xGe_2$	Crystal Structure	Space group	Lattice parameters					Residual Parameters	
			a (Å)	b (Å)	c (Å)	γ (deg)	Volume $(Å)^3$	R_{wp} %	R_p %
x = 0	M	$P112_1/a$	7.55(1)	14.75(1)	7.75 (1)	93.12(5)	862.28(6)	1.56	1.17
	O(I)	Pnma	7.66(2)	14.62(1)	7.53(1)	90	844.38(1)		
	H	$P6_3/mcm$	8.35(1)	8.35(1)	6.48(1)	120	391.22(7)		
x = 0.1	M	$P112_1/a$	7.58(1)	14.79(1)	7.77(1)	93.12(5)	869.44(6)	2.16	1.54
	O(I)	Pnma	7.59(2)	14.57(4)	7.64(2)	90	844.68(2)		
	H	$P6_3/mcm$	8.35 (1)	8.35(1)	6.48(1)	120	391.27(6)		
x = 0.2	M	$P112_1/a$	7.58 (1)	14.79(1)	7.77(1)	93.22(1)	870.38(5)	2.25	1.56
	O(I)	Pnma	7.49 (4)	14.69(1)	7.76(4)	90	853.96(5)		
	H	$P6_3/mcm$	8.35 (1)	8.35(1)	6.48(2)	120	391.59(1)		
x = 0.4	M	$P112_1/a$	7.58 (1)	14.80(1)	7.76(1)	93.21(4)	871.27(5)	1.96	1.41
	O(I)	Pnma	7.76(3)	14.78(4)	7.78(1)	90	868.15(4)		
	H	$P6_3/mcm$	8.58(1)	8.58(1)	6.27(3)	120	399.36(3)		

Figure 5.6 shows the XRD patterns of $Gd_5Si_{1.9}Co_{0.1}Ge_2$ compound at various temperatures in between 200 K and 300 K. At room temperature, the alloys exists in a combination of monoclinic, O(I) and hexagonal phases. As the temperature is decreased from 300 K, it can be seen that O(I) phase starts dominating in the system. This is evident at 255 K. The appearance of the peak corresponding to (230) at 30° at 255 K shows the presence of O(I) phase while the complete disappearance of the peak corresponding to (2-31) at 31.13° at 240 K shows the complete structural transformation of mixed M+O(I) phase to a single O(I) phase. The refined XRD patterns for 300 K and 200 K are shown in Figure 5.7 and the parameters extracted from the refinement are tabulated in Table 5.2.

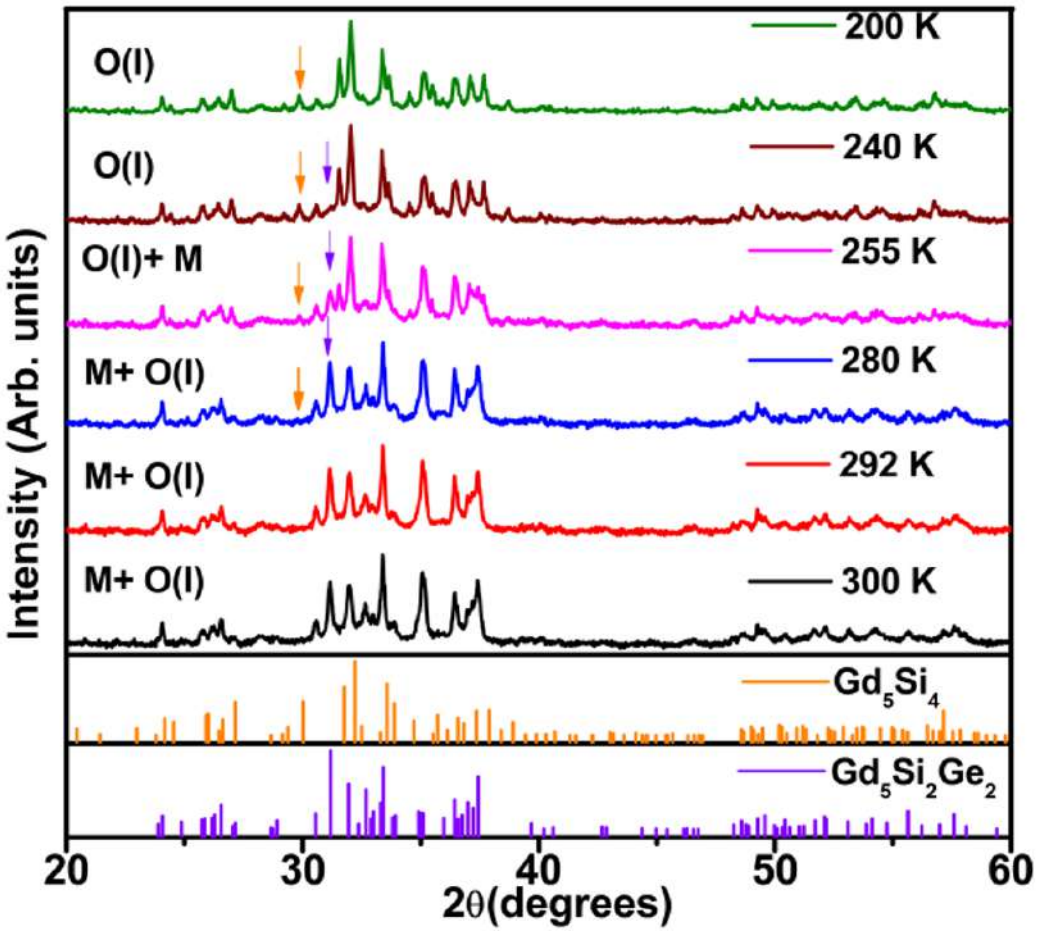

Figure 5.6. Temperature dependent XRD patterns of $Gd_5Si_{2-x}Co_xGe_2$ with x= 0.1.

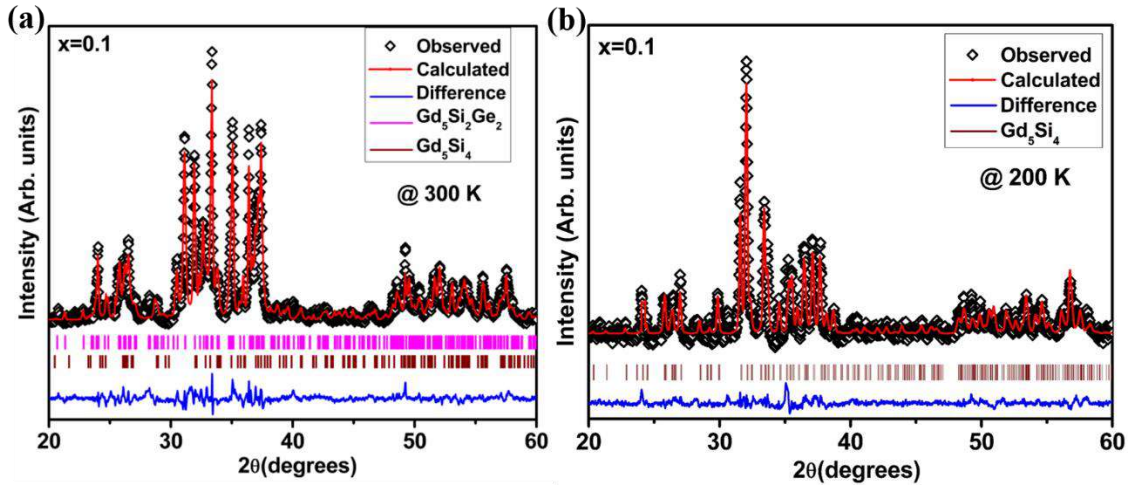

Figure 5.7. Temperature dependent XRD of $Gd_5Si_{2-x}Co_xGe_2$ with x= 0.1 at (a) 300 K and (b) 200 K.

Table 5.2. Lattice parameters and reliability factors from the Rietveld refinement of $Gd_5Si_{1.9}Co_{0.1}Ge_2$ at 300 K and 200 K.

$Gd_5Si_{1.9}Co_{0.1}Ge_2$	**300 K**			**200 K**
Crystal Structure	M + O(I) + H			O (I)
Space group	$P112_1/a$ + Pnma + $P6_3/mcm$			Pnma
Lattice Parameters				
a(Å)	7.58(1)	7.59(2)	8.35(1)	7.50(4)
b(Å)	14.79(1)	14.57(4)	8.35(1)	14.74(1)
c(Å)	7.77(1)	7.64(2)	6.48(1)	7.77(0)
γ(deg)	93.12(5)	90	120	90
Volume(Å)^3	869.44(6)	844.68(2)	391.27(6)	859.37(7)
Residual Parameters				
R_{wp}%	2.16			4.97
R_p%	1.54			3.44

5.3.2. SEM and TEM Analysis

The BSE micrographs of cobalt substituted $Gd_5Si_2Ge_2$ alloys are shown in Figures 5.8-5.10. The microstructures of the cobalt containing alloys display a multi-phase nature showing the presence of a brighter $Gd_5(Si,Ge)_4$ matrix phase (5:4-type with M + O(I) phases) along with darker $Gd_5(Si,Ge)_3$ (5:3-type) secondary phase. Elemental mapping analysis has been performed on all the samples and the results are presented in Figures 5.8-5.10. The EDS spectra of the matrix phase and darker grain boundary region for x=0.1 is shown in Figure 5.11. Elemental mapping reveals that cobalt is completely absent in the matrix phase but segregated into the grain boundary. The grain boundary phase is enriched with Si and Co as can be seen from Figures 5.8-5.10. The complete absence of Co in the dominant matrix phase 5:4, suggests that cobalt does not dissolve in the matrix but is primarily accumulated in the secondary 5:3 phase. A similar result has been observed for Fe substitution in $Gd_5(Si_xGe_{1-x})_4$ (Provenzano *et al*., 2001; Raj Kumar *et al*., 2009; Raj Kumar *et al*., 2010) and $Tb_5Si_2Ge_2$ (Pereire *et al*., 2011) wherein the substituted iron does not dissolve in the matrix but combines with silicon forming secondary phases. These results suggest that upon cobalt addition, it primarily combines with silicon giving rise to a grain boundary phase enriched with silicon and cobalt. The EDS results are summarized in Table 5.3. Moreover, the EDS results indicate that the 5:4 phase contains a greater concentration of Ge which results in the increase of lattice volume of the matrix phase (M + O(I)) with increase in Co substitution. This is concordant with our Rietveld refinement results shown in Table 5.1. From the SEM images, it is quite difficult to distinguish the presence of monoclinic and O(I) phases. Hence, to have a better understanding of the different matrix phases, we have carried out the High-Resolution Transmission electron microscopy (HRTEM) analysis on the substituted samples $Gd_5Si_{2-x}Co_xGe_2$ with x= 0, 0.1, 0.2 and 0.4 and the results are depicted in Figure 5.12.

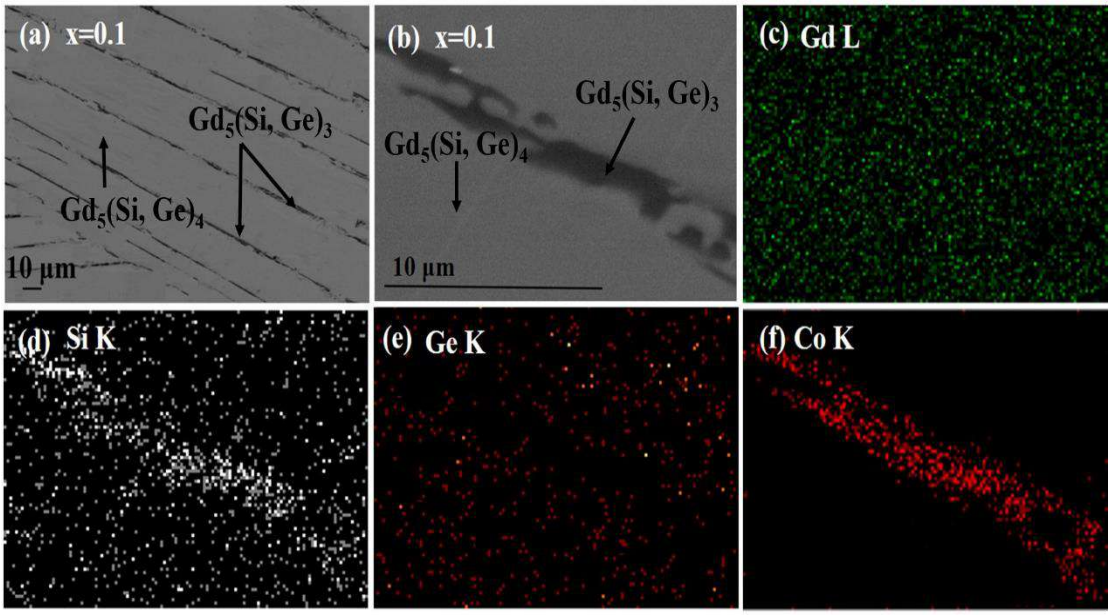

Figure 5.8. Backscattered SEM images of $Gd_5Si_{2-x}Ge_2Co_x$ alloys for (a) x=0.1 at low magnification (b) x=0.1 at high magnification (c) Gd mapping (d) Si mapping (e) Ge mapping and (f) Co mapping [Matrix phase is 5:4-type, Dark phase is 5:3-type].

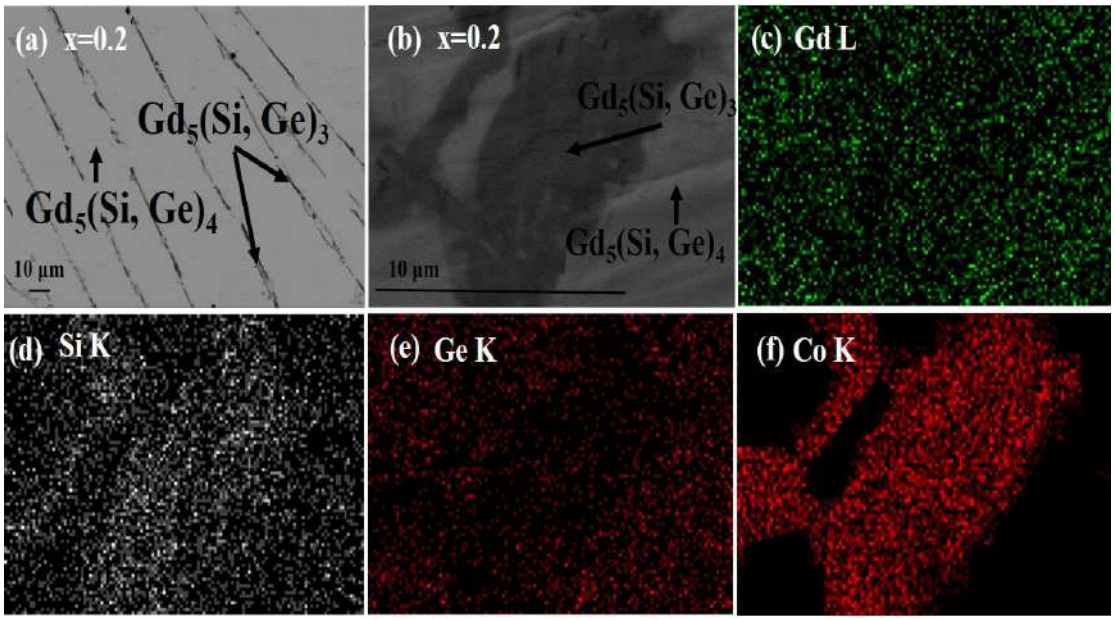

Figure 5.9. Backscattered SEM images of $Gd_5Si_{2-x}Ge_2Co_x$ alloys for (a) x=0.2 at low magnification (b) x=0.2 at high magnification (c) Gd mapping (d) Si mapping (e) Ge mapping and (f) Co mapping [Matrix phase is 5:4-type, Dark phase is 5:3-type].

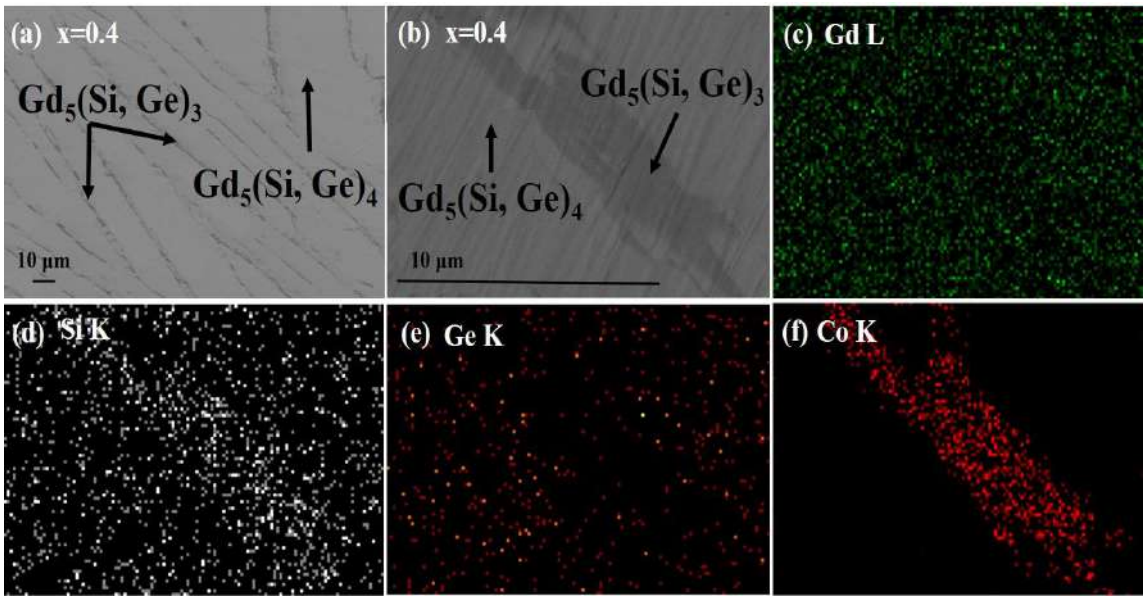

Figure 5.10. Backscattered SEM images of $Gd_5Si_{2-x}Ge_2Co_x$ alloys for (a) x=0.4 at low magnification (b) x=0.4 at high magnification (c) Gd mapping (d) Si mapping (e) Ge mapping and (f) Co mapping [Matrix phase is 5:4-type, Dark phase is 5:3-type].

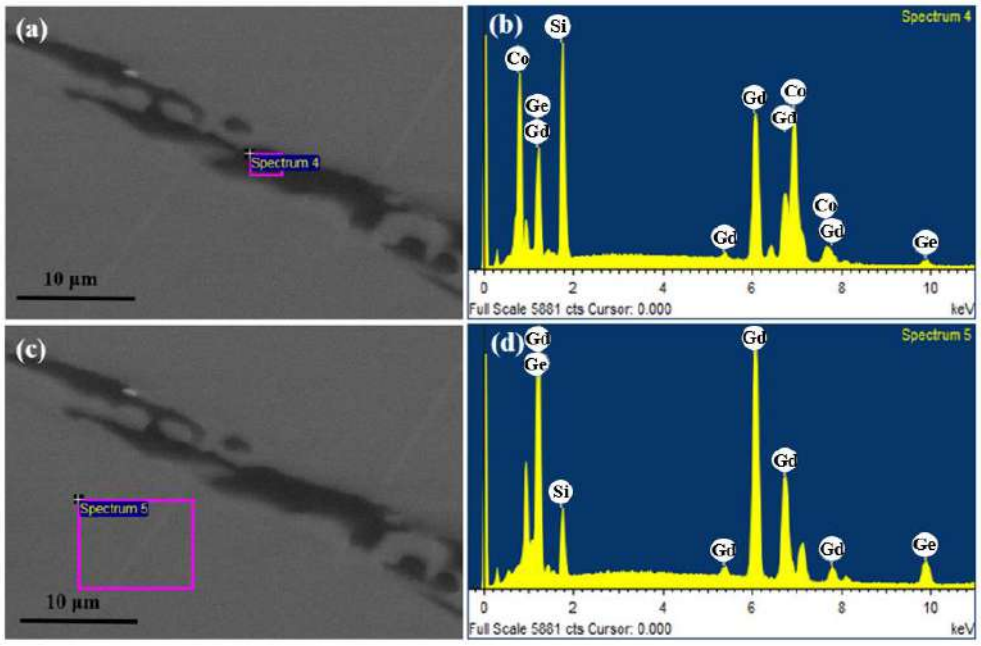

Figure 5.11. (a) Backscattered Electron image of x=0.1 in (a) the dark grain boundary region and (b) corresponding EDS spectra (c) Matrix phase and (d)corresponding EDS spectra.

Table 5.3. Compositions of $Gd_5Si_{2-x}Co_xGe_2$ with x= 0.1, 0.2 and 0.4 determined by EDS analysis. The estimated error in determining the concentration of each element is 0.1 at%.

x	Phase	Composition (at %)				Phase type
		Gd	Si	Ge	Co	
0	Matrix	55.08	22.13	22.79	-	5:4
	Grain Boundary phase	62.03	22.28	15.9	-	5:3
0.1	Matrix	55.13	20.53	24.34	-	5:4
	Grain Boundary phase	62.06	21.24	15.74	0.96	5:3
0.2	Matrix	55.48	20.5	24.02	-	5:4
	Grain Boundary phase	62.53	20.98	14.48	2.01	5:3
0.4	Matrix	55.93	20.36	23.71	-	5:4
	Grain Boundary phase	62.87	19.96	13.39	3.78	5:3

The dominant planes seen in the high-resolution bright field images matches with the planes of the monoclinic and O(I) phases. The d spacing of these planes measured from the TEM images match with the calculated values of the corresponding planes. SAED patterns recorded shows a spotty nature. The d values corresponding to these spots and the corresponding SAED patterns are indexed as shown in Figure 5.12.

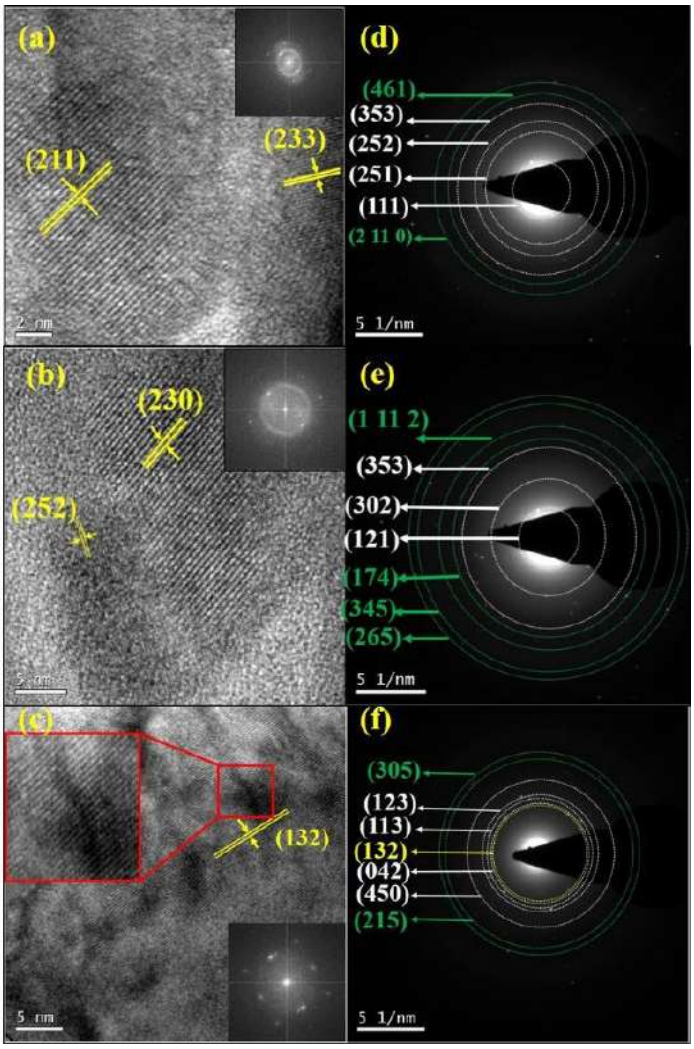

Figure 5.12. HRTEM images of the samples $Gd_5Si_{2-x}Co_xGe_2$ with (a) x= 0.1, (b) x=0.2 and (c) x=0.4 (An enlarged view of the lattice plane is also shown for x=0.4). Inset shows the corresponding FFTs. SAED patterns obtained for (d) x= 0.1, (e) x=0.2 and (f) x=0.4 (circles are a guide to the eye, white circle indicate planes corresponding to $Gd_5Si_2Ge_2$ phase and green circles indicate planes corresponding to Gd_5Si_4 phase).

5.3.3. DSC Measurements

Figure 5.13 shows the DSC curves of $Gd_5Si_{2-x}Co_xGe_2$ with x= 0.1, 0.2 and 0.4 during heating and cooling cycles. During heating, all the compounds show an endothermic dip, and an exothermic peak on cooling. The dips at 259 K, 248 K and 227 K for x=0.1, 0.2 and 0.4 during heating is attributed to a FOPT from an O(I) phase to a monoclinic phase (Fu *et al*., 2006). Furthermore, it can be noted that the phase transformation is completely reversible during the following cooling cycle. XRD,

together with DSC results, indicate that $Gd_5Si_{2-x}Co_xGe_2$ samples with x= 0.1, 0.2 and 0.4 undergoes a first-order structural phase transition on temperature change. The transition temperatures decrease with an increase in Co content up to x = 0.4.

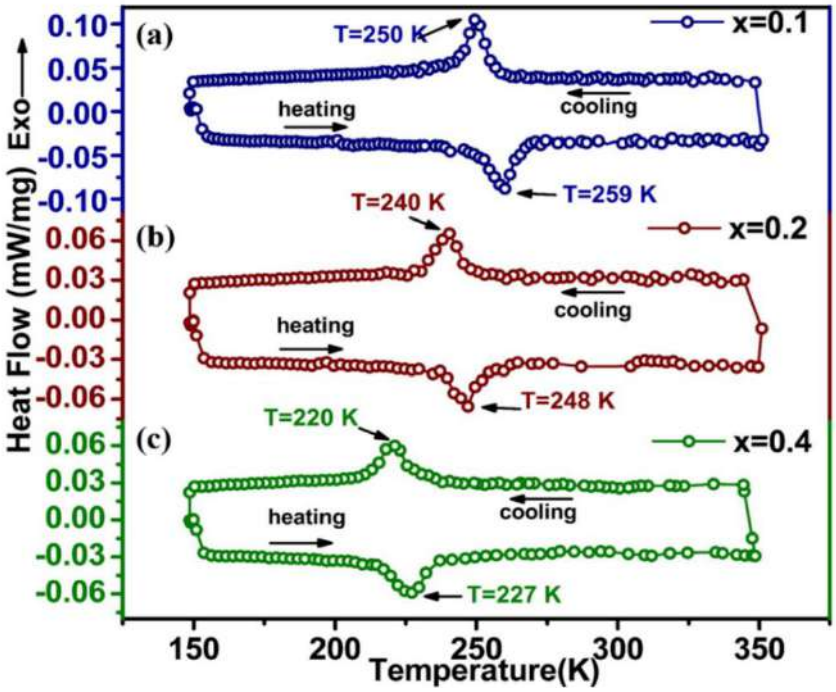

Figure 5.13. DSC scans of $Gd_5Si_{2-x}Co_xGe_2$ samples with (a) x= 0.1, (b) x= 0.2 and (c) x= 0.4.

5.3.4. Magnetic characterization

Figure 5.14 shows the temperature dependent magnetization (M-T) data taken in the Field-Cooled-Cool (FCC) and Field-Cooled-Warm (FCW) modes in an applied field of 500 Oe for x=0.1, 0.2 and 0.4. Two transitions are observed in the magnetization data for both the samples. For x=0.1, the first one at 292 K indicates a second order phase transition from O(I) FM phase to O(I) PM phase on heating. The second transition occurs at 255 K and it is a first order transition from O(I) FM phase to monoclinic PM phase as is evident from the hysteresis between the FCC and FCW data on heating. Similarly, for x=0.2, the first transition at 291 K corresponds to a second order magnetic phase transition while the second transition at 240 K is a first-order structural phase transition induced by magnetic field. The M-T results are concordant with our XRD results showing the presence of two phases coexisting in the system at room temperature giving rise to two sets of phase transitions in the system. The decrease in Curie temperature with cobalt

substitution could be attributed to the change in the Si:Ge ratio of the matrix phase as evident from the EDS results.

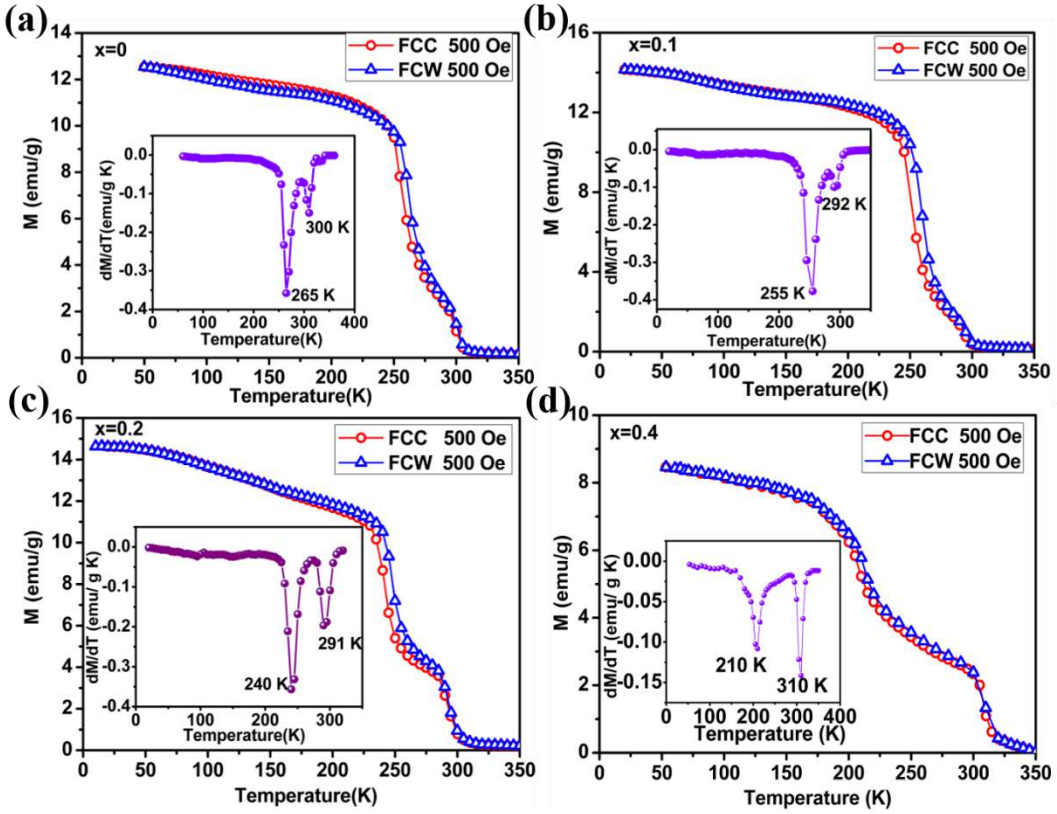

Figure 5.14. M-T curves of $Gd_5Si_{2-x}Co_xGe_2$ with x= 0, 0.1, 0.2 and 0.4 alloys measured in a magnetic field of 500 Oe during FCC and FCW processes.

M-T measurements have also been carried out in the substituted samples at different fields of 100 Oe, 500 Oe, 1000 Oe, 5000 Oe and 10000 Oe and are shown in Figure 5.15(a)-5.15(c). The smearing out of phase transitions at higher magnetic fields is clearly visible which is due to the masking of the FM signal by the rising PM background (Deisenhofer *et al*., 2005). Figure 5.15(d)-5.15(f) shows the inverse susceptibility (χ^{-1}) at different fields of 100 Oe, 500 Oe, 1000 Oe, 5000 Oe and 10000 Oe. At higher temperatures, the linear behavior of χ^{-1} with temperature indicates that χ^{-1} obeys the Curie–Weiss (CW) law, $M/H=C/(T-\theta_P)$. At large applied magnetic fields, the FM component is suppressed in the PM matrix, and the CW law is obeyed throughout the PM region and yields a PM Weiss temperature, θ_P of 260 K, 264 K, 234 K respectively for x=0.1, 0.2 and 0.4. The positive value of θ_P indicates that FM interactions are dominant in this compound. A clear deviation from CW behavior is observed for a small applied

magnetic field below a particular temperature. This is similar to the previous observations in Griffiths like phases (Magen *et al*., 2006; Pereira *et al*., 2010; Ouyang *et al*., 2010). The temperature of deviation is denoted as the Griffiths temperature T_G, and is shown in Figure 5.15(d)-5.15(f). The downturn below T_G is a signature of GP, a unique feature exhibited by magnetic materials which show a strong correlation between structural and magnetic properties. This is usually reflected as a downturn in χ^{-1} as a function of temperature above T_C. On increasing the magnetic field, the anomaly in χ^{-1} is suppressed and becomes nearly indistinguishable from the values at high temperature. It can be seen that with an increase in Co concentration to 0.4, the GP are not suppressed even at 10000 Oe, suggesting that higher fields are necessary for their complete suppression.

In the original model, Griffiths considered the percolative nature of a random Ising ferromagnet having nearest neighbor exchange interaction with strength *J* and 0 distributed randomly with probability *p* and 1 - *p*, respectively. That is, above the ferromagnetic transition point in a disordered system, there is always a finite probability of finding an arbitrary large ferromagnetic cluster. For $p<p_c$, there is no long-range FM order. Here p_c is the precolative threshold. Above p_c, the FM phase exists in a weakened form by the shortage of percolation path and hence, thermal fluctuations will destroy the FM phase at a temperature T_C, which is lower than the magnetic ordering temperature (T_G) of the undiluted/pure FM system. The region, $T_C < T < T_G$, where the system is characterized by the coexistence of FM clusters within the PM matrix, is referred to as the Griffiths phase regime. In this temperature regime, χ^{-1} could deviate from its expected Curie-Weiss linear behaviour. This deviation starts, exactly at T_G, on cooling the diluted system, as if the system somehow recalled that its magnetic ordering temperature was T_G before it became diluted (Griffiths, 1969; Bray, 1987; Vojta, 2006). The basic characteristic of the GP regime ($T_C < T < T_G$) is that in this regime due to the absence of long-range FM order, the spontaneous magnetization is zero (Sampathkumaran *et al*., 2007).

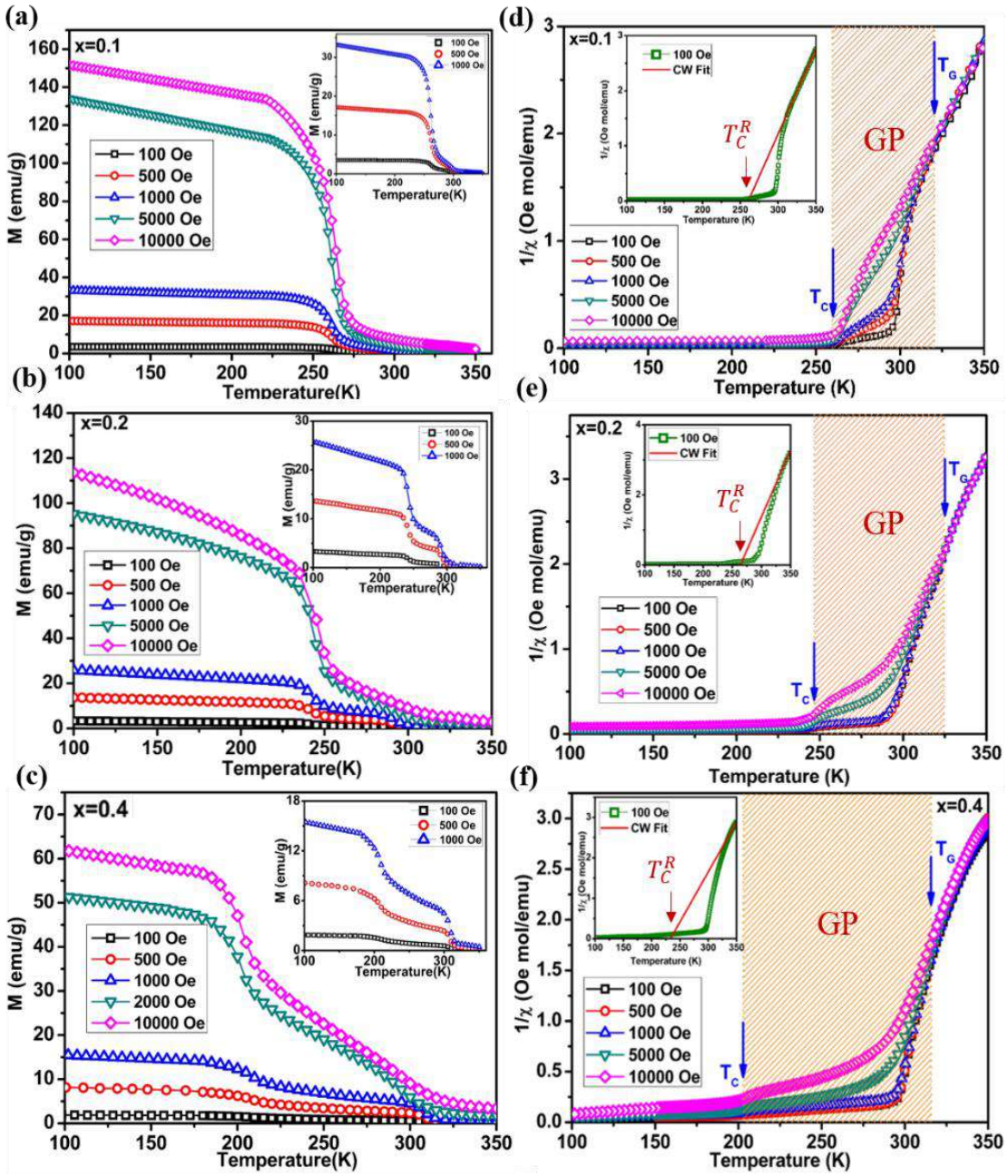

Figure 5.15. M-T curves of $Gd_5Si_{2-x}Co_xGe_2$ with (a) x= 0.1 (b) x=0.2 and (c)x=0.4 alloys measured at different fields of 100 Oe, 500 Oe, 1000 Oe, 5000 Oe and 10000 Oe and Figure 5.15. (d-f) shows the corresponding χ^{-1} versus T curves. Inset shows the Curie-Wiess Fit

In the classical Griffiths model, the exchange bonds are broken randomly but, being broken, they remain fixed relative to the crystallographic lattice. Similar observations have been made in substituted manganites. In the case of substituted manganites, GP arises mainly due to two reasons: size mismatch and due to the change in the nature of the double exchange interaction between Mn^{3+}-Mn^{4+} due to the

introduction of new cations at the A site. For example, in $La_{1-x}B_xMnO_3$ where B=Ca, Sr, Ba, (Deisenhofer *et al*., 2005; Jiang *et al*., 2008) the source of the disorder is the random substitution of La^{3+} by ions with different sizes and valence states. The probability p, for the existence of a FM bond increases with x, because the increasing number of Mn^{3+}-Mn^{4+}pairs enhances the double-exchange (DE) driven FM interaction. Because of the static Jahn-Teller (JT) distortion of the Mn^{3+} ions, the non-JT active Mn^{4+} ions and the FM bonds can be regarded as fixed within the lattice resulting in quenched disorder, which results in the development of the GP (Krivoruchko *et al*., 2010; Krivoruchko *et al*., 2014).

In $R_5(Si_xGe_{1-x})_4$ (R=rare earth), the appearance of this regime is attributed to the strong interplay between structure and magnetism present in these materials. Their complex nanostructured crystalline structure is formed by the stacking of rigid two dimensional slabs of R and T=Si/Ge. At the interface between these two building blocks, the formation/rupture of Si(Ge)-Si(Ge) dimers linked through covalent bonds occur. The actual crystallographic phase and nature of the magnetic interactions are controlled by the number of inter-layer covalent-like T-T bonds connecting the slabs, which results in the development of two different magnetic interactions in the system. The intra-slab magnetic exchange interaction, J_{intra} is ruled by the conventional 4*f*-4*f* Ruderman-Kittel-Kasuya-Yosida (RKKY) indirect exchange, and the inter-slab magnetic interactions J_{inter} are influenced by an additional *R*-*T*-*T*-*R* superexchange interaction via the existing *T*-*T* bonds ([a]Pecharsky *et al*., 2002). The intra-layer magnetic structure is essentially FM. On the other hand, depending on the number of inter-slab pairs which are covalently bonded (Pereira *et al*., 2010), the inter-layer coupling tends to be either FM or AFM. Hence, in $R_5(Si_xGe_{1-x})_4$ compounds, GP originates from the local disorder within the crystallographic lattice, which is stabilized and enhanced by the competing inter-layer and intra-layer magnetic interactions. The disorder is linked to the percolation mechanism where, Ge substitution for Si results in the breakdown of FM order. When Ge is absent, or its concentration is such that $x > x_p$ (x_p is defined as the critical Si concentration), the system stabilizes in the O(I) structure where all the inter-slab bonds are formed and the system has a FM character. At $x = x_p$, the Ge atoms start substituting Si atoms at the inter-slab sites, i.e., the system becomes more diluted. This promotes an increase in the distance

between consecutive slabs due to the higher atomic radius of Ge and the inter-slab covalent bonds begin to break leading to the destruction of the FM order and a decrease of the magnetic exchange energy resulting in a decrease in T_C. When a critical Ge concentration limit is reached (x_c), the RKKY interaction becomes negative and consequently, the antiferromagnetic state becomes the most stable one as beyond x_c, it is not possible to achieve long-range FM order. The existence of the two competing interactions J_{intra} and J_{inter} leads to the enhancement of the FM short-range correlations. Hence, it can be stated that in $R_5(Si_xGe_{1-x})_4$ compounds exhibiting GP, there is a strong competition between the M and O(I) phases. In the case of Co substituted $Gd_5Si_{2-x}Co_xGe_2$ compounds, the substitution of Co at the Si site results in the decrease of Si concentration in the system resulting in more dilution of the system. With increase in Co substitution, there is an increase in the O(I) component. As a result, due to the presence of two different phases coexisting in the system, nanometric regions of orthorhombic character with strengthened FM interactions are likely to be formed. These nanometric clusters with enhanced FM interactions are responsible for the appearance of GP. The decrease in T_C with Co substitution is attributed to the increase in Ge concentration in the matrix phase, which results in the rupturing of inter slab bonds due to the large size of Ge resulting in the decrease of magnetic exchange interactions and consequently a decrease in Tc is observed.

Usually, the susceptibility of a GP at low fields follows the power law

$$\chi^{-1}(T) \propto \left(\frac{T}{T_C^R} - 1 \right)^{1-\lambda} \qquad (5.1)$$

where λ is the magnetic susceptibility exponent ($0 \leq \lambda < 1$) and T_C^R is the random critical temperature (Pereira *et al.*, 2010; Ouyang *et al.*, 2010). T_C^R is taken as the temperature for which the equation yields a λ (λ_{PM}) value close to zero above T_G. The linear part of the plot ln (χ^{-1}) vs ln(T/T_C^R -1) is fitted with the power law, and the estimated susceptibility exponent values are shown in Figure 5.16. The value of λ lies in between 0 and 1 and decreases with increase in the field, a signature of GP. This behaviour is seen in similar compounds such as $Tb_5Si_2Ge_2$ (Pereira *et al.*, 2010) and Gd_5Ge_4 (Ouyang *et al.*, 2006) typical of short-range FM clusters in a PM matrix and is the hallmark of Griffith's singularities. As the Co substitution increases from x=0.1 to x=0.4, it can be seen that the value of λ also increases from 0.54 to 0.79 for 100 Oe and 0.31 to 0.61 for 10000 Oe

clearly suggesting an increase in the FM component within the PM matrix with Co substitution. The increase in the value of λ for Co substituted samples suggests an increase in the strength of GP. However, a thorough understanding of these short-range correlations would require small angle neutron scattering or muon spin rotation measurements (Sampathkumaran *et al*., 2007).

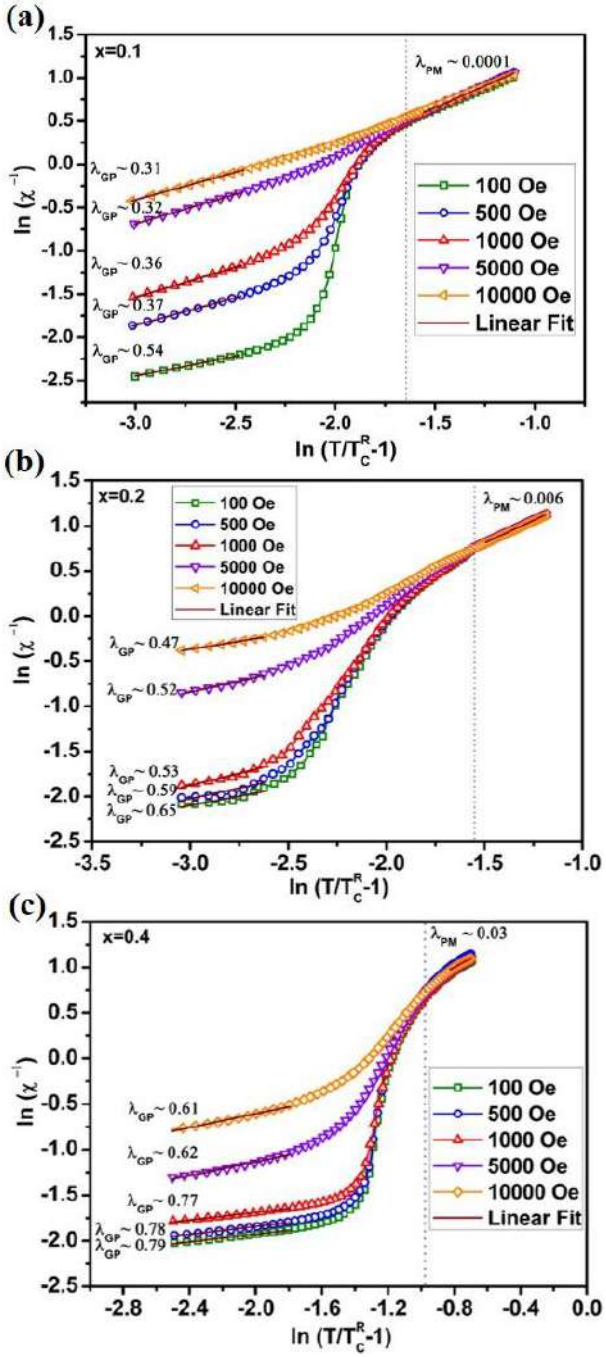

Figure 5.16. Griffiths Analysis of $Gd_5Si_{2-x}Co_xGe_2$ with (a) x= 0.1 (b) x=0.2 and (c) x=0.4.

5.3.5. ESR studies

ESR is an effective tool to probe the local and microscopic magnetic states of materials. The ESR spectra of $Gd_5Si_{1.9}Co_{0.1}Ge_2$ were recorded at various temperatures and is presented in Figure 5.17 as a representative of the series. It can be seen that the ESR spectrum is asymmetrically distorted below T_C. The temperature-dependent ESR results show that at high temperatures T=320 K, the spectra shows only one resonance with a well-characterized Lorentian line shape. In the intermediate temperatures 240 K< T< 293 K, there are two rather distinct lines and at low temperatures T <240 K, the paramagnetic resonance peak vanishes completely. When approaching T_C, the ESR spectra show a small shift toward higher fields and becomes less asymmetrical. Above T_C, however, the spectra broaden and become more symmetrical with increasing temperature (Oates *et al*., 2002; Pires *et al*., 2005; Pires *et al*., 2006). The spectrum at 320 K shows a single resonance line with a Lorentzian shape at resonance field of 323 mT. When the temperature is lowered further, two resonance peaks appear, one at the higher resonance field corresponds to a PM phase and the other at a lower field corresponds to the FM phase. This is due to the appearance of short-range spin ordering or FM magnetic clusters between T_G and T_C. As the temperature is decreased further, FM correlations grow at the expense of PM interactions and a complete PM–FM transition occurs below ~280 K. This is designated by the shift of the shoulder toward further lower-field region of the spectrum.

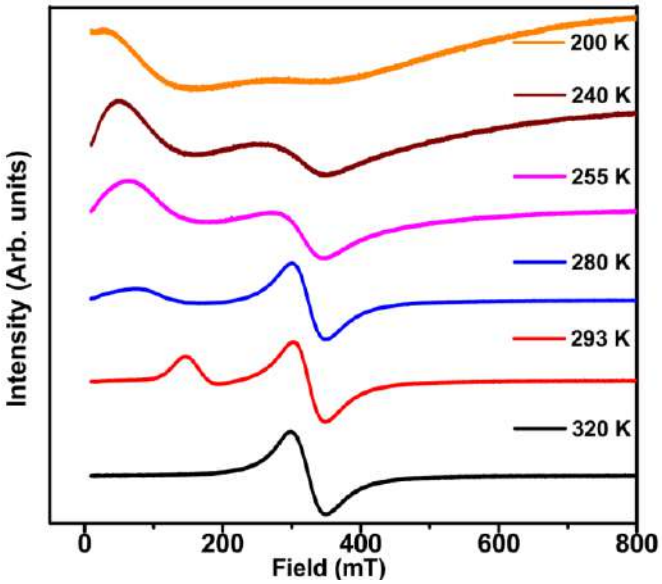

Figure 5.17. Temperature dependent ESR spectra of $Gd_5Si_{2-x}Co_xGe_2$ with x= 0.1.

5.3.6. Magnetocaloric effect

Isothermal magnetization measurements were carried out in the temperature range of 200−320 K with a temperature interval of 5 K for the alloy samples with x=0.1, 0.2 and 0.4. The field was swept from 0-50 kOe and back to 0 Oe for M-H measurement at a particular temperature, and the results are shown in Figures 5.18(a)-5.18(c). It can be noted from Figures 5.18(a)-5.18(c) that, there is a considerable magnetic hysteresis in the vicinity of the ordering temperature. This hysteresis is due to a field induced first order crystallographic phase change from monoclinic PM phase to O(I) FM phase. The field-induced phase transition reverses upon decreasing the field, suggesting the reversible character of the structural transition, at which the structure of the alloy returns to its initial state once the magnetic field is completely removed (Shull *et al*., 2006). It can be seen that the hysteresis is maximum in the vicinity of T_C, where the structural transition occurs. However, it should be noted that in addition to FOPT, second order phase transition (SOPT) is also present in the system as is evident from the M-T curves. The XRD results also confirm the co-existence of monoclinic and O(I) phases in the system. It can be seen that with increase in Co concentration, there is a reduction in the thermal hysteresis. This is attributed to the increase in the O(I) component, which is responsible for reducing the first order nature of the phase transition. Thus, Co substitution at the Si site in $Gd_5Si_2Ge_2$ favors the formation of the O(I) phase, thereby reducing the hysteresis loss. The Arrott plots (M^2 versus H/M) for all the compositions with x=0.1, 0.2 and 0.4 are plotted in Figure 5.18(d)-5.18(f). The order of magnetic transition can be determined from the slope of the isotherm plot (Banerjee *et al*., 1964). The negative slope in the Arrott plots is a clear indication of the presence of first-order phase transition in these compounds while a positive slope corresponds to a second order transition. For x=0.1 and x=0.2, the Arrott plots indicate a negative slope confirming that first order nature of phase transition is present while for x=0.4, the Arrott plots clearly show the transformation from first order to second order. Hence, it can be acclaimed that as Co concentration increases, the compounds mainly stabilise in the O(I) phase indicating that second order transition is more likely to take place.

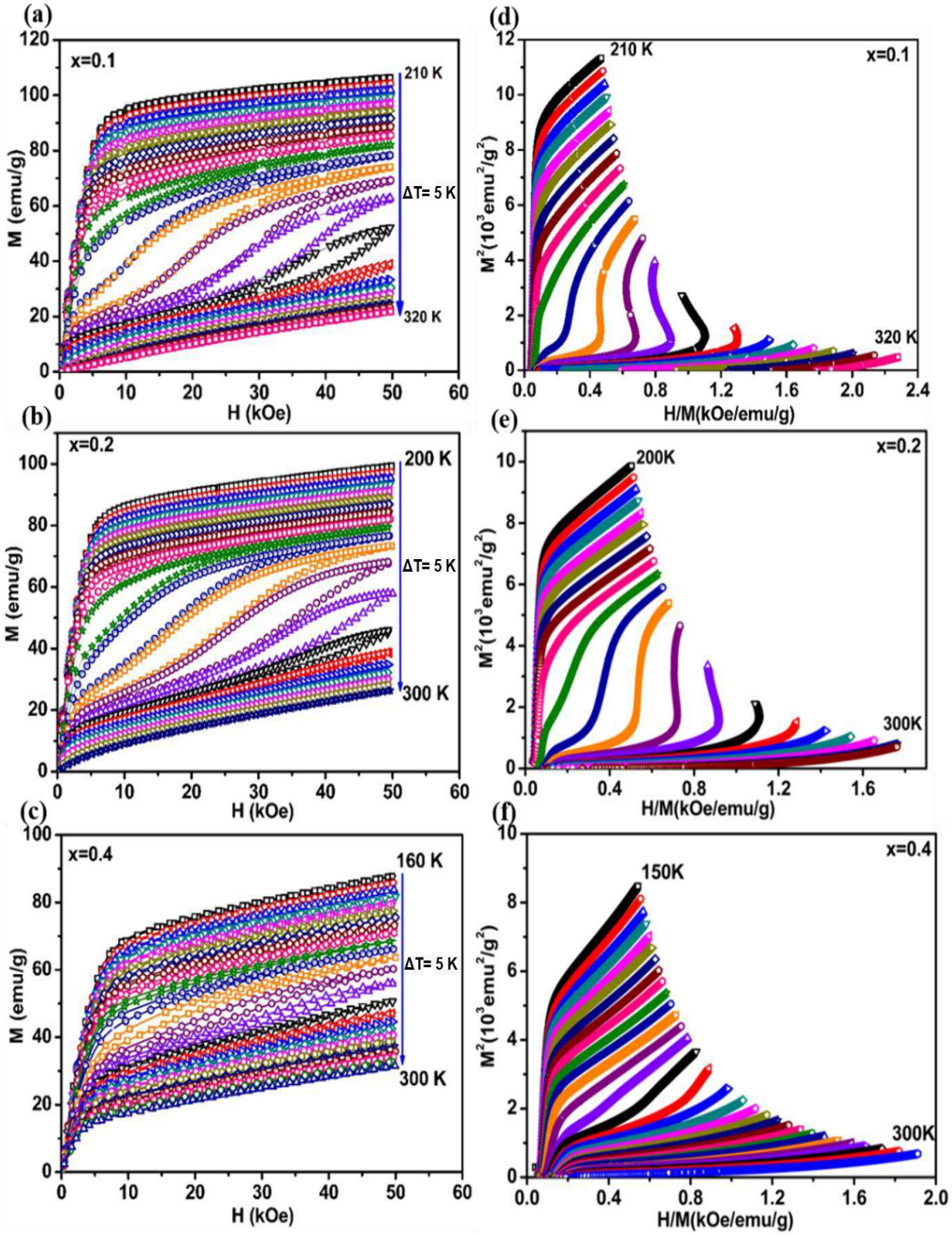

Figure 5.18. Field dependence of magnetization at different temperatures for $Gd_5Si_{2-x}Co_xGe_2$ (a) x= 0.1, (b) x= 0.2 and (c) x=0.4 and the Arrott plots for (d) x= 0.1, (e) x= 0.2 and (f) x=0.4.

MCE in these compounds has been evaluated from the isothermal magnetization data using the thermodynamic Maxwell relations (Chapter1). Figures 5.19 (a)-5.19 (c)

represent the change in magnetic entropy (ΔS_M) as a function of temperature under different magnetic fields for x= 0.1, 0.2 and 0.4 respectively. All the curves show a broad maximum of $-\Delta S_M$ around their respective T_C. The value of $-\Delta S_M$ peak increases with the field and the peak position remain nearly unaffected. Under a magnetic field variation of 50 kOe, the maximum magnetic entropy change for $Gd_5Si_{2-x}Co_xGe_2$ are 9, 8.5 and 4.2 J/kg K for x=0.1, 0.2 and 0.4 respectively. It can be seen that with increase in Co substitution, the $-\Delta S_M$ peak broadens. Also, there is a reduction in the magnetic entropy change with increase in Co substitution. This is attributed to the presence of combined phases in the system and the increase of the O(I) component with increase in Co concentration. MCE is positive over the entire temperature range as in the case for FM materials because of magnetic ordering phenomenon with the application of the magnetic field (Samanta *et al*., 2007). However, it can be seen that even though there are two transitions in the magnetization measurements, the magnetic entropy change is concentrated only in the vicinity of the first order transition region. This suggests that the entropy change associated with the second order phase transition is negligible and the isothermal entropy change is maximum around the first order transition region.

The RC and RCP has been calculated using equations (1.25) and (1.26) described in Chapter 1. The RC values obtained for x= 0.1, 0.2 and 0.4 for a field change of 50 kOe are 200, 185 and 75 J/kg. The RCP values obtained for x= 0.1, 0.2 and 0.4 for a field change of 50 kOe are 257, 204 and 106 J/kg respectively. It is to be noted that the hysteresis loss has been accounted while calculating the effective RC and RCP. The variations of effective RC and RCP as a function of field are shown in Figure 5.19 (d). The transition temperatures of the M and O(I) phases, thermal hysteresis, magnetic hysteresis, entropy changes, and the effective RC and RCP values are tabulated in Table 5.4. Co substituted compounds exhibit much higher RCP values and their operating temperature could be tuned to the desired temperature, suggesting that these compounds could be used for sub-room temperature magnetic refrigeration applications.

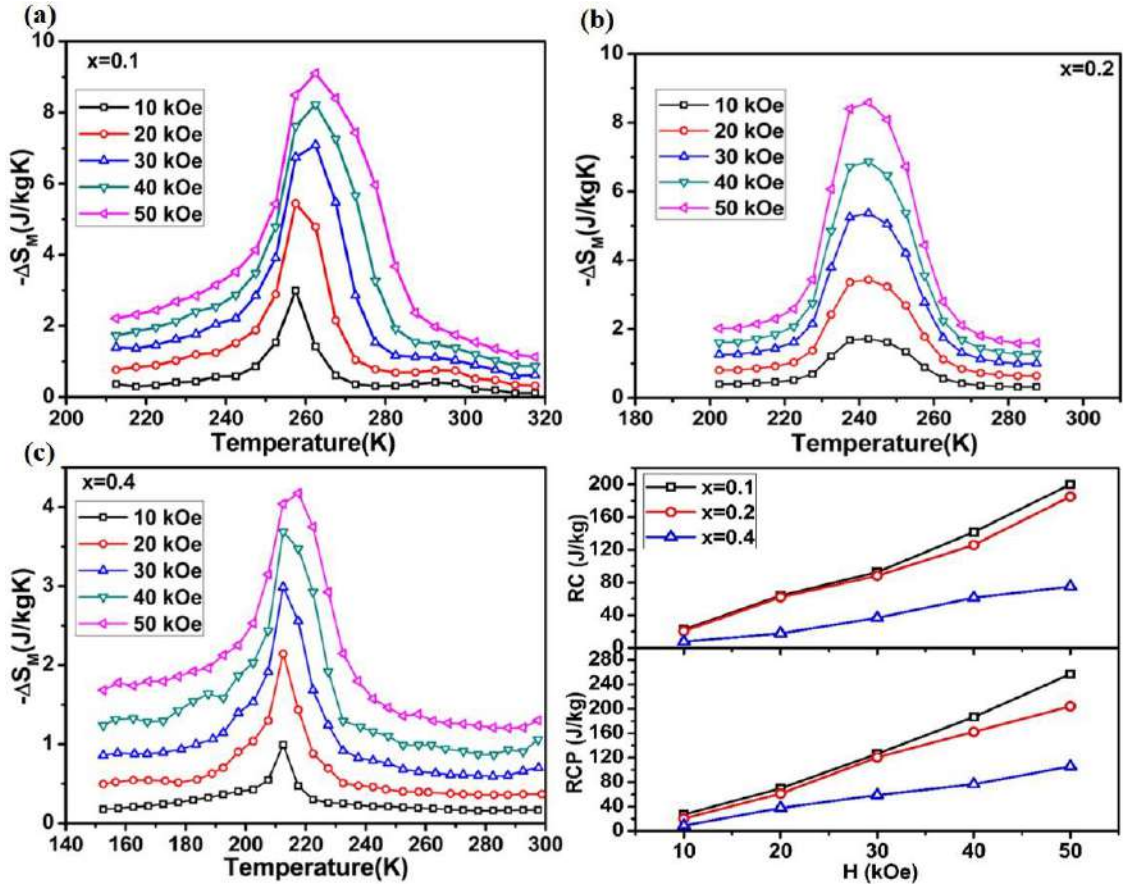

Figure 5.19. Isothermal magnetic entropy change (ΔS_M) of $Gd_5Si_{2-x}Co_xGe_2$ (a) x= 0.1, (b) x= 0.2 as a function of temperature for different field changes (d) Variation of effective RC and RCP with field for $Gd_5Si_{2-x}Co_xGe_2$ with x=0.1, 0.2 and 0.4.

Table 5.4. Transition temperatures, thermal hysteresis, magnetic hysteresis, entropy changes, effective refrigerant capacity, and relative cooling power calculated for $Gd_5Si_{2-x}Co_xGe_2$

x	Transition temperature	Thermal Hysteresis (K)	Magnetic Hysteresis at 50 kOe (J/kg)	$-\Delta S_M$ (J/kgK) ΔH=50 kOe	Effective RCP (J/kg) H=50 kOe	Effective RC (J/kg) H=50 kOe
0.1	255	5	35	9	257	200
0.2	240	5	24	8.5	204	185
0.4	210	4	10	4.2	106	75

5.3.7. Universal Curve Analysis

The Universal curves depicted in Figures 5.20(a)-5.20(c) show a transformation of phase transition from first order to second order. In Figure 5.20., it is evident that the curves do not collapse, for temperatures below T_C, indicating the first order nature of phase transition.

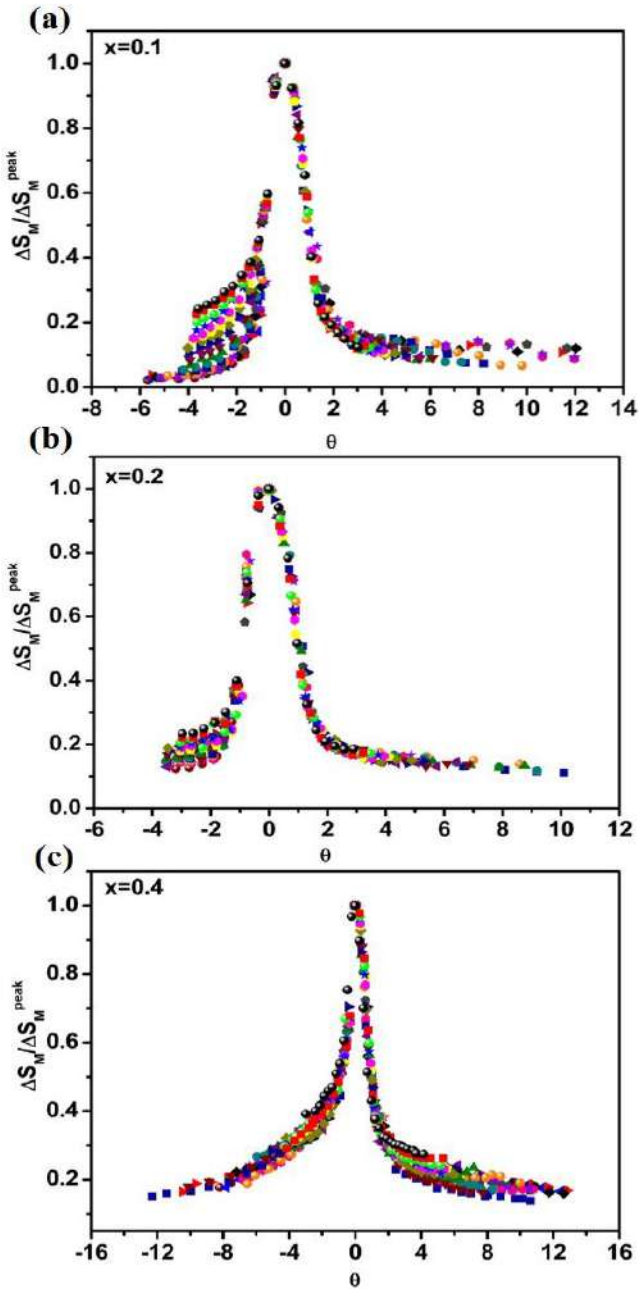

Figure 5.20. Normalized entropy change as a function of the rescaled temperature θ for (a) x=0.1, (b) x=0.2 and (c) x=0.4.

For x=0.1, the divergence of the curves above the T_C is evident. As the cobalt concentration increases to x=0.4, a gradual trend towards collapse can be seen which corresponds to the weakening of the first order transition. This is concordant with the trends observed in the Arrott plots shown in Fig. 5.18(d)-5.18(f). In the range, $-1 < \theta < 0$, the collapse is real for second order transitions and is only apparent for first order transitions. For temperatures above T_C, it can be seen that the curves do not collapse for $\theta > 0$. For $\theta > 0$, the collapse of the curves is due to the paramagnetic behaviour. However, in the case of cobalt-substituted compounds, Griffiths-like phases exist in the system indicating the presence of FM clusters in the PM matrix. Hence, the universal curves of the cobalt-substituted samples do not collapse for temperatures above T_C i.e. $\theta > 0$ indicating that some ferromagnetic clusters exist in the PM matrix above T_C.

5.4.Conclusion

In summary, the influence of Co substitution on polycrystalline samples of $Gd_5Si_{2-x}Co_xGe_2$ with x=0, 0.1, 0.2 and 0.4 has been investigated. X-ray diffraction studies together with ESR and magnetization measurements reveal a mixture of M and O(I) crystal structures at room temperature. Low field magnetization data taken in FCC and FCW mode shows the presence of two transitions, a FOPT and a SOPT for x=0, 0.1, 0.2 and 0.4. The structural transition is marked by a significant hysteresis between FCC and FCW measurements. The maximum $-\Delta S_M$ for $Gd_5Si_{2-x}Co_xGe_2$ are 9, 8.5 and 4.2 J/kg K for x=0.1, 0.2 and 0.4 for a field change of 50 kOe. The presence of Griffiths-like phase has been established, which can be a consequence of the strong correlation between the magnetic and atomic lattices and constitutes a fingerprint for strong magneto-responsive properties in this family of compounds. Universal curve analysis reveal a weakening of first order transition with increase in Co concentration.

Chapter 6

Understanding the role played by cobalt and iron in tuning the structural and magnetocaloric properties of $Gd_5Si_{1.7}Ge_{2.3}$

The chapter discusses the effect of transition metals, Co and Fe substitution on the structural, magnetic and magnetocaloric properties of $Gd_5Si_{1.7}Ge_{2.3-x}TM_x$ *with TM = Co and Fe and x = 0, 0.1, 0.2, 0.3 and 0.4. Reduction of magnetic transition temperature Co substitution was reported in Chapter5. However by tuning Si:Ge ratio and getting the composition* $Gd_5Si_{1.7}Ge_{2.3-x}Co_x$, *it is possible to increase the magnetic transition temperature from 243 K to 283 K with an entropy change (-*ΔS_M*) of 12.8, 14.5, 10.4 and 5.8 J/kg K for x=0.1, 0.2, 0.3 and 0.4 respectively, for a field change of 50 kOe. Iron substitution changes the magnetic transition temperature from 247 K to 287 K with an entropy change (-*ΔS_M*) of 11.2, 12.7, 8.3 and 7 J/kg K for x=0.1, 0.2, 0.3 and 0.4 respectively, for a field change of 50 kOe in* $Gd_5Si_{1.7}Ge_{2.3-x}Fe_x$. *Universal curve analysis has been carried out on the substituted samples to study the order of the magnetic transition.*

6.1. Introduction

The discovery of GMCE in $Gd_5Si_2Ge_2$ (Pecharsky *et al.*, 1997) led to an extensive research on $Gd_5(Si_xGe_{1-x})_4$ compounds to increase the ΔS_M and ΔT_{ad} to room temperature. Research on $Gd_5(Si_xGe_{1-x})_4$ compounds are of special interest owing to the existence of a strong correlation between its crystal structure and magnetic properties (Pereira *et al.*, 2010; Morellon *et al.*,1998). In the present chapter, we report the increase in Curie temperature of $Gd_5Si_{1.7}Ge_{2.3}$ alloys with the substitution of transition metals such as Co and Fe. The substitution of Co and Fe has a strong influence on the structure and magnetic properties of $Gd_5Si_{1.7}Ge_{2.3}$. The effect of transition metal substitution on the magnetocaloric behaviour of $Gd_5Si_{1.7}Ge_{2.3}$ is also investigated and the universal scaling analysis based on magnetic entropy change is also applied to understand the nature of magnetic transition.

6.2. Experimental details

Polycrystalline ingots with the nominal composition of $Gd_5Si_{1.7}Ge_{2.3}$, $Gd_5Si_{1.7}Ge_{2.3-x}TM_x$ (TM = Fe and Co) with x = 0, 0.1, 0.2, 0.3 and 0.4 were prepared by arc melting the constituent elements in a water cooled copper hearth under high purity argon atmosphere. The samples with cobalt content x=0, 0.1, 0.2, 0.3 and 0.4 are labelled as $Gd_5Si_{1.7}Ge_{2.3}$, Co0.1, Co0.2, Co0.3 and Co0.4 and the samples with Fe content are labelled as Fe0.1, Fe0.2, Fe0.3, and Fe0.4 respectively. The details of sample preparation have already been discussed in Chapter 4. All the samples were finely ground and subjected to X-ray powder diffraction using PANalytical X'pert Pro diffractometer with Cu-Kα radiation operated at 40 kV and 30 mA at room temperature. The diffraction measurements were performed in the 2θ range 20° to 60° with a step size of 0.017°. Rietveld refinement of the diffraction patterns was carried out using GSAS-EXPGUI software. Magnetization measurements were made as a function of both temperature and field using a Physical Property Measurement System [Quantum Design, Dynacool] up to a maximum field (H) of 50 kOe in a temperature range 100-320 K. MCE was estimated from magnetization measurements taken from PPMS (Gschneidner *et al.*, 2005).

6.3. Results and Discussion

6.3.1. Structural and Microstructural Analysis of Cobalt substituted $Gd_5Si_{1.7}Ge_{2.3}$

6.3.1.1 Structural Analysis

The XRD patterns of $Gd_5Si_{1.7}Ge_{2.3}$, Co0.1, Co0.2, Co0.3 and Co0.4 are shown in Figure 6.1. The samples $Gd_5Si_{1.7}Ge_{2.3}$, Co0.1, Co0.2 and Co0.3 crystallize in a mixed state of monoclinic (M) $Gd_5Si_2Ge_2$ phase, O(I) Gd_5Si_4 phase at room temperature and hexagonal Gd_5Si_3 phase, while the composition with higher Co content crystallizes in O(I) phase. The monoclinic $Gd_5Si_2Ge_2$ phase has been indexed with ICSD pattern No. 84084 (space group $P112_1/a$) while the O(I) Gd_5Si_4 structure has been indexed with ICSD pattern no. 84083 (Space group Pnma). The hexagonal Gd_5Si_3 phase has been indexed with ICSD pattern No. 99641 (space group $P6_3/mcm$). Rietveld refinement of all the compositions has been carried out and the results are shown in Figures 6.2 -6.6. The refinement results confirm the presence of monoclinic and O(I) phases in $Gd_5Si_{1.7}Ge_{2.3}$, Co0.1, Co0.2 and Co0.3. Co0.4 crystallizes in O(I) phase only. The lattice parameters extracted along with refinement parameters are summarized in Table 6.1.

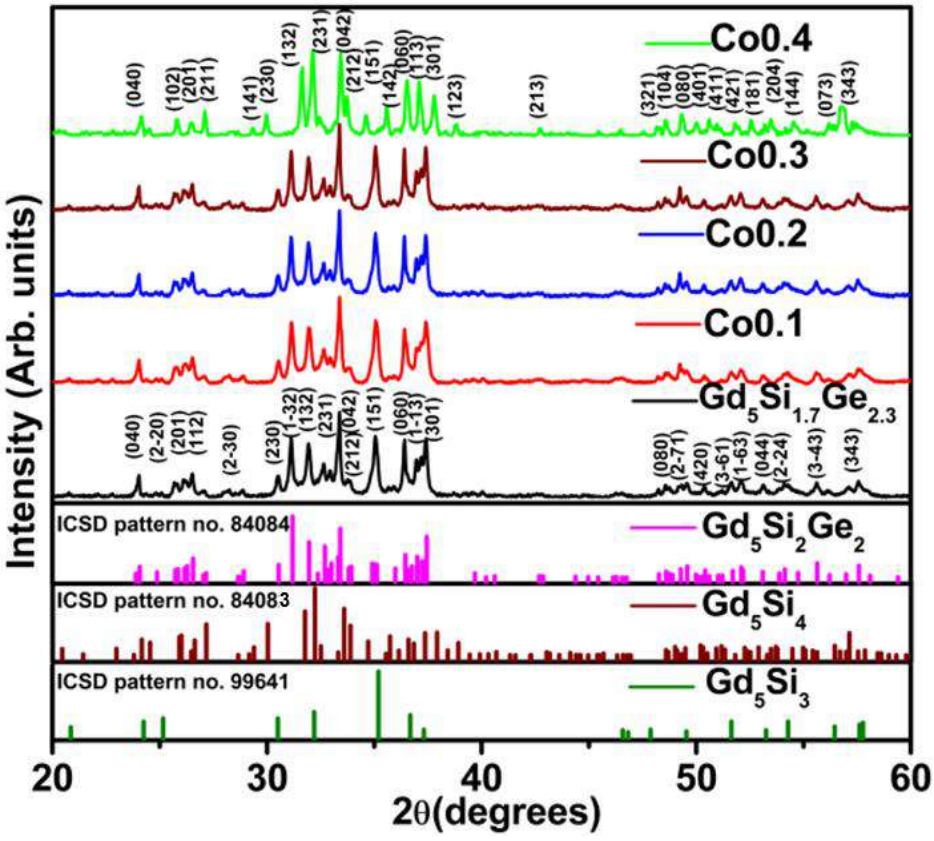

Figure 6.1. XRD patterns of $Gd_5Si_{1.7}Ge_{2.3}$, Co0.1, Co0.2, Co0.3 and Co0.4 at room temperature.

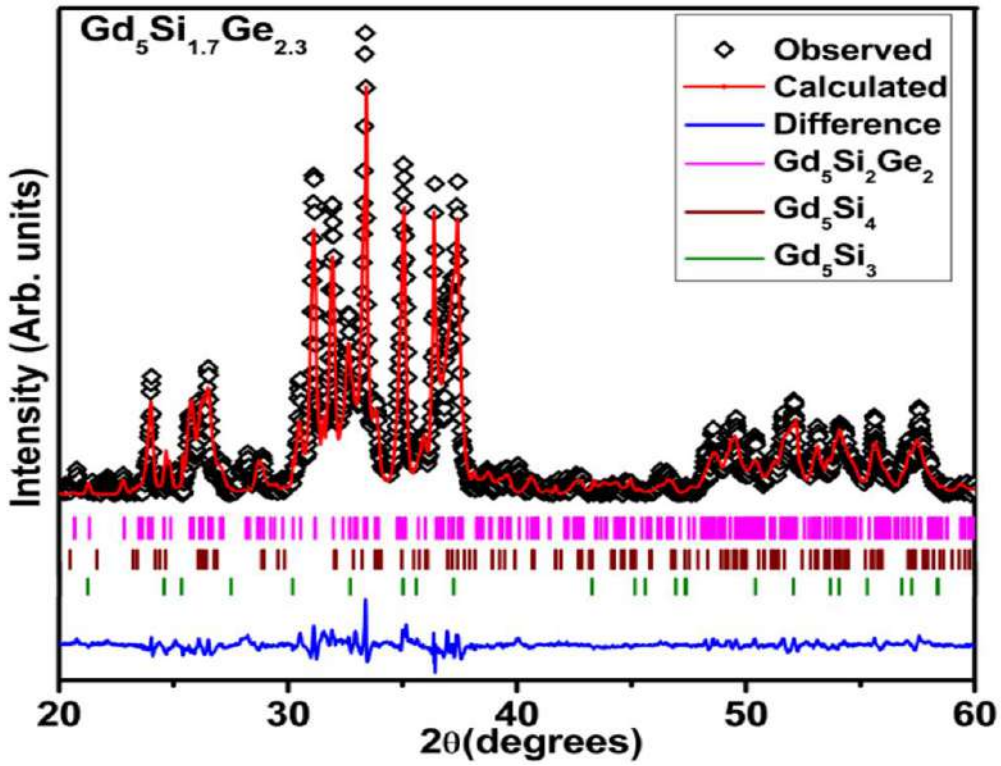

Figure 6.2. Rietveld refinement of $Gd_5Si_{1.7}Ge_{2.3}$.

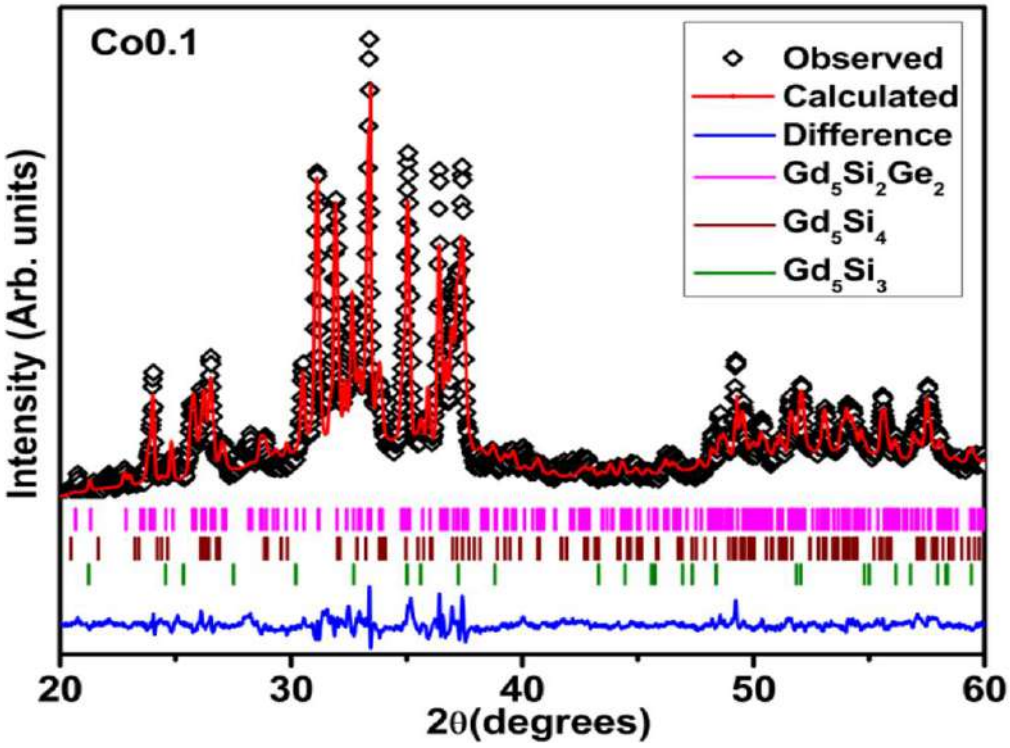

Figure 6.3. Rietveld refinement of $Gd_5Si_{1.7}Ge_{2.3-x}Co_x$ with x=0.1 (Co0.1).

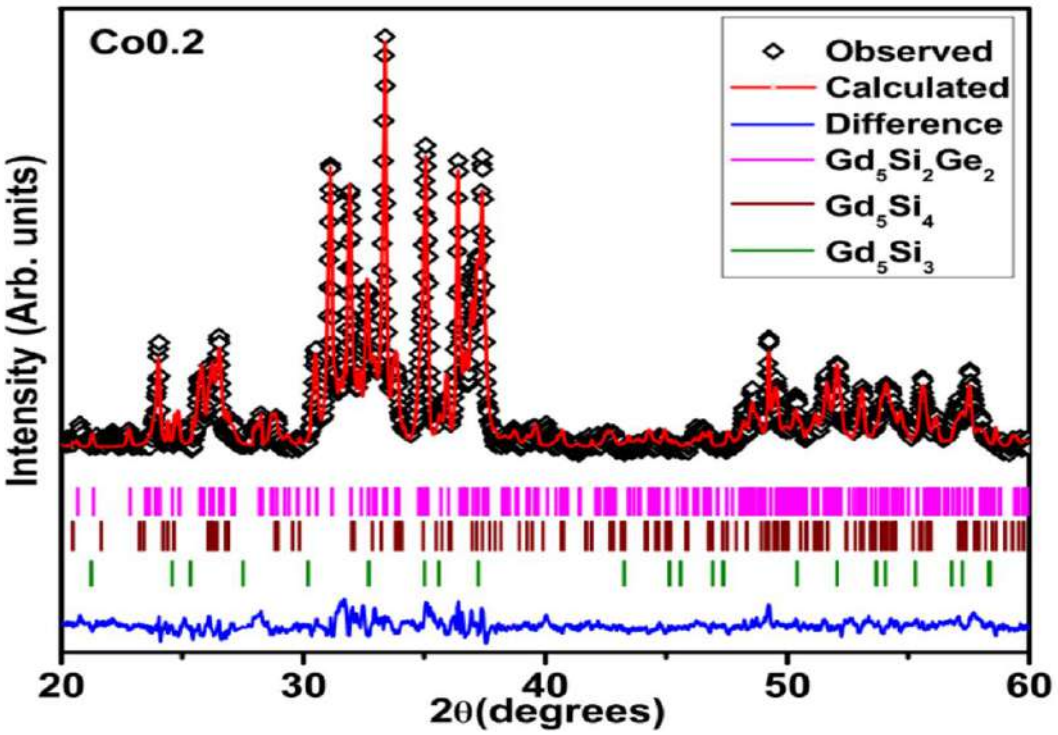

Figure 6.4. Rietveld refinement of $Gd_5Si_{1.7}Ge_{2.3-x}Co_x$ with x=0.2 (Co0.2).

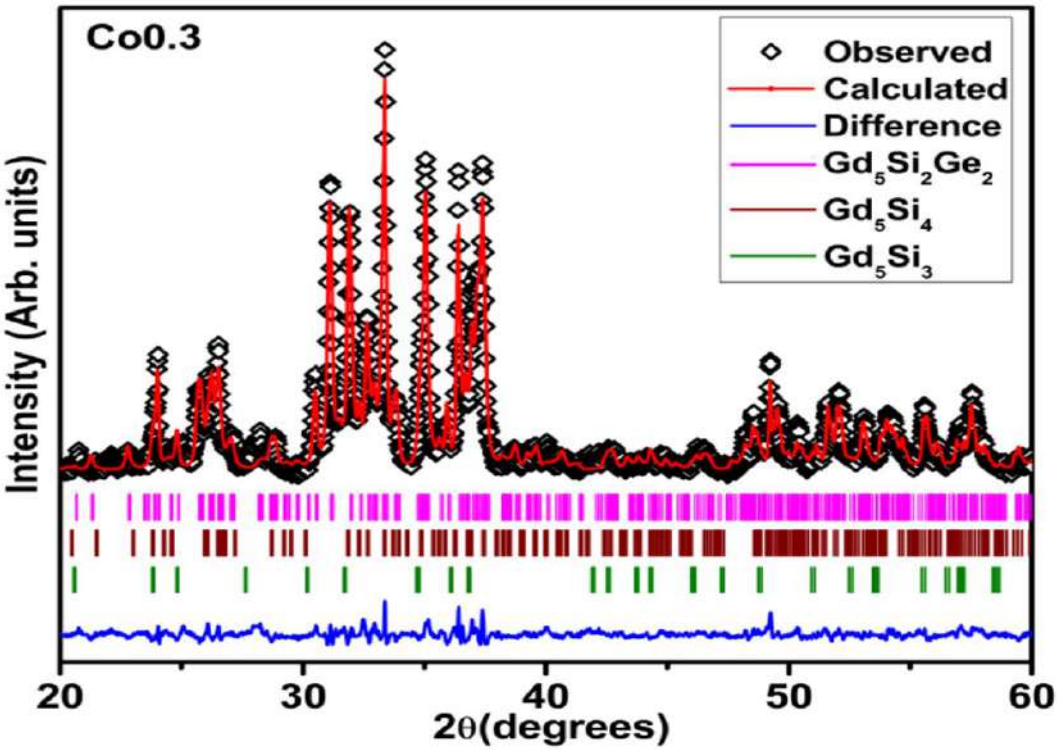

Figure 6.5. Rietveld refinement of $Gd_5Si_{1.7}Ge_{2.3-x}Co_x$ with x=0.3 (Co0.3).

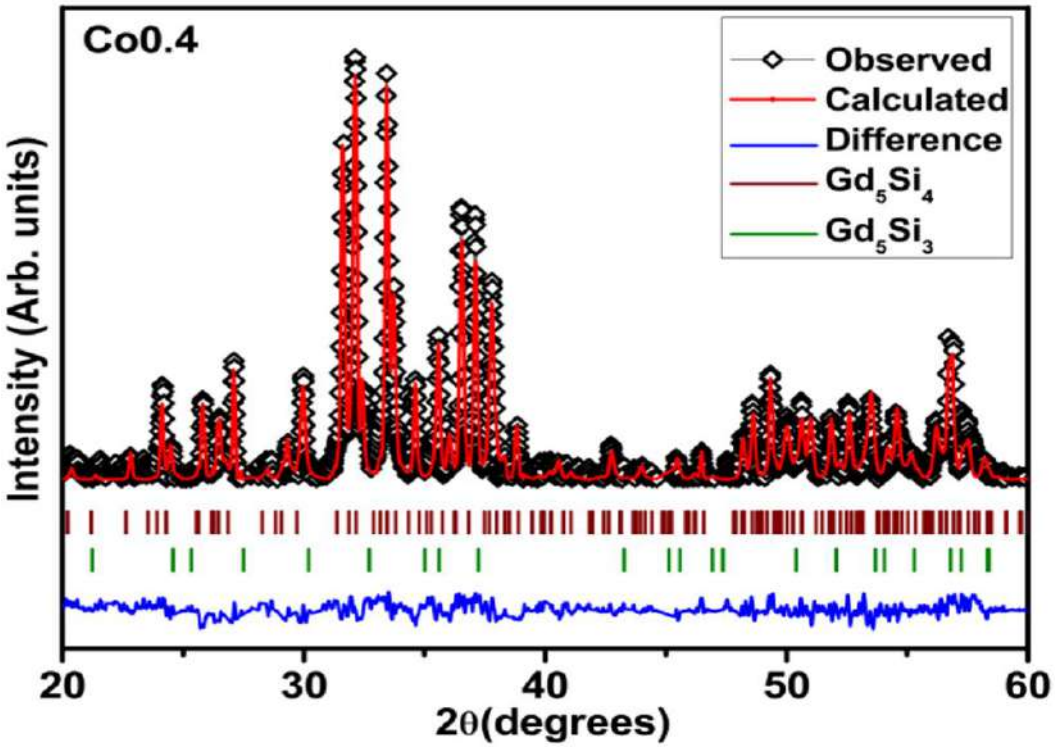

Figure 6.6. Rietveld refinement of $Gd_5Si_{1.7}Ge_{2.3-x}Co_x$ with x=0.4 (Co0.4).

Table 6.1. Lattice parameters, unit cell volume, and reliability factors from the Rietveld refinement of Cobalt substituted $Gd_5Si_{1.7}Ge_{2.3}$.

Sample	Crystal Structure	Space group	Lattice parameters					Residual Parameters	
			a (Å)	b (Å)	c (Å)	γ (deg)	Volume $(Å)^3$	R_{wp} %	R_p %
$Gd_5Si_{1.7}Ge_{2.3}$	M	$P112_1/a$	7.59(1)	14.82(1)	7.78(1)	93.09(5)	872.25(1)	3.44	2.65
	O(I)	Pnma	7.58(2)	14.58(5)	7.61(2)	90	843.16(1)		
	H	$P6_3/mcm$	8.34(1)	8.34(1)	6.47(1)	120	391.19(7)		
Co0.1	M	$P112_1/a$	7.60(1)	14.83(1)	7.79(1)	93.19(5)	874.25(1)	3.44	2.65
	O(I)	Pnma	7.59(2)	14.60(5)	7.63(2)	90	843.36(1)		
	H	$P6_3/mcm$	8.35(1)	8.35(1)	6.49(1)	120	391.22(7)		
Co0.2	M	$P112_1/a$	7.60(1)	14.84(1)	7.80(1)	93.21(1)	874.39(1)	3.26	2.53
	O(I)	Pnma	7.59(4)	14.75(1)	7.58(4)	90	845.9 (1)		
	H	$P6_3/mcm$	8.37(3)	8.37(1)	6.48(2)	120	392.67(1)		
Co0.3	M	$P112_1/a$	7.61(1)	14.84(2)	7.80(1)	93.23(1)	874.76(1)	3.25	2.44
	O(I)	Pnma	7.55(5)	14.76(4)	7.59(4)	90	844.6(2)		
	H	$P6_3/mcm$	8.37(2)	8.37(2)	6.49(2)	120	392.85(1)		
Co0.4	O(I)	Pnma	7.50(3)	14.74(4)	7.76(1)	90	857.72(5)	4.10	3.13
	H	$P6_3/mcm$	8.50(1)	8.50(1)	6.34(2)	120	396.79(1)		

6.3.1.2.Microstructural Analysis

The microstructures of cobalt substituted $Gd_5Si_{1.7}Ge_{2.3}$ alloys were examined using BSE micrographs. Figure 6.7 shows the BSE images of Co0.1. The microstructures of the cobalt containing alloys display a multi-phase nature showing the presence of a brighter $Gd_5(Si,Ge)_4$ matrix phase (5:4-type with M + O(I) phases) along with darker $Gd_5(Si,Ge)_3$ (5:3-type) secondary phase. Elemental mapping analysis has been performed on all the samples and the result for Co0.1 has been included in Figure 6.7. Elemental mapping reveals the absence of cobalt in the matrix phase. The grain boundary phase is

enriched with Si and Co as can be seen from Figure 6.7. The segregation of Fe into the grain boundary was explained by Provenzano *et al*., 2001; Raj Kumar *et al*., 2009; Raj Kumar *et al*., 2010 in $Gd_5(Si_xGe_{1-x})_4$ series and Pereire *et al*., 2011 in $Tb_5Si_2Ge_2$. In a similar manner, cobalt addition results in the segregation of Co into the grain boundary where it combines with silicon to form Gd_5Si_3 phase. The EDS results for all the compositions are summarized in Table 6.2. The increase in lattice volume with Cobalt substitution is attributed to the increase in Ge content of the matrix phase as revealed by the EDS results in Table 6.2.

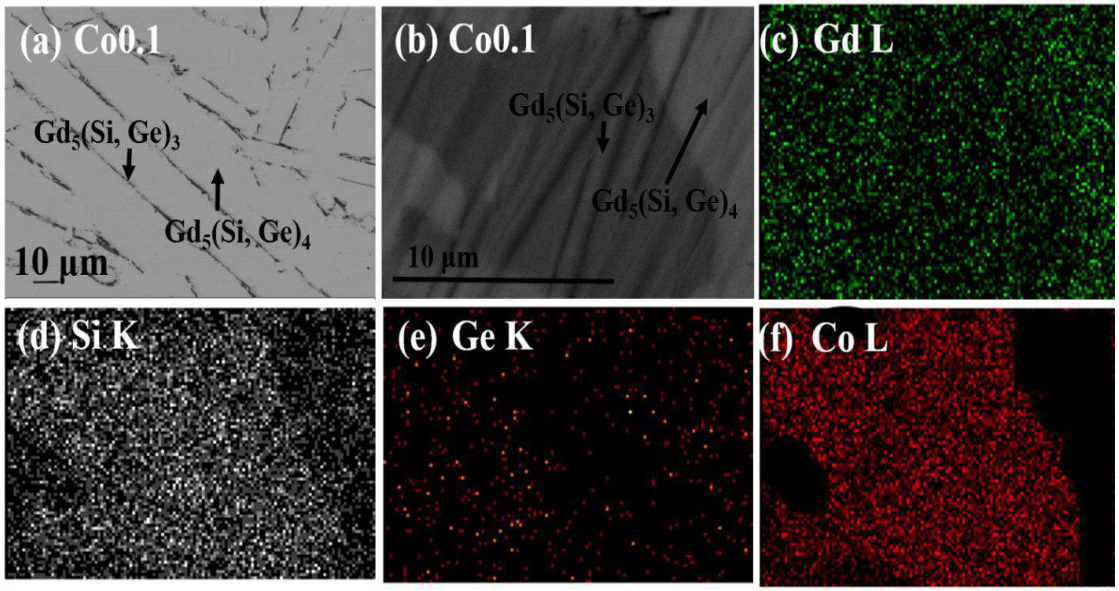

Figure 6.7. Backscattered SEM images of (a) Co0.1 at low magnification (b) Co0.1 at high magnification (c) Gd mapping (d) Si mapping (e) Ge mapping and (f) Co mapping [Matrix phase is 5:4-type, Dark phase is 5:3-type]

Table 6.2. Compositions of $Gd_5Si_{1.7}Ge_{2.3}$, Co0.1, Co0.2, Co0.3 and Co0.4 determined by EDS analysis. The estimated error in determining the concentration of each element is 0.1 at%.

x	Phase	Composition (at %)				Phase type
		Gd	Si	Ge	Co	
$Gd_5Si_{1.7}Ge_{2.3}$	Matrix	55.42	21.23	23.35	-	5:4
	Grain Boundary phase	62.04	21.33	16.63	-	5:3
Co0.1	Matrix	55.09	20.99	23.92	-	5:4
	Grain Boundary phase	62.13	21.13	15.51	1.23	5:3
Co0.2	Matrix	55.26	20.86	23.88	-	5:4
	Grain Boundary phase	62.38	20.48	14.87	2.27	5:3
Co0.3	Matrix	55.53	20.53	23.94	-	5:4
	Grain Boundary phase	62.68	20.19	14.26	2.87	5:3
Co0.4	Matrix	55.87	20.33	23.8	-	5:4
	Grain Boundary phase	62.97	19.87	13.14	4.02	5:3

6.3.2. Structural and Microstructural analysis of Fe substituted $Gd_5Si_{1.7}Ge_{2.3}$

6.3.2.1. Structural Analysis

The powder XRD patterns of $Gd_5Si_{1.7}Ge_{2.3}$, Fe0.1, Fe0.2, Fe0.3 and Fe0.4 are shown in Figure 6.8. The compositions with lower Fe content (x= 0, 0.1, 0.2 and 0.3) crystallize in a mixed state of monoclinic (M) $Gd_5Si_2Ge_2$ phase, O(I) Gd_5Si_4 phase at room temperature and hexagonal Gd_5Si_3 phase while Fe0.4 crystallise in O(I) phase. The monoclinic $Gd_5Si_2Ge_2$ phase, O(I) Gd_5Si_4 phase and hexagonal Gd_5Si_3 phase has been indexed with ICDD pattern No. 84084 (space group $P112_1/a$), 84083 (Space group Pnma) and 99641 (space group $P6_3/mcm$) rescpectively. Rietveld refinement of all the compositions has been carried out and the results are presented in Figures 6.9 -6.12. The refinement results confirm the presence of monoclinic and O(I) phases in $Gd_5Si_{1.7}Ge_{2.3}$,

Fe0.1, Fe0.2 and Fe0.3. The lattice parameters extracted along with refinement parameters are summarized in Table 6.3. The increase in lattice parameters with Fe substitution is due to the large size of Fe (1.72 Å) than Co (1.67 Å).

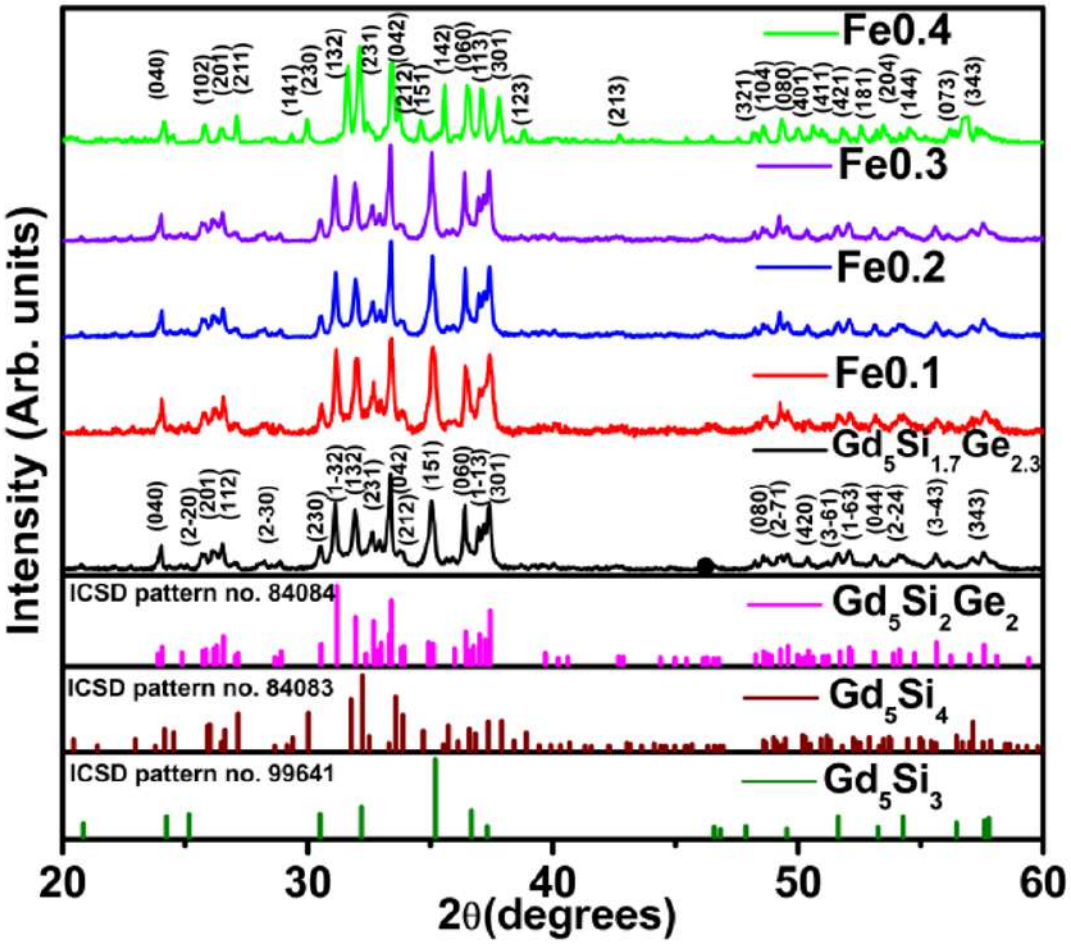

Figure 6.8. XRD patterns of $Gd_5Si_{1.7}Ge_{2.3}$, Fe0.1, Fe0.2, Fe0.3 and Fe0.4 at room temperature.

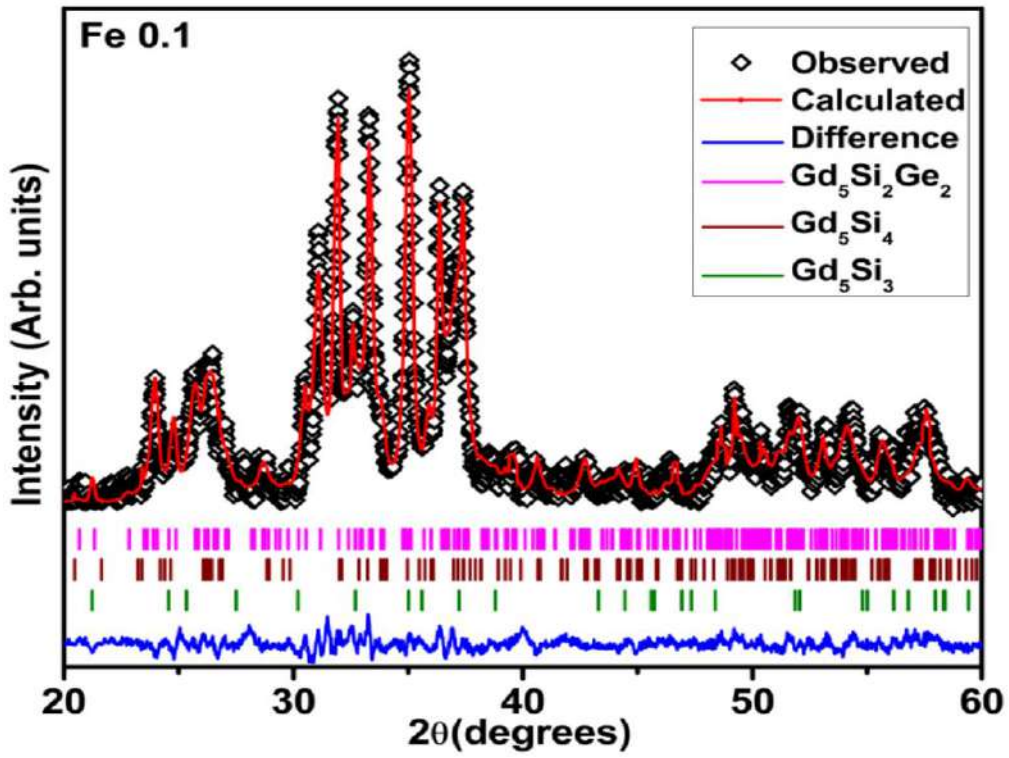

Figure 6.9. Rietveld refinement of $Gd_5Si_{1.7}Ge_{2.3-x}Fe_x$ with x=0.1 (Fe0.1).

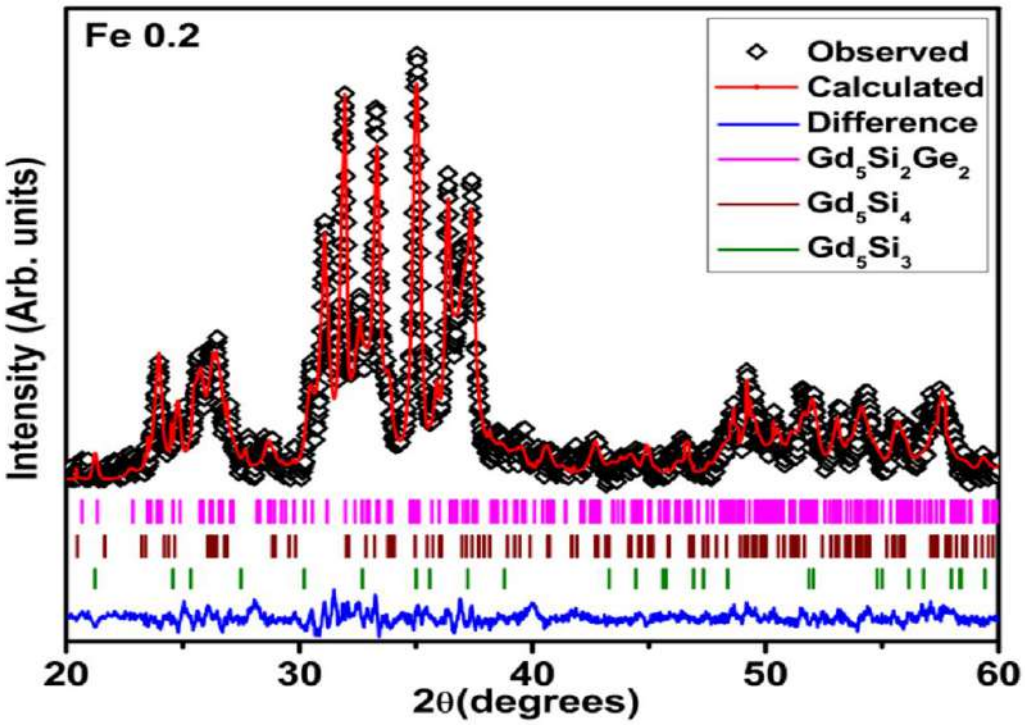

Figure 6.10. Rietveld refinement of $Gd_5Si_{1.7}Ge_{2.3-x}Fe_x$ with x=0.2 (Fe0.2).

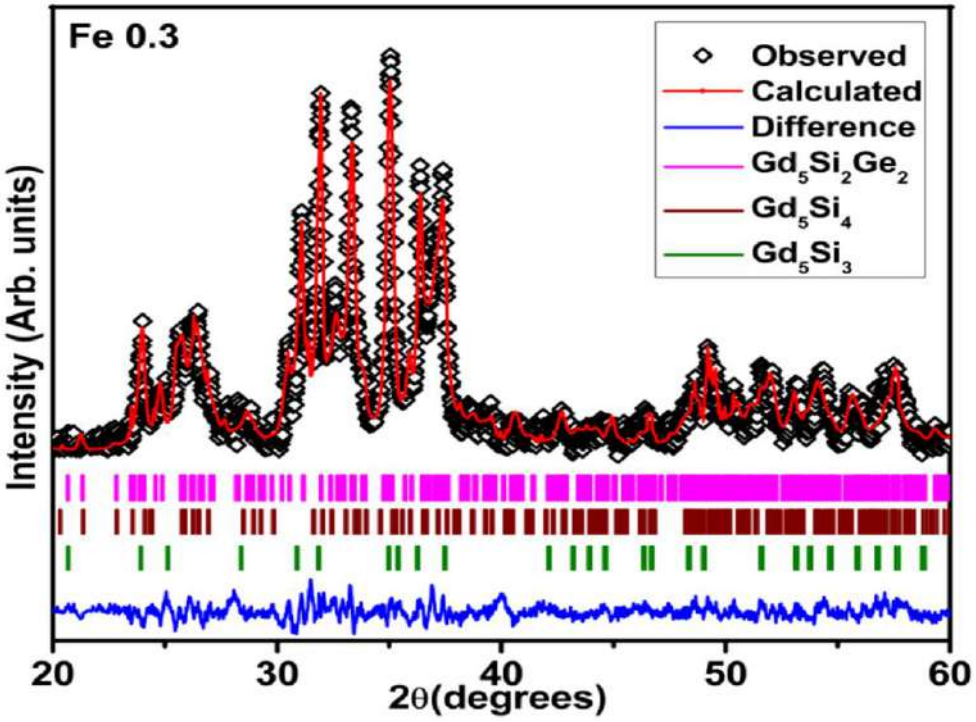

Figure 6.11. Rietveld refinement of $Gd_5Si_{1.7}Ge_{2.3-x}Fe_x$ with x=0.3 (Fe0.3).

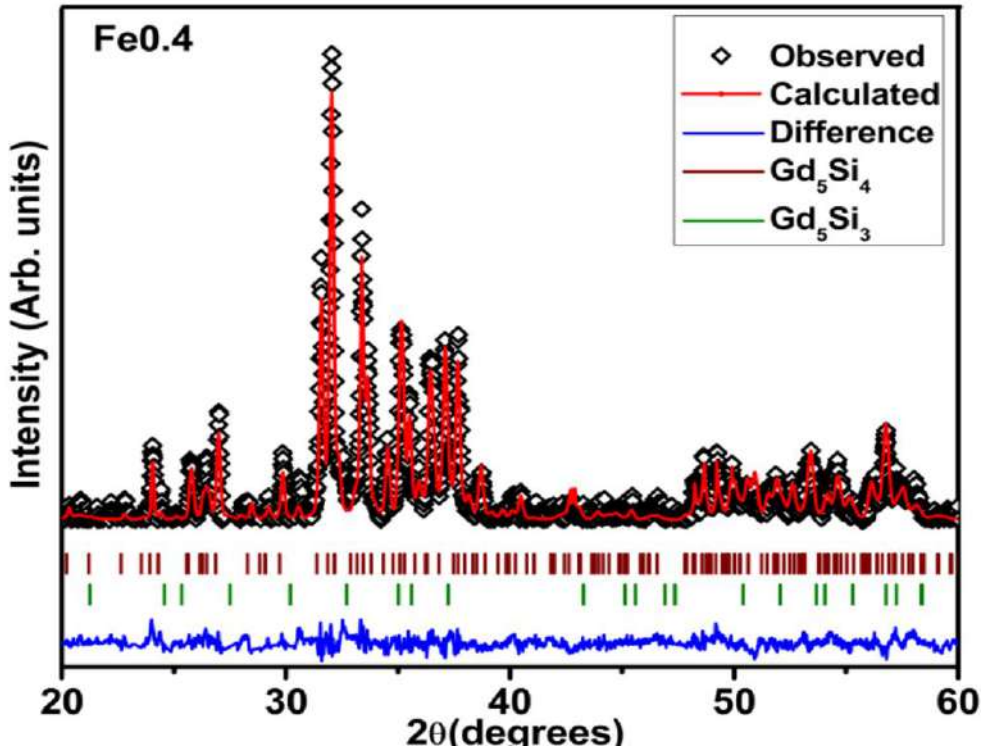

Figure 6.12. Rietveld refinement of $Gd_5Si_{1.7}Ge_{2.3-x}Fe_x$ with x=0.4 (Fe0.4).

Table 6.3. Lattice parameters, unit cell volume, and reliability factors from the Rietveld refinement of Fe substituted $Gd_5Si_{1.7}Ge_{2.3}$.

Sample	Crystal Structure	Space group	Lattice parameters					Residual Parameters	
			a (Å)	b (Å)	c (Å)	γ (deg)	Volume $(Å)^3$	R_{wp} %	R_p %
$Gd_5Si_{1.7}Ge_{2.3}$	M	$P112_1/a$	7.59(1)	14.82(1)	7.78(1)	93.09(5)	872.25(1)	3.44	2.65
	O(I)	Pnma	7.58(2)	14.58(5)	7.61(2)	90	843.16(1)		
	H	$P6_3/mcm$	8.34(1)	8.34(1)	6.47(1)	120	391.19(7)		
Fe0.1	M	$P112_1/a$	7.61(1)	14.83(1)	7.80(1)	93.23(5)	874.38(1)	3.41	2.62
	O(I)	Pnma	7.59(2)	14.61(5)	7.63(2)	90	843.80(1)		
	H	$P6_3/mcm$	8.35(1)	8.35(1)	6.50(1)	120	391.43(7)		
Fe0.2	M	$P112_1/a$	7.62(1)	14.84(1)	7.79(1)	93.25(1)	874.50(1)	3.39	2.60
	O(I)	Pnma	7.56(4)	14.75(1)	7.59(4)	90	846.31 (1)		
	H	$P6_3/mcm$	8.37(3)	8.37(1)	6.50(2)	120	392.72(1)		
Fe0.3	M	$P112_1/a$	7.63(1)	14.83(2)	7.79(1)	93.33(1)	874.79(1)	3.31	2.54
	O(I)	Pnma	7.58(5)	14.77(4)	7.56(4)	90	846.78(2)		
	H	$P6_3/mcm$	8.37(2)	8.37(2)	6.51(2)	120	392.89(1)		
Fe0.4	O(I)	Pnma	7.51(3)	14.75(4)	7.77(1)	90	857.73(5)	3.95	3.03
	H	$P6_3/mcm$	8.51(4)	8.51(4)	6.35(2)	120	397.80(2)		

6.3.2.2.Microstructural Analysis

The BSE micrographs of Fe0.1 and Fe0.4 are shown in Figures 6.13 and 6.14 respectively. Fe containing alloys display a multi-phase microstructure showing the presence of a brighter $Gd_5(Si,Ge)_4$ matrix phase (5:4-type) along with darker $Gd_5(Si,Ge)_3$ (5:3-type) secondary phase. Figures 6.13 and 6.14 shows the results of elemental mapping on Fe substituted samples. The segregation of Fe into the grain boundry was previously explained in $Gd_5(Si_xGe_{1-x})_4$ and $Tb_5Si_2Ge_2$ alloys (Provenzano *et al*., 2001; Raj Kumar *et al*., 2009; Raj Kumar *et al*., 2010) and $Tb_5Si_2Ge_2$ (Pereire *et al*., 2011). These results suggest that upon Fe addition, it primarily combines with the silicon giving rise to a grain

boundary phase enriched with silicon and iron. The BSE results are summarized below. Moreover, the BSE results indicate that the 5:4 phase contains a greater concentration of Ge which results in the increase of lattice volume of the matrix (M + O(I)) with increase in Fe substitution. This is concordant with our Rietveld refinement results shown in Table 6.3. The increase in Ge content in the matrix phase results in the increase in the lattice volume as is evident in Table 6.3.

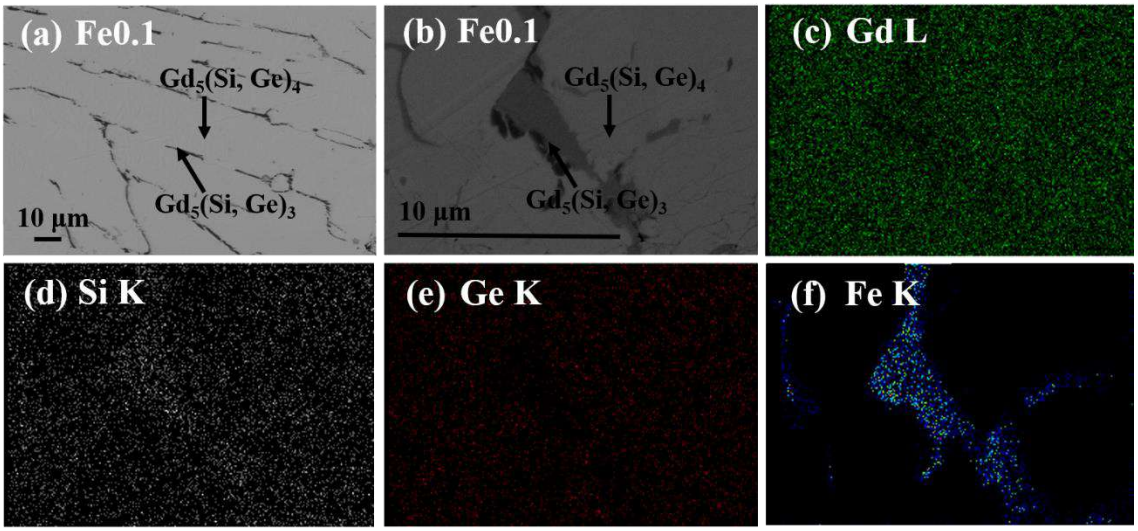

Figure 6.13. Backscattered SEM images of $Gd_5Si_{1.7}Ge_{2.3-x}Fe_x$ alloys for (a) Fe0.1 at low magnification (b) Fe0.1 at high magnification (c) Gd mapping (d) Si mapping (e) Ge mapping and (f) Fe mapping [Matrix phase is 5:4-type, Dark phase is 5:3-type]

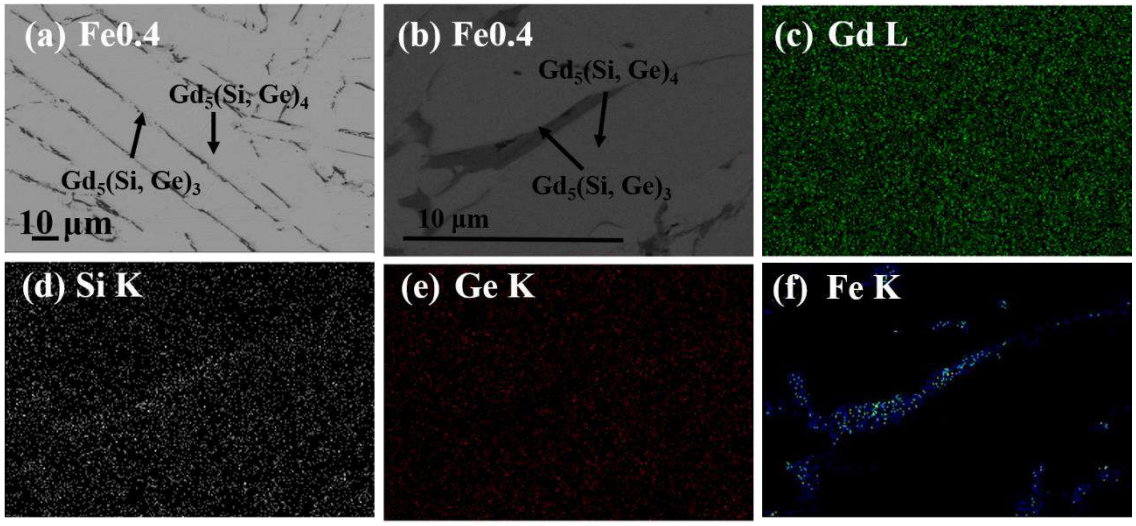

Figure 6.14. Backscattered SEM images of (a) Fe0.4 at low magnification (b) Fe0.4 at high magnification (c) Gd mapping (d) Si mapping (e) Ge mapping and (f) Fe mapping [Matrix phase is 5:4-type, Dark phase is 5:3-type].

6.3.3. Magnetic characterization of TM doped $Gd_5Si_{1.7}Ge_{2.3}$

Figure 6.15 shows the temperature dependent magnetization (M-T) data taken in the Field-Cooled-Cool (FCC) and Field-Cooled-Warm (FCW) modes in an applied field of 500 Oe for Co0.1, Co0.2, Co0.3 and Co0.4. It could be seen that two transitions are observed in the magnetization data for samples Co0.1, Co0.2 and Co0.3. For Co0.1, the first one at 287 K indicates a SOPT from O(I) FM phase to O(I) PM phase on heating. The second transition occurs at 243 K and it is a first order transition from O(I) FM phase to monoclinic PM phase as is evident from the hysteresis between the FCC and FCW data on heating. Similarly, for Co0.2 and Co0.3, the first transition at 290 K and 300 K, respectively, corresponds to a second order magnetic phase transition while the second transition at 262 K and 270 K is a first-order structural phase transition induced by magnetic field. For Co0.4, only a SOPT is observed at 283 K. The M-T results are concordant with our XRD results showing the presence of two phases coexisting in the system at room temperature for Co0.1, Co0.2 and Co0.3, giving rise to two sets of phase transitions in the system.

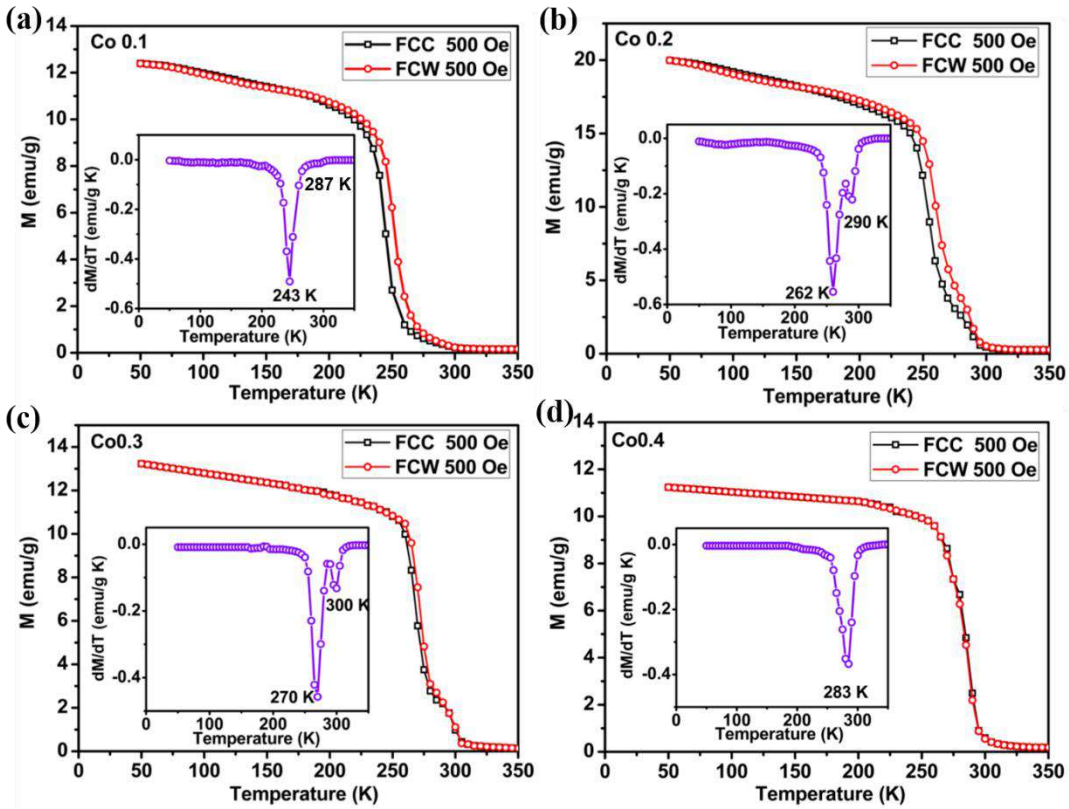

Figure 6.15. M-T curves of Co0.1, Co0.2, Co0.3 and Co0.4 measured in a magnetic field of 500 Oe during FCC and FCW processes.

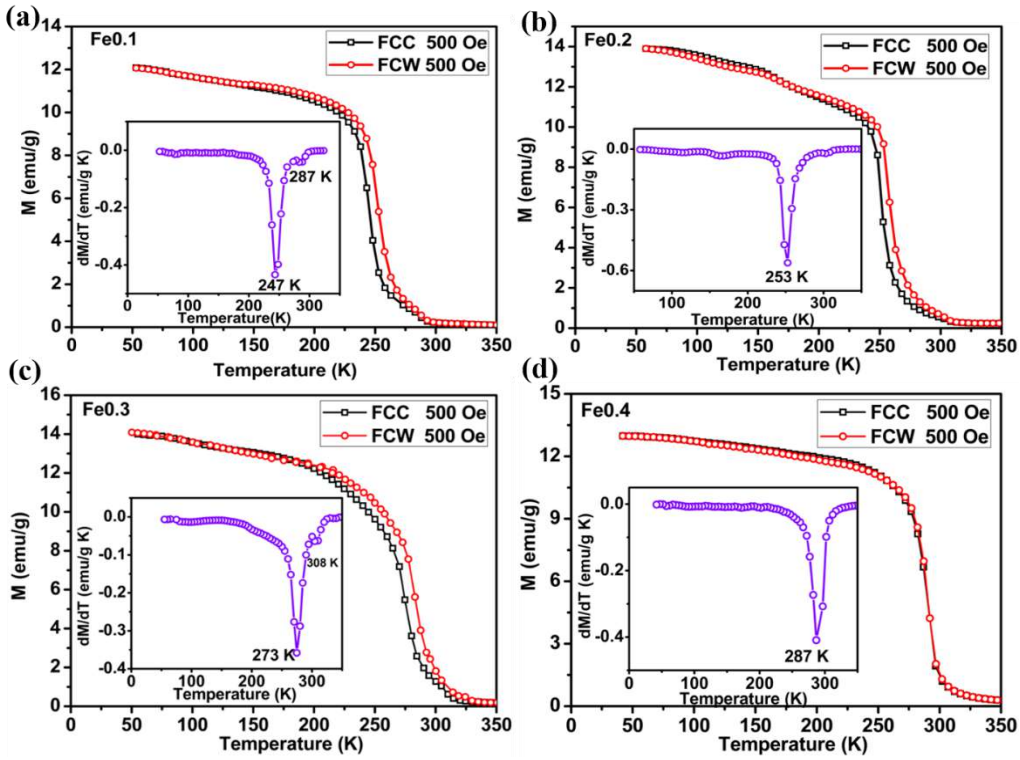

Figure 6.16. M-T curves of Fe0.1, Fe0.2, Fe0.3 and Fe0.4 alloys measured in a magnetic field of 500 Oe during FCC and FCW processes.

Similarly, for Fe substituted compounds, Fe0.1, Fe0.2 and Fe0.3 show the presence of two transitions. The transitions at 287 K, 302 K and 308 K for Fe0.1, Fe0.2 and Fe0.3 correspond to SOPT while that at 247 K, 253 K and 273 K indicate a FOPT. The compound Fe0.4 stabilises in O(I) structure and hence only a SOPT is observed. The M-T curves for Fe0.1, Fe0.2, Fe0.3 and Fe0.4 are shown in Figure 6.16.

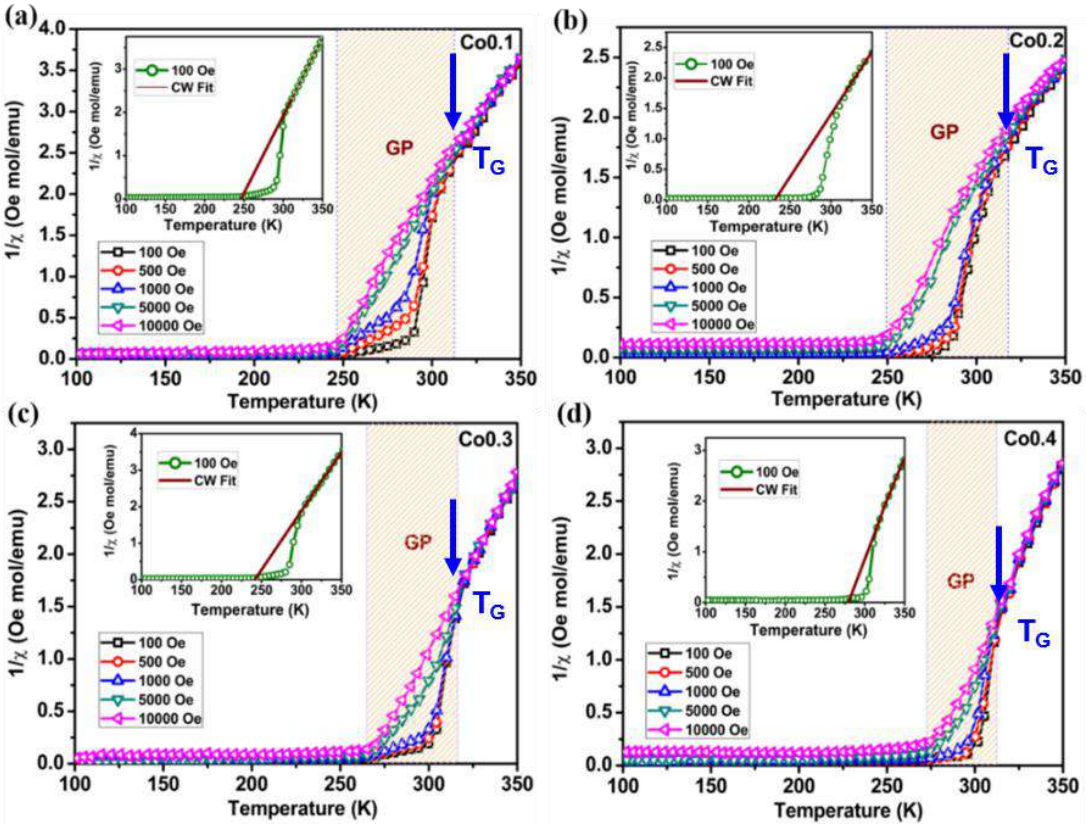

Figure 6.17. χ^{-1} versus T curves of (a) Co0.1, (b) Co0.2, (c) Co0.3 and (d) Co0.4 alloys measured at different fields of 100 Oe, 500 Oe, 1000 Oe, 5000 Oe and 10000 Oe. Inset shows the Curie-Wiess Fit.

The χ^{-1} versus temperature curves taken at different fields of 100 Oe, 500 Oe, 1000 Oe, 5000 Oe and 10000 Oe for Co substituted compounds are shown in Figure 6.17 (a)-6.17 (d). A clear deviation from CW behaviour is observed for a small applied magnetic field below a particular temperature. This is similar to the previous observations in Griffiths like phases (Magen *et al*., 2006; Pereira *et al*., 2010; Ouyang *et al*., 2010). The temperature of deviation is denoted as the Griffiths temperature T_G, and is shown in Figure 6.17 (a)-6.17 (d). The χ^{-1} versus temperature curves taken at different fields of 100 Oe, 500 Oe, 1000 Oe, 5000 Oe and 10000 Oe for Fe substituted compounds are shown in Figure 6.18 (a)-6.18 (c). The downturn below T_G is a signature of GP, a unique feature exhibited by magnetic materials which show a strong correlation between structural and magnetic properties. This is usually reflected as a downturn in χ^{-1} as a function of temperature above T_C. On increasing the magnetic field, the anomaly in χ^{-1} is suppressed and becomes nearly indistinguishable from the values at high temperature.

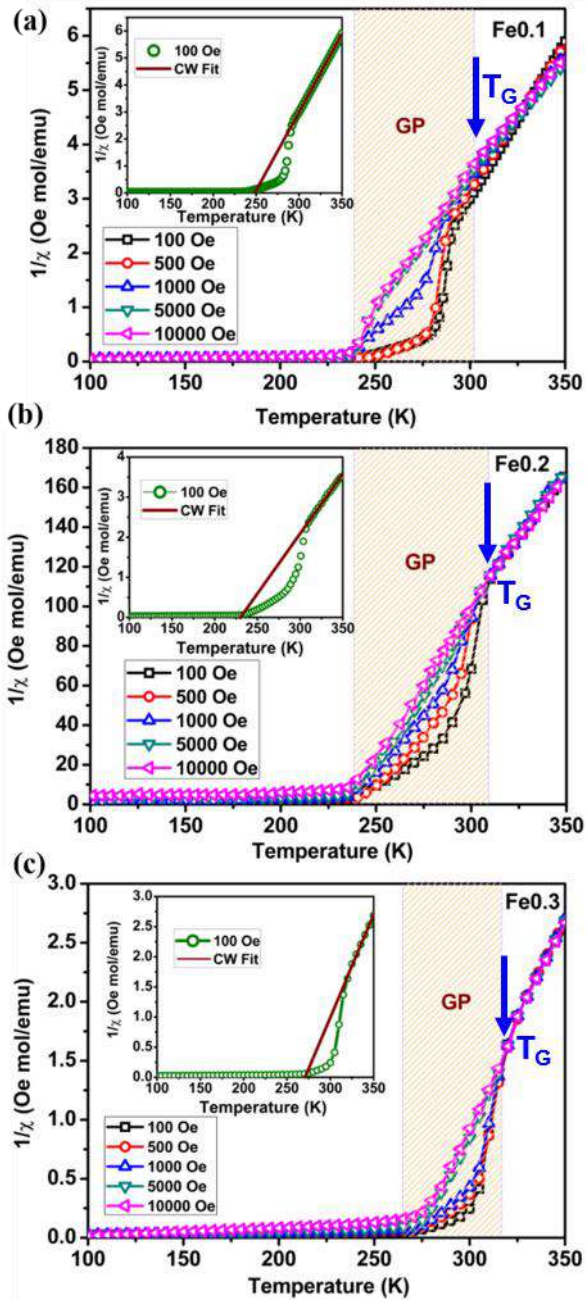

Figure 6.18. χ^{-1} versus T curves of (a) Fe0.1, (b) Fe0.2 and (c) Fe0.3 alloys measured at different fields of 100 Oe, 500 Oe, 1000 Oe, 5000 Oe and 10000 Oe. Inset shows the corresponding Curie-Wiess Fit.

The susceptibility of GP at low fields follows the power law and the value of λ, the magnetic susceptibility exponent ($0 \leq \lambda < 1$) and T_C^R is the random critical temperature (Pereira *et al*., 2010; Ouyang *et al*., 2010) is deduced from it. The linear part of the plot ln (χ^{-1}) vs ln(T/T_C^R -1) is fitted with the power law, and the estimated susceptibility exponent values are shown in Figure 6.19 and 6.20 for Co and Fe substituted compounds.

The value of λ lies in between 0 and 1 and decreases with increase in the field, a signature of GP. This behaviour has been observed in compounds such as $Tb_5Si_2Ge_2$ (Pereira *et al.*, 2010) and Gd_5Ge_4 (Ouyang *et al.*, 2006) typical of short-range FM clusters in a PM matrix and is the hallmark of Griffith's singularities. As the Co substitution increases from x=0.1 to x=0.4, it can be seen that the value of λ also increases from 0.71 to 0.87 for 100 Oe and 0.45 to 0.74 for 10000 Oe clearly suggesting an increase in the FM component within the PM matrix with Co substitution. The increase in the value of λ suggests an increase in the strength of GP.

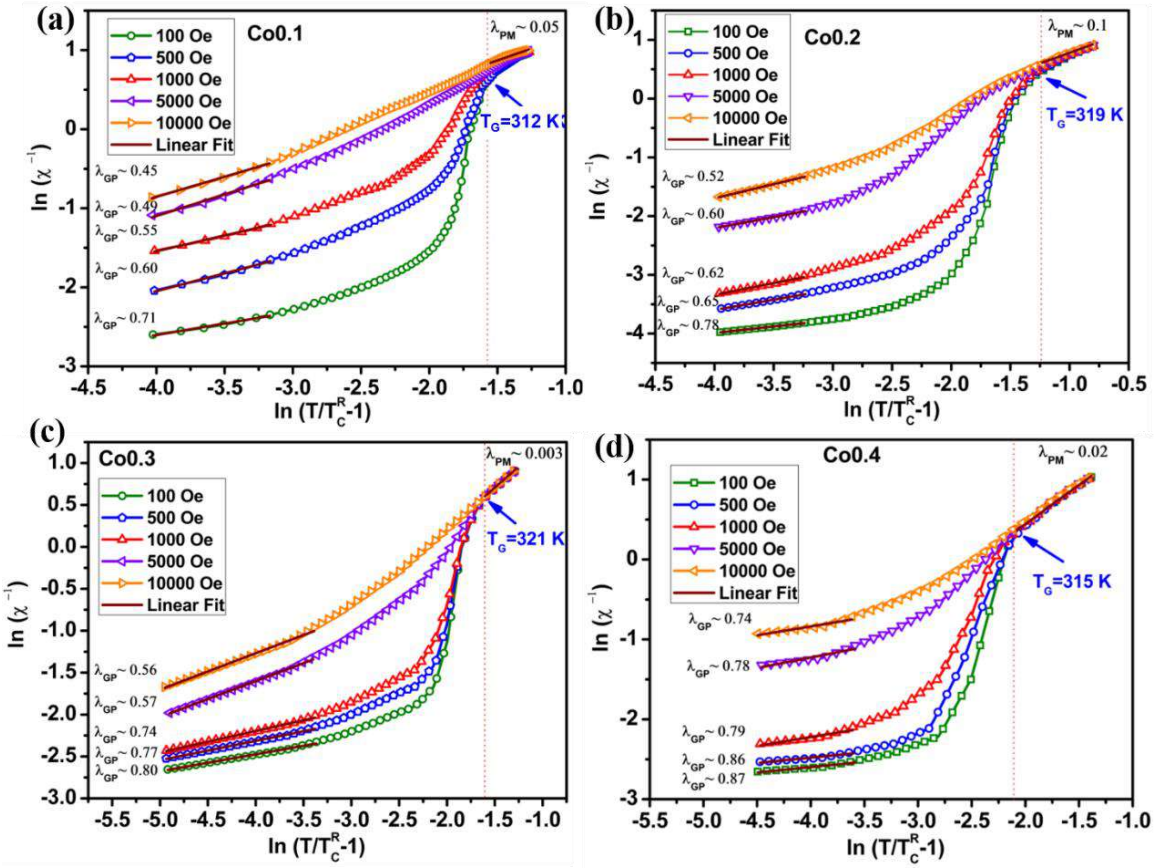

Figure 6.19. Griffiths Analysis of (a) Co0.1, (b) Co0.2, (c) Co0.3 and (d) Co0.4.

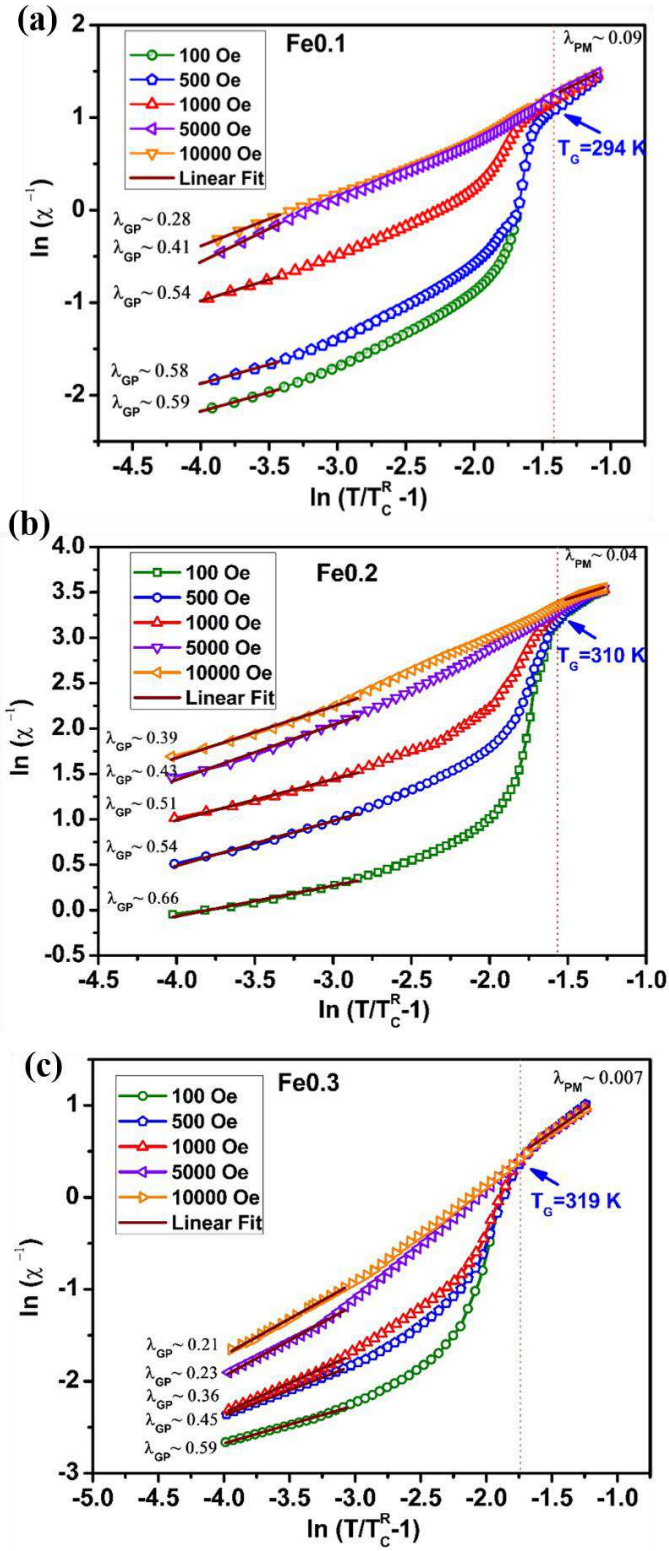

Figure 6.20. Griffiths Analysis of (a) Fe0.1, (b) Fe0.2 and (c) Fe0.3.

6.3.4. Isothermal Magnetization measurements and Magnetocaloric effect

6.3.4.1.Magnetocaloric effect in Co substituted $Gd_5Si_{1.7}Ge_{2.3}$.

Isothermal magnetization measurements were carried out in the temperature range of 200−320 K with a temperature interval of 5 K for $Gd_5Si_{1.7}Ge_{2.3-x}Co_x$ samples with x=0.1, 0.2, 0.3 and 0.4. The field was swept from 0-50 kOe and back to 0 Oe, and the results of are shown in Figure 6.21(a)-6.21(d). A considerable magnetic hysteresis in the vicinity of the ordering temperature has been observed Co0.1, Co0.2 and Co0.3, signifying that FOPT is inherent in the system. It can be seen that this field-induced phase transition reverses upon decreasing the field, but with some hysteresis around the transition region. This feature further suggests the reversible nature of the structural transition, at which the structure of the alloy returns to its initial state once the magnetic field is completely removed. However, it should be noted that in addition to FOPT, second order phase transition (SOPT) is also present in the system as is evident from the M-T curves. The XRD results also confirm the co-existence of monoclinic and O(I) phases in the system. It can be seen that for Co0.4, the thermal hysteresis is completely eliminated. This is attributed to the stabilization of the O(I) component, which is responsible for reducing the first order nature of the phase transition. The Arrott plots (M^2 versus H/M) for all the compositions are plotted in Figure 6.22(a)-6.22(d). The negative slope in the Arrott plots is a clear indication of the presence of first-order phase transition in these compounds while a positive slope indicates a second order transition. For Co0.1, Co0.2 and Co0.3, the Arrott plots indicate a negative slope confirming that first order nature of phase transition is present while for Co0.4, the Arrott plots clearly show positive slope indicating a second order phase transition. Hence, it can be acclaimed that as Co concentration increases, the compounds mainly stabilise in the O(I) phase giving rise to a SOPT.

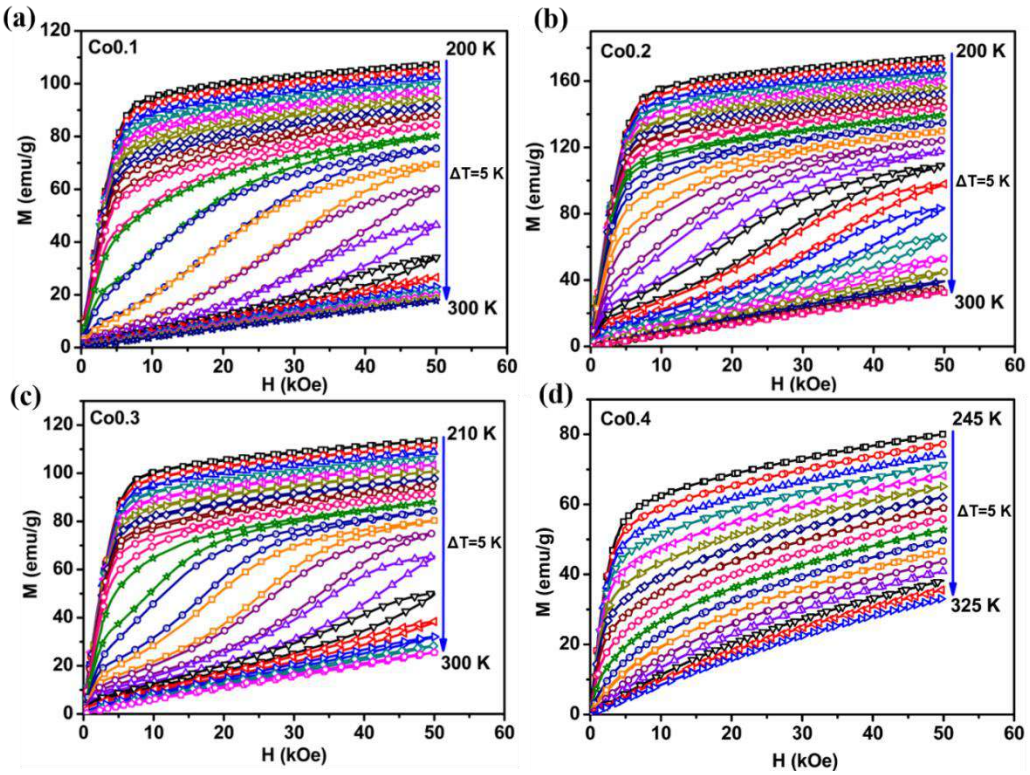

Figure 6.21. Field dependence of magnetization at different temperatures for (a) Co0.1, (b) Co0.2, (c) Co0.3, and (d) Co0.4.

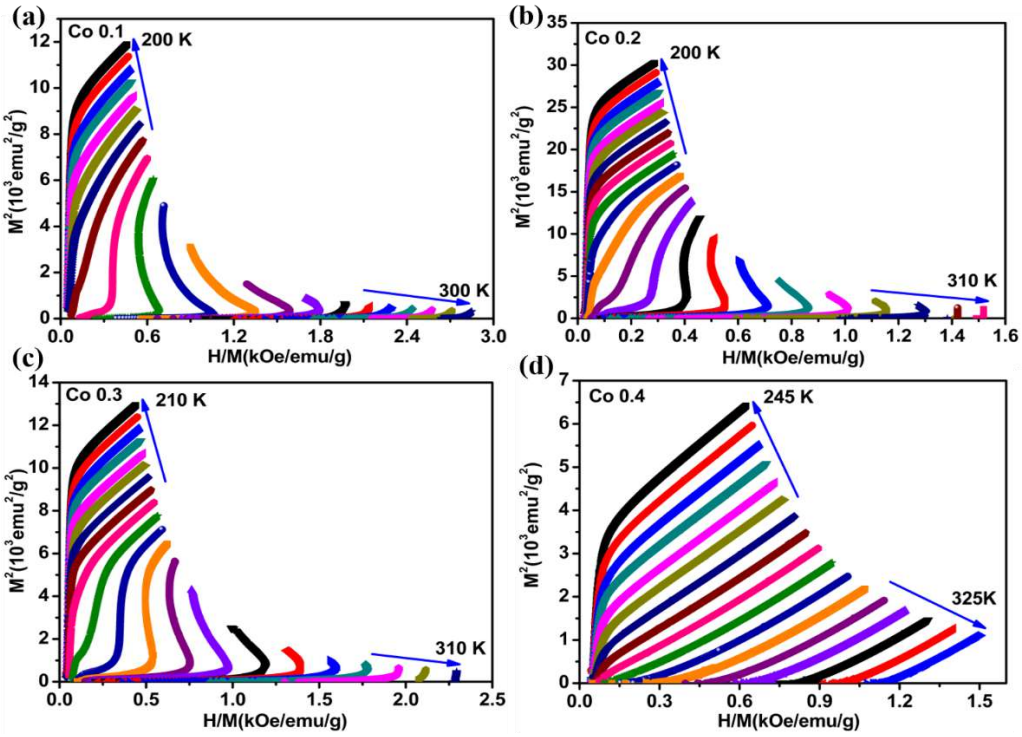

Figure 6.22. Arrott plots for (a) Co0.1, (b) Co0.2, (c) Co0.3 and (d) Co0.4.

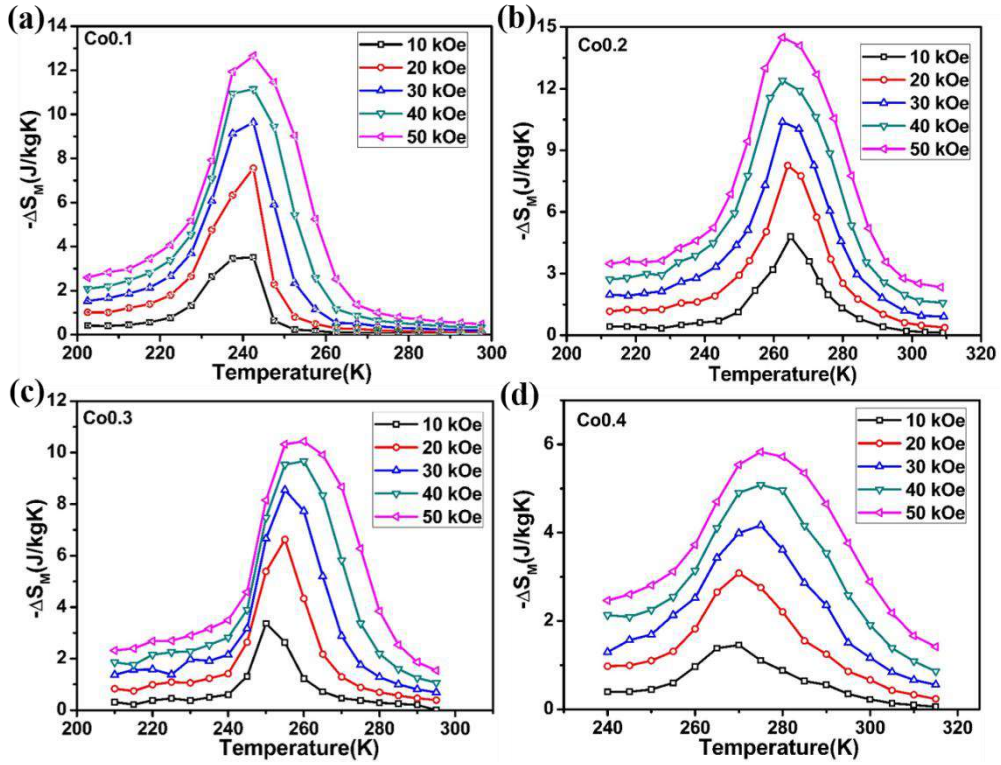

Figure 6.23. Isothermal magnetic entropy change ($-\Delta S_M$) for (a) Co0.1, (b) Co0.2 (c) Co0.3 and (d) Co0.4 as a function of temperature for different field changes

The MCE in Co substituted compounds has been evaluated from the isothermal magnetization data using the thermodynamic Maxwell relations explained in Chapter 1. Figures 6.23(a)-6.23(d) represent the change in magnetic entropy ($-\Delta S_M$) as a function of temperature under different magnetic fields for Co0.1, Co0.2, Co0.3 and Co0.4 respectively. Fora magnetic field variation of 50 kOe, the maximum ΔS_M for Co0.1, Co0.2, Co0.3 and Co0.4 are 12.8, 14.5, 10.4 and 5.8 J/kg K respectively. It can be seen that with increase in Co substitution, the $-\Delta S_M$ peak broadens. The increase in MCE for Co0.2 is attributed to the presence of a large fraction of monoclinic phase in the system. With increase in Co substitution, there is a reduction in the magnetic entropy change, which is attributed to the stabilization of the O(I) component. However, it can be seen that even though there are two transitions in the magnetization measurements, the magnetic entropy change is concentrated only in the vicinity of the first order transition region. This suggests that the entropy change associated with the second order phase transition is negligible and the isothermal entropy change is maximum around the first order transition region.

6.3.4.2.Magnetocaloric effect in Fe substituted $Gd_5Si_{1.7}Ge_{2.3}$.

Isothermal magnetization measurements were carried out for Fe substituted samples in the temperature range of 200−340 K with a temperature interval of 5 K with the field sweeping from 0-50 kOe and back to 0 Oe, and the results of are shown in Figure 6.24(a)-6.24(d). A considerable magnetic hysteresis in the vicinity of the ordering temperature observed Fe0.1, Fe0.2 and Fe0.3, signifies that FOPT is inherent in the system. The hysteresis appears due to crystallographic phase change from monoclinic PM phase to O(I) FM phase. For Fe0.4, the thermal hysteresis is completely eliminated. This is attributed to the stabilization of the O(I) component, which is responsible for reducing the first order nature of the phase transition. The Arrott plots (M^2 versus H/M) for all the compositions are plotted in Figure 6.25(a)-6.25(d). The order of magnetic transition can be determined from the slope of the isotherm plot. The negative slope in the Arrott plots is a clear indication of the presence of first-order phase transition in these compounds while a positive slope corresponds to a second order transition. For Fe0.1, Fe0.2 and Fe0.3, the Arrott plots indicate a negative slope confirming that first order nature of phase transition is present while for Fe0.4, the Arrott plots clearly show positive slope indicating a SOPT. Hence, it can be acclaimed that as Fe concentration increases, the compounds mainly stabilise in the O(I) phase indicating that second order transition is more likely to take place.

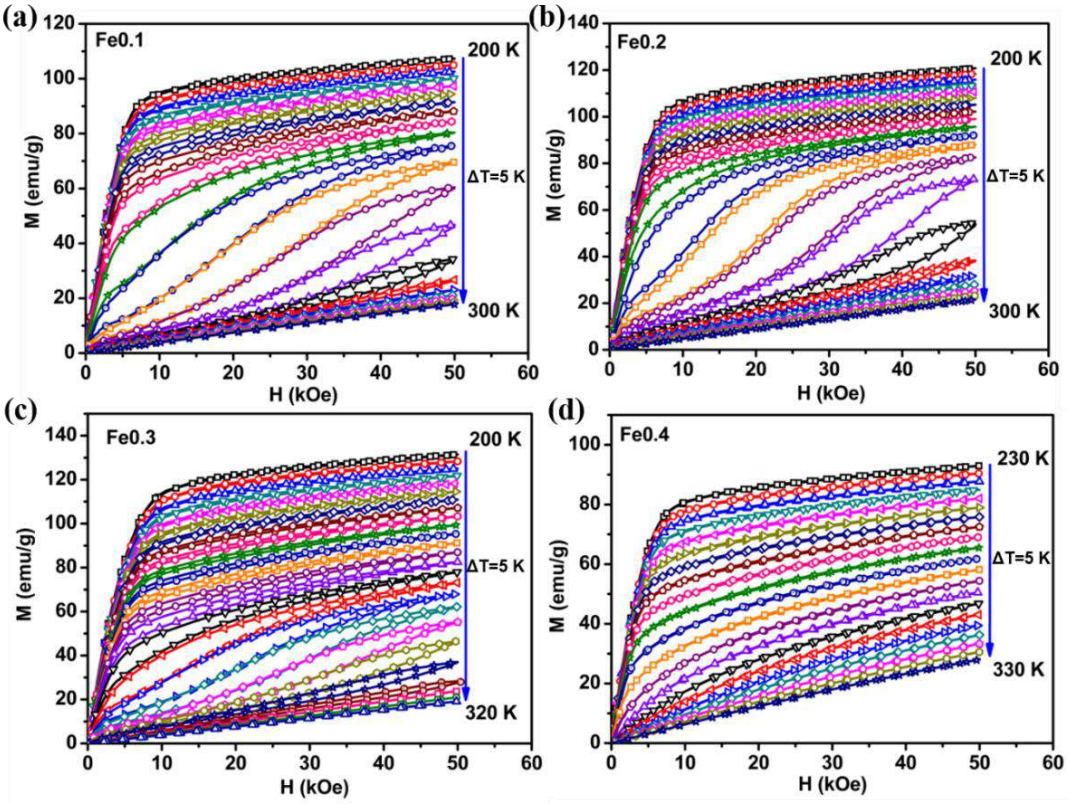

Figure 6.24. Field dependence of magnetization at different temperatures for (a) Fe0.1, (b) Fe0.2, (c) Fe0.3 and (d) Fe0.4.

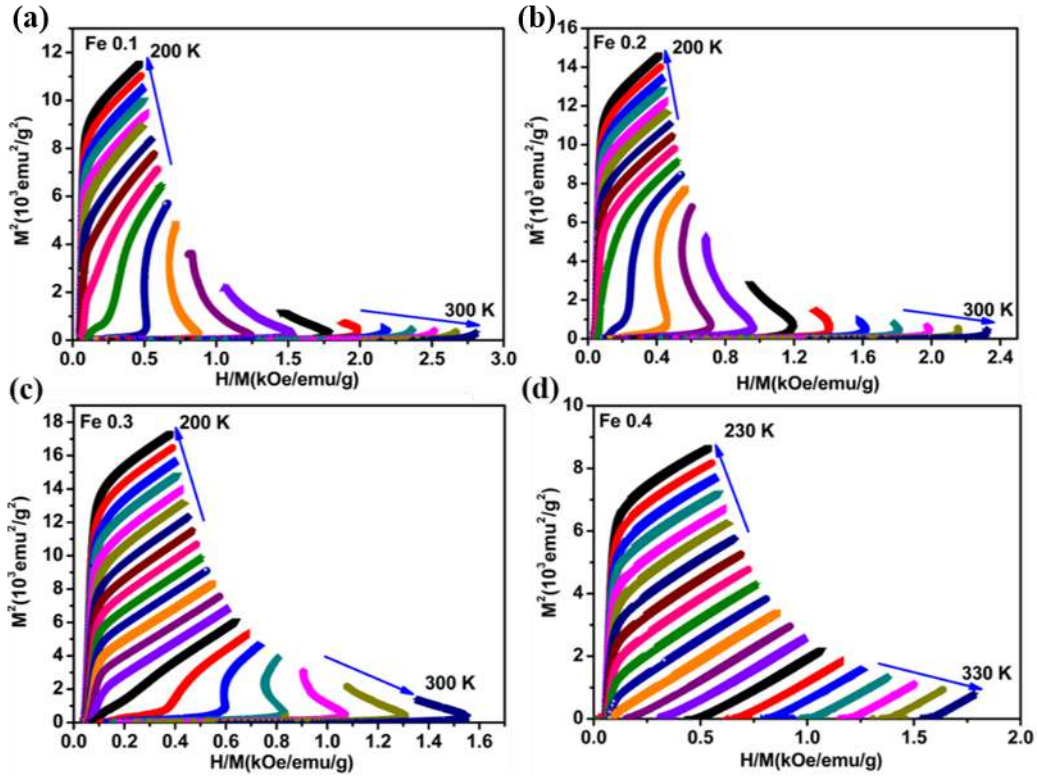

Figure 6.25. Arrott plots for (a) Fe0.1, (b) Fe0.2, (c) Fe0.3 and (d) Fe0.4.

MCE in Fe substituted compounds has been evaluated from the thermodynamic Maxwell relations explained in Chapter 1. Figures 6.26 (a)-6.26 (d) represent the change in magnetic entropy ($-\Delta S_M$) as a function of temperature under different magnetic fields for Fe0.1, Fe0.2, Fe0.3 and Fe0.4 respectively. For a field change of 50 kOe, the maximum $-\Delta S_M$ for $Gd_5Si_{1.7}Ge_{2.3-x}Fe_x$ are 11.2, 12.7, 8.3 and 7 J/kg K for Fe0.1, Fe0.2, Fe0.3 and Fe0.4 respectively. The increase in MCE for Fe0.2 is attributed to the presence of a large fraction of monoclinic phase in the system. The same has been observed with Co substitution described in the previous section. With increase in Fe substitution, there is a reduction in the magnetic entropy change, which is attributed to the stabilization of the O(I) component.

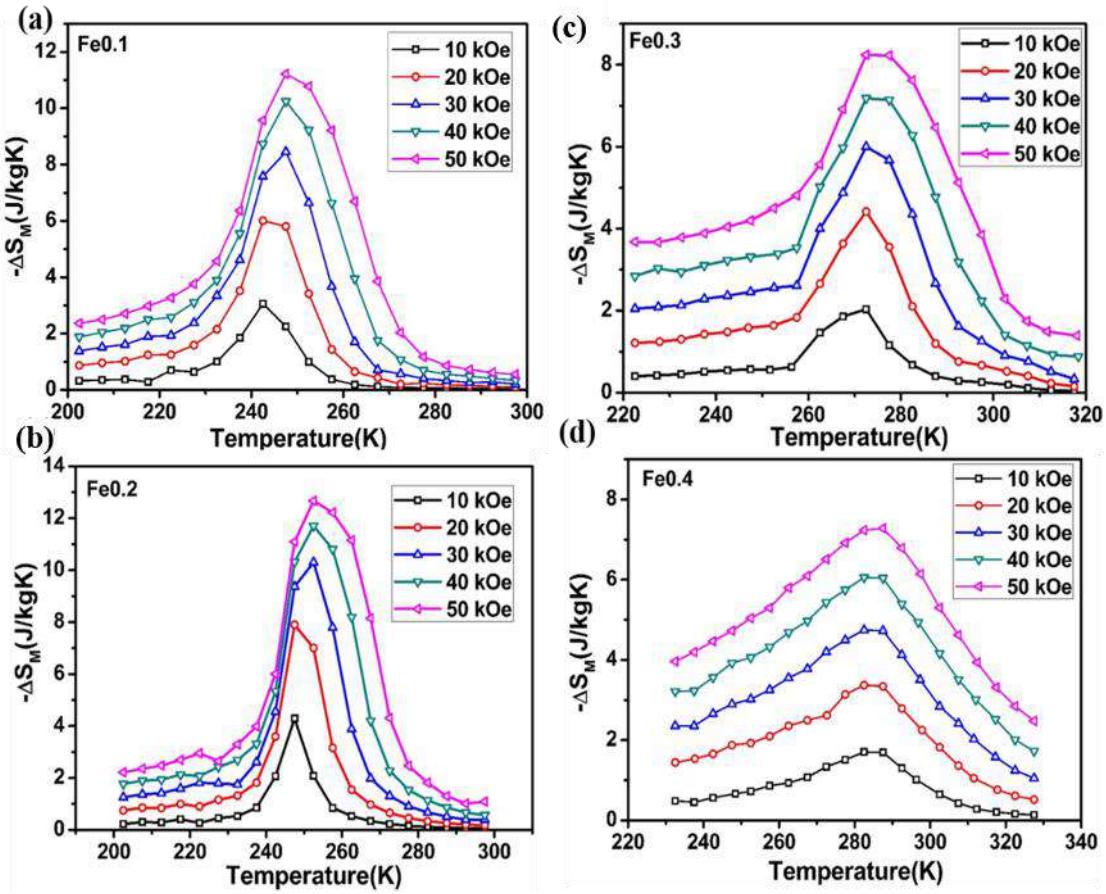

Figure 6.26. Isothermal magnetic entropy change ($-\Delta S_M$) of (a) Fe0.1, (b) Fe0.2, (c) Fe0.3 and (d) Fe0.4 as a function of temperature for different field changes.

6.3.4.3. RC and RCP in TM doped $Gd_5Si_{1.7}Ge_{2.3}$

The variation of effective RC and RCP obtained for $Gd_5Si_{1.7}Ge_{2.3-x}Co_x$ and $Gd_5Si_{1.7}Ge_{2.3-x}Fe_x$ with x= 0.1, 0.2, 0.3 and 0.4 for a field change of 50 kOe are plotted in Figure 6.27. It is to be noted that the hysteresis loss has been accounted while calculating the effective RC and RCP. The transition temperatures, entropy changes, and the effective RC and RCP values are tabulated in Table 6.4. Co substituted compounds exhibit much higher RCP values and their operating temperature could be tuned to the desired temperature, suggesting that these compounds could be used for sub-room temperature magnetic refrigeration applications.

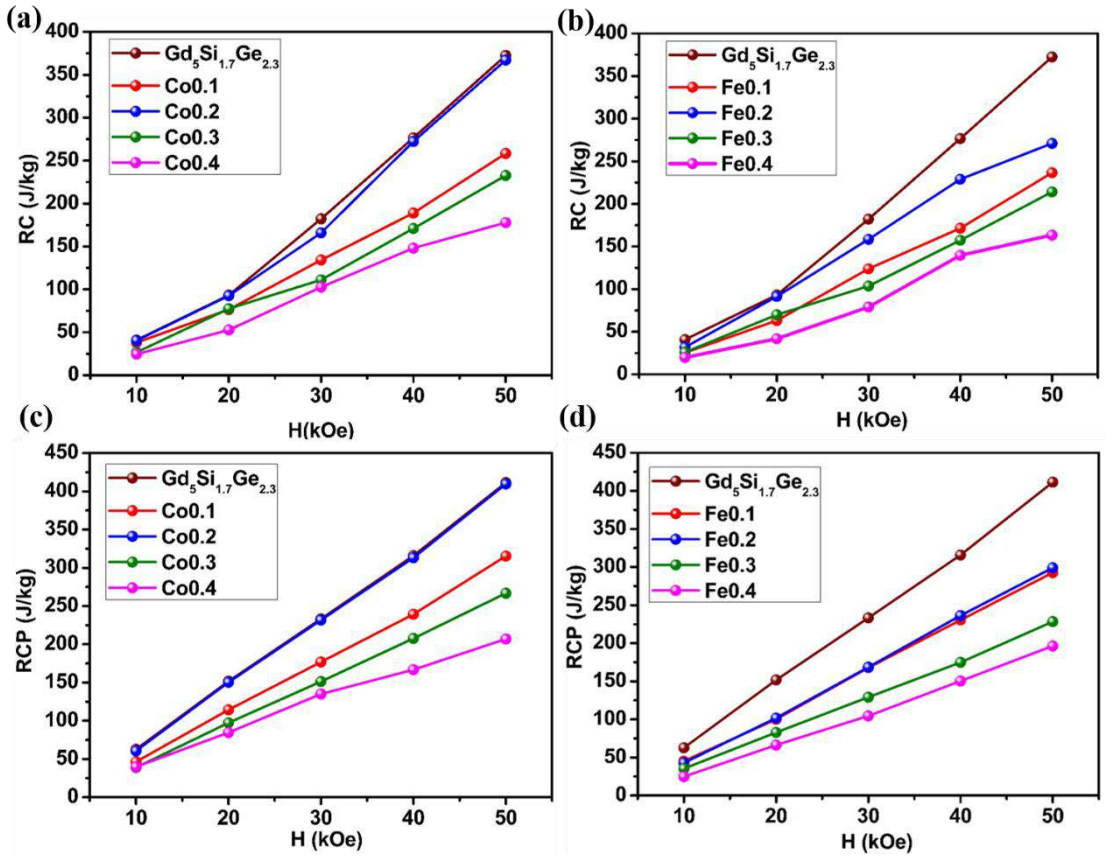

Figure 6.27. Variation of effective RC with field for (a) $Gd_5Si_{1.7}Ge_{2.3-x}Co_x$ and (b) $Gd_5Si_{1.7}Ge_{2.3-x}Fe_x$ with x=0.1, 0.2, 0.3 and 0.4 and RCP with field for (c) $Gd_5Si_{1.7}Ge_{2.3-x}Co_x$ and (d)$Gd_5Si_{1.7}Ge_{2.3-x}Fe_x$ with x=0.1, 0.2, 0.3 and 0.4.

TABLE 6.4. Transition temperatures, entropy changes, effective refrigerant capacity, and relative cooling power calculated for $Gd_5Si_{1.7}Ge_{2.3-x}Co_x$ and $Gd_5Si_{1.7}Ge_{2.3-x}Fe_x$

$Gd_5Si_{1.7}Ge_{2.3-x}TM_x$ (TM=Co and Fe)	Transition temperature	$-\Delta S_M$ J/kgK ΔH=50 kOe	Effective RCP (J/kg) H=50 kOe	Effective RC (J/kg) H=50 kOe
$Gd_5Si_{1.7}Ge_{2.3}$	240	19	411	373
Co 0.1	243	12.8	316	258
Co 0.2	262	14.5	417	367
Co 0.3	270	10.4	267	233
Co0.4	283	5.8	207	178
Fe 0.1	247	11.2	292	214
Fe 0.2	253	12.7	300	210
Fe 0.3	273	8.3	228	187
Fe 0.4	287	7	196	156

6.3.5. Universal Analysis

Universal curve has been proposed as a means for determining the order of phase transition based on the re-scaling of magnetic entropy change curves (Franco *et al*., 2006; Dong *et al*., 2006; Bonilla *et al*., 2010). The universal curves for Co0.1, Co0.2, Co0.3 and Co0.4 are plotted in Figure 6.28 and that plotted for Fe0.1, Fe0.2, Fe0.3 and Fe0.4 are shown in Figure 6.29 respectively.

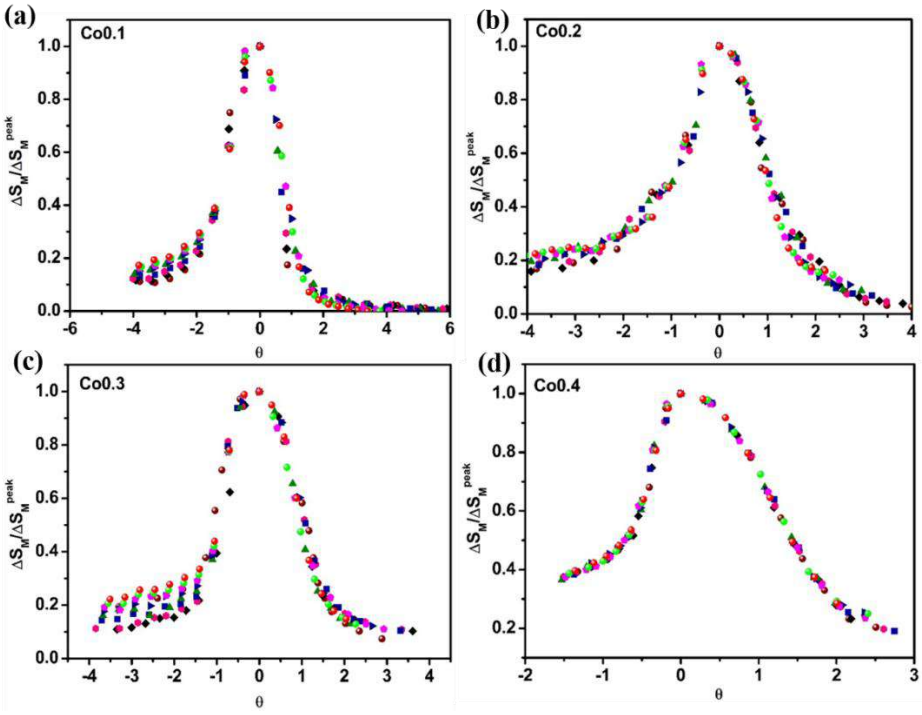

Figure 6.28. Normalized entropy change as a function of the rescaled temperature θ for (a) Co0.1, (b) Co0.2, (c) Co0.3 and (d) Co0.4.

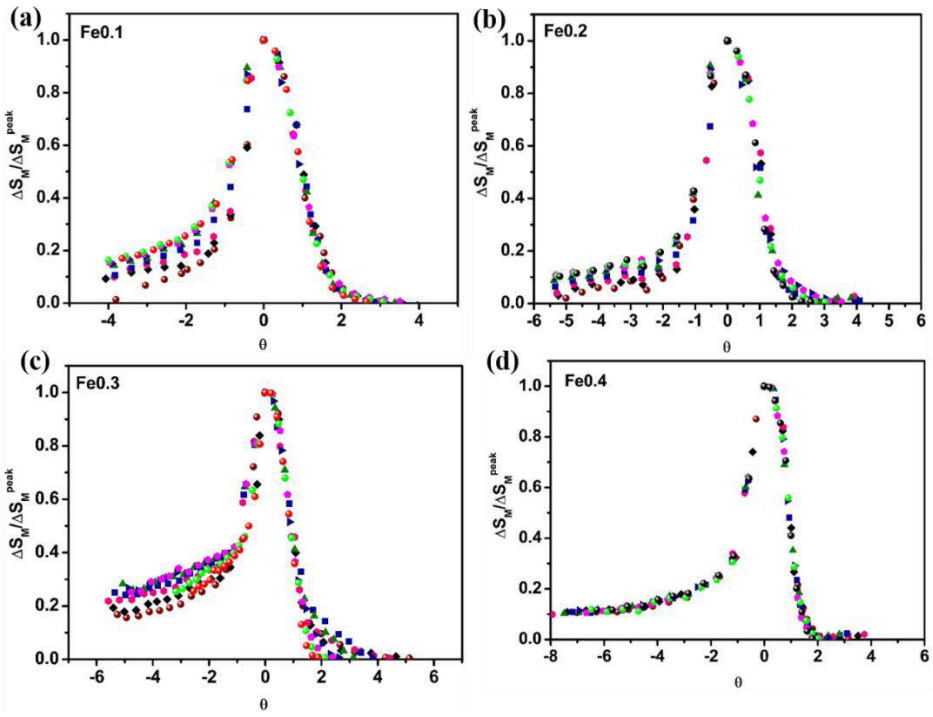

Figure 6.29. Normalized entropy change as a function of the rescaled temperature θ for (a) Fe0.1, (b) Fe0.2, (c) Fe0.3 and (d) Fe0.4.

In Figure 6.28 and 6.29, it is evident that the curves do not collapse, for temperatures below T_C, indicating the first order nature of phase transition. As the transition metal

concentration increases to x=0.4, the curves collapse on to a single curve. This is concordant with the trends observed in the Arrott plots shown in Figures 6.22 and 6.25. In the range, $-1 < \theta < 0$, the collapse is real for second order transitions and is only apparent for first order transitions. For temperatures above T_C, it can be seen that the curves do not collapse for $\theta > 0$ for the compositions with x=0.1, 0.2 and 0.3 in Co and Fe substituted compounds which could be due to the presence of Griffiths-like phases existing in the system. For $\theta > 0$, the collapse of the curves is due to the paramagnetic behaviour. However, in the case of composition with x=0.4, the curves collapse onto a single curve indicating second order nature of the transition.

6.4. Conclusions

In summary, the influence of transition metal substitution such as Co and Fe on the polycrystalline samples of $Gd_5Si_{1.7}Ge_{2.3-x}TM_x$ (TM=Co, Fe) with x=0, 0.1, 0.2, 0.3 and 0.4 has been investigated. X-ray diffraction studies together with magnetization measurements reveal a mixture of M and O(I) crystal structures at room temperature for higher doping concentrations while the higher doping concentration result in an O(I) structure. Low field magnetization data taken in FCC and FCW mode shows the presence of two transitions, a FOPT and a SOPT for x=0, 0.1, 0.2 and 0.3 while only a SOPT is evident for the composition with x=0.4. The maximum $-\Delta S_M$ for $Gd_5Si_{1.7}Ge_{2.3-x}Co_x$ are 12.8, 14.5, 10.4 and 5.8 J/kg K for x=0.1, 0.2, 0.3 and 0.4 respectively, for a field change of 50 kOe. For $Gd_5Si_{1.7}Ge_{2.3-x}Fe_x$ compounds, $-\Delta S_M$ is 11.2, 12.7, 8.3 and 7 J/kg K for x=0.1, 0.2, 0.3 and 0.4 respectively, for a field change of 50 kOe. The presence of Griffiths-like phases has been observed all the compositions for Co substituted compounds. In Fe substituted compounds, evident for compositions upto x=0.3 while no GP behaviour has been observed for x=0.4. Universal curve analysis reveal the transition from first order to second order with increase in Co and Fe concentration.

Chapter 7

Structural properties, magnetic interactions, magnetocaloric effect and critical behavior of cobalt doped $La_{0.7}Te_{0.3}MnO_3$

This chapter describes the effect of cobalt doping on the structural, magnetic and magnetocaloric properties of electron-doped manganite $La_{0.7}Te_{0.3}Mn_{1-x}Co_xO_3$ (x = 0, 0.1, 0.2, 0.25, 0.3 and 0.5) has been investigated. A structural transition from rhombohedral to orthorhombic structure occurs with increase in cobalt substitution. The presence of competing ferromagnetic and antiferromagnetic interactions leads to a glassy behaviour at low temperatures for low Co doping concentrations. However, for higher Co concentrations, no such behaviour is observed. Arrott plots reveal a second order nature of magnetic transition for all the samples. The magnetic exchange interactions for x = 0.3 and 0.5 follow the mean-field model. Magnetization results show that the magnetocaloric property of the electron-doped manganite is slightly affected by the substitution of Co at Mn sites. Relatively large values of relative cooling power and broad temperature interval of the magnetocaloric effect make the present compounds promising for sub-room temperature magnetic refrigeration applications.

7.1. Introduction

Doped manganese perovskites $Ln_{1-x}A_xMnO_3$ (Ln=Rare earth and A= divalent or tetravalent ions etc.) have attracted considerable attention owing to their peculiar magnetic properties and their promise for future technological applications such as colossal magnetoresistance (CMR), devices for information storage and magnetic sensors, magnetic refrigeration (MR), spintronics, etc. (Yang *et al*., 2007). The parent compound $LaMnO_3$ is a charge-transfer insulator with trivalent manganese arranged in different layers coupled among themselves antiferromagnetically through superexchange mechanism. But within a layer, these Mn^{3+} ions are coupled ferromagnetically (Zaanen *et al*., 1985; Mandal *et al*., 1997). The doping of $LaMnO_3$ with divalent or tetravalent ions drives the manganese ions into a mixed valence state. The introduction of divalent ions like Sr^{2+}, Ca^{2+} into the manganite system drives the manganese ions into a mixed valence state of Mn^{3+} (t_{2g}^3 e_g^1) and Mn^{4+} (t_{2g}^3), but if the rare-earth ion is partially replaced by some tetravalent ions like Te^{4+}, Ce^{4+}, etc., the manganese ion exist in Mn^{2+} (t_{2g}^3 e_g^2) and Mn^{3+} states (Mandal *et al*., 1997). Recently, considerable research has emphasised on electron-doped compounds such as $La_{1-x}B_xMnO_3$ where B= Te (Tan *et al*., 2003; Tan *et al*., 2003; Guo *et al*., 2004; Yang *et al*., 2004; Yang *et al*., 2004; Yang *et al*., 2005), Ce (Mandal *et al*., 1997; Gebhardt *et al*., 1999; Raychaudhuri *et al*., 2003; Mitra *et al*., 2003; Wang *et al*., 2006), Hf (Guo *et al*., 2011), Sb (Duan *et al*., 2004), Zr (Roy *et al*., 2001), etc., since both electron-doping and hole-doping in ferromagnetic (FM) manganites opens up interesting applications in the emerging field of spintronics. The introduction of the tetravalent ion drives Mn^{3+} ions of $LaMnO_3$ into Mn^{2+} ions, which is equivalent to introducing an electron into the e_g band. CMR behavior occurs in these compounds due to the mixed-valence state of Mn^{2+} /Mn^{3+}. The basic physics is explained in terms of Hund's coupling between e_g electrons and t_{2g} core electrons and the Jahn-Teller (JT) effect due to the Mn^{3+} JT ions.

Electron-doped manganites have also been found to exhibit large magnetocaloric effect (MCE) under moderately applied fields, revealing that CMR manganites are possible candidates for magnetic refrigeration applications (Yang *et al*., 2007). Doping at Mn sites in perovskite oxides is very effective to alter their physical properties owing to the core role played by Mn ions in manganites. Amongst the doping at Mn sites with

transition elements, cobalt doping is more prominent due to the different electron configurations and spin states of Mn and Co. Park *et al.* studied cobalt-doped manganite $LaMn_{0.85}Co_{0.15}O$ by X-ray absorption spectroscopy (XAS) at Co and Mn $L_{2,3}$-edges (Park *et al*., 1997; Park, 1999). They reported that a charge redistribution (CR); $Mn^{3+} + Co^{3+}$ —›$Mn^{4+} + Co^{2+}$ occurs in Co-doped manganese perovskites, thereby making the system Mn^{3+} - Mn^{4+} mixed valent. The X-ray photoelectron spectroscopy (XPS) measurements of $La_{0.7}Ba_{0.3}Mn_{1-x}Co_xO_3$ (Tai *et al*., 2000, Chang *et al*., 2000), $Pr_{0.5}Ca_{0.5}Mn_{0.95}Co_{0.05}O_3$ (Toulemonde *et al*., 2001)and $La_{0.9}Te_{0.1}Mn_{1-x}Co_xO_3$ (Zheng *et al*., 2006) perovskites also predict the same results. These results indicate that the $Mn^{4+} + Co^{2+}$ ionic configuration is more stable than the $Mn^{3+} + Co^{3+}$, due to the CR process of $Mn^{3+} + Co^{3+}$—›$Mn^{4+} + Co^{2+}$. The presence of Co^{2+} ions through the CR process is expected to have a role in determining the structural and magnetic properties of Co-substituted manganites. In the present paper, we report the influence of cobalt doping on the structural, magnetic, magnetocaloric properties and critical behavior of electron-doped $La_{0.7}Te_{0.3}MnO_3$. Cobalt doping induces a structural transition from rhombohedral (R-3 c space group) to orthorhombic (Pbnm space group). This is attributed to the breakdown of structural symmetry in the doped compounds due to the disordered distribution of Mn and Co ions which is in accordance with the XPS results. An enhancement of Curie temperature T_c, has been observed for $x \geq 0.2$, indicating a strong ferromagnetic exchange interaction. Relatively large values of relative cooling power (RCP) and broad temperature interval of MCE makes the present compounds promising candidates for sub- room temperature magnetic refrigeration applications.

7.2. Experimental details

Polycrystalline samples of $La_{0.7}Te_{0.3}Mn_{1-x}Co_xO_3$ (x=0, 0.1, 0.2, 0.25, 0.3, 0.5) were synthesized by solid state reaction route in air. Stoichiometric amounts of La_2O_3 (Sigma-Aldrich, 99.99%), TeO_2 (Sigma-Aldrich, 99.99+%), MnO_2 (Sigma-Aldrich, 99.99+%), and Co_3O_4 (Sigma-Aldrich, 99.99+%) were mixed well and calcined at 700°C for 24 hours followed by 1050°C for 12 hours with intermediate grindings. Prior to mixing, La_2O_3 powder was preheated at 1000°C for 10 hours. The powders thus obtained were ground, pelletized, and sintered at 1050°C for 12 hours with two intermediate grindings for homogenization to get the phase pure material. The crystal structure of the

samples were determined by powder x-ray diffraction (XRD) using Cu Kα radiation (PANalytical X'pert Pro diffractometer) operated at 40 kV and 30 mA at room temperature. Rietveld refinement of the diffraction patterns was carried out using GSAS (General Structure Analysis System) software. X-ray photoelectron spectroscopy (XPS) measurements were carried out using an Omicron Nanotechnology Multiprobe Instrument. XPS spectra were obtained using a high- resolution hemisphere analyzer EA 125 HR equipped with a detection system consisting of seven channeltrons. A monochromated Al Kα source of hν = 1486.6 eV was used to probe $La_{0.7}Te_{0.3}Mn_{1-x}Co_xO_3$ pellets with x=0.1 and x=0.3 attached by double-sided tape to the molybdenum sample holder. Pressure in the XPS chamber during the measurements was 5×10^{-10} mbar. The binding energies were corrected by C 1s as reference energy (C 1s = 284.8 eV) (Moulder *et al*., 1992). A wide scan was collected to ensure that no foreign materials were present on the sample surface. Narrow scans of Mn 2p and Co 2p regions were collected at an analyzer pass energy of 20 eV. Curve fitting to the XPS spectrum was done using CasaXPS software. Background subtraction was done using the Shirley method. Magnetization measurements were performed as a function of both temperature and field using a Physical Property Measurement System [Quantum Design, Dynacool] up to a maximum field (H) of 50 kOe in the temperature range 5 K-300 K. MCE was estimated, in terms of isothermal magnetic entropy change ($-\Delta S_M$), from Maxwell's relations (equation (1.19) described in Chapter 1. Relative cooling power has been calculated using the relation (1.26) in Chapter 1.

7.3. Results and discussion

7.3.1. Phase and structural analysis-Rietveld refinement

Figure 7.1 shows the X-ray diffraction patterns of $La_{0.7}Te_{0.3}Mn_{1-x}Co_xO_3$ with x=0, 0.1, 0.2, 0.25, 0.3 and 0.5. The samples with x=0 and 0.1 were indexed using ICDD Pattern No. 86-1234 with space group R-3c with rhombohedral symmetry while that with x≥0.2 were indexed using ICSD Pattern No. 82820 with space group Pbnm with orthorhombic symmetry. It can be seen that with increase in Co substitution, there is a structural transition from rhombohedral to orthorhombic. This transition is associated with the breakdown of structural symmetry, which may be attributed to the disordered distribution of Mn^{2+}/Mn^{3+} and Co^{2+}/Co^{3+} ions (Tai *et al*., 2000). When the doping level

of cobalt is increased to 0.2, noticeable changes occur in the structure, which is evident from the change in behavior of the main peak in the XRD data. It can be clearly seen that the double peaks at about 32.7° transforms into a single well defined peak as the Co doping concentration is increased to 0.2 suggesting a possible change in the structure. The splitting vanishes for higher Co doping concentrations. This is attributed to the transformation of rhombohedral structure for x=0 and 0.1 to orthorhombic structure for x≥0.2. The refinement results for all the compositions are shown in Figures 7.2-7.7. The lattice parameters, bond angles and bond distances obtained from Rietveld refinement are tabulated in Table 7.1. The change in crystal structure from rhombohedral to orthorhombic is schematically depicted in Figure 7.8. It can be seen that there is an increase in the lattice parameters a, b, c and unit cell volume with increase in Co concentration in rhombohedral structured samples (x =0 and 0.1) with R-3c space group. On the other hand, there is a reduction in the unit cell volume in the orthorhombic samples with Pbnm space group (x=0.2, 0.25, 0.3 and 0.5).

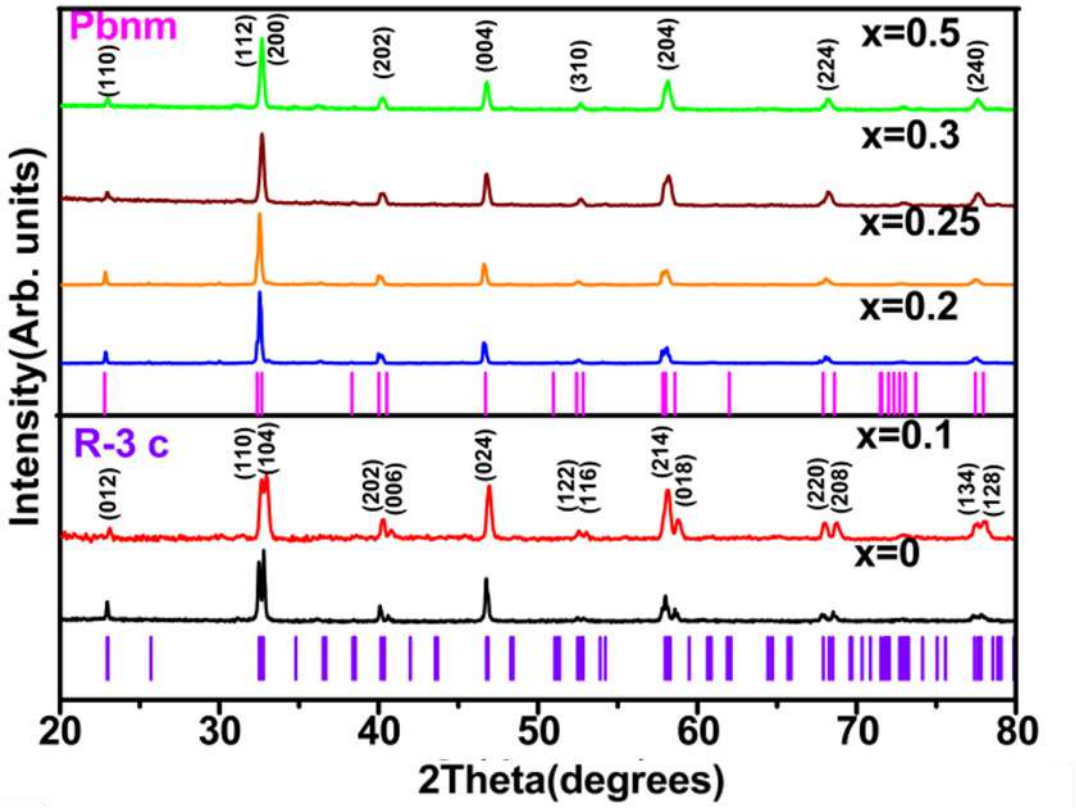

Figure 7.1. XRD patterns of $La_{0.7}Te_{0.3}Mn_{1-x}Co_xO_3$ (x=0, 0.1, 0.2, 0.25, 0.3 and 0.5)

The lattice distortion and the bending of Mn-O-Mn bond increase as the crystal structure transform from rhombohedral to orthorhombic. The possible origins of lattice distortion in perovskites is the deformation of the MnO_6 octahedra originating from Jahn-Tellar effect which is directly related to the concentration of Mn^{3+} ions (Yang *et al.*, 2004). For the present samples, the average ionic radius of A-site (r_A) is fixed. Hence, the observed lattice distortion is caused by the average ionic radius of the B-site element (r_B), which is governed by the tolerance factor

$$t = (r_A + r_o) / \sqrt{2}(r_B + r_o) \qquad (7.1)$$

where r_i (i=A, B, or O) represents the average ionic radii of each element. When t is close to 1, the cubic perovskite structure is expected to form. As t decreases, the lattice structure transforms to rhombohedral (R-3 c), and then to the orthorhombic (Pbnm) structure. In these samples, the observed lattice distortion is caused by the partial replacement of Mn by Co. For the low Co concentration $0 \leq x \leq 0.1$, the lattice volume increases with increase in Co concentration to x=0.1, also an increase in Mn–O bond length and a decrease in the average Mn–O–Mn bond angle are observed. The change in

the ionic radius of Mn at the dopant site from the average value causes a strain in the Mn–O bonds. Only a bigger ion at the dopant site can compress some of the Mn–O–Mn bonds which result in reducing the average Mn–O–Mn bond angle. The substitution of Co introduces Co^{2+} and Co^{3+} ions into the system, in which the former is introduced through a charge redistribution (CR) process (Park *et al*., 1997; Park, 1999; Tai *et al*., 2000, Chang *et al*., 2000). The Co^{2+} ionic radius (0.745 Å) is larger than the average radius of Mn ion (0.704 Å). Hence the increase in lattice volume with increase in cobalt content from x=0 to 0.1 is due to the replacement of Mn^{3+} ions (0.645 Å) by larger Co^{2+} ions (0.745 Å) (Zheng *et al*., 2006; Shannon *et al*., 1976). The presence of Mn^{4+} ions produced through the CR process has been confirmed by XPS analysis. However, for higher doping concentrations, the unit-cell volume decreases. The Mn–O bond length and the average Mn–O–Mn bond angle also decreases with increasing Co concentration. When the ionic radius of the dopant site is smaller than the average Mn radius, the neighboring Mn–O bonds contract, resulting in a decrease in the average Mn–O–Mn bond angle. Hence, the decrease in the orthorhombic lattice volume with increase in cobalt content from x=0.2 to 0.5 is caused by the replacement of Mn^{3+} ions (r= 0.645 Å) by smaller Co^{3+} ions (0.61 Å) (Zheng *et al*., 2006; Shannon *et al*., 1976).

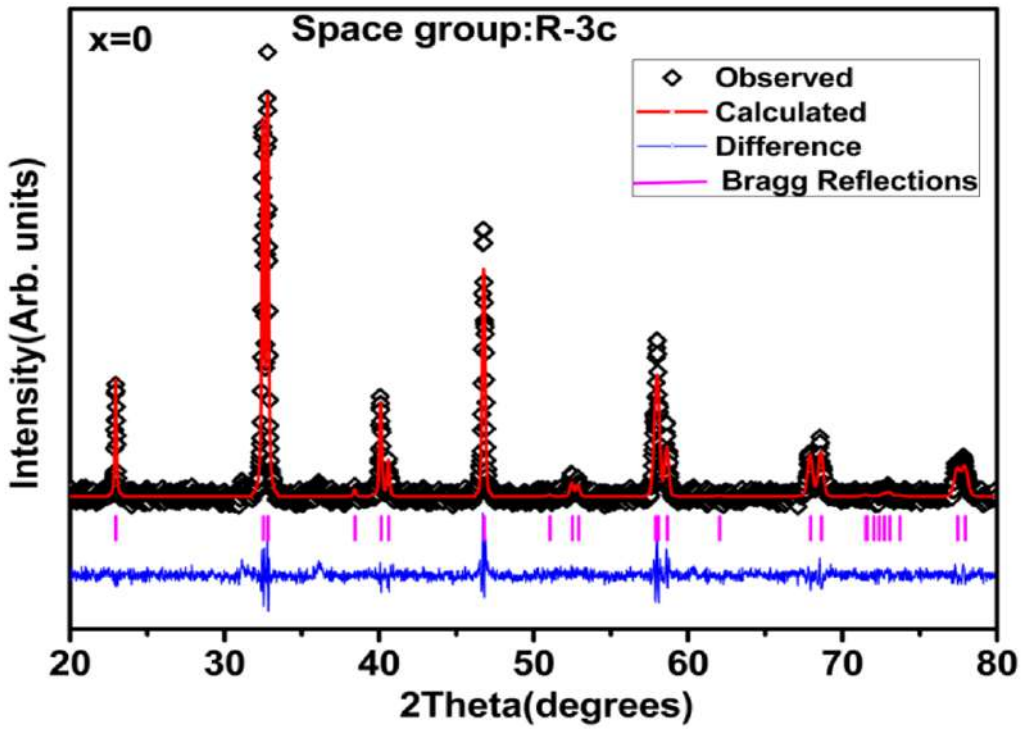

Figure 7.2. Rietveld refined XRD patterns of $La_{0.7}Te_{0.3}MnO_3$ (x=0).

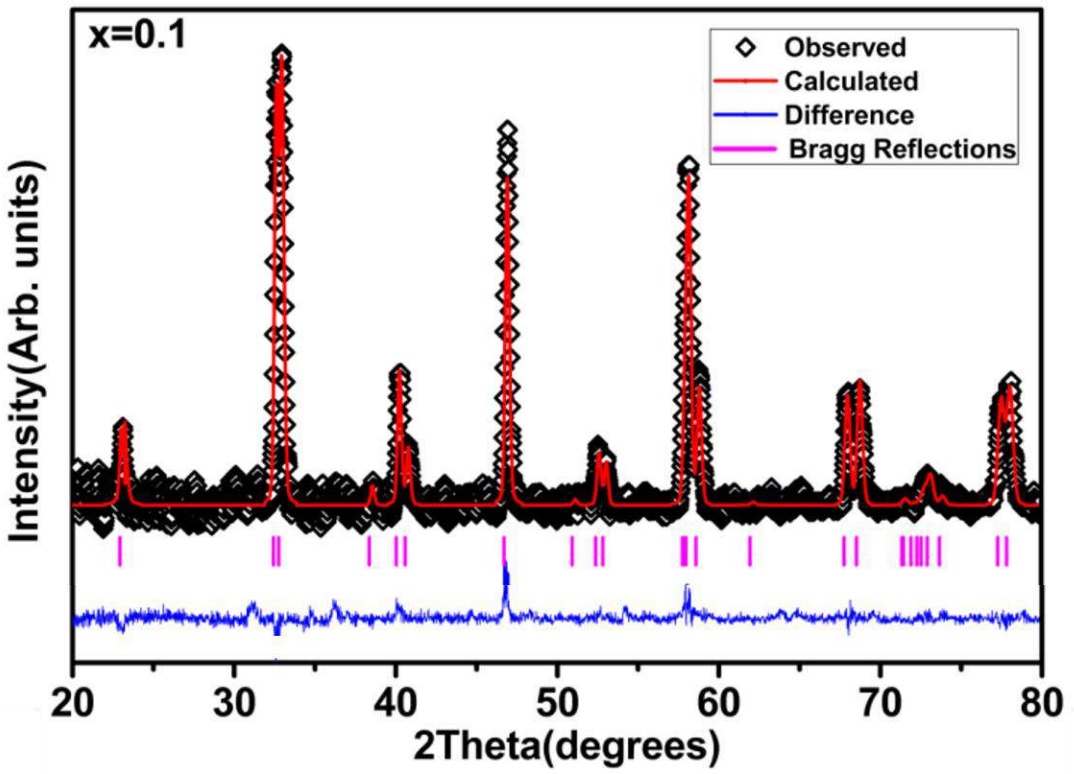

Figure 7.3. Rietveld refined XRD patterns of $La_{0.7}Te_{0.3}Mn_{0.9}Co_{0.1}O_3$ (x=0.1).

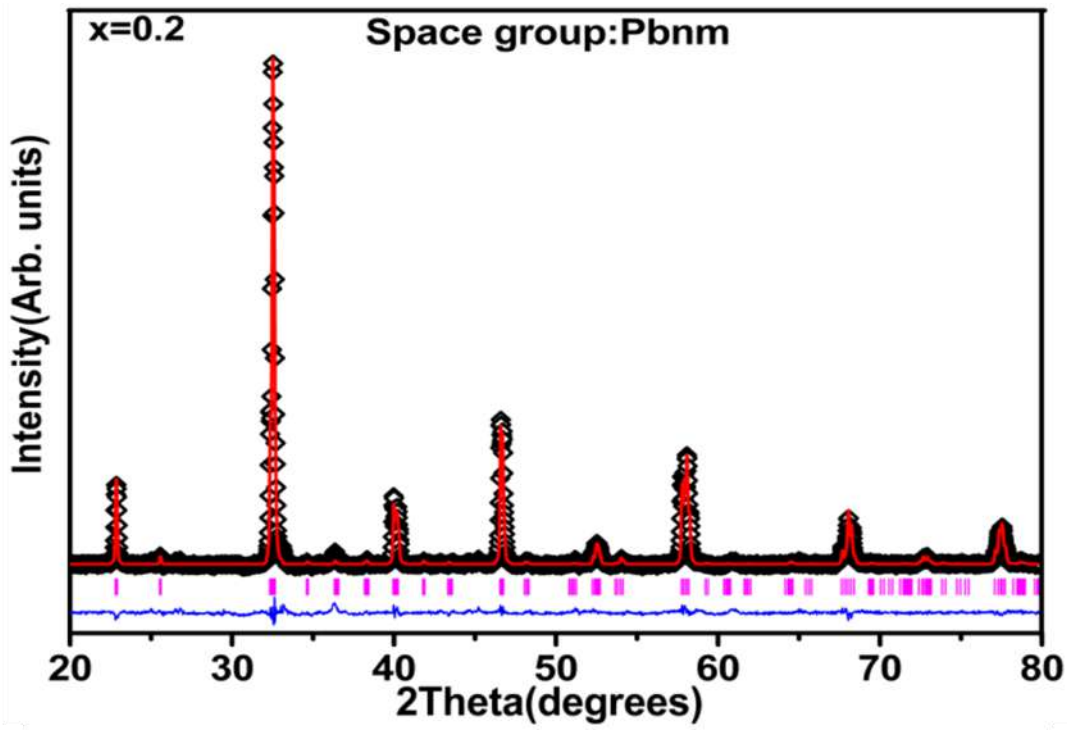

Figure 7.4. Rietveld refined XRD patterns of $La_{0.7}Te_{0.3}Mn_{0.8}Co_{0.2}O_3$ (x = 0.2).

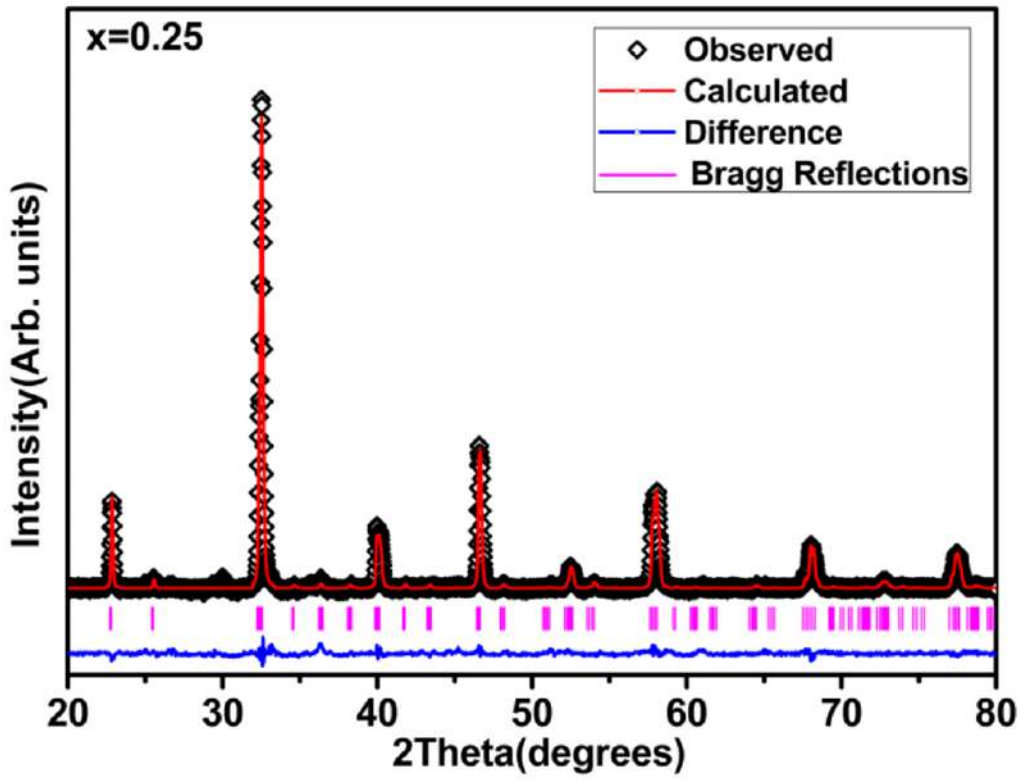

Figure 7.5. Rietveld refined XRD patterns of $La_{0.7}Te_{0.3}Mn_{0.75}Co_{0.25}O_3$ (x = 0.25).

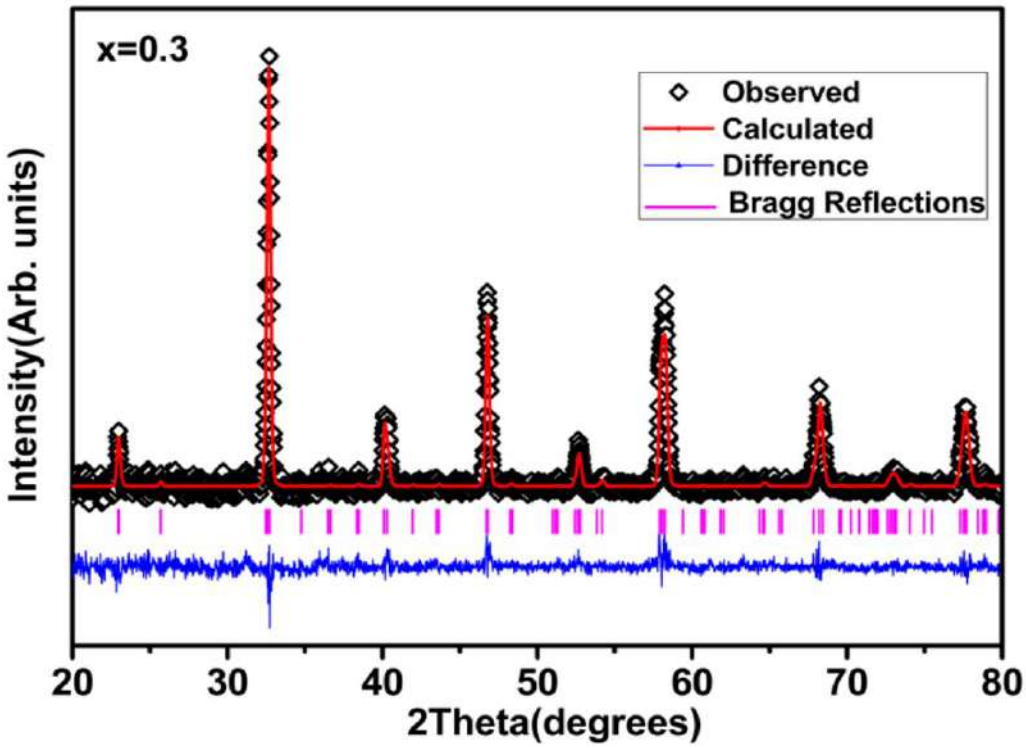

Figure 7.6. Rietveld refined XRD patterns of $La_{0.7}Te_{0.3}Mn_{0.7}Co_{0.3}O_3$ (x = 0.3).

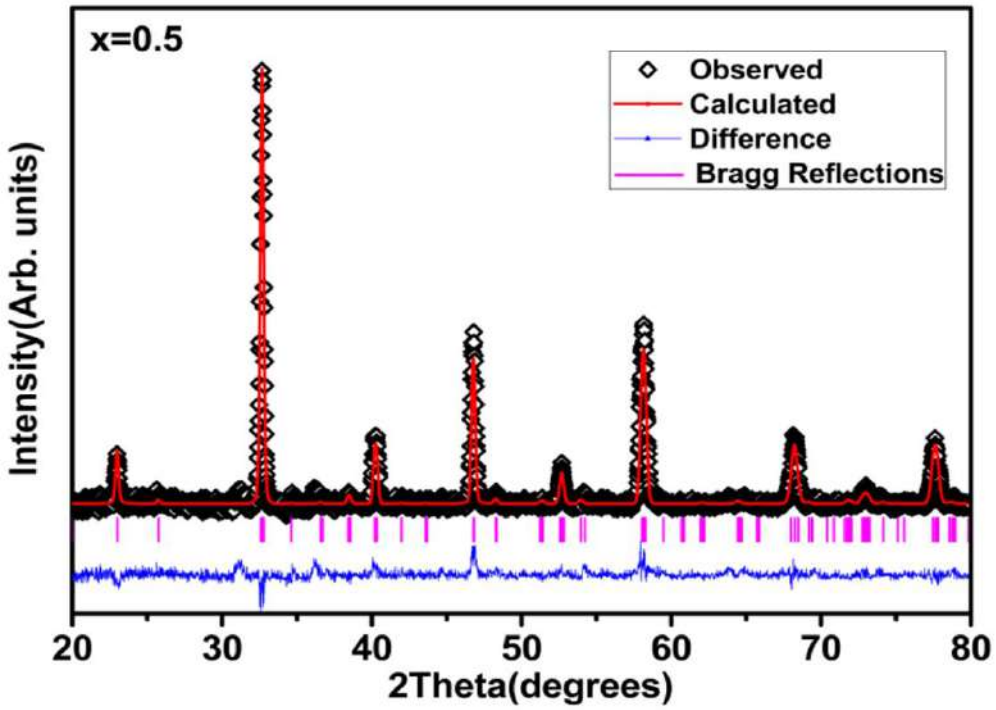

Figure 7.7. Rietveld refined XRD patterns of $La_{0.7}Te_{0.3}Mn_{0.5}Co_{0.5}O_3$ (x = 0.5).

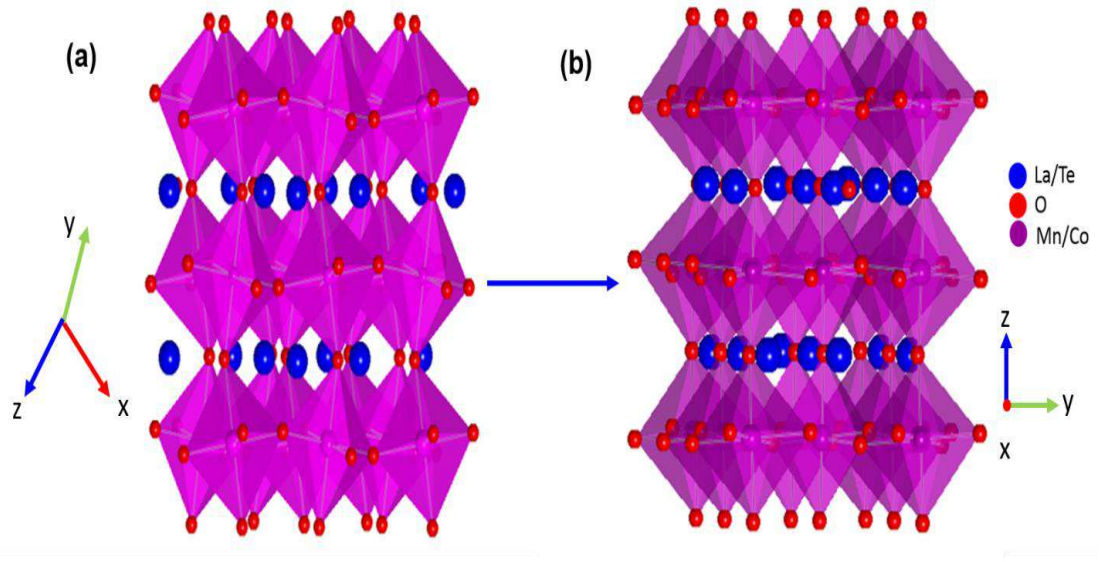

Figure 7.8. Projections of (a) the rhombohedral R-3c crystal structure and (b) the orthorhombic Pbnm crystal structure

Table 7.1. Lattice parameters, unit cell volume, bond angles and bond distances determined from Rietveld refinement of $La_{0.7}Te_{0.3}Mn_{1-x}Co_xO_3$ (x=0, 0.1, 0.2, 0.25, 0.3 and 0.5)

Sample	x=0	x=0.1	x=0.2	x=0.25	x=0.3	x=0.5
Space Group	R -3 c	R -3 c	Pbnm	Pbnm	Pbnm	Pbnm
Lattice parameters						
a (Å)	5.52 (0)	5.53(1)	5.54(0)	5.53(1)	5.53(1)	5.52(1)
b (Å)	5.52 (0)	5.53(1)	5.50(1)	5.49(0)	5.49(1)	5.49(1)
c (Å)	13.35(1)	13.35(1)	7.79(1)	7.78(0)	7.78(0)	7.78(1)
Volume(Å)	352.69(4)	353.97(1)	237.13(4)	236.56(4)	236.34(1)	236.10(1)
Atomic Positions						
La/Te x	0	0	0.998(0)	0.996(0)	0.997(0)	0.998(1)
La/Te y	0	0	0.017(0)	0.019(0)	0.018(0)	0.022(1)
La/Te z	0.25	0.25	0.25	0.25	0.25	0.25
Mn/Co x	0	0	0.5	0.5	0.5	0.5
Mn/Co y	0	0	0	0	0	0
Mn/Co z	0	0	0	0	0	0
O_1 x	0.455(0)	0.430(0)	0.05(0)	0.04(0)	0.04(0)	0.03(0)
O_1 y	0	0	0.47(1)	0.48(0)	0.50(0)	0.50(0)
O_1 z	0.25	0.25	0.25	0.25	0.25	0.25
O_2 x	-	-	0.70(1)	0.69(1)	0.69(0)	0.70(0)
O_2 y	-	-	0.25(1)	0.26(0)	0.32(0)	0.30(0)
O_2 z	-	-	0.03(0)	0.02(0)	0.02(0)	0.04(0)
Bond distance						
Mn-O_1 (Å)	1.96(7)	1.98(5)	1.97(1)	1.96(1)	1.96(1)	1.95(1)
Mn-O_2 (Å)	-	-	1.76(1)	1.78(0)	2.04(9)	2.01(1)
Mn-O_2 (Å)	-	-	2.18(9)	2.18(1)	2.00(0)	2.02(0)
Bond angle						
Mn-O_1-Mn(°)	165.5(0)	157.3(5)	161.7(9)	164.9 (0)	167.1(1)	169.7(2)
Mn-O_2-Mn(°)	-	-	163.7(6)	159.9 (0)	148.9(0)	150.1(2)
χ^2	1.3	2.8	2.7	2.3	3.6	2.6

7.3.2. XPS analysis

To determine the surface elemental composition and oxidation states of Mn and Co in the near-surface range, X-ray photoelectron spectra (XPS) of $La_{0.7}Te_{0.3}Mn_{1-x}Co_xO_3$ (x=0.1 and 0.3) was recorded. The wide scan XPS spectra of x=0.1 and 0.3, is presented in the supplementary data, Figure 7.9. Evidently, all the peaks can be ascribed to the elements La, Te, Mn, Co and O in the near-surface range which is in good agreement with our expectation. No other element is found from the XPS spectrum, indicating the purity of the sample. The high-resolution Co 2p and Mn 2p spectra were recorded. Figure 7.10 shows the Mn $2p_{3/2}$ high resolution XPS spectrum recorded for x=0.1 and x=0.3 respectively. The high resolution spectra of Co 2p for x=0 and x=0.3 are shown in Figures 7.11 and 7.12 respectively.

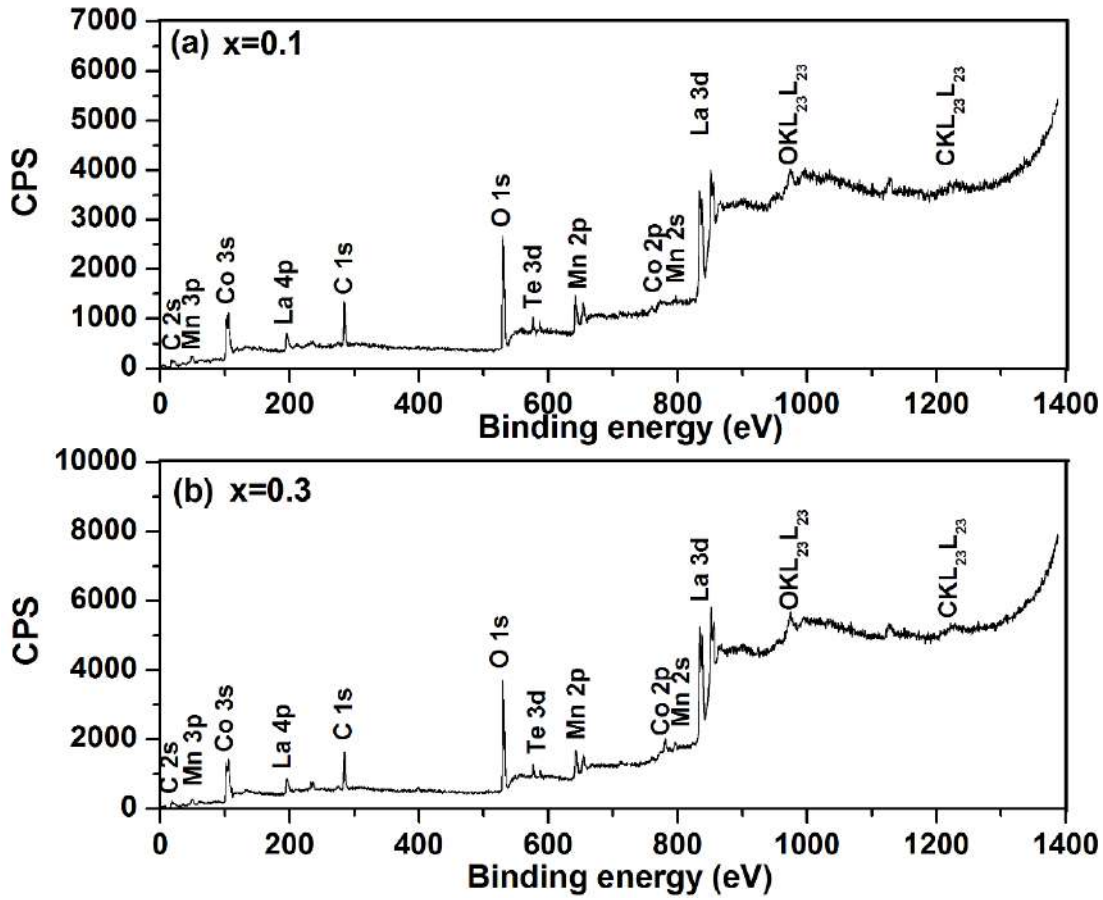

Figure 7.9. XPS wide scan spectra of $La_{0.7}Te_{0.3}Mn_{1-x}Co_xO_3$ (a) x=0.1 and (b) x=0.3.

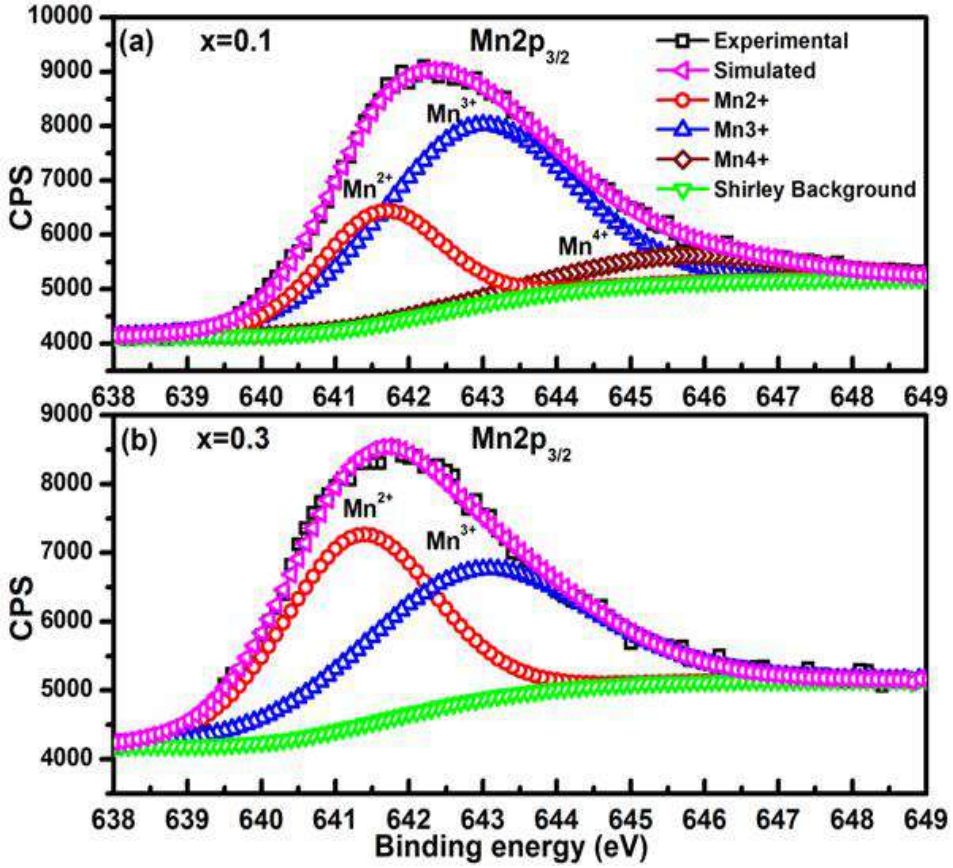

Figure 7.10. Mn $2p_{3/2}$ XPS spectra of $La_{0.7}Te_{0.3}Mn_{1-x}Co_xO_3$ (a) x=0.1 and (b) x=0.3.

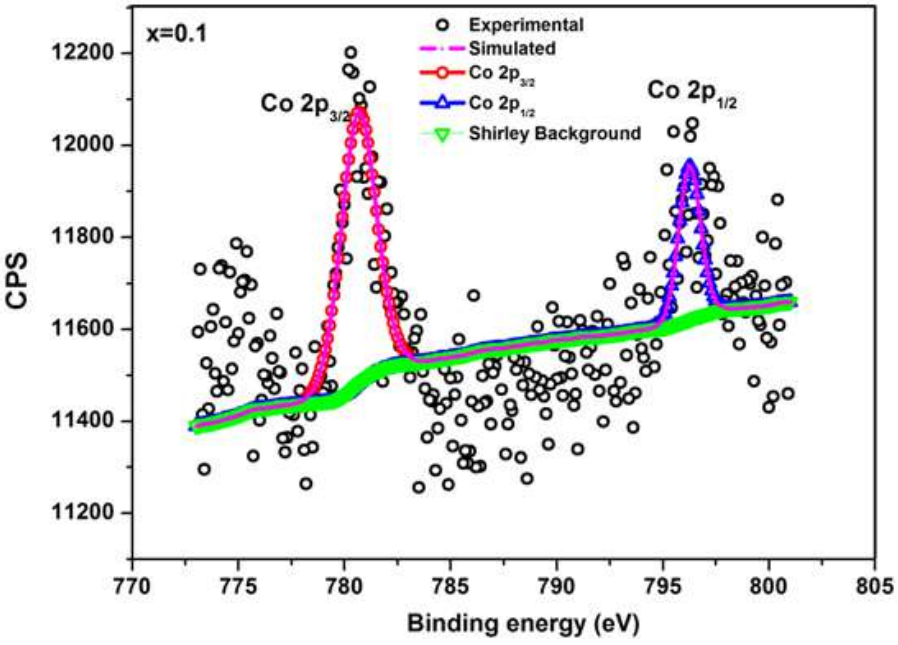

Figure 7.11. Co 2p XPS spectra of $La_{0.7}Te_{0.3}Mn_{1-x}Co_xO_3$for x=0.1.

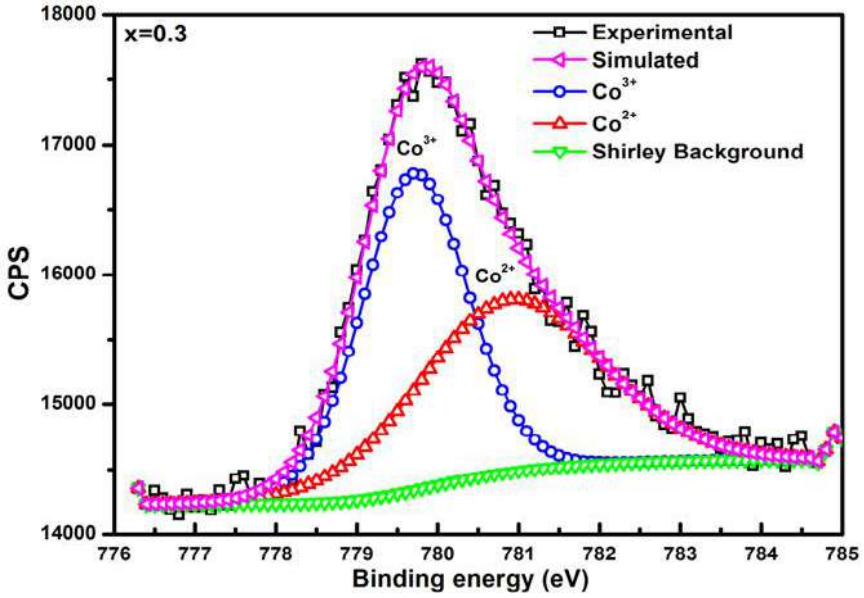

Figure 7.12. Co $2p_{3/2}$ XPS spectra of $La_{0.7}Te_{0.3}Mn_{1-x}Co_xO_3$ for x=0.3

For x=0.1, the Mn $2p_{3/2}$ XPS spectrum decompose into three components corresponding to Mn^{2+}, Mn $^{3+}$ and Mn^{4+} located at 641.6, 642.9 and 645.6 eV, whereas for x=0.3, the Mn $2p_{3/2}$ XPS spectrum decompose only into two components corresponding to Mn^{2+} and Mn^{3+} located at 641.3 and 642.8 eV respectively (Huang *et al*., 2015; Jha *et al*., 2014). Regarding the Co $2p_{3/2}$ XPS spectrum of x=0.3, the binding energies observed at 779.7 and 780.9 eV corresponds to Co^{3+} and Co^{2+} respectively (Jha *et al*., 2014). The presence of Mn^{4+} ions in x=0.1 samples suggest that a charge redistribution process has occurred at low cobalt doping concentrations. It can be seen that there is a decrease in the Mn^{3+} concentration in x=0.3 when compared to that in x=0.1. This is attributed to the replacement of Mn^{3+} ions with Co^{3+} ions when x increases to 0.3. Correspondingly, the Mn^{2+} ions increases to maintain the charge neutrality. Therefore, the distribution of Mn^{2+}/Mn^{3+} and Co^{2+}/Co^{3+} ions induces a structural transition in these compounds when x increases to 0.2.

7.3.3. Magnetization measurements

7.3.3.1.Temperature dependent magnetization studies

In order to investigate the effect of Co doping on the magnetic properties of $La_{0.7}Te_{0.3}Mn_{1-x}Co_xO_3$, the temperature dependence of magnetization was measured under zero field cooled (ZFC) and field cooled cool (FCC) mode in an applied field of 100 Oe for x=0, 0.1, 0.2, 0.25, 0.3 and 0.5. The results are presented in Figure 7.13. All the

samples exhibit a paramagnetic (PM) to ferromagnetic (FM) transition. The M (T) curves of x=0 and x=0.1 clearly indicate a double transition under 100 Oe field; the first one is a very sharp transition at higher temperatures ≥ 160 K, resembling a PM to FM transition, and the other one is at lower temperatures below 75 K, resembling a spin glass state. With increase in Co doping to x=0.3, the PM-FM phase transition become broader implying a wide distribution of the magnetic exchange interactions in the Mn-O-Mn network with the increase of magnetic inhomogeneity (Zheng *et al*., 2006). The Curie temperatures (T_C) have been determined from the derivative of the M-T curves and are 165 K, 160 K, 162 K, 167 K, 180 K and 220 K respectively for x=0, 0.1, 0.2, 0.25, 0.3 and 0.5. The decrease in the average bond angle results in the weakening of the DE interactions leading to a decrease in the Curie temperature from 165 K in x=0 to 160 K in x=0.1. The increase in Co concentration causes the Mn-O_1-Mn bond angle to increase indicating a stronger Mn-O-Mn exchange interaction leading to an increase in the Curie temperature for x ≥ 0.2 (Bejara *et al*., 2007; Craus *et al*., 2010). The divergence between ZFC and FCC curves becomes more and more obvious because of the increase in magnetic frustration arising from the bending of Mn-O-Mn bond, which is in accordance with the structural refinement results (Yang *et al*., 2004). This irreversibility in ZFC and FCC magnetization curves arises possibly due to the canted nature of the spins or due to the random freezing of spins as observed in systems with FM cluster coexisting in AFM matrix and is ascribed to the appearance of the spin glass (SG) or cluster glass (CG) induced by the competing FM and antiferromagnetic (AFM) exchange interactions (Yang *et al*., 2004; Dho *et al*., 2002). The substitution of Co introduces Co^{2+} and Co^{3+} ions into the system. Moreover, Mn^{4+} ions are also introduced into the system through a CR process as in the case of $LaMn_{1-x}Co_xO_3$ (Park *et al*., 1997; Park *et al*., 1999) and the hole-doped manganite $La_{0.7}Ba_{0.3}Mn_{1-x}Co_xO_3$ (Tai *et al*., 2000; Chang *et al*., 2000). Therefore, there exist FM exchange interactions viz. Mn^{2+}-O-Mn^{3+}, Mn^{3+}-O-Mn^{4+}, Mn^{2+}-O-Mn^{4+} and Co^{2+}-O-Mn^{4+} and AFM exchange interactions viz. Co^{2+}-O-Co^{2+}, Mn^{4+}-O-Mn^{4+}, Co^{3+}-O-Co^{3+} and Co^{2+}-O-Mn^{3+} in the studied samples competing each other, and this competition leads to the appearance of magnetic inhomogeneity in the samples (Zheng *et al*., 2006). It can be seen that for x=0 and x=0.1, a drop in ZFC magnetization is observed around 75 K on lowering the temperature. This is also attributed to the glassy state present in the system.

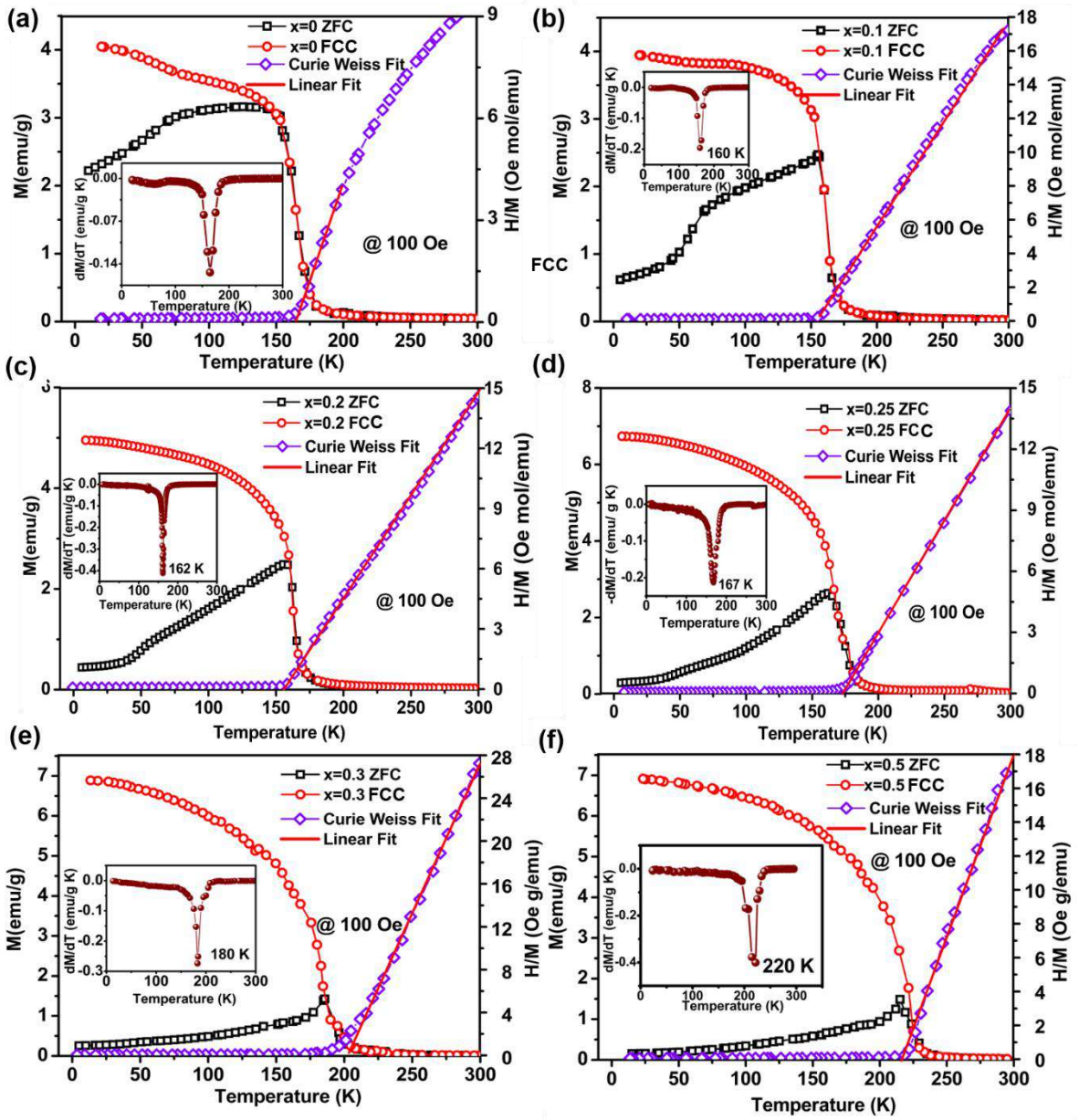

Figure 7.13. Magnetization as a function of temperature for $La_{0.7}Te_{0.3}Mn_{1-x}Co_xO_3$ (a) x=0, (b) x= 0.1, (c) x= 0.2, (d) x=0.25, (e) x=0.3 and (f) x= 0.5 measured at H = 100 Oe under the ZFC and FCC modes and the corresponding Curie-Weiss fit. Inset shows the derivative of the M-T curves.

For further analysis, we have carried out the AC susceptibility studies of x=0 and x=0.1. The results of temperature dependent AC susceptibility measurements at different frequencies is presented in Figure 7.14. It can be seen from Figure 7.14 (a) and 7.14 (b), that there is a sharp peak near 165 K and 160 K respectively for x=0 and x=0.1 and a drop in the susceptibility below 75 K for both the samples, akin to the features observed in the

ZFC magnetization presented in Figure 7.13 (a) and 7.13 (b). The two peaks in the χ'(T) curves reflect the ferromagnetic and spin-glass phase transitions and are denoted as T_c and T_f respectively, reminiscent of those of reentrant ferromagnets. The higher temperature FM-PM transition shows no frequency dependence, while the low temperature transition shows a clear frequency dependence suggesting a glassy state (Jonason *et al*., 1996; Mathieu *et al*., 2000, Choudhury *et al*., 2012).

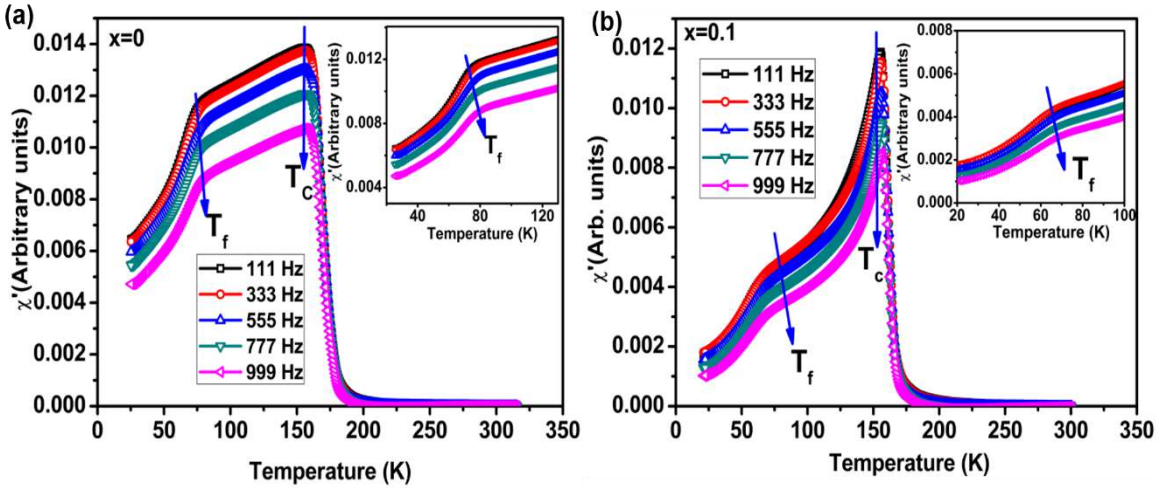

Figure 7.14. Temperature dependence of AC susceptibility of (a) x=0 and (b) x=0.1 at different frequencies. Insets of (a) and (b) shows the frequency dependence of the samples at low temperatures.

A detailed analysis of the susceptibility data at T_f has been carried out to analyse the spin glass behavior. The maximum change in the freezing temperature, ΔT_f is denoted as $\Delta T_f(\omega) = T_f^{999\ Hz} - T_f^{111\ Hz}$ where $T_f^{999\ Hz}$ and $T_f^{111\ Hz}$ represents T_f at 999 Hz and 111 Hz, respectively. The relative shift in freezing temperature $\Delta T_f = \Delta T_f(\omega)/T_f\, \Delta\log(\omega)$ is used to describe the magnetic order of the system. This value typically lies between 0.005 and 0.08 for spin glass and is 2 for non-interacting super paramagnetic materials. The relative shift obtained for x=0 and x=0.1 are 0.054 ± 0.001 and 0.058 ± 0.006 respectively, which characterize our system to be of reentrant spin glass type (RSG) (Anil kumar *et al*., 2014; Chatterjee *et al*., 2010; Chandrasekhar *et al*., 2012). The frequency-dependent T_f (in χ'(T) versus T plot) fitted to an Arrhenius law showed unreasonable fitting. Hence, Vogel- Fulcher (VF) law, $\tau = \tau_0 \exp\left(\frac{E_{VF}}{k_B(T_f - T_{VF})}\right)$ was employed to understand the nature of interaction in the spin glass system, where E_{VF} and T_{VF} are the activation energy

and Vogel- Fulcher temperature respectively. The obtained fitting parameters are E_{VF}/k_B= 9.3 ± 0.8, T_{VF}= (64.8 ± 0.1) K and τ_o = (2.06 ± 0.01) x 10^{-5} s respectively for x=0 and E_{VF}/k_B= 5.6 ± 0.4, T_{VF}= (53.2 ± 0.1) K and τ_o = (5.14 ± 0.07) x 10^{-5} s respectively for x=0.1. Dynamical scaling analysis was also performed using the critical power law, $\frac{\tau}{\tau_0}=\left(\frac{T_f}{T_g}-1\right)^{-z\upsilon}$, where τ is the relaxation time corresponding to the measured frequency f ($\tau = 1/2\pi f$), τ_o, the characteristic relaxation time of single spin flip and indicates the nature typical of atomic-scale spin-glass state caused by the geometrical frustration (Mathieu *et al*., 2004) and are obtained as (2.90 ± 0.01) x 10^{-6} s and (9.79 ± 0.03) x 10^{-6} s respectively for x=0 and x=0.1.

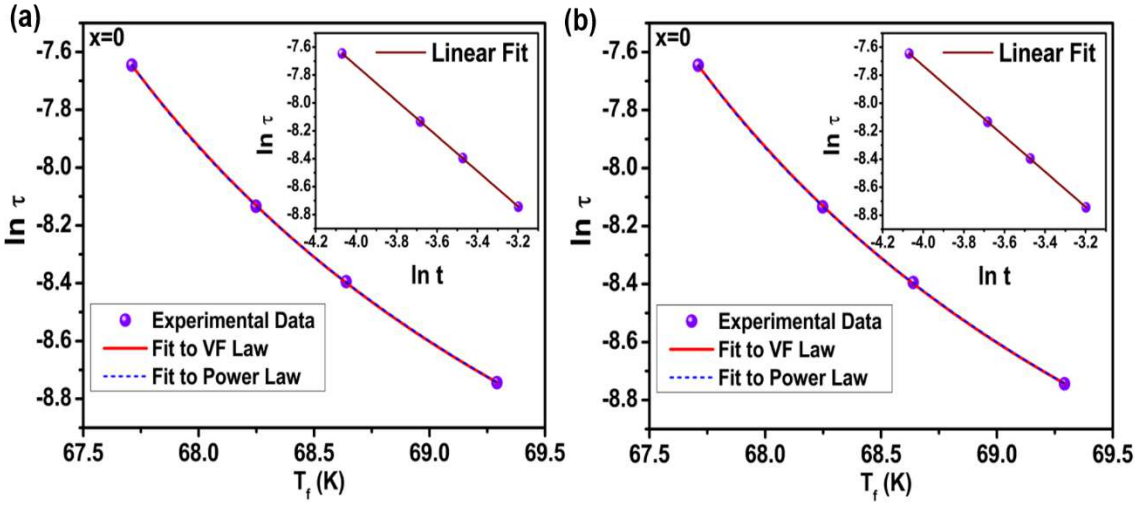

Figure 7.15. Relaxation time τ versus maximum spin freezing temperature T_f fitted to the Vogel-Fulcher Law (solid line) and Power law (Dashed line). Inset shows ln(τ) vs. ln(t) where reduced temperature, t= $(T_f-T_g)/T_g$. Solid line is a linear fit to the Power Law.

Figure 7.15 shows the fit to the VF law and critical power law. From the analysis, the critical spin glass ordering temperature as frequency tends to zero, T_g, and the dynamic critical exponent, zν are determined as 66.56 ± 0.03 K and 1.27 ± 0.03 for x=0 and 54.47 ± 0.01 K and 1.03 ± 0.01 for x=0.1 respectively. Here, z and ν denote the dynamical critical exponent and the critical exponent of the spin correlation length, $\xi=\left(\frac{T_f}{T_g}-1\right)^{-\upsilon}$ respectively. For a spin-glass system, τ_o ~10^{-10}-10^{-13} s and zν are typically

found to lie between 4 and 12. Hence, the higher values of τ_o and lower value of zv obtained for x=0 and x=0.1 implies that the relaxation is slower indicating slower spin flipping and that the RSG phase is attributed to the presence of randomly oriented ferromagnetic clusters, instead of atomic level randomness. Such higher τ_o values have also been reported in other RSG systems such as $LaCo_{0.5}Ni_{0.5}O_3$ (Viswanathan *et al*., 2009), Heusler alloys (Chatterjee *et al*., 2010; Halder *et al*., 2010), pyrochlore molybdates (Hanasaki *et al*., 2007), etc.

7.3.3.2. Isothermal magnetization studies and magnetocaloric effect

Figure 7.16 shows the isothermal magnetization studies for all the samples carried out in a field range of 0−50 kOe at various temperatures between 120 K-240 K in a temperature interval of 5 K. It can be seen that the magnetization increases sharply at lower fields and then increases gradually with increasing field and does not show any sign of saturation, even at 50 kOe.

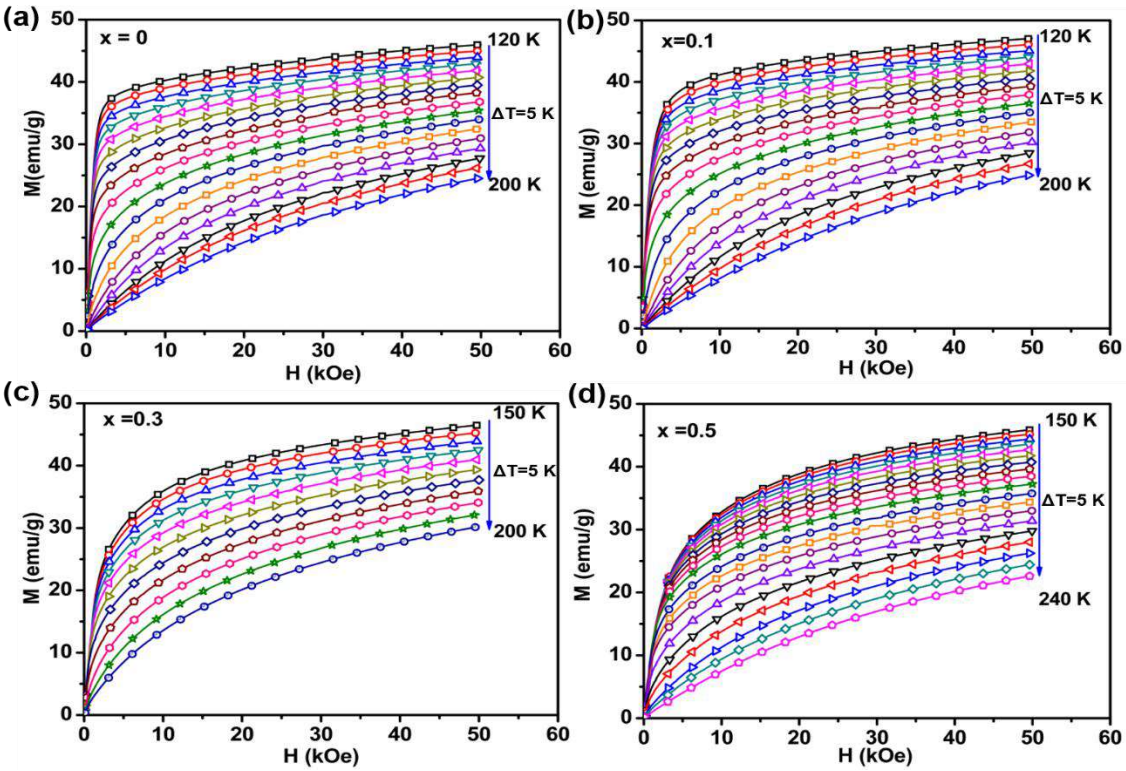

Figure 7.16. Isothermal magnetization curves measured at different temperatures between 120 K and 240 K for $La_{0.7}Te_{0.3}Mn_{1-x}Co_xO_3$ (x=0, 0.1, 0.3 and 0.5).

The isothermal M-H curves were used to estimate the magnetic entropy change ($-\Delta S_M$) for all the samples using Equation 1.19 described in Chapter 1 and are shown in Figure 7.17. All the curves show a broad maximum of $-\Delta S_M$ around their respective T_C. The value of $-\Delta S_M$ peak increases with the field and the peak position remain nearly unaffected. Under a magnetic-field variation of 50 kOe, the maximum magnetic entropy change for $La_{0.7}Te_{0.3}Mn_{1-x}Co_xO_3$ is 2.1, 2.3, 2.4, 2.2 J/kg K for x=0, 0.1, 0.3 and 0.5 respectively. It can be seen that with increase in Co substitution, the $-\Delta S_M$ peak broadens. Also, there is only a gradual increase in the magnetic entropy change with increase in Co substitution. It can be clearly seen that MCE strongly depends on the values of ΔM.

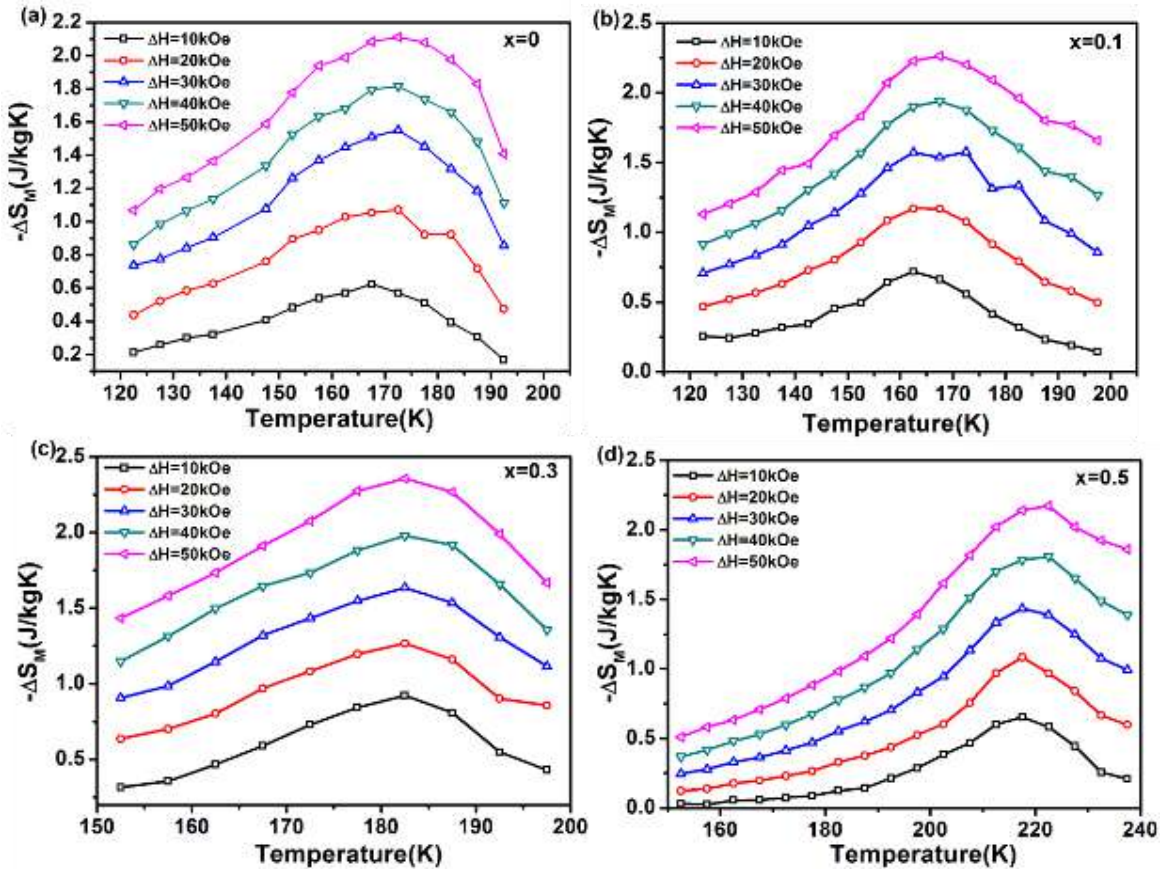

Figure 7.17. The magnetic entropy change $-\Delta S_M$ as a function of temperature in various magnetic fields for $La_{0.7}Te_{0.3}Mn_{1-x}Co_xO_3$ (x=0, 0.1, 0.3 and 0.5).

In addition to the magnetic entropy change, RCP corresponds to the amount of heat that can be transferred between the cold and hot reservoirs of the refrigerator in an

ideal thermodynamic cycle (Gschneidner *et al*., 2000). The goodness of the RCP in a given magnetic field is reflected in the efficiency of the refrigerator. The magnetic cooling efficiency of a magnetocaloric material can be evaluated by Equation (1.26) described in Chapter 1. The RCP values obtained for x= 0, 0.1, 0.3 and 0.5 for a field change of 50 kOe are 94, 110 and 115 and 121 J/kg respectively and is shown in Figure 7.18. The compounds show considerable RCP making it promising candidate for magnetic refrigeration applications in the sub room temperatures.

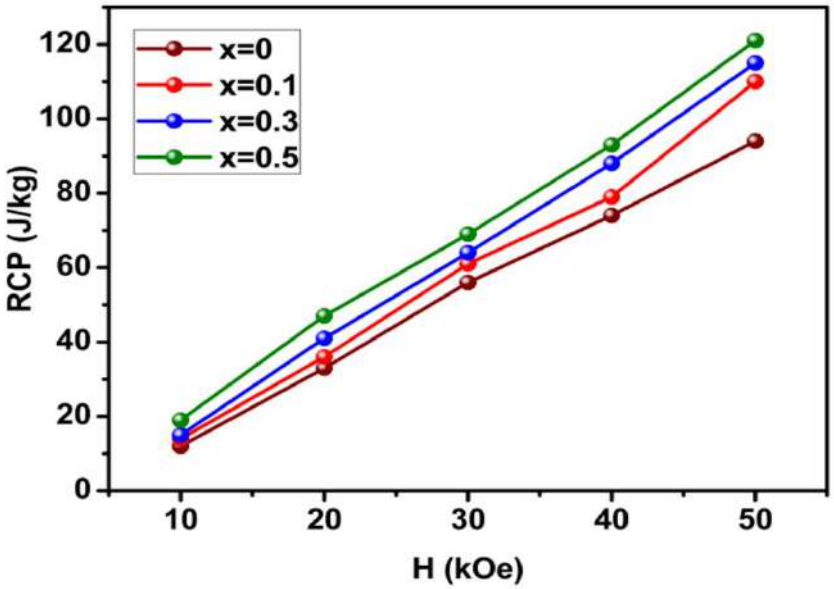

Figure 7.18. RCP of $La_{0.7}Te_{0.3}Mn_{1-x}Co_xO_3$ (x=0, 0.1, 0.3 and 0.5) at different fields.

7.3.4. Critical exponent analysis

In an attempt to understand the exact nature of the FM-PM phase transition, Arrott plots (M^2 vs. H/M) were constructed for all the compositions x= 0, 0.1, 0.3 and 0.5 at different temperatures and is shown in Figure 7.19. Arrott plots are generally used to determine the order of the magnetic phase transitions. According to the criterion proposed by Banerjee, the order of magnetic transition can be determined from the slope of the isotherm plot (Banerjee, 1964). If the M^2 versus H/M curves show a negative slope, the transition is of first order while a positive slope corresponds to a second order transition. In our samples, the Arrott plots show a positive slope, thus confirming the second order nature of phase transition from PM to FM phase. This result is consistent with the absence of thermal hysteresis in the vicinity of the PM to FM transition as shown in Figure 7.13, thereby confirming the second order nature of this transition.

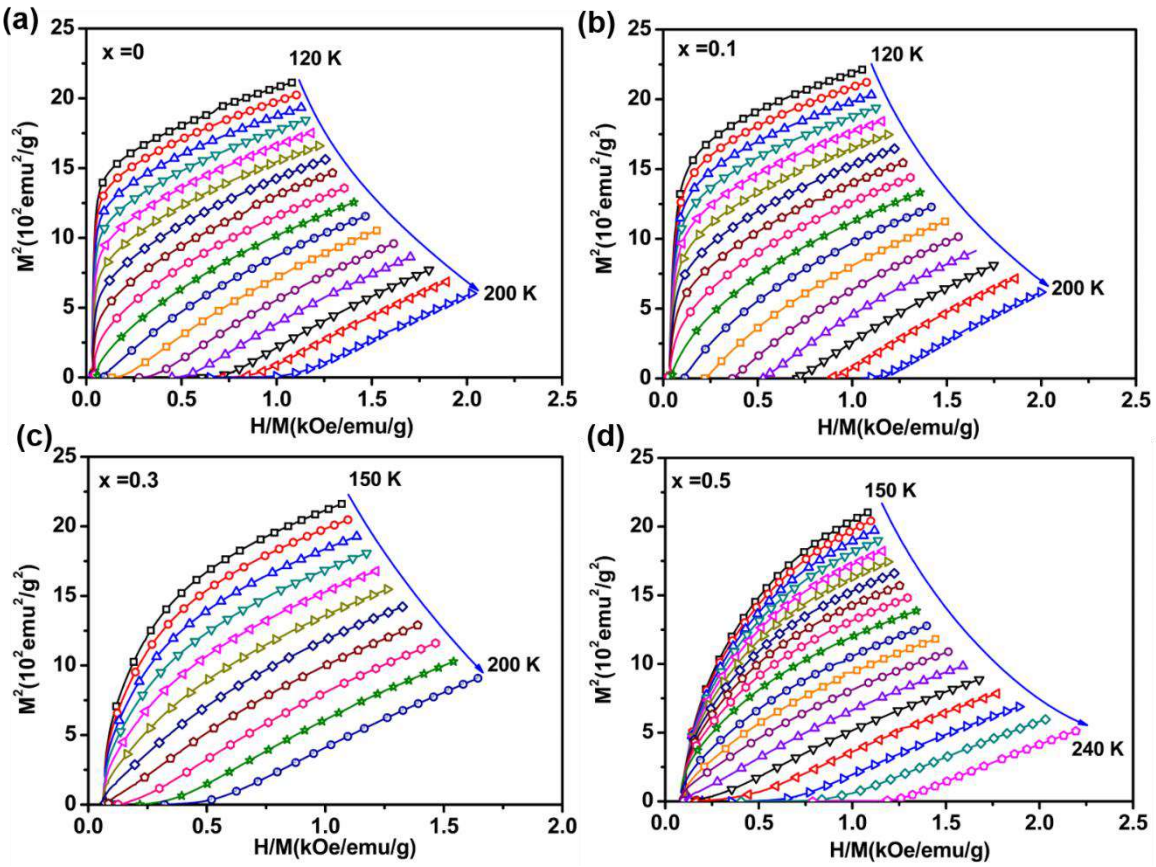

Figure 7.19. Arrott plots for $La_{0.7}Te_{0.3}Mn_{1-x}Co_xO_3$(x=0, 0.1, 0.3 and 0.5).

In order to understand the exact nature of magnetic phase transitions, we have carried out a detailed critical exponent analysis using scaling hypothesis for all the compositions. According to the scaling hypothesis, the critical behavior of magnetic systems showing second order magnetic phase transition near the Curie temperature is characterized by a set of interrelated critical exponents, β associated with the spontaneous magnetization (Ms), γ associated to the initial magnetic susceptibility (χ_0), and δ associated with the critical magnetization isotherm (Stanley *et al*., 1971). These critical exponents are mathematically expressed as:

$$M_S(T) = M_0(-t)^{\beta} \qquad t<0, T<T_c \qquad (7.2)$$

$$\chi_0^{-1}(T) = \frac{h_0}{M_0}(t)^{\gamma} \qquad t>0, T>T_c \qquad (7.3)$$

$$M = DH^{\frac{1}{\delta}} \qquad t=0, T=T_c \qquad (7.4)$$

where t =(1-T/T_C) is the reduced temperature and M_0, h_0/M_0 and D are the critical amplitudes. The critical exponents have been deduced from the field dependence of MCE, as reported by Franco *et al.* (Franco *et al.*, 2006; Franco *et al.*, 2007). The field dependence of the magnetic entropy change of materials with a second order phase transitions can be expressed as

$$\Delta S_M = a\, H^n \qquad (7.5)$$

where n depends on the magnetic state of the sample (Oesterreicher *et al.*, 1984). The value of n is determined from the linear plot of ln (-ΔS_M) vs. ln (H) at T_C and is shown in Figure 7.20 (a) and 7.20 (b). The obtained values of n are 0.79(1), 0.73(8), 0.66(1) and 0.73(8) for x=0, 0.1 0.3 and x=0.5 respectively. The critical exponents are determined by

$$n = 1 + \frac{1}{\delta}\left(1 - \frac{1}{\beta}\right) \qquad (7.6)$$

$$n = 1 + \frac{\beta - 1}{\beta + \gamma} \qquad (7.7)$$

The value of δ is independently determined from the slopes of ln M vs. ln H plot at T_C for all the compositions and the obtained values of δ are 3.9191 (4), 4.2063 (4), 3.5872 (7) and 3.0540 (7) respectively (insets of Figure 7.20 (a) and 7.20 (b)). The values of n, β, γ and δ are tabulated in Table 7.2. It can be seen that the nature of magnetic transition lie between the 3D Heisenberg model and the mean field model in these compounds. For x=0 and 0.1, none of the theoretical models, i.e., the 3D Heisenberg model or the Ising model with short range magnetic exchange interaction or the mean field model with long-range magnetic exchange interactions describe the magnetic phase transition completely. However, the deduced values of the critical exponents for x = 0.3 and 0.5 are close to that of the mean field model, though the value of γ is slightly higher than that predicted for the mean field model indicating long range magnetic interactions.

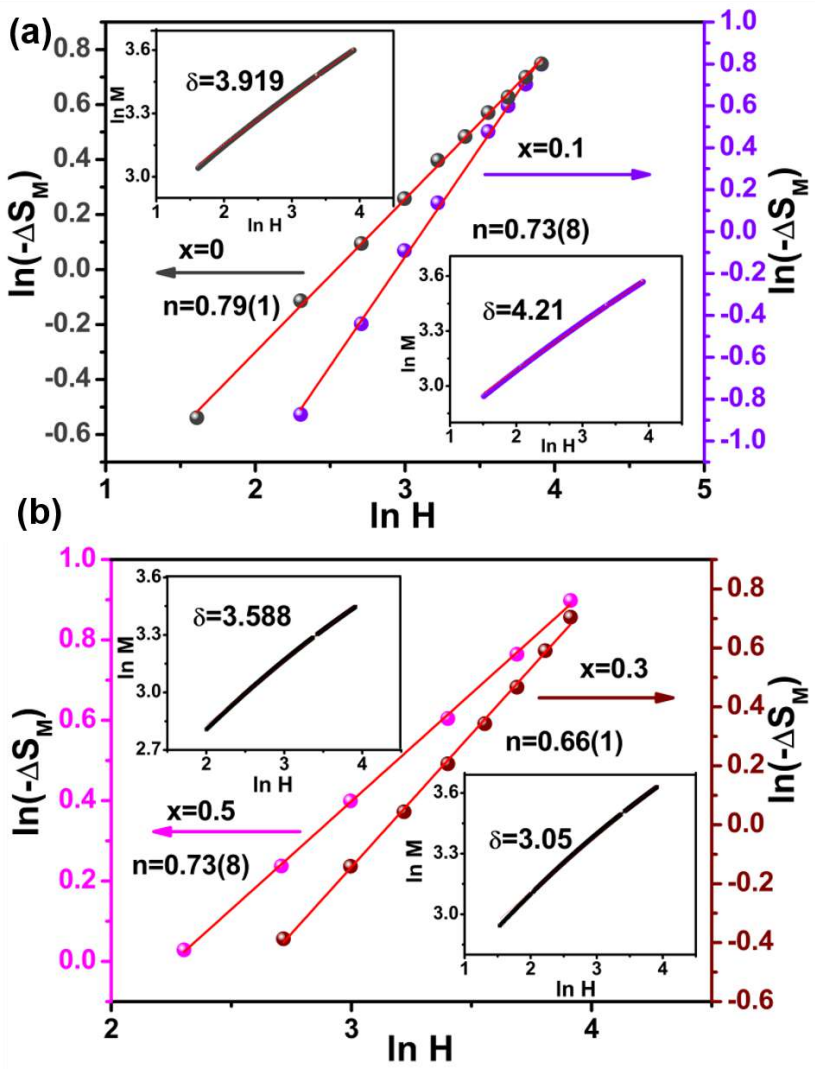

Figure 7.20. ln ($-\Delta S_M$) vs. ln (H) for $La_{0.7}Te_{0.3}Mn_{1-x}Co_xO_3$ (a) x=0 and x=0.1 and (b) x=0.3 and 0.5. Inset shows ln M vs ln H plots for $La_{0.7}Te_{0.3}Mn_{1-x}Co_xO_3$.

The reliability of the calculated exponents β and γ can be confirmed by using the scaling theory. According to the scaling hypothesis (Stanley *et al.*, 1999), M(H, t) is a universal function of T and H and the experimental M(H) curves in the critical region are expected to collapse into the universal curve following the relation

$$M(H,t)|t|^{-\beta} = f_{\pm}H|t|^{-(\beta+\gamma)} \qquad (7.8)$$

where f_+ and f_- are regular analytical functions which results in two different branches, i.e., for the paramagnetic state (+) for $T > T_C$ and the ferromagnetic state (−) for $T < T_C$ respectively and are depicted in Figure 7.21.

Table 7.2. Comparison of critical parameters for electron-doped manganite $La_{0.7}Te_{0.3}Mn_{1-x}Co_xO_3$ with the various theoretical models

Composition $La_{0.7}Te_{0.3}Mn_{1-x}Co_xO_3$	T_c(K)	n	β	γ	δ	Ref.
x=0	160	0.79±0.01	0.55±0.01	1.60±0.02	3.92±0.01	This work
x=0.1	165	0.73±0.01	0.47±0.01	1.50±0.01	4.21±0.01	This work
x=0.3	180	0.73±0.01	0.45±0.01	1.17±0.01	3.59±0.01	This work
x=0.5	220	0.66±0.01	0.55±0.01	1.13±0.02	3.05±0.01	This work
Mean Field model	-	-	0.5	1	3	Kaul, 1985
3D Heisenberg model	-	-	0.365±0.003	1.336±0.004	4.80±0.04	Kaul, 1985
3D Ising model	-	-	0.325±0.002	1.241±0.002	4.82±0.02	Kaul, 1985
Tricritical mean field theory	-	-	0.25	1	5	Kaul, 1985

Hence, the construction of the universal curves for these compositions can be considered as a test of the accuracy of the critical exponents estimation presented here. For low applied field values, the curves of $\ln Mt^{-\beta}$ versus $\ln Ht^{-(\beta+\gamma)}$ have two branches, one for the isothermal curves at temperatures just below the critical temperature (upper branch) and the other for the curves at temperatures just above it (lower branch). For higher fields, these two branches converge into a single universal curve which confirms the fact that these compounds do belong to the same universality class. It can be clearly seen that all the data fall on two curves, one for $T<T_C$ and another for $T>T_C$ indicating that the obtained values of T_C, β, γ and δ are reasonably accurate.

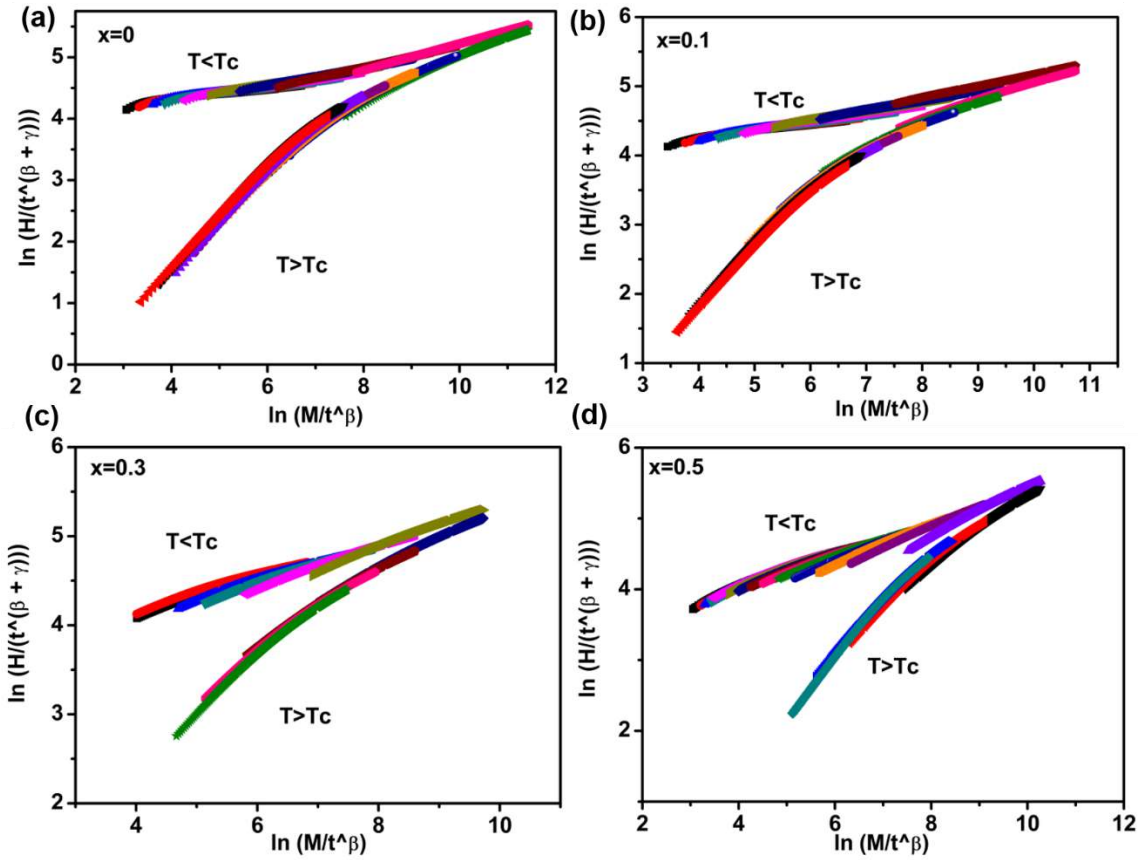

Figure 7.21. Scaling plots ($Mt^{-\beta}$ vs $Ht^{-(\beta+\gamma)}$) of $La_{0.7}Te_{0.3}Mn_{1-x}Co_xO_3$(x=0, 0.1, 0.3 and 0.5) below and above T_C in ln–ln scale.

7.4.Conclusions

The effect of Co doping at Mn-site on the structural, magnetic and magnetocaloric properties in the electron-doped manganites $La_{0.7}Te_{0.3}Mn_{1-x}Co_xO_3$ (x=0, 0.1, 0.2, 0.25, 0.3 and 0.5) has been investigated. XRD and Rietveld refinement confirm structural transition from rhombohedral (x=0 and x=0.1) to orthorhombic (x≥0.2). The structural transition is attributed to the disordered distribution of Mn^{2+}/Mn^{3+} and Co^{2+}/Co^{3+} ions which has been confirmed from XPS analysis. All samples undergo a paramagnetic–ferromagnetic phase transition. With increase in Co content to x=0.1, the T_c decreases, indicating the weakening of the double exchange interaction. However, with further increase in Co concentration, T_c increases, indicating a strong ferromagnetic exchange interaction. Reentrant spin glass behavior is observed at low doping concentrations due to the presence of competing FM-AFM exchange interactions. Magnetocaloric property of the electron-doped manganite has been investigated. Relatively large values and broad

temperature interval of MCE makes the present compounds promising candidates for sub-room magnetic refrigeration applications. Arrott plots reveal second order nature of magnetic transition for all the samples. Critical exponents have been deduced from the field dependence of MCE. The field and temperature dependent magnetization behavior follows the scaling theory, and all the data points fall on the two distinct branches; one for $T<T_C$ and the other for $T>T_C$ indicating that the critical exponents thus obtained are reasonably accurate. The magnetic exchange interactions for x=0.3 and 0.5 follow the mean-field theory.

Chapter 8

Summary and Scope for future work

This chapter provides a brief summary of the observations made during the investigation and scope for the future work. The significant results of the investigation are also outlined in this chapter.

8.1. Summary

The thesis is a detailed investigation on the structure, magnetic and magnetocaloric properties of Gd-Si-Ge based Intermetallics and Lanthanum Tellurium Manganites. The primary interest for choosing these alloys for the present investigation is to identify novel compositions exhibiting considerable MCE, which can act as a room temperature magnetic material. During the literature survey on Gd-Si-Ge based intermetallics, it was found that the presence of monoclinic phase gives rise to a GMCE in these materials due to the presence of FOPT. However, hysteresis associated with the FOPT lowers the use of these materials for practical applications. In this regard, efforts were made to develop materials with reduced hysteresis and MCE near room temperature. Electron doped manganites were also made a subject of study and the MCE property in these materials with Cobalt substitution is also investigated

8.1.1. Tuning the structural and magnetocaloric properties of $Gd_5Si_2Ge_2$ with Nd substitution

- $Gd_{5-x}Nd_xSi_2Ge_2$ based alloys with x=0, 0.05, 0.1 and 0.2 were synthesized by arc melting and the structure was investigated by Rietveld refinement. The parent compound crystallizes in a mixed phase of monoclinic and orthorhombic structures at room temperature. The Nd substituted compound with x=0.05 crystallizes in a monoclinic $Gd_5Si_2Ge_2$ structure with $P112_1/a$ space group and undergoes a first order phase transition with a Curie temperature of 275 K while the higher compositions adopt the orthorhombic Gd_5Si_4 structure with Pnma space group. With Nd substitution, the Curie temperature could be tuned to 300 K for x=0.1.
- Among the compounds studied, an MCE of 7.9, 3.7, and 3.2 J/kg K, respectively, for a field change of 20 kOe, and 12.8, 7.6, and 7.2 J/kg K, respectively, for 50 kOe has been obtained for x=0.05, 0.1 and 0.2 respectively. A large relative cooling power of 295, 205, and 188 J/kg are obtained for x = 0.05, 0.1, and 0.2, respectively, fulfilling the required criteria for a potential magnetic refrigerant in the room temperature regime.
- The effect of other rare earths such as Sm and Pr are discussed in Appendix A.

8.1.2. Observation of short range ferromagnetic interactions and magnetocaloric effect in cobalt substituted $Gd_5Si_2Ge_2$

- Cobalt substituted $Gd_5Si_{2-x}Co_xGe_2$ with x = 0, 0.1, 0.2 and 0.4 has been synthesized by arc melting and the structural studies using Rietveld refinement indicate that the samples crystallize in a combination of $Gd_5Si_2Ge_2$ and Gd_5Si_4 phases. Low-temperature X-ray diffraction measurements confirm the complete transformation from monoclinic to orthorhombic phase. It is found that martensitic transition temperature has been decreased by Co substitution.

- Double transition –first order and second order transitions are observed in $Gd_5Si_{2-x}Co_xGe_2$ with x = 0, 0.1, 0.2 and 0.4 with the appearance of short-range ferromagnetic correlations. The first order phase transition is due to a combined magneto structural transition from monoclinic paramagnetic phase to orthorhombic ferromagnetic phase on cooling while the second order transition arises from an orthorhombic paramagnetic to ferromagnetic phase on cooling. DC magnetization measurements reveal an anomalous low field magnetic behaviour indicating a Griffiths-like phase. This unusual behavior is attributed to the local disorder within the crystallographic structure indicating the presence of short-range magnetic correlations and ferromagnetic clustering, which is stabilized and enhanced by competing intra-layer and inter-layer magnetic interactions.

- The magnetostructural transition results in an MCE of 9 J/kg K at 260 K for x = 0.1, 8.5 J/kg K at 245 K for x = 0.2 and 4.2 J/kg K at 210 K for x = 0.4 for a field change of 50 kOe. Co substitution induces compelling crystallographic and magneto responsive effects in the Gd-Si-Ge system, which could be useful for potential and smart applications such as solid-state magnetic refrigeration and sensitive magnetic switching from paramagnetic to ferromagnetic state. Universal curve analysis has been carried out on the substituted samples to study the order of the magnetic transition.

8.1.3. Understanding the role played by cobalt and iron in tuning the magnetocaloric properties of $Gd_5Si_{1.7}Ge_{2.3}$

- A series of Cobalt substituted $Gd_5Si_{1.7}Co_xGe_{2.3-x}$ alloys with x = 0, 0.1, 0.2, 0.3 and 0.4 and iron substituted $Gd_5Si_{1.7}Fe_xGe_{2.3-x}$ alloys with x = 0, 0.1, 0.2, 0.3 and 0.4 has been synthesized by the arc melting process.
- X-ray diffraction studies together with magnetization measurements reveal a mixture of M and O(I) crystal structures at room temperature for lower doping concentrations ($x \leq 0.3$) while the higher doping concentrations result in an O(I) structure. Low field magnetization data taken in FCC and FCW mode indicate the presence of two transitions, a FOPT and a SOPT for x=0, 0.1, 0.2 and 0.3 while only a SOPT is evident for the composition with x=0.4.
- The maximum $-\Delta S_M$ for $Gd_5Si_{1.7}Ge_{2.3-x}Co_x$ are 12.8, 14.5, 10.4 and 5.8 J/kg K for x=0.1, 0.2, 0.3 and 0.4 respectively, for a field change of 50 kOe. For $Gd_5Si_{1.7}Ge_{2.3-x}Fe_x$ compounds, $-\Delta S_M$ is 11.2, 12.7, 8.3 and 7 J/kg K for x=0.1, 0.2, 0.3 and 0.4 respectively, for a field change of 50 kOe.
- The presence of Griffiths-like phases has been observed all the compositions for Co substituted compounds. In Fe substituted compounds, GP is evident for compositions upto x=0.3 while no such behavior has been observed for x=0.4. Universal curve analysis reveal the transition from first order to second order with increase in Co and Fe concentration.

8.1.4. Structural properties, magnetic interactions, magnetocaloric effect and critical behavior of cobalt doped $La_{0.7}Te_{0.3}MnO_3$

- Cobalt substituted $La_{0.7}Te_{0.3}Mn_{1-x}Co_xO_3$ (x = 0, 0.1, 0.2, 0.25, 0.3 and 0.5) has been synthesized by solid state reaction route in air. A structural transition from rhombohedral to orthorhombic structure occurs with increase in Cobalt substitution. XPS results indicate that the structural transition is due to the disordered distribution of Mn^{2+}/Mn^{3+} and Co^{2+}/Co^{3+} ions.
- For lower Co concentrations, the Curie temperature initially decreases from 165 K in parent compound to 160 K in x=0.1. With increase in Co concentration to x=0.2, the Curie temperatature increases to 162 K reaching 220 K for x=0.5. The increase in Curie temperature for higher doping concentrations is attributed to the

increase in magnetic exchange interactions with Co substitution. The presence of competing ferromagnetic and antiferromagnetic interactions leads to a glassy behaviour at low temperatures for low Co doping concentrations. However, for higher Co concentrations, no such behaviour is observed.

- Arrott plots reveal a second order nature of magnetic transition for all the samples. The magnetic exchange interactions for x = 0.3 and 0.5 follow the mean-field model. Magnetization results show that the magnetocaloric property of the electron-doped manganite is only slightly affected by the substitution of Co at Mn sites. Relatively large values of relative cooling power and broad temperature interval of the magnetocaloric effect make the present compounds promising for sub-room temperature magnetic refrigeration applications.

6.2. Scope for future work

- Temperature dependent neutron diffraction technique could provide deeper insight into the magnetic structure of substituted $Gd_5(Si_xGe_{1-x})_4$ alloys and Lanthanum Tellurium manganite. A detailed neutron diffraction measurement has to be performed to explore the exact reason behind the observation of Griffith's like behavior, spin-glass behavior and other properties.
- In addition to the MCE, the investigation of other functional properties such as magnetoresistance in substituted $Gd_5(Si_xGe_{1-x})_4$ can be useful in exploring the multifunctional characteristics suitable for various possible applications.
- The effect of other transition element on the magnetocaloric behavior and magnetoresistance of Lanthanum tellurium manganite will be explored.

Appendix A

Effect of Rare earths such as Sm and Pr on the MCE of $Gd_5Si_2Ge_2$

The effect of other rare earths such as Sm and Pr in $Gd_5Si_2Ge_2$ was investigated and did not yield any promising results. The results of Sm substitution is presented below. With Sm substitution $Gd_{5-x}Sm_xSi_2Ge_2$ with x=0.1, the Curie temperature was found to decrease to 245 K with decrease in $-\Delta S_M$ to 3.6 J/kg K at a field change of 50 kOe. This could be attributed to a second order transition taking place in the compound. Since samarium substitution produced very low entropy change, higher compositions were not attempted. On the other hand, with Pr substitution, the sample was found to oxidise very quickly. Since stable compositions are required as magnetic refrigerants, Pr substitution was not attempted.

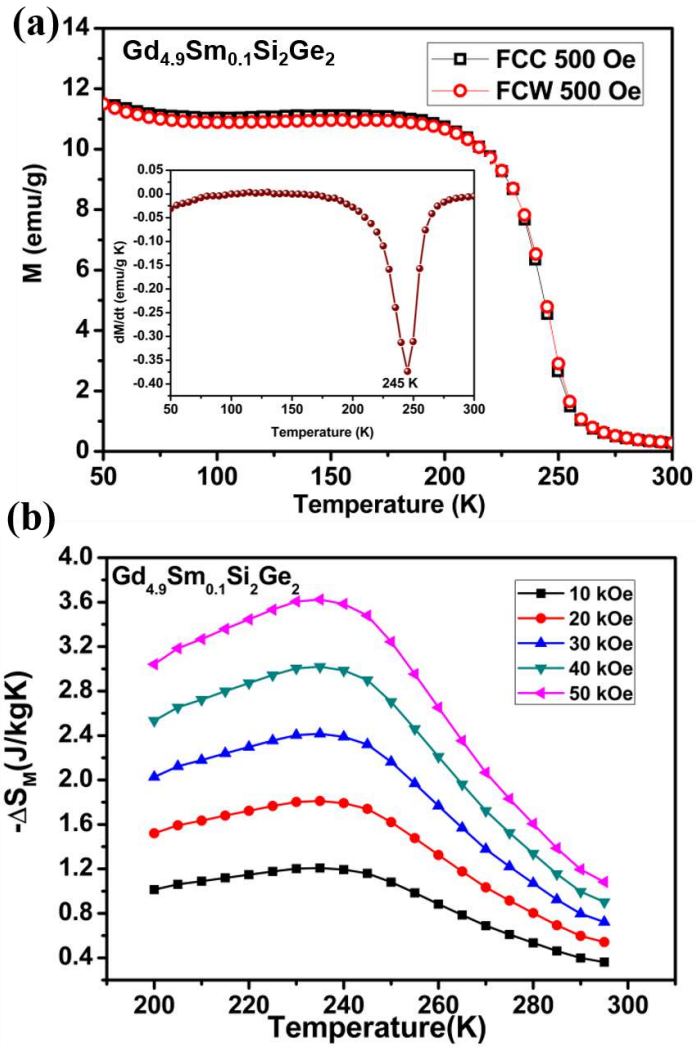

Figure A (a). Magnetization versus temperature curve of $Gd_{5-x}Sm_xSi_2Ge_2$ with x=0.1 at 500 Oe in FCC and FCW modes. Inset shows the dM/dT curves, (b) Entropy change for $Gd_{5-x}Sm_xSi_2Ge_2$ with x=0.1 at different fields.

List of Publications in SCI journals

1. **Bhagya Uthaman**, P. Manju, Senoy Thomas, Deepshikha Jaiswal Nagar, K. G. Suresh and Manoj Raama Varma, "Observation of short range ferromagnetic interactions and magnetocaloric effect in cobalt substituted $Gd_5Si_2Ge_2$", ***Phys. Chem. Chem. Phys.,*** 19, 12282 **(2017)**.
2. G. R. Raji, **Bhagya Uthaman**, Rajesh Kumar Rajan, Sharannia M. P., Senoy Thomas, K. G. Suresh and Manoj Raama Varm, "Martensitic transition, spin glass behavior and enhanced exchange bias in Si substituted $Ni_{50}Mn_{36}Sn_{14}$ Heusler alloys", ***RSC Adv.***, 6, 32037**(2016)**.
3. **Bhagya Uthaman**, K.S.Anand, Rajesh Kumar Rajan, Htet H. Kyaw, Senoy Thomas, Salim Al-Harthi, K.G.Suresh and Manoj Raama Varma, "Structural properties, magnetic interactions, magnetocaloric effect and critical behaviour of cobalt doped $La_{0.7}Te_{0.3}MnO_3$", ***RSC Adv.,*** 5, 86144 **(2015)**.
4. **Bhagya Uthaman** and Manoj Raama Varma, "Effect of Nd substitution on the structural and magnetocaloric properties of $Gd_5Si_2Ge_2$", ***Mater. Sci. Forum***, Vols. 830-831, 501 **(2015)**.
5. G. R. Raji, **Bhagya Uthaman**, Senoy Thomas, K. G. Suresh, and Manoj Raama Varma, "Magnetocaloric properties, exchange bias, and critical behavior of Ge substituted $Ni_{50}Mn_{36}Sn_{14}$ Heusler alloys", ***J. Appl. Phys.***, 117, 103908 **(2015)**.
6. **Bhagya Uthaman**, G. R. Raji, Senoy Thomas, K. G. Suresh, and Manoj Raama Varma, "Tuning the structural and magnetocaloric properties of $Gd_5Si_2Ge_2$ with Nd substitution", ***J. Appl. Phys.***, 117, 013910 **(2015)**.
7. **Bhagya Uthaman**, G. R. Raji, Rojerce Brown Job, Senoy Thomas, K. G. Suresh, and Manoj Raama Varma," Understanding the role played by Fe and Co in tuning the structural, magnetic and magnetocaloric properties of $Gd_5Si_{1.7}Ge_{2.3}$ (manuscript under preparation)

List of International/ National Conference Papers

1. **Bhagya Uthaman** and Manoj Raama Varma**,** "Observation of Short Ferromagnetic Interactions and Magnetocaloric Effect in Co and Fe doped $Gd_5Si_{1.7}Ge_{2.3}$", presented at International Conference on Magnetic Materials and Applications (ICMAGMA – 2017) held at Hyderabad, India during February 1 – 3, 2017. **(Poster Presentation)**
2. **Bhagya Uthaman** and Manoj Raama Varma,"Observation of Short Ferromagnetic Interactions and Magnetocaloric Effect in Cobalt substituted $Gd_5Si_2Ge_2$", presented at the 29th Kerala Science Congress held Mar Thoma College, Thiruvalla, Pathanamthitta during January 28-30, 2017.**(Oral Presentation)**
3. **Bhagya Uthaman**, Senoy Thomas and Manoj Raama Varma,"Observation of short-range ferromagnetic interactions and magnetocaloric effect in cobalt doped $Gd_5Si_2Ge_2$", presented at the National Conference on Materials Science and Technology (NCMST 2016) being organized during July 12-14, 2016 at the IIST (Valiamala) campus.**(Oral Presentation)**
4. **Bhagya Uthaman** and Manoj Raama Varma,"Effect of Nd substitution on the structural and magnetocaloric properties of $Gd_5Si_2Ge_2$ " presented at the International Conference on Advanced Materials and Manufacturing Processes for Strategic Sectors (ICAMPS 2015) held at Thiruvananthapuram during May 13-15, 2015. **(Poster Presentation)**
5. **Bhagya Uthaman**, G. R. Raji, Senoy Thomas, K. G. Suresh, and Manoj Raama Varma, "Tuning the structural and magnetocaloric properties of $Gd_5Si_2Ge_2$ with Nd substitution" presented at the International Conference on Science, Technology and Applications of Rare Earths (ICSTAR 2015) held at Thiruvananthapuram during April 23-25, 2015. **(Poster Presentation)**
6. **Bhagya Uthaman** and Manoj Raama Varma, "Synthesis and Characterization of Rare Earth substituted $La_{0.7}Sr_{0.3}MnO_3$ nanoparticles" presented at the 27th Kerala Science Congress held at Camelot Convention Centre, Pathirapally, Alappuzha during January 27-29, 2015. **(Poster Presentation)**
7. **Bhagya Uthaman**, V. R. Akshay, A. V. Anoop, M. Vasundhara and Manoj Raama Varma, "Structural and Magnetic properties of Nd-doped $Gd_5Si_2Ge_2$" presented at the International Conference on Magnetic Materials and

Applications, MagMA-2013 held at IIT Guwahati during December 5-7, 2013. **(Poster Presentation)**

References

Aghababyan, E.V., Harutyunyan, N.P., "Dynamic magnetic susceptibility of compounds in $Gd_5Si_{2-x}Ge_{2-x}Sn_{2x}$ (2x = 0 − 0.1) system", *J. Contemp. Phys. (Armenian Acad. Sci.),* 44, 2009, 197.

Ahmad, S.N., Akin, Y., Shaheen, S.A., "$Gd_5(Si,Ge)_4$ and Gd_2C compounds: Candidates for hyperthermia treatment of cancer", *J. Appl. Phys.*, 97, 2005, 10Q902.

Ahmad, S.N., Shaheen, S.A., "Optimization of $(Gd)_5 Si_4$ based materials: A step toward self-controlled hyperthermia applications", *J. Appl. Phys.*, 106, 2009, 064701.

Aksoy, S., Yucel, A., Elerman, Y., Krenke, T., Acet, M., Moya, X., Man ˜osa, L., "The influence of gallium on the magnetocaloric properties of $Gd_5Si_2Ge_2$", *J. Alloys Compd.*, 460, 2008, 94.

[a]Alves, C.S., Gama, S., Coelho, A.A., Plaza, E.J.R., Calvalho, A.M.G., Cardoso, L.P., Persiano, A.C., "Giant magnetocaloric effect in $Gd_5(Si_2Ge_2)$ alloy with low purity Gd", *Mater. Res.*, 7, 2004, 535.

[b]Alves, C. S., Colucci, C. C., Gama, S., Carvalho, A. M. C., Coelho, A. A., "Influence of hydrogen on the magnetic behaviour of Gd5Ge2Si2Hx, 0.1 ≤ x ≤2.5", *J. Magn. Magn. Mater.*, 272–276, 2004, 2391.

Anderson, P. W., "Antiferromagnetism: Theory of Superexchange Interaction" *Phy. Rev.*, 79, 1950, 350.

Anil Kumar, P., Mathieu, R., Nordblad, P., Sugata Ray, Olof Karis, Gabriella Andersson, Sarma, D. D., "Reentrant Superspin Glass Phase in a $La_{0.82}Ca_{0.18}MnO_3$ Ferromagnetic Insulator", *Phys. Rev. X*, 4, 2014, 011037.

Arai, Y., "Chemistry of powder production," Springer, London, 1996.

Banerjee, S. K., "On a generalised approach to first and second order magnetic transitions", *Phys. Lett.*, 12, 1964, 16.

Bejara, M., Feki, H., Dhahri, E., Ellouze, M., Balli, M., Hlil, E.K., "Effects of substituting divalent by monovalent ion on the physical properties of $La_{0.7}Ca_{0.3-x}K_xMnO_3$ compounds", *J. Magn. Magn. Mater.*, 316, 2007, e707.

Belo, J. H., Pereira, A. M., Ventura, J., Oliveira, G. N. P. , Araújo, J. P., Tavares, P. B., Fernandes, L., Algarabel, P. A., Magen, C., Morellon, L., Ibarra, M. R., "Phase control studies in $Gd_5Si_2Ge_2$ giant magnetocaloric compound", *J. Alloys Compd.*, 529, 2012, 89.

Belo, J. H., Pereira, A. M., Magen, C., Morellon, L., Ibarra, M. R., Algarabel, P. A., Araujo, J. P., "Critical magnetic behavior of magnetocaloric materials with the Gd_5Si_4- type structure", *J. Appl. Phys.*, 113, 2013, 133909.

Bish, D. L., Post, J. E., *Modern powder diffraction. Reviews in mineralogy*, Mineralogical society of America, Washington, 1989

Blundell, S., *Magnetism in condensed matter*, Oxford master series in condensed matter physics, Oxford university press, 2001.

Bonilla, C. M., HerreroAlbillos, J., Bartolome, F., Garcia, L. M., Parra-Borderias, M., Franco, V., "Universal behavior for magnetic entropy change in magnetocaloric materials: An analysis on the nature of phase transitions", *Phys. Rev. B: Condens. Matter Mater. Phys.*, 81, 2010, 224424.

Bray, A. J., "Nature of the Griffiths phase" *Phys. Rev. Lett.*, **59**, 586 (1987).

Brown, G.V., “Magnetic heat pumping near room temperature”, *J. Appl. Phys.* 47, 1976, 3673.

Bruck, E., “Developments in magnetocaloric refrigeration”,*J. Phys. D: Appl. Phys.*, 38, 2005, R381.

Carvalho, A. M. G., Alves, C. S., de Campos, A., Coelho, A. A., Gama, S., Gandra, F. C. G., von Ranke, P. J., Oliveira, N. A., “The magnetic and magnetocaloric properties of $Gd_5Ge_2Si_2$ compound under hydrostatic pressure”, *J. Appl. Phys.*, 97, 2005, 10M320.

Carvalho, A.M.G., Alves, C.S., Colucci, C.C., Bolanho, M.A., Coelho, A.A., Gama, S., Nascimento, F.C., Cardoso, L.P., “Effect of hydrogen on the structural, magnetic and magnetocaloric properties of the $Gd_5Ge_{2.1}Si_{1.9}$ compound”, *J. Alloys Compd.*, 432, 2007, 11.

Carvalho, A.M.G, Tedesco, J. C. G., Pires, M. J. M., Soffner, M. E. Guimaraes, A. O., Mansanares, A. M. and Coelho, A. A. “Large magnetocaloric effect and refrigerant capacity near room temperature in as-cast $Gd_5Ge_2Si_{2-x}Sn_x$ compounds”, *Appl. Phys. Lett.*, 102, 2013, 192410.

Chandrasekhar, K. D., Das, A. K., Venimadhav, A., “Spin glass behaviour and extrinsic origin of magnetodielectric effect in non-multiferroic La_2NiMnO_6 nanoparticles”, *J. Phys.: Condens. Matter*, 24, 2012, 376003.

Chang, C. L., Tai, M. F., Chung, T.W., Lee, F. Y., Su, Y. W., Liu, S. Y., Hwang, C. S., Tseng, P. K., Shi, J. B., “X-ray absorption spectroscopy study of the $La_{0.7}Ba_{0.3}Mn_{1-x}Co_xO_3$ system ”, *J. Magn. Magn. Mater.*, 209, 2000, 240.

Chatterjee, S., Giri , S., De, S. K., Majumdar, S., “Reentrant-spin-glass state in $Ni_2Mn_{1.36}Sn_{0.64}$ shape-memory alloy”, *Phys. Rev. B*, 79, 2010, 092410.

Chen, X., Chen, Y., Tang Y, Y., "Influence of 1523 K annealing on phase and magnetic properties in $(Gd_{1-x}Er_x)_5Si_2Ge_2$ compounds", *Bull. Mater. Sci.*, 34, 2011, 1103.

Choe, W., Pecharsky, V.K., Pecharsky, A.O., Gschneidner Jr., K.A., Young, V.G., Miller, G.J., "Making and Breaking Covalent Bonds across the Magnetic Transition in the Giant Magnetocaloric Material $Gd_5Si_2Ge_2$", *Phys. Rev. Lett.*, 84, 2000, 4617.

[a]Choe, W., Miller, G.J., Meyers, J., Chumbley, S., Pecharsky, A.O., ""Nanoscale Zippers" in the Crystalline Solid. Structural Variations in the Giant Magnetocaloric Material $Gd_5Si_{1.5}Ge_{2.5}$", *Chem. Mater.*, 15, 2003, 1413.

[b]Choe, W., Pecharsky, A.O., Worle, M., Miller, G.J., ""Nanoscale Zippers" in $Gd_5(Si_xGe_{1-x})_4$: Symmetry and Chemical Influences on the Nanoscale Zipping Action", *Inorg. Chem.*, 42, 2003, 8223.

Choudhury, D., Mandal, P., Mathieu, R., Hazarika, A., Rajan, S., Sundaresan, A., Waghmare, U. V., Knut, R., Karis, O., Nordblad, P., Sarma, D. D., "Near-Room-Temperature Colossal Magnetodielectricity and Multiglass Properties in Partially Disordered La_2NiMnO_6", *Phys. Rev. Lett.*, 108, 2012, 127201.

Coey, J. M. D., *Magnetism and magnetic materials*, Cambridge University Press, Cambridge, 2009.

Craus, M.L., Cornei , N., Lozovan , Mita, M., C., Dobrea, V., "Influence of Na and Cr substitutions on electronic phase diagram of $La_{0.54}Ho_{0.11}Ca_{1-x}Na_xMn_{1-y}Cr_yO_3$ manganites", *Rom. Rep. Phys.*, 62, 2010, 780.

Cullity, B. D., "Introduction to magnetic materials," Addison-wesely, USA, 1972.

Debye, P., "Einige Bemerkungen zur Magnetisierung bei tiefer Temperatur", *Ann. Phys. (Leipzig)*, 386, 1926, 1154.\

Deisenhofer, J., Braak, D., Krug von Nidda, H.-A., Hemberger, J., Eremina, R. M., Ivanshin, V. A., Balbashov, A. M., Jug, G., Loidl, A., Kimura , T., Tokura, Y. , "Observation of a Griffiths Phase in Paramagnetic $La_{1-x}Sr_xMnO_3$", *Phys. Rev. Lett.*, 95, 2005, 257202.

[a]Deng, J.Q., Zhuang, Y.H., Li, J.Q., Zhu, Q.M., "The magnetocaloric effect in $(Gd_{0.74}Tb_{0.26})_5(Si_xGe_{1-x})_4$ alloys", *Materials Letters*, 61, 2007, 2359.

[b]Deng, J.Q., Zhuang, Y.H., Li, J.Q., Zhou, K. W., "Magnetic phase transition and magnetocaloric effect in $(Gd_{1-x}Tb_x)_5Si_{1.72}Ge_{2.28}$ compounds", *J. Alloys Compd.*, 428, 2007,28.

Dho, J., Kim, W. S., Hur, N. H., "Reentrant Spin Glass Behavior in Cr-Doped Perovskite Manganite", *Phys. Rev. Lett.*, 89, 2002, 027202.

Dong, Q. Y. , Zhang, H. W., Sun, J. R., Shen, B. G. and Franco V., "A phenomenological fitting curve for the magnetocaloric effect of materials with a second-order phase transition", *J. Appl. Phys.*, 103, 2008, 116101.

Duan, P., Dai, S. Y., Tan, G. T., Lu, H. B., Zhou, Y. L., Cheng, B. L., Chen, Z. H., "Transport and magnetic properties of bulk $La_{1-x}Sb_xMnO_3$ (x = 0.05,0.1)", *J. Appl. Phys.*, 95, 2004, 5666.

Ewing, J.A., "On Effects of Retentiveness in the Magnetisation of Iron and Steel. (Preliminary Notice.)", *Proc. Roy. Soc.*, 24, 1882, 39.

Foldeaki, M., Chahine, R., Bose, T. K., "Magnetic measurements: A powerful tool in magnetic refrigerator design," *J. Appl. Phys.*, 77, 1995, 3528.

Foner, S., “Versatile and sensitive vibrating–sample magnetometer” *Rev. Sci. Instrum*., **30***, 1959,* 548.

Franco, V., Blazquez, J. S., Conde, A., “Field dependence of the magnetocaloric effect in materials with a second order phase transition: A master curve for the magnetic entropy change”, *Appl. Phys. Lett.*, 89, 2006, 222512.

Franco, V., Conde, C. F., Conde, A., and Kiss, L.F., “Enhanced magnetocaloric response in Cr/MoCr/Mo containing Nanoperm-type amorphous alloys”, *Appl. Phys. Lett.*, 90, 2007, 052509.

Franco, V., Conde, A., Provenzano, V., Shull, R.D., “Scaling analysis of the magnetocaloric effect in $Gd_5Si_2Ge_{1.9}X_{0.1}$ (X=Al, Cu, Ga, Mn, Fe, Co)”, *J. Magn. Magn. Mater.*, 322, 2010, 218.

Franco, V., Blazquez, J. S., Ingale, B., Conde, A., “The Magnetocaloric Effect and Magnetic Refrigeration Near Room Temperature: Materials and Models”, *Annu. Rev. Mater. Res.*, 42, 2012, 305.

Fu, H., Zu, X. T. and Shen, T. D. “Structure and phase transformation of melt-spun $Gd_5Ge_2Si_2$”, *Thermochim. Acta,* 445, 2006, 53.

Fujita, A., Fujieda, S., Hasegawa, Y., Fukamichi, K., “Itinerant-electron metamagnetic transition and large magnetocaloric effects in $La(Fe_xSi_{1-x})_{13}$ compounds and their hydrides”, *Phys. Rev. B*, 67, 2003, 104416.

Gama, S., Alves, C.S., Coelho, A.A., Ribeiro, C.A., Persiano, A.I.C., Silva, D., “On the determination of the phase composition of the $Gd_5Ge_2Si_2$ alloy”, *J. Magn. Magn. Mater.*, 272–276, 2004, 848.

Gebhardt, J. R., Roy, S., Ali, N., “Colossal magnetoresistance in Ce doped manganese oxides”, *J. Appl. Phys.*, 85, 1999, 5390.

Giauque, W.F., "A Thermodynamic Treatment of Certain Magnetic Effects. A Proposed Method of Producing Temperatures Considerably Below 1° Absolute", *J. Am. Chem. Soc.*, 49, 1927, 1864.

Giauque, W.F. and MacDougall, D.P. "Attainment of Temperatures Below 1◦ Absolute by Demagnetization of $Gd_2(SO_4)_3 \cdot H_2O$.", *Phys. Rev.* 43, 1933, 768.

Goldschmidt, V. M., "Die gesetze der krystallochemie," *Naturwissenschaften,* 14, 1926, 477.

Goodenough, J. B., "Theory of the Role of Covalence in the Perovskite-Type Manganites (La,M(II))MnO3" *Phys. Rev.*, 100, 1955, 564.

Goodenough, J. B., Wold, A., Arnott R. J., Menyuk, N., "Relationship Between Crystal Symmetry and Magnetic Properties of Ionic Compounds Containing Mn3+" *Phy. Rev.*, 124, 1961, 373.

Goodenough, J. B., "*Magnetism and chemical bond*" Interscience Publishers, New York, 1963.

Goodenough, J. B., "Handbook on the Physics and Chemistry of Rare Earths," Elsevier, 33, 2003, 249.

Griffiths R.B, "Nonanalytic behavior above the critical point in a Random Ising Ferromagnet", *Phys. Rev. Lett*., 23, 1969, 17.

Gschneidner Jr., K.A., Pecharsky, V.K., "Magnetic refrigeration materials (invited)", *J. Appl. Phys.*, 85 (8), 1999, 5365.

[a]Gschneidner Jr. K.A., Pecharsky, V. K., "Magnetocaloric materials", *Annu. Rev. Mater. Sci.*, 30, 2000, 387.

[b]Gschneidner Jr., K.A., Pecharsky, V.K., "The influence of magnetic field on the thermal properties of solids ", *Mater. Sci. Eng. A*, 287, 2000, 301.

Gschneidner Jr. K.A., Pecharsky, V. K., Tsokol, A. O., "Recent developments in magnetocaloric materials", *Rep. Prog. Phys.*, 68, 2005, 1479.

Guo, E. J., Wang, L., Wu, Z. P., Wang, L., Lu, H. B., Jin, K. J., Gao, J., "Phase diagram and spin-glass phenomena in electron-doped $La_{1-x}Hf_xMnO_3$ ($0.05 \leq x \leq 0.3$) manganite oxides", *J. Appl. Phys.*, 110, 2011, 113914.

Guo, H. Z., Chen, Z. H., Liu, L. F., Ding, S., Zhou, Y. L., Lu, H. B., Jin, K. J., Cheng, B., "Structural properties and spin–phonon coupling effect of $La_{1-x}Te_x MnO_3$ thin films", *Appl. Phys. Lett.*, 85, 2004, 3172.

Haldar, A., Suresh, K. G., Nigam, A. K., "Observation of re-entrant spin glass behavior in $(Ce_{1-x}Er_x)Fe_2$ compounds", *Europhys. Lett.*, 91, 2010, 67006

Hanasaki, N., Watanabe, K., Ohtsuka, T., Kézsmárki, I., Iguchi, S., Miyasaka, S., Tokura, Y., "Nature of the Transition between a Ferromagnetic Metal and a Spin-Glass Insulator in Pyrochlore Molybdates", *Phys. Rev. Lett.*, 99, 2007, 086401.

Haskel, D., Lee, Y.B., Harmon, B.N., Islam, Z., Lang, J.C., Srajer, G., Mudryk, Ya., Gschneidner Jr., K.A., Pecharsky, V.K., "Role of Ge in Bridging Ferromagnetism in the Giant Magnetocaloric $Gd_5(Ge_{1-x}Si_x)_4$ Alloys" Phys. Rev. Lett. 98, 2007, 247205.

Holtzberg, F., Gambino, R.J., McGuire, T.R., "New ferromagnetic 5 : 4 compounds in the rare earth silicon and germanium systems", *J. Phys. Chem. Solids*, 28, 1967, 2283.

Hou, X., Jie, X., Huang, J., Zeng, Z., Hu, H., Zhang, G., Xu, H., "Effect of B alloying on magnetocaloric effect of $Gd_{5.1}Si_2Ge_2$ alloy in low magnetic

field", *Progress in Natural Science: Materials International*, 21, 2011,413.

Hu, F. X., Shen, B. G., Sun, J. R., Cheng, Z. H., Rao, G. H., Zhang, X. X., "Influence of negative lattice expansion and metamagnetic transition on magnetic entropy change in the compound $LaFe_{11.4}Si_{1.6}$", *Appl. Phys. Lett.*, 78, 2001, 3675.

Huang, K., Statistical Machanics 2nd ed., Wiley, New York, 1987.

Hull, A. K., "A new method of chemical analysis" *Phil. Mag.*, **17**, 739, 1919.

Iglesias, J.E., Steinfink, H., "The crystal structure of Gd_5Si_4", *J. Less-Common Met.*, 26, 1972, 45

Jha, Mhamane, D., Suryawanshi, A., Joshi, S. M., Shaikh, P., Biradar, N., Ogale, S., Rode, C.V., *Catal. Sci. Technol.*, 2014, 4, 1771.

Jiang, W. J., Zhou, X. Z. , Williams, G., Mukovskii Y. and Glazyrin, K., "Griffiths phase and critical behavior in single-crystal $La_{0.7}Ba_{0.3}MnO_3$: Phase diagram for La1-*x*Ba*x*MnO3 ($x \leq 0.33$)" *Phys. Rev. B: Condens. Matter Mater. Phys.*, 77, 2008, 064424.

Jonason, K., Mattsson. J., Nordblad, P., "Dynamic susceptibility of a reentrant ferromagnet", *Phys. Rev. B*, 53, 1996, 6507.

Joule, J., "On the Calorific Effects of Magneto-Electricity, and on the Mechanical Value of Heat", *Phil. Mag.*, 23, 1843, 263.

Kanamori, J., "Superexchange interaction and symmetry properties of electron orbitals" *Phys. Chem. Solids*, 10, 1959, 87.

Kang, S. J. L., “Sintering, Densification, Grain Growth and Microstructure,” Elsevier Science, 2004.

Kapusta, C., Riedi, P. C., Sikora, M., Ibarra, M. R., “NMR Probe of Phase Segregation in Electron Doped Mixed Valence Manganites”, *Phys. Rev. Lett.*, 84, 2000, 4216.

Kaul, S. N., “Static critical phenomena in ferromagnets with quenched disorder”, *J. Magn. Magn. Mater.*, 53, 1985, 5.

Khmelevskyi, S., Mohn, P., “The order of the magnetic phase transitions in RCo_2 (R = rare earth) intermetallic compounds”, *J. Phys. Condens. Matter* 12, 2000, 9453–64.

Krenke, T., Duman, E., Acet, M., Wassermann, E., Moya, X., Mañosa, L., Planes, A., “Inverse magnetocaloric effect in ferromagnetic Ni–Mn–Sn alloys”, *Nature Mater.*, 4, 2005, 450.

Krivoruchko, V. N., Marchenko M. A., Melikhov, Y., “Griffiths phase, metal-insulator transition, and magnetoresistance of doped manganites”, *Phys. Rev. B: Condens. Matter Mater. Phys.*, 82, 2010, 064419.

Krivoruchko, V. N, “The Griffiths phase and the metal-insulator transition in substituted manganites”, Low Temp. Phys., 40(7), 2014, 586.

Levin, E. M., Pecharsky, V. K., Gschneidner, Jr. K. A., “Unusual magnetic behavior in $Gd_5(Si_{1.5}Ge_{2.5})$and $Gd_5(Si_2Ge_2)$”, *Phys. Rev. B*, 62, 2000,R14625.

Lewis, L.H., Yu, M.H., Welch, D.O., Gambino, R.J., “Manipulation of the metamagnetic transition and entropy change in $Gd_5(Si,Ge)_4$”, *J. Appl. Phys.*, 95, 2004, 6912.

Li, J.Q., Sun, W.A., Jian, Y.X., Zhuang, Y.H., Huang, W.D., Liang, J.K., "The giant magnetocaloric effect of $Gd_5Si_{1.95}Ge_{2.05}$ enhanced by Sn doping", *J. Appl. Phys.*, 100, 2006, 073904.

Magen, C., Morellon, L., Algarabel, P. A., Ibarra, M. R., Ritter, C., Pecharsky, A. O., Gschneidner, Jr. K. A., Pecharsky, V. K., "Evidence for a coupled magnetic-crystallographic transformation in $Nd_5(Si_{0.6}Ge_{0.4})_4$",*Phys. Rev. B*, 70, 2004,224429.

Magen, C., Morellon, L., Algarabel, P. A., Ibarra, M. R., Arnold Z., Kamarad, J., Lograsso, T. A., Schlagel, D. L., Pecharsky, V. K., Tsokol, A. O. and Gschneidner, Jr., K. A., "Hydrostatic pressure control of the magnetostructural phase transition in $Gd_5Si_2Ge_2$ single crystals", *Phys. Rev. B: Condens. Matter Mater. Phys*., 72, 2005, 024416.

Magen, C., Algarabel, P. A., Morellon, L., Araujo, J. P. , Ritter, C., Ibarra, M. R., Pereira, A. M. and Sousa, J. B., "Observation of a Griffiths-like Phase in the Magnetocaloric Compound $Tb_5Si_2Ge_2$", *Phys. Rev. Lett.*, 96, 2006, 167201

Mahato, R. N., Sethupathi, K., Sankaranarayanan, V.,R. Nirmala, "Co-existence of giant magnetoresistance and large magnetocaloric effect near room temperature in nanocrystalline $La_{0.7}Te_{0.3}MnO_3$", *J. Magn. Magn. Mater.*, 322 , 2010, 2537.

Mahato, R. N., Sethupathi, K., Sankaranarayanan, V., "Influence of grain size on magnetocaloric effect in the nanocrystalline $La_{0.8}Te_{0.2}MnO_3$", *Int. J. Nanosci.*, 10, 2011, 597600.

Maignan, A., Martin, C., Damay, F., Raveau, B., "Factors Governing the Magnetoresistance Properties of the Electron-Doped Manganites $Ca_{1-x}A_xMnO_3$ (A=Ln, Th)", *Chem. Mater.*, 10, 1998, 950.

Mandal, P., Das, S., "Transport properties of Ce-doped $RMnO_3$ (R= La, Pr, and Nd) manganites", *Phys. Rev. B*, 56, 1997, 15073.

Markovich, V., Puzniak, R., Wisniewski, F. A., Mogilyansky, D., Dolgin, B., Gorodetsky, G., Jung, G., "Irreversibility, remanence, and Griffiths phase in $Sm_{0.1}Ca_{0.9}MnO_3$ nanoparticles", *J. Appl. Phys.*, **113**, 2013, 233911.

[a]Mathieu, R., Svedlindh, P., Nordblad, P., "Memory and rejuvenation in a spin glass", *Europhys. Lett.*, 52, 2000, 441.

[b]Mathieu, R., Akahoshi, D., Asamitsu, A., Tomioka, Y., Tokura, Y., "Colossal Magnetoresistance without Phase Separation: Disorder-Induced Spin Glass State and Nanometer Scale Orbital-Charge Correlation in Half Doped Manganites", *Phys. Rev. Lett.*, 93, 2004, 227202.

McMichael, R. D., Ritter, J. J., Shull, R. D., "Magnetocaloric effects in RNiIn (R=Gd-Er) intermetallic compounds", *J. Appl. Phys.*, 73, 1993,6946.

Meenakshi, Kumar, A., Mahato, R. N., "Effect of Fe substitution on the structural, magnetic and magnetocaloric properties of nanocrystalline $La_{0.7}Te_{0.3}Mn_{1-x}Fe_xO_3$ (x=0.1 and 0.3)", *Physica B: Condensed Matter*., 511, 2017, 83

[a]Meyers, J., Chumbley, S., Choe, W., Miller, G.J., 2002a. "Microstructural analysis of twinned β-$Gd_5Si_2Ge_2$", *Phys. Rev. B*, 66, 2002, 012106.

[b]Meyers, J.S., Chumbley, L.S., Laabs, F., Pecharsky, A.O., "Determination of phases in as prepared $Gd_5(Si_xGe_{1-x})_4$, where $x \cong 1/2$", *Scripta Mater.*, 47, 2002, 509.

Min, L., Bing-feng, Y. U., "Development of magnetocaloric materials in room temperature magnetic refrigeration application in recent six years," *J.Cent. South Univ. Technol.*, 16, 2009, 1.

Misra, S., Miller, G.J., "On the distribution of tetrelide atoms (Si, Ge) in $Gd_5(Si_xGe_{1-x})_4$", J. *Solid State Chem.* 179, 2006, 2290.

Mitra, C., Raychaudhuri, P., Dorr, K., Müller, K. H., Schultz, L., Oppeneer, P. M., Wirth, S., "Observation of Minority Spin Character of the New Electron Doped Manganite $La_{0.7}Ce_{0.3}MnO_3$ from Tunneling Magnetoresistance", *Phys. Rev. Lett.*, 90, 2003, 017202.

Morelli, D.T., Mance, A. M., Mantese, J.V., Micheli, A. L., "Magnetocaloric properties of doped lanthanum manganite film", *J. Appl. Phys.* 79, 1996, 373

Morellon, L., Algarabel, P. A., Ibarra, M. R., Blasco, J., Garcia-Landa, B., Arnold, Z., Albertini, F., "Magnetic-field-induced structural phase transition in $Gd_5(Si1.8Ge_{2.2})$", *Phys. Rev. B*, 58, 1998, R14721.

Moulder, J.F., Stickle, W.F., Sobol, P. E., Bomben, K.D., *Handbook of X-ray Photoelectron Spectroscopy*, Perkin-Elmer Corporation, United States of America, 1992.

Mozharivskyj, Y., Pecharsky, A.O., Pecharsky, V.K., Miller, G.J., 2005. "On the high temperature phase transition of $Gd_5Si_2Ge_2$", *J. Am. Chem. Soc.*, 127, 2005, 317.

Mudryk, Y., Pecharsky, V.K. and Gschneidner, Jr., K.A., *Handbook on the Physics and Chemistry of Rare Earths*, Elsevier Science & Technology Books, North Holland, 2013.

Mydosh, J. A., *Spin Glasses: An Experimental Introduction*, Taylor and Francis, London, 1993.

Nanni, P., Viviani, M., Buscaglia, V., “Synthesis of dielectric ceramic materials, Handbook of Low and High Dielectric Constant and their Applications,” Academic Press, New York, 1999.

Navrotsky, A., Weidner, D. J., *Perovskite: A Structure of Great Interest to Geophysics and Material Science*, Eds. American Geophysical Union, Washington D. C., 1989.

[a]Nirmala, R.D., Morozkin, A. V.,Malik, S. K., “Magnetism and heat capacity of $Dy_5Si_2Ge_2$”, *Phys. Rev. B*, 75, 2007,094419.

[b]Nirmala, R.D., Kundaliya, C., Shinde, S.R., Amish G. Joshi., Morozkin, A.V., Malik,S.K., “Magnetism and magnetocaloric effect in $(Dy_xGd_{5-x})Si_2Ge_2$ ($0<x<5$) compounds”,*J. Appl. Phys.*, 101, 2007,123901.

Oesterreicher, H., Parker, F. T., “Magnetic cooling near Curie temperatures above 300 K”, *J. Appl. Phys.*, 55, 1984, 4334.

Onoda, G. Y., Hench, L. L., “Ceramic Processing before Firing,” Wiley Interscience, New York, 1978.

Opel, M., “Spintronic oxides grown by laser-MBE” *J. Phys. D: Appl. Phys.*, 45, 033001, 2012.

Ouyang Z. W., “Griffiths-like behavior in Ge-rich magnetocaloric compounds $Gd_5(Si_xGe_{1-x})_4$”, *J. Appl. Phys.*, 108, 2010, 033907.

Palacios, E., Rodrı ´guez-Velamaza ´n, J.A., Wang, G.F., Burriel, R., Cuello, G., Rodrı ´guez-Carvajal, J., “Magnetic structure of $Gd_5Si_2Ge_2$ and $Gd_5Si_2Ge_{1.9}M_{0.1}$ (M = Ga, Cu)”, *J. Phys. Condens. Matter*, 22, 2010, 446003.

Pakhomov, A. B., Wong, C. Y., Zhang, X. X., Wen, G. H., Wu, G.H., "Magnetization and Magnetocaloric Effect in Magnetic Shape Memory Alloys Ni–Mn–Ga", I*EEE Trans. Magn.*, 37, 2001, 2718.

Park, J. H., Cheong, S. W., Chen, C. T., "Double-exchange ferromagnetism in La ($Mn_{1-x}Co_x$)O_3", *Phys. Rev. B*, 55, 1997, 11072.

Park, J. H., "Reply to ''Comment on 'Double-exchange ferromagnetism in La ($Mn_{1-x}Co_x$)O_3'' *Phys. Rev. B*, 60, 1999, 7651.

Paul-Boncour, V., Mazet, T.,"Investigation of compounds for magnetocaloric applications: $YFe_2H_{4.2}$, $YFe_2D_{4.2,}$ and $Y_{0.5}Tb_{0.5}Fe_2D_{4.2}$", *J. Appl. Phys.* 105, 2009, 013914.

Pecharsky,V. K., Gschneidner, Jr., K. A., "Comparison of the Magnetocaloric Effect Derived from Heat Capacity, Direct and Magnetization Measurements," *Adv. Cryo. Engg.*, 42, 1996, 423.

[a]Pecharsky, V. K., Gschneidner, Jr. K. A., "Giant Magnetocaloric Effect in $Gd_5Si_2Ge_2$", *Phys. Rev. Lett.*, 78 (23), 1997, 4494.

[b]Pecharsky V. K. and Gschneidner, Jr., K. A., "Tunable magnetic regenerator alloys with a giant magnetocaloric effect for magnetic refrigeration from 20 to 290 K", *Appl. Phys. Lett.* 70 (24), 1997, 3299.

[c]Pecharsky, V. K., Gschneidner, Jr. K. A., "Phase relationships and crystallography in the pseudobmary system Gd_5Si_4-Gd_5Ge_4" *J. Alloys Compd.*, 260, 1997, 98.

[d]Pecharsky, V. K., Gschneidner, Jr. K. A., "Effect of alloying on the giant magnetocaloric effect of $Gd_5Ge_2Si_2$", *J. Magn. Magn. Mater.*,167, 1997, L179.

Pecharsky, V.K., Gschneidner Jr., K.A., 1998. Adv. Cryog. Eng. 43, 1729.

[a]Pecharsky V. K. and Gschneidner, Jr., K. A., "Magnetic refrigeration materials (invited)", *J. Appl. Phys.*, 85, 1999, 5365.

[b]Pecharsky V. K. and Gschneidner, Jr. K. A., "On the Calorific Effects of Magneto-Electricity, and on the Mechanical Value of Heat", *J. Magn. Magn. Mater.*, 200, 1999, 44

Pecharsky, V. K., Gschneidner, Jr., K. A., "$Gd_5(Si_xGe_{1-x})_4$: An Extremum Material", *Adv. Mater.*, 13, 2001, 683.

[a]Pecharsky, A. O., Gschneidner, Jr., K. A., Pecharsky, V. K., Schindler, C. E., "The room temperature metastable/stable phase relationships in the pseudo-binary Gd Si –Gd Ge system", *J. Alloys Compd.*, 338, 2002, 126.

[b]Pecharsky, V. K., Pecharsky, A. O., Gschneidner, Jr. K. A., "Uncovering the structure–property relationships in R_5 (Si_x Ge_{4-x}) intermetallic phases", *J. Alloys Compd.*, 344, 2002, 362.

[c]Pecharsky, V.K., Pecharsky, A.O., Gschneidner Jr., K.A., "Uncovering the structure–property relationships in $R_5(Si_xGe_{4-x})$ intermetallic phases", *J. Alloys Compd.*, 344, 2002, 362.

[a]Pecharsky, A. O., Gschneidner, Jr. K. A., Pecharsky, V. K., "The giant magnetocaloric effect of optimally prepared $Gd_5Ge_2Si_2$", *J. Appl. Phys.*, 93, 2003, 4722.

[b]Pecharsky, V.K., Holm, A.P., Gschneidner Jr., K.A., Rink, R., "Massive Magnetic-Field-Induced Structural Transformation in Gd_5Ge_4 and the Nature of the Giant Magnetocaloric Effect", *Phys. Rev. Lett.*, 91, 2003, 197204.

Pecharsky, V. K., Gschneidner, Jr. K. A., "Structure, magnetism, and thermodynamics of the novel rare earth-based R_5T_4 intermetallics", *Pure Appl. Chem.*, 79, 2007, 1383.

Pecharsky, V. K., Gschneidner, Jr., K.A., Mudryk, Y., Paudyal, D., "Making the most of the magnetic and lattice entropy changes", *J. Magn. Magn. Mater*. 321, 2009, 3541–47.

Pereira, A. M., Sousa, J. B., Araujo, J. P., Magen, C., Algarabel, P. A., Morellon, L., Marquina, C., Ibarra, M. R., "Structural and magnetic properties of $Ho_5(Si_xGe_{1-x})_4$", *Phys. Rev. B*, 77, 2008,134404.

Pereira, A. M., Morellon, L., Magen, C., Ventura, J., Algarabel, P. A., Ibarra, M. R., Sousa, J. B., Araujo, J. P., "Griffiths-like phase of magnetocaloric $R_5(Si_xGe_{1-x})_4$ (R = Gd, Tb, Dy, and Ho)",*Phys. Rev. B*, 82, 2010, 172406.

Pereira, A. M., dos Santos, A. M., Magen, C., Sousa, J. B. Algarabel, P. A. Ren, Y., Ritter, C., Morellon, L., Ibarra, M. R. and Arau ´jo, J. P., "Understanding the role played by Fe on the tuning of magnetocaloric effect in $Tb_5Si_2Ge_2$", *Appl. Phys. Lett.*, 98, 2011, 122501.

[a]Phan, M.H., Yu, S.C., "Review of the magnetocaloric effect in manganite materials", *J. Magn. Magn. Mater.*, 308, 2007, 325.

[b]Phan, M. H., Yu, S. C., "Magnetocaloric manganites: Progress and challenges," *Phys. Stat. Sol.*, 204, 2007, 4091.

[a]Podmiljs ˇak, B., McGuiness, P.J., Miklavic ˇ, B., Z ˇuz ˇek Roz ˇman, K., Kobe, S., "Magnetocaloric properties and nanoscale structure of Fe-doped $Gd_5Ge_2Si_2$ alloys", *J. Appl. Phys.*, 105, 2009, 07A941

[b]Podmiljs ˇak, B., S ˇkulj, I., Markoli, B., Z ˇuz ˇek Roz ˇman, K., McGuiness, P.J., Kobe, S., "Microstructural changes in Fe-doped $Gd_5Ge_2Si_2$", *J. Magn. Magn. Mater.*, 321, 2009, 300.

[c]Podmiljs ˇak, B., McGuiness, P.J., Mattern, N., Ehrenberg, H., Kobe, S., "Magnetocaloric Properties in the $Gd_5(Si_2Ge_2)_{1-z}$ Fe_z (z = 0 - 0.75) System and the Magnetic Properties of the Newly Formed $Gd_5(Si,Ge)_3$ Phase ", *IEEE Trans. Magn.*, 45, 2009, 4364.

Prahabar, K., Raj Kumar, D.M., Manivel Raja, M., Palit, M., Chandrasekaran, V., "Solidification behaviour and microstructural correlations in magnetocaloric Gd–Si–Ge–Nb alloys", *Mater. Sci. Eng. B*, 172, 2010, 294.

Prabahar, K., Raj Kumar, D. M., Manivel Raja, M., Chandrasekaran, V., "Phase analysis and magnetocaloric properties of Zr substitutedGd–Si–Ge alloys", *J. Magn. Magn. Mater.*,323, 2011,1755.

Pramanik, A. K., Banerjee, A., "Griffiths phase and its evolution with Mn-site disorder in the half-doped manganite $Pr_{0.5}Sr_{0.5}Mn_{1-y}Ga_yO_3$ (y=0.0, 0.025, and 0.05)" *Phys. Rev. B*, 81, 2010, 024431.

Provenzano, V., Li, J., King, T., Canavan, E., Shirron, P., Di Pirro, M., Shull, R. D., "Enhanced magnetocaloric effects in $R_3(Ga_{1-x}Fe_x)_5O_{12}$ (R=Gd, Dy, Ho; $0 \leq x \leq 1$) nanocomposites", *J. Magn. Magn. Mater.*, 266, 2003, 185.

Provenzano, V., Shapiro, A. J., Shull, R. D., "Reduction of hysteresis losses in the magnetic refrigerant $Gd_5Ge_2Si_2$ by the addition of iron", *Nature*, 429, 2004, 853.

Raj Kumar, D.M., Manivel Raja, M., Goplan, R., Balamuralikrishnan, R., Singh, A.K., Chandrasekaran, V.,. "Microstructure and magnetocaloric effect in $Gd_5Si_2(Ge_{1-x}Ga_x)_2$ alloys", *J. Alloys Compd.*, 461, 2008, 14.

Raj Kumar, D.M., Manivel Raja, M., Gopalan, R., Sambasiva Rao, A., Chandrasekaran, V., "Effect of Fe-substitution on microstructure, hysteresis behaviour and magnetocaloric effect in $Gd_5Si_2Ge_2$ Alloys", J. Magn. Magn. Mater. 321, 2009, 1300

Rajkumar, D.M., Manivel Raja, M., Gopalan, R., Singh, A.K., Chandrasekaran, V., Suresh, K.G., "Effect of Fe addition on microstructure and magnetocaloric effect in $Gd_5Si_xGe_{3.9-x}Fe_{0.1}$ alloys with varying Si/Ge ratio", *Intermetallics,* 18, 2010, 518.

Rao, G.H., "Correlation between crystal structure and magnetic properties of $Gd_5(Si_xGe_{1-x})_4$ compounds", *J. Phys. Condens. Matter*, 12, 2000, L93.

Raveau, B., Maignan, A., Martin, C., Hervieu, M., "Colossal Magnetoresistance Manganite Perovskites: Relations between Crystal Chemistry and Properties", *Chem. Mater.*, 10, 1998, 2641.

Raychaudhuri, P., Mitra, C., Mann, P. D. A., Wirth, S., "Phase diagram and Hall effect of the electron doped manganite $La_{1-x}Ce_xMnO_3$", *J. Appl. Phys.*, 93, 2003, 8328.

Rietveld, H. M., "A profile refinement method for nuclear and magnetic structures"*J. Appl. Cryst.*, **2**, 65, 1969.

Roy, S., Ali, N., "Charge transport and colossal magnetoresistance phenomenon in $La_{1-x}Zr_xMnO_3$", *J. Appl. Phys.*, 89, 2001, 7425.

Samanta, T., Das, I., Banerjee, S., "Giant magnetocaloric effect in antiferromagnetic $ErRu_2Si_2$ compound", *Appl. Phys. Lett.*, 91, 2007, 152506.

Sampathkumaran, E. V., Mohapatra, N., Rayaprol S., Iyer, K. K., "Magnetic anomalies in the spin-chain compound Sr_3CuRhO_6: Griffiths-phase-like

behaviour of magnetic susceptibility", *Phys. Rev. B: Condens. Matter Mater. Phys*., 75, 2007, 052412.

Shannon, R.D., "Revised effective ionic radii and systematic studies of interatomic distances in halides and chalcogenides", *Acta Crystallographica Section A: Crystal Physic*, 32, 1976, 751.

Shull, R. D., Provenzano, V., Shapiro, A. J., Fu, A., Lufaso, M. W., Karapetrova, J., Kletetschka, G., Mikula, V., "The effects of small metal additions (Co,Cu,Ga,Mn,Al,Bi,Sn) on the magnetocaloric properties of the $Gd_5Ge_2Si_2$ alloy", *J. Appl. Phys.*, 99, 2006, 08K908.

Singh, N. K., Suresh, K.G., Nigam, A.K., Mali, S.K., Coelho, A.A., Gama, S., "Itinerant electron metamagnetism and magnetocaloric effect in RCo_2-based Laves phase compounds", *J. Magn. Magn. Mater.* 317, 2007, 68

Smith, G.S., Tharp, A.G., Johnson, Q., "Crystallographic Data on New Rare Earth- Germanium and Silicon Compounds", *Nature*, 210, 1966, 1148.

[a]Smith, G.S., Johnson, Q., Tharp, A.G., "Crystal Structure of Sm_5Ge_4" *Acta Cryst.* 22, 1967, 269.

[b]Smith, G.S., Tharp, A.G., Johnson, Q., "Rare earth-germanium and-silicon compounds at 5: 4 and 5: 3 compositions", *Acta Cryst.* 22, 1967, 940.

Smith, A., "Who discovered the magnetocaloric effect? Warburg, Weiss, and the connection between magnetism and heat", *Eur. Phys. J. H*., 38, 2013, 507.

Spladin, N. A., *Magnetic materials Fundamentals and Applications*, Cambridge University Press, New York, 2011.

[a]Stanley, H. E., *Introduction to Phase Transition and Critical Phenomena*, Oxford University Press, London, 1971.

[b]Stanley, H. E., "Scaling, universality, and renormalization: Three pillars of modern critical phenomena", *Rev. Mod. Phys.*, 71, 1999, S358.

Tai, M. F., Lee, F.Y., Shi, J. B., "Co doping effect on the crystal structure, magnetoresistance and magnetic properties of an $(La_{0.7}Ba_{0.3})(Mn_{1-x}Co_x)O_3$ system with x=0-1.0" *J. Magn. Magn. Mater.*, 209, 2000, 148.

[a]Tan, G. T., Dai, S. Y., Duan, P., Zhou, Y. L., Lu, H. B., Chen, Z. H., "Structural, electric and magnetic properties of the electron-doped manganese oxide: $La_{1-x}Te_xMnO_3$ (x = 0.1, 0.15)", *J. Appl. Phys.*, 93, 2003, 5480.

[b]Tan, G. T., Dai, S. Y., Duan, P., Zhou, Y. L., Lu, H. B., Chen, Z. H., "Colossal magnetoresistance behavior and ESR studies of $La_{1-x}Te_xMnO_3$ ($0.04 \leq x \leq 0.2$)", *Phys. Rev. B*, 68, 2003, 014426.

[c]Tan, G., Duan, P., Dai, S., Chen, Z. H., Lu, H. B., Zhou, Y. L., "Colossal magnetoresistance and spin-glass properties of $La_{1-x}Te_xMnO_3$ (x = 0.04, 0.1)", *Chin. Sci. Bull.*, 48(13), 2003, 1321.

[a]Tegus, O., Bruck, E., Buschow, K. H. J., deBoer, F. R., "Transition-metal-based magnetic refrigerants for room-temperature applications", *Nature*, 415, 2002,150.

[b]Tegus, O., Dagula, O., Bruck, E., Zhang, L., deBoer, F. R., Buschow,K. H. J., "Magnetic and magneto-caloric properties of $Tb_5Ge_2Si_2$", *J. Appl. Phys.*, 91, 2002,8534.

Thomson, W., *Cyclopedia of the Physical Sciences*, 2nd edn., J.P. Nichol (ed.). Richard Green and Company, London and Glasgow, 1860.

Thomson, W., "On the Thermoelastic, Thermomagnetic, and Pyroelectric Properties of Matter", *Phil. Mag.*, 5, 1878, 4.

Thuy, N. P., Nong, N. V., Hien, N. T., Tai, L. T., Vinh, T. Q., Thang, P. D., Bruck, E.,"Magnetic properties and magnetocaloric effect of $Tb_5(Si_xGe_{1-x})_4$ compounds", *J. Magn. Magn. Mater.*,242–245, 2002, 841.

Tishin, A. M., *Handbook of Magnetic Materials*, edited by K. H. J. Buschow, North Holland, Amsterdam, 1999.

Tishin, A.M., Gschneidner, Jr., K.A., Pecharsky, V. K., "Magnetocaloric effect and heat capacity in the phase-transition region", *Phys. Rev. B*, 59, 1999, 503.

Tishin, A. M., Spichkin, Y. I., "*The Magnetocaloric Effect and its Applications*," Taylor & Francis, Bristol, 2003.

Toby, B. H., "EXPGUI, a graphical user interface for GSAS," *J. Appl. Cryst.*, 34, 2001, 210.

Tokura, Y., Tomioka, Y, "Colossal magnetoresistive manganites" *J. Mag. Mag. Mater.*, **200**, 1999, 1.

Tokura, Y., "*Colossal magnetoresistive oxides*," Gordon and Breach Science, The Netherlands, 2000.

Toulemonde, O., Studer, F., Raveau, B., "Magnetic interactions studies of Co and Ni-doped manganites using soft XMCD "*Solid State Commun.*, 118, 2001, 107.

Viswanathan, M., Kumar, P. S. A., "Observation of reentrant spin glass behavior in $LaCo_{0.5}Ni_{0.5}O_3$", *Phys. Rev. B*, 80, 2009, 012410.

Vojta, T., "Rare region effects at classical, quantum and nonequilibrium phase transitions" *J. Phys. A: Math. Gen.*, 39, 2006, R143.

Wada, H., Tanabe, Y., “Giant magnetocaloric effect of MnAs1-xSbx”, *Appl. Phys. Lett.,* 79, 2001, 3302.

Wang, D. J., Sun, J. R., Zhang, S. Y., Liu, G. J., Shen, B. G., Tian, H. F., Li, J. Q., “Hall effect in $La_{0.7}Ce_{0.3}MnO_{3+}$ films with variable oxygen content”, *Phys. Rev. B,* 73, 2006, 144403.

Wang, Y. C., Yang, H. F., Huang, Q., Duan, L. B., Lynn, J. W., Rao, G. H., “Magnetic and crystal structures of the polymorphic $Pr_5Si_2Ge_2$ compound”, *Phys. Rev. B,* 76, 2007, 064425.

Wang, Y., Fan, H. J., “Magnetic phase diagram and critical behavior of electron-doped $La_xCa_{1-x}MnO_3$ ($0 \leq x \leq 0.25$) nanoparticles ”, *Phys. Rev. B,* 83, 2011, 224409.

Warburg, E., “Magnetische Untersuchungen. Ueber einige Wirkungen der Co¨ ercitivkraft”, *Ann. Phys. (Leipzig),* 249, 1881, 141.

Warburg, E and H¨onig, L., “Ueber die W¨ arme, welche durch periodisch wechselnde Kr¨ afte im Eisen erzeugt wird”, *Ann. Phys. (Leipzig),* 256, 1882, 814.

Weiss, P. and Piccard, A., “Le ph´ enom` ene magn´ etocalorique”, *J. Phys. (Paris),* 7, 1917, 103.

Weiss, P. and Piccard, A., “Sur un nouveau ph´ enom` ene magn´ etocalorique”, *Comptes Rendus,* 166, 1918, 352.

Wohlfarth, E.P., Rhodes, P., “Collective electron metamagnetism”, *Philos. Mag.* 7, 1962, 1817.

Wu, W., Tsokol, A.O., Gschneidner Jr., K.A., Sampaio, J.A.," Influence of oxygen on the giant magnetocaloric effect of $Gd_5Si_{1.95}Ge_{2.05}$ ", *J. Alloys Compd.*, 403, 2005, 118.

Yan, A., Handstein, A., Kerschl, P., Nenkov, K., Mu ¨ller, K.-H., Gutfleisch, O., 2004. "Effect of composition and cooling rate on the structure and magnetic entropy change in $Gd_5Si_xGe_{4-x}$", *J. Appl. Phys.*, 95, 2004, 7064.

[a]Yang, J., Zhao, B. C., Zhang, R. L., Ma, Y. Q., Sheng, Z. G., Song, W. H., Sun, Y. P., "The effect of grain size on electrical transport and magnetic properties of $La_{0.9}Te_{0.1}MnO_3$", *Solid State Commun.*, 132, 2004, 83.

[b]Yang, J., Song, W. H., Ma, Y. Q., Zhang, R. L., Zhao, B. C., Sheng, Z. G., Zheng, G. H., Dai, J. M., Sun, Y. P., "Structural, magnetic and transport properties in the Pr-doped manganites $La_{0.9-x}Pr_xTe_{0.1}MnO_3$ ($0 \leq x \leq 0.9$)", *Phys. Rev. B*, 70, 2004, 144421.

[c]Yang, J., Song, W. H., Ma, Y. Q., Zhang, R. L., Zhao, B. C., Sheng, Z. G., Zheng, G. H., Dai, J. M., Sun, Y. P., "Structural, magnetic, and transport properties of the Cu-doped manganite $La_{0.85}Te_{0.15}Mn_{1-x}Cu_xO_3$ ($0 \leq x \leq 0.20$)", *Phys. Rev. B*, 70, 2004, 092504.

Yang, J., Song, W. H., Ma, Y. Q., Zhang, R. L., Zhao, B. C., Sheng, Z. G., Zheng, G. H., Dai, J. M., Sun, Y. P., Sun, "Insulator–metal transition and the magnetic phase diagram of $La_{1-x}Te_xMnO_3$ ($0.1 \leq x \leq 0.6$)", *Mater. Chem. Phys*, 94, 2005, 62.

Yang, J., Lee, Y. P., Li, Y., "Magnetocaloric effect of electron-doped manganite $La_{0.9}Te_{0.1}MnO_3$", J. Appl. Phys., 102, 2007, 033913.

Young, R. A., *The method of rietveld analysis*, Oxford University Press, 1993.

Yu, B. F., Gao, Q., Zhang, B., Meng, X. Z., Chen, Z., "Review on research of room temperature magnetic refrigeration," *Int. J. Refrig.*, 26, 2003, 622.

Yucel, A., Elerman, Y., Aksoy, S., "Changes in the phase structure and magnetic characteristics of $Gd_5Si_2Ge_2$ when alloyed with Mn", *J. Alloys Compd.*, 420, 2006, 182.

Yuzuak, E., Dincer, I., Elerman, Y., "Magnetocaloric properties of the $Gd_5Si_{2.05-x}Ge_{1.95-x}Mn_{2x}$ compounds", *J. Rare Earths*, 28, 2010, 477.

Zaanen, J., Sawatzky, G. A., Allen, J. W., "Band Gaps and Electronic Structure of Transition-Metal Compounds", *Phys. Rev. Lett.*, 55, 1985, 418.

Zener, C., "Interaction Between the d Shells in the Transition Metals" *Phys. Rev.*, 81, 1950, 440.

Zener, C., "Interaction between the d-Shells in the Transition Metals. II. Ferromagnetic Compounds of Manganese with Perovskite Structure" *Phy. Rev.*, 82, 1951, 403.

Zhang, Q., Cho, J.H., Li, B., Hu, W.J., Zhang, Z.D., "Magnetocaloric effect in Ho_2In over a wide temperature range", *Appl. Phys. Lett.* 94, 2009, 182501.

Zhang, T., Chen, Y., Tang, Y., Du, H., Ren, T., Tu, M., "The phase formation and thermal hysteresis of $Gd_5Si_2Ge_2$ with the addition of transition elements (Mn, Fe, Co, Ni)", *J. Alloys Compd.*, 433, 2007, 18

Zhang, T., Chen, Y., Tang, Y., Ren, T., Tu, M., "The easy formation of the monoclinic MCE phase in $Gd_5Si_2Ge_2$ with the addition of Sn", *Mater. Char.*, 59, 2008, 1518.

Zhang, X. X., Tejada, J., Xin, Y., Sun, G.F., Wong, K.W., Bohigas, X., "Magnetocaloric effect in $La_{0.67}Ca_{0.33}MnO_{\delta}$ and $La_{0.60}Y_{0.07}Ca_{0.33}MnO_{\delta}$ bulk materials", *Appl. Phys. Lett.* 69, 1996, 3596.

Zhuang, Y.H., Li, J.Q., Huang, W.D., Sun, W.A., Ao, W.Q.,"Giant magnetocaloric effect enhanced by Pb-doping in $Gd_5Si_2Ge_2$ compound", *J. Alloys Compd.*, 421, 2006, 49

Sun, Y.P., Zhu, X.B., Song, W.H., "Structure, magnetic, and transport properties of the Co-doped manganites $La_{0.9}Te_{0.1}Mn_{1-x}Co_xO_3$ ($0 \leq x \leq 0.25$) ", *Solid State Commun.*, 137, 2006, 326.

Zheng, G.H., Ma, Y.Q., Zhu, X.B., Sun, Y. P., "Effects of Cr doping in electron-doped manganites $La_{0.9}Te_{0.1}MnO_3$", *Solid State Comm.*, 142, 2007, 217.

Zou, J. D., "Magnetocaloric and barocaloric effects in a $Gd_5Si_2Ge_2$ compound", *Chin. Phys. B*, 21(3), 2012, 037503.

Zhong, X. C., Min, J. X., Liu, Z. W., Zheng, Z. G., Zeng, D. C., Franco, V., Ramanujan, R. V., "Low hysteresis and large room temperature magnetocaloric effect of $Gd_5Si_{2.05-x}Ge_{1.95-x}Ni_{2x}$ ($2x = 0.08, 0.1$) alloys", *J. Appl. Phys.*, 113, 2013,17A916.

Zhou, W., Ouyang, C., Wu, J., Zhang, F., Huang, J., Gao, Y., Chu, J., "High performance of Mn-Co-Ni-O spinel nanofilms sputtered from acetate precursors", *Scientific Reports*, 5, 2015, 10899.

Zhuang, Y.H., Li, J.Q., Huang, W.D., Sun, W.A., Ao, W.Q., "Giant magnetocaloric effect enhanced by Pb-doping in $Gd_5Si_2Ge_2$ compound", *J. Alloys Compd.*, 421, 2006, 49.

Zimm, C., Jastrab, A., Sternberg, A., Pecharsky, V. K., Gschneidner Jr., K. A., Osborne, M. and Anderson, I., "Description and Performance of a Near-

Room Temperature Magnetic Refrigerator", *Adv. Cryog. Eng.*, 43, 1998, 1759.